**CENTER OF RESEARCH AND ADVANCED STUDIES**
**OF THE NATIONAL POLYTECHNICAL INSTITUTE**

**UNIT IN MÉRIDA**

**DEPARTAMENT OF APPLIED PHYSICS**

# $K^0_S$ production at high $Q^2$ in deep inelastic $ep$ scattering at H1

A dissertation submitted by

**Julia Elizabeth Ruiz Tabasco**

for the degree of

**Doctor in applied physics**

Thesis Supervisor
Dr. Jesús Guillermo Contreras Nuño.

Mérida, Yucatán, México.                                    May 2010

**CENTRO DE INVESTIGACIÓN Y DE ESTUDIOS AVANZADOS DEL INSTITUTO POLITÉCNICO NACIONAL**

**UNIDAD MÉRIDA**

**DEPARTAMENTO DE FÍSICA APLICADA**

# Producción de $K_S^0$ a $Q^2$ altas en dispersión $ep$ inelástica profunda en H1

Tesis que presenta

**Julia Elizabeth Ruiz Tabasco**

para obtener el grado de

**Doctora en Ciencias**

en la especialidad de

**Física Aplicada**

Director de Tesis
Dr. Jesús Guillermo Contreras Nuño.

Mérida, Yucatán, México.                    Mayo de 2010

All truths are easy to understand once they are discovered;

the point is to discover them.

(Galileo Galilei)

# Acknowledgements

*Eduard de la Cruz Burelo, Dr. Francisco Larios Forte, Dr. Juan José Alvarado Gil, and Dr. J. Guillermo Contreras Nuño.*

*To Ms. Angela Lucati for the beautiful friendship, the tasty apple pies and the pleasant talks in the office. For her interest in learning Spanish and the enormous support offered during the time living in Hamburg, but mainly for her patience and disposition to help during my first days of stay at DESY. To Dr. Andrea Vargas for her company in the search of Mexican ingredients in Hamburg, for the nice afternoons cooking in her house and the nice talks that reminded me my country.*

*To Anastasia Grebenyuk, Tobias Toll, Lluis Marti, Federico Von Samson, Axel Cholewa, Michal Deak, Zlatka Staykova, Krzysztof Kutak, Albert Kutson and Krzysztof Nowak for doing the life so funny in Hamburg, for the laughters in the meetings of 'physics and cookies' and also, why not?, for the discussions of politic, economy, literature and physics.*

*And the last in the list but the first in my heart, to my dear friends of the drunk band: Dulce Valdes, José Luis Albornoz, Benjamín Palma, Roberto Ramírez, Miguel López, Roberto Escalante, Marco Izozorbe, Carlos Perera and Johny Martínez, to offer me their invaluable friendship and for acceptting me among them, but specially for letting me be the strange girl.*

# Agradecimientos

*Agradezco enormemente a mis padres, el Prof. Agustín Ruiz y Uex y la Sra. María Elizabeth Tabasco Ruz por la educación brindada, por enseñarme a luchar contra los obstaculos y no dejar las cosas sin terminar. Por el continuo apoyo apesar de mis espontáneas decisiones respecto a la vida académica y privada, e incluso por esos adioses y buenos deseos acompañados de bonitas sonrisas aun cuando en el fondo no querían dejarme ir. Gracias a mis cuatro hermanas Nalleli, Adriana, Delmira y Leydi por los bonitos momentos que hemos compartido a lo largo de nuestros años juntas, especialmente a Nalle por aquellas 'pláticas ' que se convertían en interminables risas hasta que el estomago dolía. Gracias a tí y a Delmi por darme la alegría de ser niña otra vez al jugar con mis sobrinos. Gracias eternas a esa casa de locos en Tizimín que me convirtió en lo que ahora soy.*

*Quiero agradecer también a mi esposo el Ing. Luis R. Dzib Eliodoro por su apoyo incondicional, por darme la oportunidad de desarrollarme profesionalmente y alentarme a realizar las cosas aún cuando todo parece estar en contra. Por esa manera optimista de vivir, por ayudarme a sobrellevar mis frustraciones y decepciones en esas largas conversaciones bebiendo una cerveza, pero sobre todo por emprender a mi lado una linda etapa de la vida.*

*Gracias especiales a mi supervisor de tesis, el Dr. Jesús Guillermo Contreras Nuño por confiar en mi capacidad, por contestar a mis interminables preguntas no solo del trabajo sino todas aquellas que en algun momento formulé. Por responder a mis cientos de emails cuando no era posible coincidir en el mismo lugar. Por el apoyo durante los dias de enojo o desánimo, por saber como tratar conmigo apesar de mi caracter y por brindarme la oportunidad de trabajar a su lado.*

*Un agradecimiento eterno para el Dr. Daniel Traynor de la universidad Queen Mary de Londres por aceptar ser supervisor de mi análisis durante el tiempo que es-*

xiii

# Abstract

The production of $K_S^0$ mesons is studied using deep-inelastic scattering events (DIS) recorded with the H1 detector at the HERA $ep$ collider. The measurements are performed in the phase space defined by the four-momentum transfer squared of the photon, 145 GeV$^2$ < $Q^2$. The differential production cross sections of the $K_S^0$ meson are presented as function of the kinematic variables $Q^2$ and $x$, the transverse momentum $p_T$ and the pseudorapidity $\eta$ of the particle in laboratory frame, and as function of the momentum fraction $x_p^{BF}$ and transverse momentum $p_T^{BF}$ in the Breit Frame. Moreover, the $K_S^0$ production rate is compared to the production of charged particles and to the production of DIS events in the same region of phase space. The data are compared to theoretical predictions, based on leading order Monte Carlo programs with matched parton showers. The Monte Carlo models are also used for studies of the flavour contribution to the $K_S^0$ production and parton density function dependence.

# Resumen

La producción de mesones $K_S^0$ es estudiada usando eventos de dispersión inelástica profunda (DIS) tomados con el detector H1 en el colisionador $ep$ HERA. Las mediciones se realizan en el espacio fase definido por el cuadrado del cuadrimomento transferido del fotón, $145 \text{ GeV}^2 < Q^2$. Las secciones trasversales diferenciales de la producción de $K_S^0$ se presentan en función de las variables cinemáticas $Q^2$ y $x$, el momento transverso $p_T$ y la pseudorapidez $\eta$ de la partícula en el marco del laboratorio, y en función de la fracción de momento $x_p^{BF}$ and momento transverso $p_T^{BF}$ en el marco Breit. Mas aún, la producción de los mesones $K_S^0$ se compara a la producción de partículas cargadas y a la producción de eventos DIS en la misma región de espacio fase. Los resultados se comparan a predicciones teóricas basadas en programas Monte Carlo de primer orden unidos a cascadas de partones. Los modelos Monte Carlo también se usan para el estudio de la contribución de sabor a la producción de $K_S^0$ y la dependencia de la función de densidad de partones.

# Preface

The understanding of the composition of matter and the way it interacts has been, since a long time ago, the topic of investigation of several physicist whose theoretical and experimental researches have contributed to the formulation of ideas about the structure of the atoms. The first models indicated that the protons, neutrons and electrons are the basic components, but further studies revealed that the proton and neutrons are formed by other elementary pieces called quarks [1].

In 1969, ideas from Bjorken and Feynman were fundamental for the development of a model able to explain a nucleon as a particle composed of quarks. The composition of the nucleon was described through the so called structure functions. This model, known as the quark parton model or QPM [2] [3], expresses the structure function $F_2$ as the weighted sum of the momentum distribution of the quarks $q_i(x)$ and antiquarks $\bar{q}_i(x)$ in the nucleon times the square of their electric charge $e_i$:

$$F_2(x) = \sum_i e_i^2 x[q_i(x) + \bar{q}_i(x)] \tag{1}$$

where $x$ is the fraction of the proton momentum carried by the probed quark. The quarks, in this model, carry only longitudinal momentum.

The proton $(uud)$ is formed by two up $u$ quarks and one down $d$ quark, then:

$$\int_0^1 (u(x) - \bar{u}(x))\, dx = 2 \qquad \int_0^1 (d(x) - \bar{d}(x))\; dx = 1. \tag{2}$$

The QPM interpretation had some success, but further studies [4] showed that only 50% of the proton momentum is carried by the quarks, then the missing momentum should be carried by another kind of partons with no electric charge. Some time later, between 1973-78 the gluons were discovered, and quantum chromodynamics (QCD) was proposed: the QCD age had started.

QCD considers that the quarks carry not only electric charge but also colour charge. The exchange of colour is mediated by the gluons with spin 1. Due to the new assumption, QCD also should consider the possibility that quarks radiate gluons, and the possibility of gluon fluctuations into quarks which is the source of the sea of quarks inside the proton. These processes complicate the calculations of proton structure function $F_2$ but good experimental results have been obtained as shown in Figure 1 where $F_2$ is plotted versus the four-momentum squared of the transfer photon in the DIS events, $Q^2$. The $F_2$ data for $x$ values around 0.25 is flat as a function of $Q^2$, this is called Bjorken scaling. For smaller values of $x$, $F_2$ grows logarithmically with $Q^2$, this is called scaling violation.

QCD together with the electroweak theory form the so called Standard Model (SM) which is a very successful theory of elementary particles, in spite of its known shortcomings.

The SM includes 61 elementary particles, 48 of them of spin 1/2 (or fermions): 36 quarks (the quarks up, down, charm, strange, top and bottom, presented in three different colors; and their antiparticles) and 12 leptons (the electron, muon, tau, their neutrinos, and their respective antiparticles) which are classified according to their way of interaction. The SM explains the forces as resulting from matter particles exchanging other particles, the mediating particles (12 elementary particles) with spin 1 (bosons): the photon $\gamma$ for the very well known electromagnetic force, the $W^{\pm}$ and $Z^0$ boson for the weak interactions and the gluon $g$ (8 different gluons) for the strong interaction. Figure 2 shows the Standard Model of the elementary particles. The Higgs boson (also considered as elementary particles) is still an hypothetical particle, that would explain the fundamental mass of the particles.

Hadrons, strongly interacting particles, are classified as mesons or baryons if they are made of a quark-antiquark pair ($q\bar{q}$) or of three quarks ($qqq$), respectively. The proton is an stable baryon as far as we know. The nucleon, another baryon, is relatively stable only when bound in a nuclei. All other hadrons decay very fast, in a human time scale, so they are not found in ordinary matter. This characteristic is
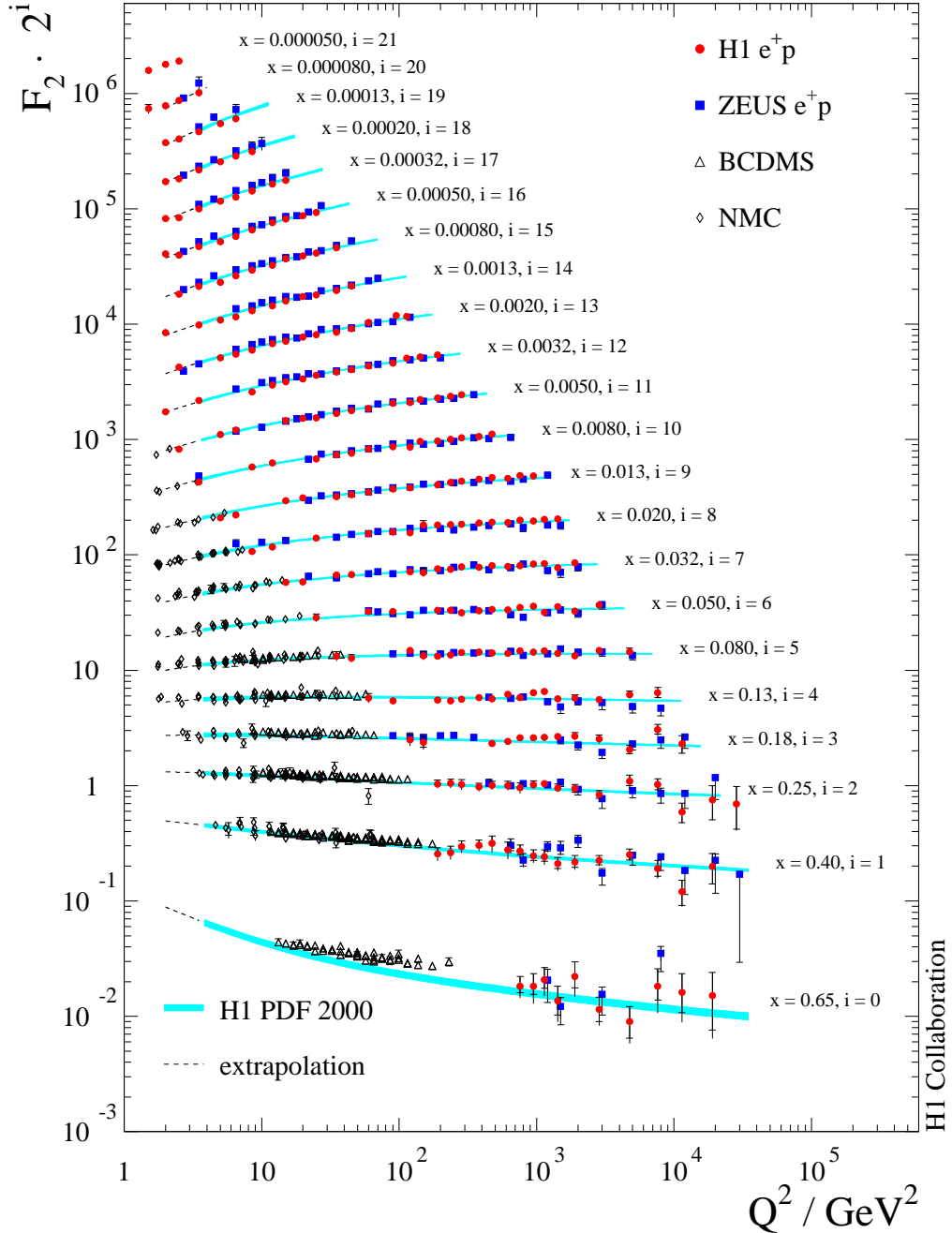
Figure 1: Experimental results of the $F_2$ structure function of the proton as function of the four-momentum squared of the transfer photon $Q^2$ and the proton momentum fraction carried by the struck quark $x$, compared to NLO calculations in QCD (solid line shows the H1 PDF 2000 [5]). At low $Q^2$, the H1 data are complemented with the fixed target experiments BCDMS[6] and NMC[7], [8] data.
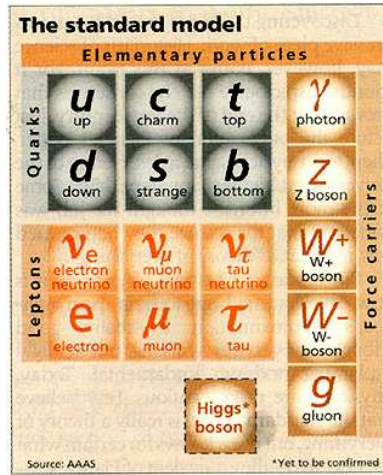
Figure 2: Standard model constituents.

one of the issues that makes important their study in particle physics.

This thesis is focused in the research of a meson known as the $K_S^0$ which belongs to the family of strange mesons due to the presence of a strange $s$ quark in its composition.

The first observed mesons were the pion $\pi$ and the kaon $K$, in 1947 [9] using a cloud chamber. The kaon decay was observed by G.D. Rochester and C.C. Butler, then other mesons were observed in several experiments. The lifetimes differences of the kaons and the observation of pair production of strange particles from strong interaction of non-strange hadrons, as that one shown in Figure 3, suggested that they contain a new quark, the *strange* quark $s$, having the same electric charge as the $d$ quark but higher mass because $K$ and $\Sigma$ are heavier than $\pi^+$ and $p$. Then a new quantum number, called *strangeness*, was introduced by M. Gell-Mann and A. Pais [10]. The strangeness quantum number is conserved in strong, but violated in weak interactions.

The discovery of hadrons with strangeness quantum number marked the beginning of an exciting age in particle physics which, after more than 60 years, have not found its conclusion yet. However the studies continue, as the one carried out for this doctoral thesis whose main goal is the analysis of the lightest strange meson,
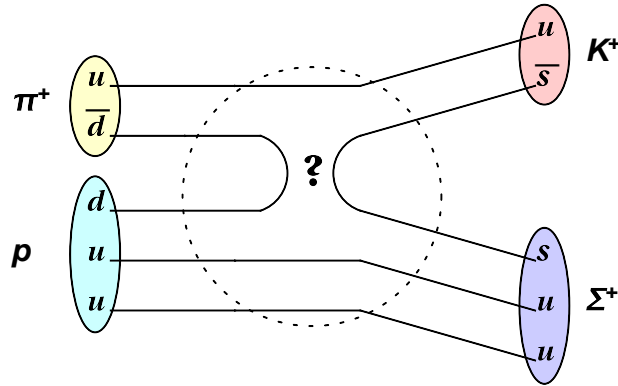
Figure 3: The production of strange particles in the interaction of non-strange hadrons $\pi^+ + p \rightarrow K^+ + \Sigma^+$.

the $K_S^0$, decaying mainly into two pions with opposite electric charges.

The goal of this thesis is to contribute to the strangeness studies throught the determination of the total and differential cross sections of the $K_S^0$ meson production at high $Q^2$ range using HERA II data from 2004 to 2007, since they provide plenty of statistics making possible the study at this range which was not been possible in the previous years of HERA operation, and provide valuable information of fundamental aspects in QCD dynamics, understanding of $K_S^0$ production, comparison of parton density functions and strangeness factor values for MC tests.

The thesis is structured as follows. In the first chapter the deep inelastic scattering and its kinematics are introduced, the main aspects of the theoretical framework in which the Monte Carlo simulation programs are based can also be found there.

The second chapter consists on the presentation of the $K_S^0$ meson, the production mechanisms and the importance of the strangeness studies. Previous results of different experiments corresponding to the strange topic are briefly summarized, the most recent measurements of strange particles by the H1 collaboration are emphasized as the main introduction to the work presented here.

The third chapter is dedicated to the description of the HERA collider and the H1 detector components as well as to the explanation of the performance of trackers and calorimeter detection devices, trigger system and luminosity measurement.

The fourth chapter concentrates on the selection criteria of deep inelastic scattering events. The $K_S^0$ reconstruction through the identification of its track daughters and the signal extraction from its invariant mass distribution can also be found in this chapter. The selection criteria to obtain the charged particle sample needed for cross section ratios are explained in the last subsection.

Chapter five introduces the procedure to determine the total and differential cross sections. The main corrections needed in the measurements and the statistical and systematic uncertainties sources are explained in detail.

The last chapter, number six, is reserved to the results of the $K_S^0$ production, differential cross sections in the laboratory and Breit frames, production ratios of the $K_S^0$ to charged particle and DIS events, double differential cross section, as well as complementary studies such as the PDFs dependence and flavour contribution to the $K_S^0$ production are shown. The last section presents the conclusions.

# Contents

# Chapter 1

# Theoretical framework

The *ep* HERA collider at DESY enables through deep inelastic scattering (DIS) events the study of the proton composition and the test of the Standard Model and other aspects of Quantum Chromo Dynamics. The kinematic variables for the description of the events are presented in this chapter, as well as the theoretical framework of the simulation programs for DIS processes. The Lund fragmentation model of hadronization describing the mechanism of hadron creation, an essential part of the Monte Carlo programs, is presented.

## 1.1   Deep inelastic scattering

In 1911, Rutherford unexpectedly discovered the subatomic structure using the scattering technique. An analogue of such a technique is used today in high energy particle physics to study the substructure of hadrons. For DIS at HERA, the hadron is a proton studied by the scattering of an electron beam off it.

The **Deep Inelastic Scattering** process at HERA consists in the interaction of incoming electrons[1] with incoming protons through the exchange of a virtual boson [4]. The proton breaks up resulting in a final hadronic state system.

---

[1]For simplicit, the incoming and scattered electrons are always referred as 'electrons', although the data studied here were obtained with both electorns and positron beams.

The DIS process can be of two types depending on the kind of the exchanged boson. The neutral current process (NC-DIS), $ep \rightarrow eX$, consists in the exchange of a neutral gauge boson, a photon $\gamma$ or a $Z^0$ boson, $X$ represents the hadronic final states. The charged current process (CC-DIS), $ep \rightarrow \nu_e X$, is mediated by a charged gauge boson $W^\pm$, at the end there are a hadronic state system and a neutrino of the electron.

Figure 1.1 shows the diagram of a NC-DIS event, the incoming electron $e$ with four-momentum $k$ interacts with a quark of the incoming proton $p$ which carries a $xP$ fraction of the four-momentum $P$ of the proton, through the interchange of a neutral virtual gauge boson ($\gamma$ or $Z^0$) with four-momentum $q$. After the interaction, the scattered electron $e'$ has final four-momentum $k'$ and the proton breaks up into a multiparticle state of hadrons denoted as $X$. The contribution of the $Z^0$ boson to the process only becomes significant at very high $Q^2$ values compared to its mass[2] squared. The CC-DIS events are not considered in this analysis.
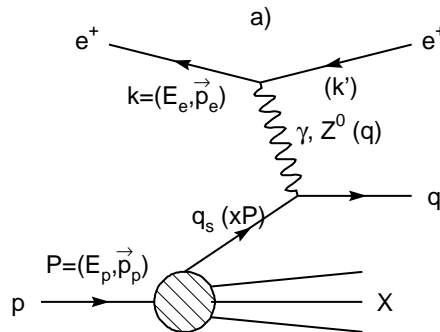


Figure 1.1: Neutral Current Deep Inelastic Scattering diagram, the four-momentum of the incoming electron ($k$), the scattered electron ($k'$) and the incoming proton ($P$) are shown. The transfer gauge boson can be $\gamma$ or $Z^0$.

The $Q^2$ variable provides the specific wavelength $\lambda = h/\sqrt{Q^2}$ that allows to quantify the resolution power of the experiment for the study of the proton components:

---

[2] $M_{Z^0} = 91.1876 \pm 0.0021$ GeV  [11].

if it increases then the resolution also increases.

## 1.1.1 Kinematics

The kinematics of the DIS process, for a fixed center of mass energy $\sqrt{s}$, can be described by two independent variables commonly chosen from the Lorentz invariant variables: the negative squared of the four-momentum of the virtual exchanged boson $-q^2 = Q^2$, the invariant mass squared of the final hadronic system $W^2$, the dimensionless Bjorken scaling variable $x$ and the inelasticity $y$. $x$ represents the fraction of the proton momentum carried by the struck quark and $y$ corresponds to the fractional energy transferred from the electron to the hadronic system in the proton rest frame. The variables can be determined by the expressions: take values in

$$s = (k + P)^2 \tag{1.1}$$

$$Q^2 = -q^2 = -(k - k')^2 \tag{1.2}$$

$$W^2 = (p + P)^2 \tag{1.3}$$

$$x = \frac{Q^2}{2P \cdot q} \tag{1.4}$$

$$y = \frac{P \cdot q}{P \cdot k} \tag{1.5}$$

Neglecting the mass of the proton, the following relations are satisfied:

$$s \approx 4E_e E_P \tag{1.6}$$

$$Q^2 \approx sxy \tag{1.7}$$

$$W^2 \approx Q^2 \left( \frac{1 - x}{x} \right) \tag{1.8}$$

where $E_e$ and $E_P$ are the energies of the incoming electron and proton, respectively. The correct reconstruction of DIS kinematics depends on how well the detector measures the neccessary variables for the calculation. Typically, the variables used for reconstruction are the energy of the incoming and scattered electron $E_e$, $E'_e$, the polar angle $\Theta_e$ of the scattered electron, the sum $\Sigma = E_h - p_{z,h}$ of each hadronic

final particle $h$ and the inclusive angle $\gamma$ of the hadronic system. There are three basic methods sensitive to kinematic reconstruction [12]: those based on electron information only ($e$ electron method), those based on hadronic final measurements only ($\Sigma$ sigma method) and those combining electron and hadronic information (DA double angle method). To know more about the different methods of reconstruction see appendix A. The method chosen for this analysis is the electron method.

## 1.2   Theoretical DIS cross section

In the lowest-order perturbation theory for QCD, the DIS cross section can be expressed in terms of the product of leptonic and hadronic tensors associated with the coupling of the exchanged bosons at the upper and lower vertices:

$$\frac{d^2\sigma}{dxdy} = \frac{2\pi y \alpha^2}{Q^4} \sum_j \eta_j L_j^{\mu\nu} W_{\mu\nu}^j.$$

where the summation is over $j = \gamma, Z$ for NC-DIS, $\eta_j$ denotes the corresponding propagators and couplings, $L_j^{\mu\nu}$ is the lepton tensor associated with the coupling of the exchange boson to the leptons and the hadronic tensor $W_{\mu\nu}^j$ describes the interaction of the appropiate electroweak currents with the proton.

The part of the lepton tensor is very well understood but the proton structure functions defined in terms of the hadronic tensor are not. The best attempt of the complete modeling of DIS event is made by the Monte Carlo simulation programs.

## 1.3   Event generators: Monte Carlo programs

The Monte Carlo programs (MC) are computational tools for simulation in the physical and mathematical sciences, business, economy, telecommunications, design, and even games. They are very useful and successful methods due to their ability for modeling systems with a large number of degrees of freedom, many-body problems and/or systems under complicated conditions.

The applications to high energy physics are related to the design of detectors, accelerators and detectors performance, difficult QCD calculations by the evaluation of difficult integrals and sample random variables governed by complicated probability density functions.

In MC programs for DIS particle physics, the hadronic tensor part of the cross section is considered as a convolution of matrix elements $ME$, parton density functions $PDFs$ and fragmentation functions $D_{frag}$. The separation of matrix elements (the interaction of the parton with the boson) and PDFs (the partonic structure of the proton) is given by the factorization scale $\mu_F$ as shown in Figure 1.2. The meaning of $\mu_F$ can be understood roughly as: if the emission with transverse momenta is below $\mu_F$ they are accounted within the PDF, if it is higher than $\mu_F$ are included in the interaction. In inclusive DIS, the default choice for the scales is usually $\mu_F = Q^2$.
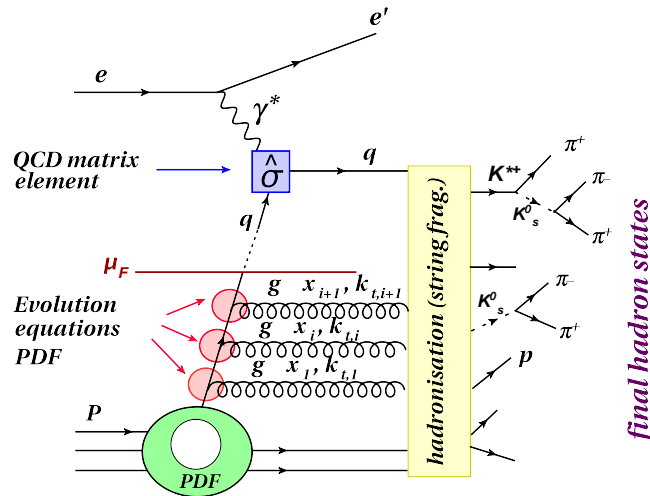


Figure 1.2: The factorization scheme of a DIS event showing the perturbative cross section $e\gamma^*$, the non-perturbative parton density function (PDF).

PDFs are non-perturbative objects which can not be computed within pQCD, but the evolution of PDFs as they move in phase space can be computed perturbatively. Several groups have proposed fits for the PDFs based on different theoretical

assumptions, the two most famous approaches are the DGLAP [13] (Dokshitzer, Gribov, Liatov, Altarelli, Parisi) and the BFKL [14] (Balitsky, Fadin, Kuraev, Lipatov) evolution equations.

The MC event generators involve several stages, the generation of an event starts with the random generation of the kinematics and partonic channels of whatever hard scattering process (the ME) the user has requested. This is then followed by the parton cascade (CDM and MEPS as chosen in the MCs simulated for this analysis, see section 1.3.1) down to a scale $\sim 1$ GeV that separates the perturbative and non-perturbative part of the simulation. These cascades are governed by a model of the evolution equations previously mentioned. Once the partonic configuration has been generated, the fragmentation process (where the parton fragmentation functions take place) starts to model the hadronization of the final state system. The Lund string model has been chosen for the MCs used in this analysis, the description can be found in the subsection 1.3.2.

### 1.3.1   Colour dipole model and parton showers

As mention above, two different parton cascade approaches are applied for the two DIS MCs used in this thesis: the colour dipole mode (CDM) and the parton showers (MEPS).

The CDM model describes the parton radiation in terms of a colour field generated by a chain of radiating colour dipoles extending between a pair of colour charges. A gluon is emitted from a colour dipole forming two independent colour dipoles as shown in Figure 1.3 a). Further gluons can be radiated, leading to a chain of colour dipoles, where one gluon connects two dipoles, and one dipole connects two gluons. The CDM evolving parton cascade has no strong ordering in the transverse momenta $k_T$ of the emitted gluons.

On the other hand, the MEPS model considers that a parton of the proton can initiate a parton shower by radiating gluons, which become increasingly space-like ($m^2 < 0$) after each branching, see Figure 1.3 b). After the exchanged electroweak
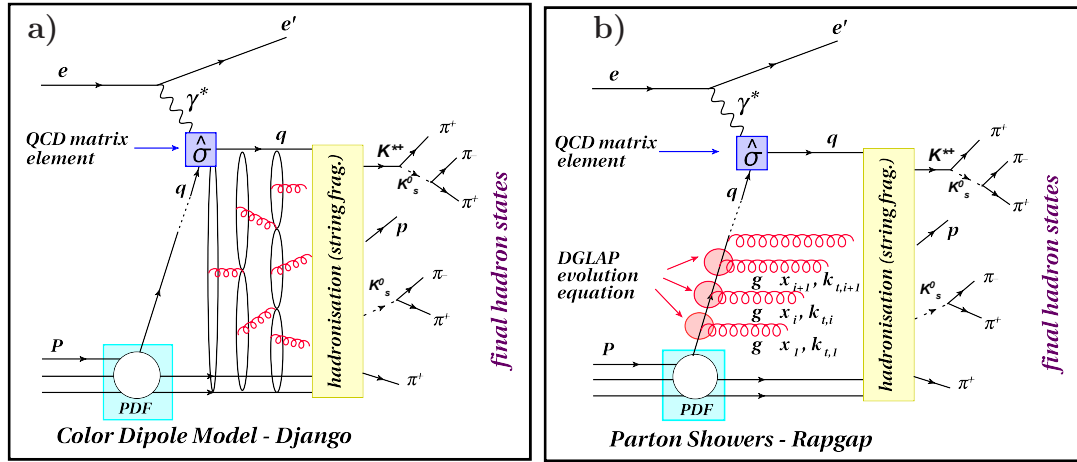
Figure 1.3: The Django and Rapgap MCs scheme used in this thesis. It is possible to observe the MC treatment of the DIS events: the matrix elements, marked $\hat{\sigma}$, the parton density funcion PDF and the parton cascade simulated according to a) the colour dipole model and b) the parton shower, and the hadronization process modeled with the string fragmentation model.

boson is absorbed, the struck quark becomes on-shell (has a time-like virtuality $m^2 > 0$). In the latter case a final state shower will result, with both the virtuality of the struck quark and the off-shell mass of the radiated gluon decreasing after each successive branching. Any time-like parton produced in an initial shower will have a similar evolution.

The parton shower is based on DGLAP equations with strong ordering in the transverse momenta $k_T$ of the emitted gluons.

## 1.3.2 Fragmentation and hadronization

The hadronization process is a long-distance transition from the free coloured quarks at parton level to the colour neutral final states or hadrons, involving only small momentum transfers. The idea is based on the independent splitting or fragmentation of each parton, gluon or quark from the parton cascade or the hard process, which then mix (hadronize) to create the final baryons and mesons.

The fragmentation process evolves perturbatively, so the fragmentation functions can be determined describing the production of hadrons $h$ from a quark $q$ at a given $x$-Bjorken value and four-momentum transfer squared $Q^2$. However, the hadronization mechanism can not be treated perturbatively so detailed phenomenological predictions have been developed. The two commonly used models are the cluster fragmentation and the string fragmentation, both are expected to be universal which means that should reproduce results from $e^+e^-$ collisions and $ep$ scattering. For the MCs generated for this analysis only the string fragmentation model is used, since have been found that the cluster model does not describe the DIS physics.
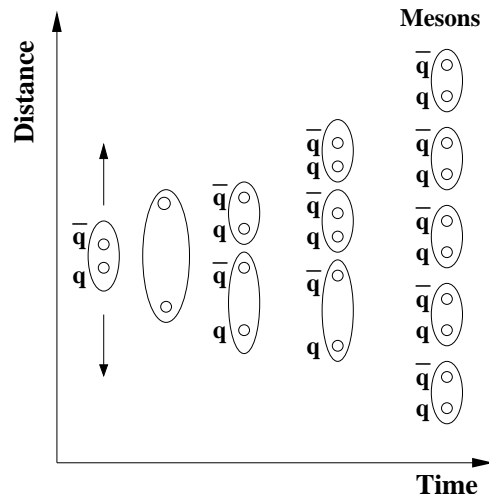


Figure 1.4: The string fragmentation model.

The scheme of hadronization by the Lund string fragmentation model [15] considers the colour field between the partons, quarks and gluons, to be the fragmenting entity rather than the partons themselves. In it, a produced quark-antiquark can be viewed as moving apart from their common production vertex in opposite directions, losing kinetic energy to the colour field, represented by a colour string stretching between them and providing a linear rise of the potential energy stored in the colour string due to their separation. When the potential becomes energetically favourable, the string breaks up into two new $q\bar{q}$ colour strings forming out of the vacuum (or

colour field). If the invariant mass of either of these two resulting colour strings is large enough, the breaking continues iteratively, creating more $q\bar{q}$ pairs, see Figure 1.4. The gluons are supposed to produce kinks on the string, each initially carrying localized energy and momentum equal to that of its parent gluon.

In this model, the string break up process proceeds until only on mass-shell string fragments combined into mesons and baryons remain. The $q\bar{q}$ pairs are created according to the probability of a quantum mechanical tunneling process. The production probability can be estimated from the product of the $q$ and the $\bar{q}$ wave functions and the colour field potential [16]. Due to the dependence on the parton mass and/or the hadron mass, the production of strange and, in particular, the heavy quark hadrons is suppresed. The relative production is assumed as $u : d : s : c \approx 1 : 1 : 0.3 : 10^{-11}$. The charm and heavier quarks ($b$ and $t$) are not expected to be produced in the soft fragmentation, but only in perturbative cascade branchings $g \rightarrow q\bar{q}$.

The model considers as important free parameters for the production of strange particles the following relative production probabilities:

- The *strangeness suppression factor* $\lambda_s = P(s)/P(q)$, expresing the ratio production probability of strange quark $s$ to light quarks up $u$ and down $d$.

- The *diquark suppression factor* $\lambda_{qq} = P(qq)/P(q)$, which gives the production probability of a light diquark pair $P(qq)$ relative to a light single quark pair $P(q)$.

- The *strange diquark suppression factor* $\lambda_{sq} = (P(sq)/P(qq))/(P(s)/P(q))$ providing the ratio probability of a diquark pair production containing a strange quark $P(sq)$ to the diquark pair production $P(qq)$, normalised to the strangeness suppression factor.

Although in detail, the string motion and fragmentation is more complicated with the appearance of additional string regions during the time evolution of the

system, the scheme is *infrared safe*. After the particles have been produced with the hadronization model, the MC programs use the measured decay channels and branching ratios to simulate their decays, yielding at the end of the process a list of stable particles.

## 1.4   Django and Rapgap Monte Carlo programs

In this analysis, two Monte Carlo generators are considered: Django and Rapgap. Both MCs simulate lepton-nucleon scattering physics, the difference radicates in the treatment of the parton cascade process: Django is based on CDM and Rapgap in MEPS. The hadronization process is chosen to be the Lund string fragmentation model [15] as implemented in the JETSET program [17], tuned to ALEPH parameter values [18]: $\lambda_s = 0.286$, $\lambda_{qq} = 0.108$ and $\lambda_{sq} = 0.690$.

Two sets of MCs are generated for each Django and Rapgap, one including the possibility of the initial and final radiation which is called the *radiative MC* and one without including this possibility, the so called *non-radiative MC*.

The radiative events are passed through the GEANT [19] simulation of the H1 apparatus in order to reproduce the detector response (*reconstructed MC*) whereas the non-radiative MC are produced only at the parton level. Both are used for data corrections.

The MC's for comparison to data are generated without including initial and final radiation with CTEQ PDF for the three different strangeness values $\lambda_s$ =0.22, $\lambda_s$ =0.286 and $\lambda_s$ =0.3. And other MC samples are produced with $\lambda_s$ =0.286 but considering as PDFs the CTEQ6L, H12000LO and GRV98.

### 1.4.1   Django

The Django [20] simulator of *ep* scattering events assigns the event properties, as the phase space, the initial conditions and the kinematic cuts with HER-ACLES [21] [22]. The QCD part is implemented by LEPTO [23] or ARIADNE [24].

Django as used for this work uses ARIADNE to generate the cascade of partons and is based on the colour dipole model CDM.

Different PDFs can be used with the MCs. For this MC, the used PDFs are CTEQ6LO [25], GRV98 [26], and H12000LO [5]. The renormalisation and factorization scale are placed to $\mu_R = \mu_F = Q^2$.

In total, there are four simulated radiative samples of events with Django, each corresponding to the data periods where HERA ran either with electrons or positrons.

From the Django samples, one corresponds to the $2004e^+p$ period, has 7 millons of events and luminosity value equals to 1535 pb$^{-1}$; for $0405e^-p$ year there are 14 million events with corresponding luminosity of 3048 pb$^{-1}$; for $2006e^-p$ the MC has 7 millions of events corresponding to a luminosity value of 1524 pb$^{-1}$ and the sample for $0607e^+p$ with 20 millions of events and 4383 pb$^{-1}$ of luminosity.

The non-radiative files for each year period correspond to samples of 20 million of events with luminosity of approx. 6320 pb$^{-1}$ for the samples with $e^-p$ and approximately 6379 pb$^{-1}$ for the samples with $e^+p$.

### 1.4.2   Rapgap

In Rapgap MC [27] the DIS events are simulated by LEPTO. The hard interaction is taken as the standard model electroweak cross section and the implementation of QCD parton showers at leading order are based on DGLAP splitting functions in leading order $\alpha_s$. The matrix elements for leading order $\alpha_s$ processes, as BGF and QCDc, and the QED corrections are included by the interface to HERACLES event generator.

The same PDFs (CTEQ6LO, GRV98 and H12000LO), normalisation and factorization scales ($\mu_R = \mu_F = Q^2$) as in Django, were used for Rapgap in order to be congruent in the comparison between both models.

The radiative samples for Rapgap are of 6 millons of events for $2004e^+p$ with luminosity of 1529 pb$^{-1}$; for $0405e^-p$ are 12 millions of events with luminosity of 3034 pb$^{-1}$; the 6 millions of events for the $2006e^-p$ period has luminosity equals

to 1516 pb$^{-1}$ and for 0607$e^+p$ period are 12 millions of events and luminosity of 3056 pb$^{-1}$.

The non-radiative samples consist of 20 millions of events for each year with $\mathcal{L} = 6920$ pb$^{-1}$ for the periods with $e^-p$ collisions and $\mathcal{L} = 6996$ pb$^{-1}$ for those with $e^+p$.

# Chapter 2

# Strange mesons

There are several interesting topics in particle physics which are not completely understood yet. The study of $K^0_S$ meson production in DIS improves the current understanding of the particle creation during hadronization, the mechanism of strangeness production, QCD aspects related to strange quarks, and allows to study the resonant production of particles including $K^0_S$ in their decay modes, like heavier standard particles or exotic particles like glueballs.

In this chapter, the most relevant properties of the $K^0_S$ particles, their different production mechanisms and previous related results obtained in $e^+e^-$, heavy ion and $ep$ collisions are presented. Special emphasis is given to most recent results of the H1 collaboration $K^0_S$ production at low $Q^2$ values.

## 2.1  What is a $K^0_S$ meson?

As mentioned in the preface, nature is made of strongly interacting particles called hadrons. There are two kind of hadrons, baryons and mesons. The baryons are bound states of three quarks, while mesons are bound states of a quark and an antiquark.

Mesons have also angular momentum J = L+S, where L represents the orbital angular momentum (L = 0,1,2,...) and the meson spin is denoted by S (S = 0,1).

When the meson has L $= 0$, it is called *pseudoscalar* or *vector* depending whether S $= 0$ or S $= 1$, respectively.

If only the three lighter quarks (up $u$, down $d$ and strange $s$) of the standard model are taken into account, something known as SU(3) algebra, there are eight pseudoscalar and eight vector mesons. Using their properties – the strangeness quantum number $S$, charge $Q$, isospin $I_3$ or mass – it is possible to plot the particles in a coordinate system and obtain geometric figures of remarkable shape, as the octect of pseudoscalar mesons [11] shown in the Figure 2.1 and listed in Table 2.1.
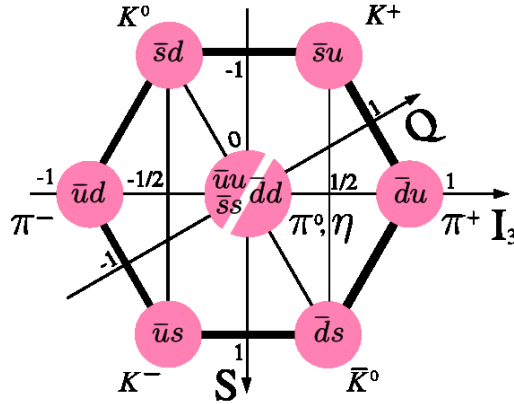


Figure 2.1: Octect of the pseudoscalar mesons plotted in the axis corresponding to strangeness quantum number $S$, charge $Q$ and isospin $I_3$.

An important observation is that $K^0$ can be produced by non-strange particles together with a hyperon [28], but $\overline{K^0}$ is only produced in association with a Kaon or a hyperon:

$$\pi^+ + p \rightarrow \Lambda + K^0$$

$$S \quad \ 0 \quad \ \ 0 \quad -1 \quad +1$$

$$\pi^+ + p \rightarrow K^+ + \overline{K^0} + p$$

$$S \quad \ \ 0 \quad \ \ 0 \quad +1 \quad -1 \quad \ \ 0$$

this indicates that $K^0$ and $\overline{K^0}$ have different strangeness quantum number. Then, the question is how to establish the presence of these two mesons.

Table 2.1: List of the pseudoscalar and vector mesons with the specification of their quark content.

| Pseudoscalar | | Vector | |
|---|---|---|---|
| Particle symbol | Quark content | Particle symbol | Quark content |
| $\pi^-$ | $\overline{u}d$ | $\rho^-$ | $\overline{u}d$ |
| $\pi^0$ | $1/\sqrt{2}(d\overline{d} - u\overline{u})$ | $\rho^0$ | $1/\sqrt{2}(u\overline{u} - d\overline{d})$ |
| $\pi^+$ | $u\overline{d}$ | $\rho^+$ | $u\overline{d}$ |
| $K^0$ | $d\overline{s}$ | $K^{*0}$ | $d\overline{s}$ |
| $K^+$ | $u\overline{s}$ | $K^{*+}$ | $u\overline{s}$ |
| $K^-$ | $\overline{u}s$ | $K^{*-}$ | $\overline{u}s$ |
| $\overline{K^0}$ | $\overline{d}s$ | $\overline{K^{*0}}$ | $\overline{d}s$ |
| $\eta'$ | $s\overline{s}$ | $\phi$ | $s\overline{s}$ |

Although both are usually produced via the strong force, they decay weakly. As weak interactions do not conserve strangeness, once they are created one can turn into another. The $K^0$ can turn into a $\overline{K^0}$ and then turning back to the original $K^0$, and so on. The Figure 2.2 shows a strange quark in the $\overline{K^0}$ turning into a down quark by successively emitting two W-bosons of opposite charge. The down antiquark in the $\overline{K^0}$ turns into a strange antiquark by absorbing them.
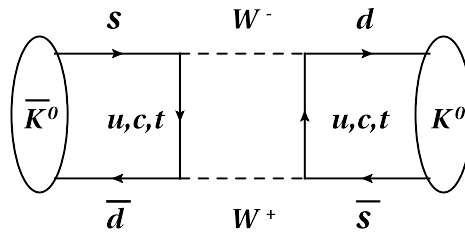


Figure 2.2: Diagram of the $K^0$ turning into a $\overline{K^0}$. A strange (down) quark (anti-quark) from the $\overline{K^0}$ turns into a down (strange) quark (antiquark) by the emission of two $W$-bosons of opposite charge.

Experimentally it was found that a $K^0$ produced by strong interactions decays

with two different lifetimes [28]: $K^0 \to \pi\pi$ and $K^0 \to \pi\pi\pi$, so $K^0$ seems to be two different particles when studying its weak decays. The same is observed for $\overline{K^0}$. This implies that if one has a pure $K^0$ state at $t = 0$, at any later time $t$ one will have a superposition of both $K^0$ and $\overline{K^0}$ (equation 2.1). It is known that particles decaying by weak interactions are eigenstates of charged parity (CP), expressed as the equation 2.2.

$$|K(t)> \ = \ \alpha(t)\,|K^0> \ + \ \beta(t)\,|\overline{K^0}>, \tag{2.1}$$

$$CP\,|K^0> \ = \ |\overline{K^0}> . \tag{2.2}$$

Since $K^0$ and $\overline{K^0}$ are not CP eigenstates, there must be linear combinations:

$$|K_S^0> \ = \ \frac{1}{\sqrt{2}}\left(|K^0> \ + \ |\overline{K^0}>\right) \qquad CP = +1, \tag{2.3}$$

$$|K_L^0> \ = \ \frac{1}{\sqrt{2}}\left(|K^0> \ - \ |\overline{K^0}>\right) \qquad CP = -1. \tag{2.4}$$

These two different modes of decay were observed by Leon Lederman and his coworkers in 1956, establishing the existence of the two weak eigenstates called $K_S^0$ as referred in equation 2.3 and $K_L^0$ as referred in equation 2.4. Later, James Cronin and Val Fitch in 1964 (Nobel Prize in 1980) showed that a small CP symmetry violation exists, but the states already assumed are still a very good approximation.

Since the mass of $K_L^0$ is just a little larger than the sum of the masses of three pions, this decay proceeds very slowly, about 600 times slower than the decay of $K_S^0$ into two pions.

The main properties of the $K_S^0$ are $I(J^P) = \frac{1}{2}(0^-)$, the mass value of $497.648 \pm 0.022$ MeV and the lifetime value $\tau = 0.8953 \text{ x } 10^{-10} \pm 0.0005$ s or $c\tau = 2.6786$ cm [11]. The $K_S^0$ mesons decay by three different general modes: hadronic, with photons or lepton anti-lepton $l\bar{l}$, and semileptonic. The hadronic modes containing the most frequent decay channels are listed in Table 2.2.

Table 2.2: The $K_S^0$ most frequent hadronic decay channels and their branching ratio values [11].

| $K_S^0$ Decay channel | Branching ratio |
|:---:|:---:|
| $\pi^0\pi^0$ | $30.69 \pm 0.05$ (%) |
| $\pi^+\pi^-$ | $69.20 \pm 0.05$ (%) |
| $\pi^+\pi^-\pi^0$ | $3.5^{+1.1}_{-0.9}$ x $10^{-7}$ |

## 2.2 Production of $K_S^0$

The strange quark $s$ is not so heavy as the bottom ($m_b = 4.2\ ^{+0.17}_{-0.07}$ GeV), charm ($m_c = 1.27\ ^{0.07}_{-0.11}$ GeV) or top quarks ($m_t = 171.2 \pm 1.1 \pm 1.2$ GeV) but it is also not light as up ($m_u = 2.55\ ^{+0.75}_{-1.05}$ MeV) or down ($m_d = 5.04\ ^{+0.96}_{-1.54}$ MeV) quarks. It has a mass value of $105^{+25}_{-35}$ MeV [11] what allows its creation in $ep$ collisions at HERA.

There are different mechanisms of strange particle production, which are illustrated schematically in Figure 2.3, the hard interaction or QPM process, the boson gluon fusion process (BGF), heavy decays and hadronization processes.

**_The hard interaction or QPM process_** occurs when the photon of the DIS event interacts directly with a $s$ quark belonging to the quarks of the proton sea. This process involves a large momentum transfer, Figure 2.3 a).

The strange production through **_BFG process_** consists of the photon interacting with a gluon emitted by the proton, which splits into a $s\bar{s}$ quark pair, see Figure 2.3 b). As the gluon density of the proton increases at small Bjorken scaling variable $x$, the BFG becomes more important at low $x$ values.

The Figure 2.3 c) shows the **_heavy decay process_**. It is similar to the BFG process but in this case the gluon splits into heavy quarks ($c$ and $b$); then they decay into $s$ quarks. Due to the small probability to find $c$ and $b$ quarks in the proton sea, this is the main mechanism of strangeness production by heavy quarks. At low $Q^2$ values this process is highly suppressed due to the masses of the heavy quarks, but
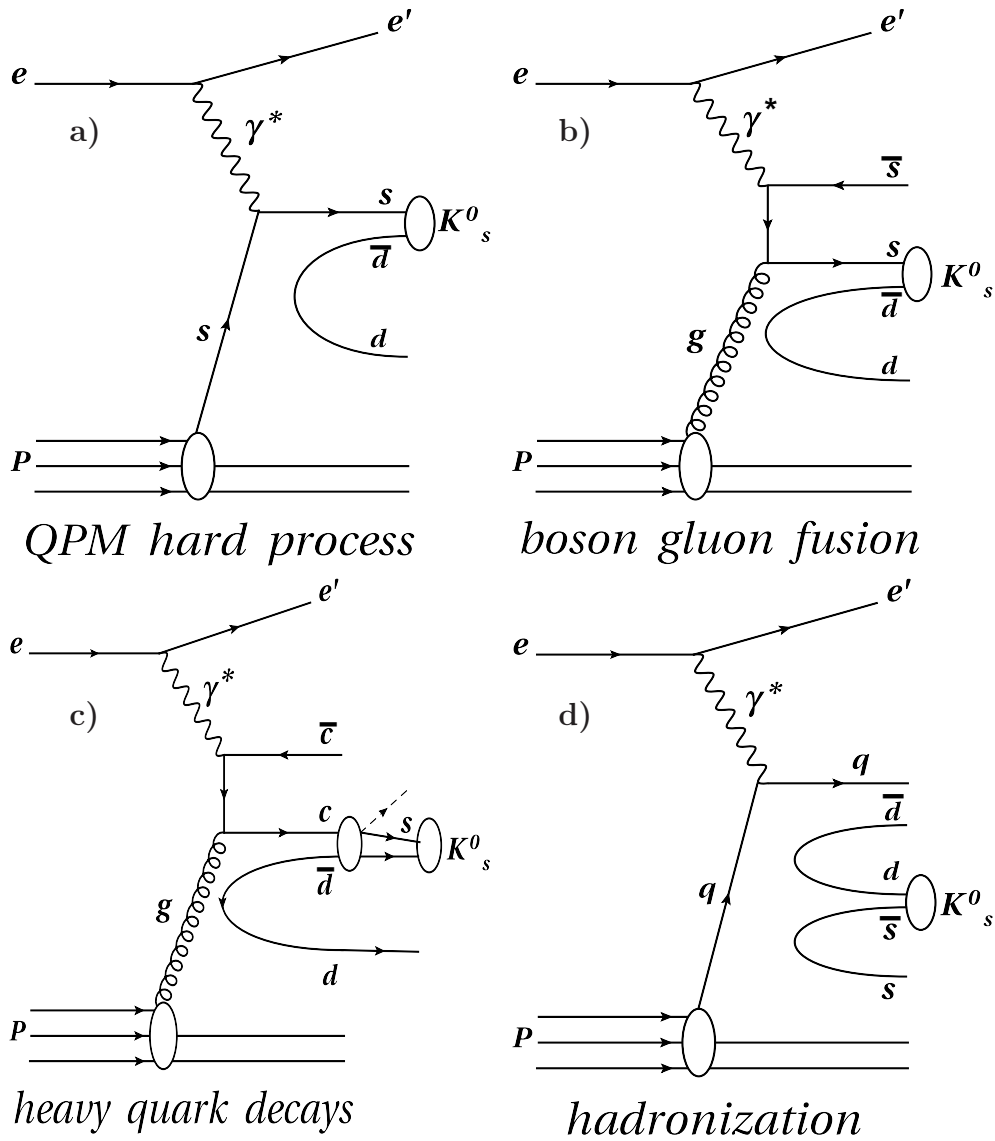
Figure 2.3: The four different mechanisms of strange particle production: a) hard interaction or QPM process, b) boson gluon fusion (BGF), c) heavy quarks decays and d) hadronization.

at very high $Q^2$ where the quark masses are not relevant with respect to the process scales, this process can contribute significantly.

**The hadronization process** is due to the colour field fragmentation as showed in Figure 2.3 d). This is the only process which can not be treated perturbatively, so phenomenological models are needed for its description, such as the LUND string model. Furthermore, this process provides the largest contribution of strangeness production over most of the phase space.

## 2.3 Why strangeness studies are important?

The study of strangeness has been done since the discovery of the first two mesons, the pion and the kaon, in cosmic rays in 1947 which marked the birth of this subject on particle physics.

It is interesting because the strange flavour does not exist in ordinary matter, it appears at colliding machines when the center of mass energy of the reaction is much larger than the strange hadron masses. The strange mesons and baryons produced are also not present at the beginning of the collision, they should be *cooked* in the reaction in some way, therefore the study of strangeness production provide essential information about the physical environment created in the collisions.

The strange particle properties make them also interesting, they are all unstable particles living very short time before decaying into stable particles. The decay channels and production rates are of considerable interests because they should reflect the dynamics of the strong interaction.

Since the dynamics of flavour production in colour confinement processes is one of the big open questions in particle physics, the production of strange hadrons in high energy reactions provides an extremely valuable study, so the mechanism of strangeness production has attracted considerable attention, both in perturbative and non-perturbative regimes. The study of the hadronization process of strange particle production (an other particles in general) bring us towards a deeper under-

standing of the strong forces responsible of the confinement.

The rate of strange quark production as compared to production rates for light up or down quarks depends on the energy density in the colour field providing therefore a measurement of the energy density and the string constant, in other words, the typical scales of space, time and momentum transfer involved in the confinement process.

The phonomenologycal models can also be tested by the comparison to strangeness results from data, and the optimization of their parameters can be performed. This is very important since due to our limited knowledge some tests rely strongly on phenomenological models only.

So far, the Lund string model which provides a rather convincing phenomenology of hadron production in general, and of strange particle production in particular, uses the strange to light flavours ratio as a natural explanation calling it, the strangeness suppression factor $\lambda_s$ (see also subsection 1.3.2).

Studies of the strangeness production cross section in different regions of the phase space have been compared to simulation based on the Lund string model, but certainly no unique $\lambda_s$ describes the data perfectly. What has been found is that a $\lambda_s$ value between 0.2 - 0.3 gives a surprisingly good description, not only of the inclusive strange-particle production, but also of correlations between strange particles, being the only models of baryon production which have survived the experimental tests including as well the diquark strangeness factors to assume occasional diquark-antidiquark pair production in the confinement process to explain the formations of baryons.

The studies of different ratios providing rather direct measurement of $\lambda_s$, $\lambda_{qq}$ and/or $\lambda_{sq}$, as the strange to non-strange ratio: $K_S^0 / \pi$, $\Lambda/p$, strange to non-strange charmed mesons and strange to non-strange bottom mesons can also provide good information but no experimental data is available for all of them.

The same suppression factor is expected to describe both the meson and the baryon sector, however a perfect determination of $\lambda_s$ requires knowledge of the cross

sections and determination of all resonances feeding into stable hadrons which is very difficult and is not yet fully complete.

The availability of data from different collision types is an advantage for the strangeness production studies and MC tests due to the differences in the physics escenarios, but also the compatibility among them in some regions. At the end the comparisons can test the strangeness universality if all methods yield the same $\lambda_s$.

The particle production in $pp$ collisions at a given $\sqrt{s_{pp}}$ compared to $e^+e^-$ annihilation at $\sqrt{s} = \sqrt{s_{pp}}/2$ have not shown drastic differences in the strange-particle production rates.

The $e^+e^-$ annihilation advantage is the detection of the baryon polarization because the configuration of the colour field is much better known, providing a further excellent test of string models. Baryon production is best studied in processes without incident baryons, such as this case, since the strange diquark is hence more strongly suppressed than a strange quark.

The heavy ion collisions also play important roles in many aspects, for instance an enhancement of the strange particle production in nucleus-nucleus collisions relative to proton-proton reactions have been established, finding that it depends on the strangeness content of the particle type, that is the reason of investigations of the energy and system size dependence of strangeness production. The enhancement was one of the first suggested signatures for quark gluon plasma QGP formation [29].

Another important point that makes the strange particle analysis interesting is the search for exotic states as pentaquarks (states with more quarks than the conventional $qqq$ and $q\bar{q}$ states) and glueballs (e.g. looking for glueball decaying to $K_S^0 K_S^0$ states).

The particle data group [11] lists a number of unestablished resonances, such as $\Theta^+$ state whose signal has been reported in previous experimental studies [30] looking for decaying modes including $K_S^0$ particles. In the same aspect some other particles for instance $D^0$, $\Lambda_c$ and $K^*$ also have $K_S^0$ mesons in their decay modes, so a good selection of the $K_S^0$ mesons can help to the reconstruction and study of these

heavy particles.

Other possible studies include the strangeness content of the pomeron in diffractive DIS and the determination of the strange structure function $F_2(s)$.

## 2.4   Previous strangeness production studies

Several studies have been done since many years ago in the strangeness field looking for mesons, baryons, resonances and even exotic signals. Not only at HERA $ep$ experiments, but also in $p\bar{p}$, heavy ions and $e^+e^-$ collisions at either linear or ring colliders at different center of mass energies and regions of phase space.

### 2.4.1   At $e^+e^-$ colliders

The DELPHI detector at LEP presented results on inclusive production rates per hadronic Z decay of $\Sigma^- = 0.081 \pm 0.010$ and $\Lambda(1520) = 0.029 \pm 0.007$. The total production rates of vector, tensor and scalar mesons and of baryons follow phenomenological laws related to the spin, isospin, strangeness and mass of the particles. This statement was confirmed by other LEP experiments (ALEPH, L3 and OPAL). In the same study, the ratio $\Lambda(1520)/\Lambda$ production increases with increasing scaled momentum $x_p$. A similar behaviour was found for the ratio of tensor to vector meson production, $f_2(1270)/\rho^0$ but no increase was seen for $f_0(980)/\rho^0$ and $a_0^\pm(980)/\rho^\pm$ [31]. The strange pentaquark search was performed by the DELPHI collaboration. None of the states that were searched for was found. Upper limits were established at 95% CL on the average production rates of such particles and their charge-conjugate states per hadronic decay.

The $\pi^0$, $\eta$, $K_S^0$ and charged particle multiplicities were determined for quark and gluons jets by OPAL collaboration. The multiplicity enhancement in gluon jets was found to be independent of the studied particle species. The measurement of charged particle multiplicity in strange flavoured $Z^0$ decays gave $< n_s >= 20.02 \pm 0.13$(stat.) $^{+0.39}_{-0.37}$ (syst.), while the strangeness factor $\lambda_s$ determined was $0.422 \pm 0.049$ (stat.) $\pm$

0.059 (syst.) [32].

The L3 collaboration measurement of the $\Lambda$ and $\Sigma_0$ cross sections at center of mass energies from 91 GeV to 218 GeV by the processes $\gamma\gamma \to \Lambda\overline{\Lambda}$ and $\gamma\gamma \to \Sigma^0\overline{\Sigma}^0$ were extracted as function of the center of mass energy and compared with CLEO collaboration results, as well to quark-diquark model and three quark model predictions [33]. Other analysis provided the average number of $< N_{\Sigma_+} > + < N_{\overline{\Sigma}_+} >= 0.114 \pm 0.011$ (stat.) $\pm 0.009$ (syst.) and $< N_{\Sigma_0} > + < N_{\overline{\Sigma_0}} >= 0.095 \pm 0.015$ (stat.) $\pm 0.013$ (syst.) finding that JETSET, HERWIG and ARIADNE predictions subestimated the measurements [34].

The measurement of inclusive production of the $\Lambda$, $\Xi^-$ and $\Xi^*(1530)$ baryons in two-photon collision with the L3 detector were described by PYTHIA and PHO-JET Monte Carlo programs, the comparison to $e^+e^-$ annihilation processes provides evidence for the universality of fragmentation function in both reactions; while the search for inclusive production of the pentaquark $\Theta^+(1540)\to pK_S^0$ showed no signal [35].

The CLAS collaboration at Jefferson laboratory presented a work with main goal of measuring observables related to the propagation of a quark struck by the virtual photon from DIS through cold nuclear matter and compared with quark propagation through hot QCD matter, or quark gluon plasma (QGP) formed in relativistic heavy ion collisions at RHIC. That work presented for the first time results for $K_S^0$ hadronization plotting the multiplicity ratios of $K_S^0$ over DIS events versus the energy fraction $z$ [36].

### 2.4.2 At $pp$ and heavy ions collisions

The KAOS collaboration with $CC$ and $AuAu$ collisions at 1-2 GeV where the kaon emission is a rare process, reported studies of $K^+$ and $K^-$ particle production, showing a dependence on the mass number A of the colliding system, as well as differences between the $K^+$ and $K^-$ cross sections $\sigma$ per $A^{5/3}$. The same conclusion was made for the same particle at different kinetic energies for three different systems

and various beam energies [37].

The FOPI detector studying nuclear matter at high temperatures/high density in the heavy ion collider GSI in SIS have studied $\Lambda p$, $\Lambda$, $K^0$, $\phi$, $\Sigma^*(1385)$ and $K^*(892)$. The inclusive $K^0$ cross section results as function of the target nucleus A after using $\pi^-$ beam against target nuclei $C$, $Al$, $Cu$, $Sn$, and $Pb$, showed an increase at higher A values [38] and confirming the KAOS collaboration results.

The HADES collaboration also made measurements of strangeness ($K^+$,$K^-$, $\Lambda$, $\rho$, $K_S^0$ and $\Xi$ particles) in Ar+KCl system at 1.756A GeV. The results of measured yields and slopes of the transverse mass of kaons and $\Lambda$ agrees with KAOS and FOPI studies [39]. An effective temperature of the kinetic freeze-out of $T_{Eff} = 92.0 \pm 0.5 \pm 4.1$ MeV [40] is achieved for the $K_S^0$ .

The CERES studied the $K_S^0$ yield at midrapidity $dN/dy$ and transverse momentum distributions in central $PbAu$ collisions at top SPS energy [41]. The results were compared to NA49 [42] and NA57 [43] measurements. An agreement with NA57 $K_S^0$ was found in the overlapping rapidity bins within errors.

The PHENIX ($pp$) [44] and the STAR ($AuAu$) [45] collaborations at RHIC with $\sqrt{200}$ AGeV center of mass energy have measured the ratio of $K/\pi$ giving a value between 0.1 - 0.5 and showing very similar results at low $p_T$ although a slight hint of strangeness enhancement (around 20%) is indicated in nucleus collision relative to $pp$ collisions. The same is expected at LHC [46].

The NA49 collaboration at SPS have also identified $K^*(892)$, $K^\pm$, $\rho$, $\Xi$ and $\Omega$ particles [47] and measured the $K^*/K^\pm$ ratio as function of the average number of wounded nucleons $N_w$ and the resonance lifetime $c\tau$; while another paper from the STAR collaboration colliding $CuCu$ and $AuAu$ at $\sqrt{s} =62$ GeV, presented the mid-rapidity $dN/dy$ for $K_S^0$ , $\Lambda$, $\Xi$ and $\Omega$ particles and also mid-$p_T$ results of the $\Lambda/K_s^0$ ratio, concluding that the centrality dependance of $dN/dy$ per $< N_{part} >$ has similar trends to a parametrisation on the fraction of participants that undergo multiple collisions. The ratio $R_{AA} = (dN_{AA}/dy)/(dN_{pp}/dy)$ for $K_S^0$ showed to be greater than the same ratio for $\pi$, providing evidence for parton flavour conversions in heavy-ion

collisions [48].

Other studies with $pp$ collisions have tried to determine the total cross section of still scarce reactions as $pp \to nK^+\Sigma^+$, $pp \to nK^+\Sigma^0$ and $pp \to nK^+\Lambda$ [49] including contributions from previously ignored $\Delta^*(1620)$ and $N^*(1535)$ resonances. They shown that these resonances play dominant roles for strangeness production in $pp$ collisions.

At this section one also ask about the new LHC age, although it consists of four experiments only ALICE has planes of strangeness studies (in part because the detector design allows it), a lot of prediction was done concluding the easy and clear identification of $K_S^0$, $\Lambda$, $\Xi$, $\Omega$ particles and some resonances [50] but no measurement are public until today. It is, however, natural to expect that in the high energy-density phase (quark gluon plasma, QGP) up, down and strange quarks have similar populations and play equivalent roles. RICH results didn't confirm that but it could becomes a good approximation at LHC energies at QGP. Maybe the expected enhancement of strange anti-baryon production, as proposed by Müller and Rafelski [29] will be observed.

Can we expect that more final-state strange particles are produced with larger transverse momenta and pQCD is going to provide more precise predictions?. The role of strangeness will change at the LHC energies? Do the $s$ quark behave as light $u$ and $d$ quarks and does charm appear as the first massive flavour?. These and other questions can find answer in the following few years, being a good reason to continue with strangeness studies.

### 2.4.3   At $ep$ colliders

The HERA experiments, HERMES, HERA-B, ZEUS and H1, have also done measurements of several strange particles, mainly of $K_S^0$ meson, $\Lambda$, $\overline{\Lambda}$ baryons, $K_s^0 K_s^0$ and baryonic resonance production.

The fixed target HERA-B experiment measured the cross section rates of $K_S^0$, $\Lambda$ and $\overline{\Lambda}$ [51], $K^{*0}$, $\overline{K}^{*0}$ and $\rho$ mesons using $C$, $Ti$ and $W$ as target materials showing

a power law dependence with the atomic mass of the target. And also reporting a smaller production of $K^*$ and $\overline{K}^{*0}$ compared with $K^+$ and $K^-$ [52].

The HERMES detector showed that $s$ quarks of $\Lambda$, $\overline{\Lambda}$ originate predominantly from $s$ pair production from $\gamma$ [53].

The Zeus experiment have made a high statistics study of the $K_s^0 K_s^0$ system using the full HERA II data set in the phase space $p_T(K_s^0) \geq 0.25$ GeV and $|\eta| \leq 1.6$. A number of 672418 $K_s^0 K_s^0$ pairs coming mainly from photoproduction were identified, reporting an observation of states at 1537 MeV and 1726 MeV consistent with $f_2'(1525)$ and close to $f_0(1710)$, also an enhancement near 1300 MeV which may arise from the production of $f_2(1270)$ and/or $a_2^0(1320)$ [54]. Agreement with the measurements done by L3 [55] and TASSO [56] collaborations at $\gamma\gamma \rightarrow K_s^0 K_s^0$ was found. The H1 collaboration have not confirmed these results since no paper or thesis of these measurements exist until now.

The pentaquark searches at Zeus have looked for baryonic states decaying to $K_S^0\, p$ and $K_S^0\, \overline{p}$ [57]; e.g., the pentaquark $\Theta^+(uudd\overline{s})$ (reported for fixed-target experiments [30]). They find a peak with 221±48 events at $1521.5 \pm 1.5(\text{stat.})^{+2.8}_{-1.7}(\text{syst.})$ MeV for $Q^2 \simeq 20$ GeV$^2$ providing further evidence for the existence of a narrow baryon resonance consistent with the predicted $\Theta^+$ pentaquark state. Another study at $Q^2 > 1$ GeV$^2$ for $\Xi^-\pi^-$, $\Xi^-\pi^+$ decay channels [58] by ZEUS also gives a clear signal for $\Xi^0(1530) \rightarrow \Xi^-\pi^+$, but no other signal at higher masses ($\Xi_{3/2}^{--}$ and $\Xi_{3/2}^+$) was observed. The H1 studies of these resonances are presented in the subsection 2.5.1.

Concerning measurements of the $K_S^0$ and $\Lambda$ production, baryon-antibaryon asymmetry, baryon to meson ratio and strange to light hadrons ratio: The results of ZEUS in the phase spaces corresponding to photoproduction ($Q^2 \simeq 0$) and DIS ($2 < Q^2 < 25$ GeV$^2$ and 25 GeV$^2 < Q^2$) collected at $\sqrt{s} = 319$ GeV compared to different ARIADNE and PYTHIA MC models [59] conclude that the DIS results are reproduced by ARIADNE with $\lambda_s = 0.22$ in gross features, while PYTHIA describes the cross section as functions of $p_T$ and $\eta$ but doesn't for $x$ dependence. No $\Lambda$ - $\overline{\Lambda}$ asymmetry is found. The strange to light quarks ratio is in agreement with $e^+e^-$

results but the baryon to meson ratio is larger that $e^+e^-$ measurements.

The H1 experiment has very nice and recent results of the $K_S^0$ and $\Lambda$ production rates at DIS low $Q^2$ which can be found at references [60], [61] and [62]. The last published results are discussed extensively in the subsection 2.5.3. The first measurement of the $K^*(892)$ vector by the H1 collaboration at low $Q^2$ is presented in the subsection 2.5.2.

## 2.5  Previous H1 results of strangeness at low $Q^2$

The most important studies carried out by the H1 experiment involving the identification of $K_S^0$ meson or other strange particles are the search of predicted resonances as $\Theta^+ \to K_S^0\, p^\pm$ and $\Xi^0(1530) \to \Xi^-\pi^+$, the identification of $K^*(892)$ meson and the analysis of $K_S^0$ meson and $\Lambda$ baryon. All of them through the analysis of data at low $Q^2$.

### 2.5.1  Search of resonances
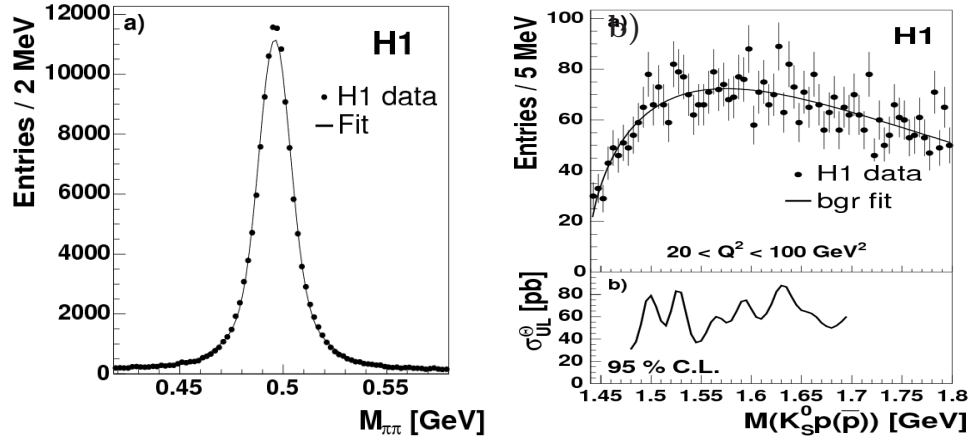


Figure 2.4: Invariant mass spectra of a) $K_S^0$ candidates reconstructed by the decay mode $\pi^+\pi^-$ and b) $\Theta^+$ candidates decaying to $K_S^0\, p^\pm$, no signal is observed in the mass range of 1.48 to 1.7 GeV.

A search of the hypothetical baryon $\Theta^+$ in the decay channels $K_S^0$ $p^\pm$ as observed by several fixed-target experiments is done at H1, in the phase space $5<$ $Q^2 <100$ GeV$^2$ and $0.1< y <0.6$. The data were taken during the years 1996-2000 (HERA I[1]) with a luminosity of 74 pb$^{-1}$.

The $K_S^0$ is reconstructed by looking for $\pi^\pm$ tracks coming from a secondary vertex in the central part of the detector. The invariant mass distribution fitted to two Gaussian functions is showed in Figure 2.4 a). A number of 133,000 $K_S^0$ candidates are obtained after subtracting the background.

The combination of the $K_S^0$ candidate with the proton candidates gives the reconstruction of $\Theta$. The detailed procedure is explain in [63]. The mass range considered for the search is 1.48 to 1.7 GeV since the reported masses are between 1520 and 1540 MeV. No signal for the resonance $\Theta^+$ production is observed in the studied decay modes as shown in the mass distribution spectra in Figure 2.4 b) where the corresponding upper limits are also shown.

The analysis was repeated at large $Q^2$ and low proton momentum region in which ZEUS collaboration made its observation but no evidence was found.

The analysis of baryonic resonances and their antiparticles $X^{--}$ and $X^0$ in the mass range 1600 to 2300 MeV is also carried out with the H1 detector. The search is perfomed in the region defined by $2< Q^2 <100$ GeV$^2$ and $0.05< y <0.7$ using data taken in 1996-1997 and 1999-2000 with $\mathcal{L} = 100.5$ pb$^{-1}$. The particle decay modes are $X^{--} \rightarrow \Xi^- \pi^- \rightarrow [\Lambda \pi^-]\pi^- \rightarrow [(p\pi^-)\pi^-]\pi^-$ and $X^0 \rightarrow \Xi^- \pi^+ \rightarrow [\Lambda \pi^-]\pi^+ \rightarrow [(p\pi^-)\pi^-]\pi^+$.

The identification of these particles is done first by looking for the $\Lambda$ ($\overline{\Lambda}$) baryon by their $p$ ($\bar{p}$) and $\pi^-$ ($\pi^+$) daugther signals, second it is made a combination of the $\Lambda$ candidate with negatively charged track assumed to be a pion and third, the $X^{--/0}$ candidates are formed by combining each of these $\Xi^-$ candidates with an additional pion track; for extended explanation of the reconstruction, see references [64] or [61].

In Figure 2.5 one can see the resulting invariant mass spectra for the neutral

---

[1]The description of the HERA I and HERA II data can be found in the chapter 3.
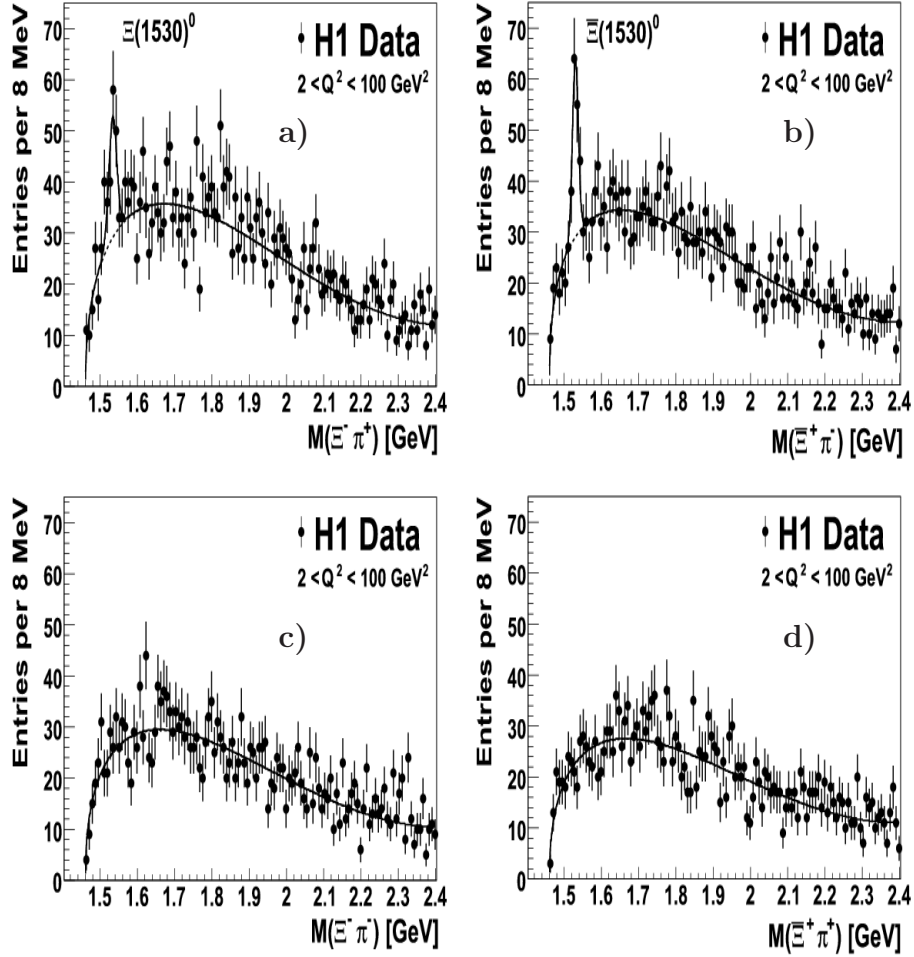
Figure 2.5: Invariant mass distribution of the combinations a) $\Xi^-\pi^+$, b) $\Xi^+\pi^-$, c) $\Xi^-\pi^-$ and d) $\Xi^+\pi^+$ with the fit to signal and background. A clear signal of the $\Xi^0(1530)$ baryon is observed for the neutral combinations in the mass range of 1600 to 2300 MeV.

$\Xi^-\pi^+$ and $\Xi^-\pi^+$, and the doubly charged combinations $\Xi^-\pi^-$ and $\Xi^+\pi^+$. In the neutral particle distributions, a peak is observed corresponding to the established $\Xi^0(1530)$ state. A fit using a Gaussian function for the signal and $p_1(M - m_\Xi - m_\pi)^{p_2} * (p_3 + p_4 M + p_5 M^2)$ for the background is applied to the mass spectra yielding a total of $171 \pm 26$(stat) $\Xi^0(1530)$ baryons in the mass range of 1600-2300 MeV. In the other hand, for the doubly charged combinations no signal is found.

The results showed compatibility with ZEUS measurement at $2< Q^2 <100$ GeV$^2$ looking for the same decay modes.

## 2.5.2   Analysis of $K^*(892)$ meson production

The H1 collaboration has made important progress in the $K^*(892)$ vector meson cross section measurement both in the laboratory and in the hadronic center of mass system $(\gamma^*p)$ frames. The meson was studied looking for the decay channel $K^*(892) \to K_s^0\pi^\pm \to (\pi^+\pi^-)\pi^\pm$ with BR $= 23.06\%$ in the data period 2005-2007 with a corresponding accumulated luminosity of 302 pb$^{-1}$. The events where selected in the phase space defined by $5< Q^2 <100$ GeV$^2$, $0.1< y <0.6$, $-1.5< \eta(K^*) <1.5$ and $p_T(K^*) > 1$ GeV. The detailed selection criteria of the kinematics, the electron, the tracks, the $K_S^0$ and the $K^*$ can be found in reference [65].

The number of $K^*(892)$ are extracted from a fit to the invariant mass of the Breit Wigner function for the signal description and the $p_1(m_0 - (m_{K_s^0 + m_\pi})^{p_2}) * Exp(p_3 m + p_4 m^2 + p_5 m^3)$ function for the background. At the end, 80000 $K^{*\pm}$ candidates are identified after the background subtraction and used for the cross section determination:

$$\sigma_{vis} = 7.36 \pm 0.087(\text{stat.}) \pm 0.88(\text{syst.}) \; nb. \tag{2.5}$$

The differential cross section measurement of the $K^*(892)$ in the laboratory and $\gamma^*p$ frames are compared to the Monte Carlo simulation programs Django and Rapgap, both simulated with matrix elements plus colour dipole model (CDM) and parton showers (MEPS) respectively convoluted with CTEQ6L parton density function
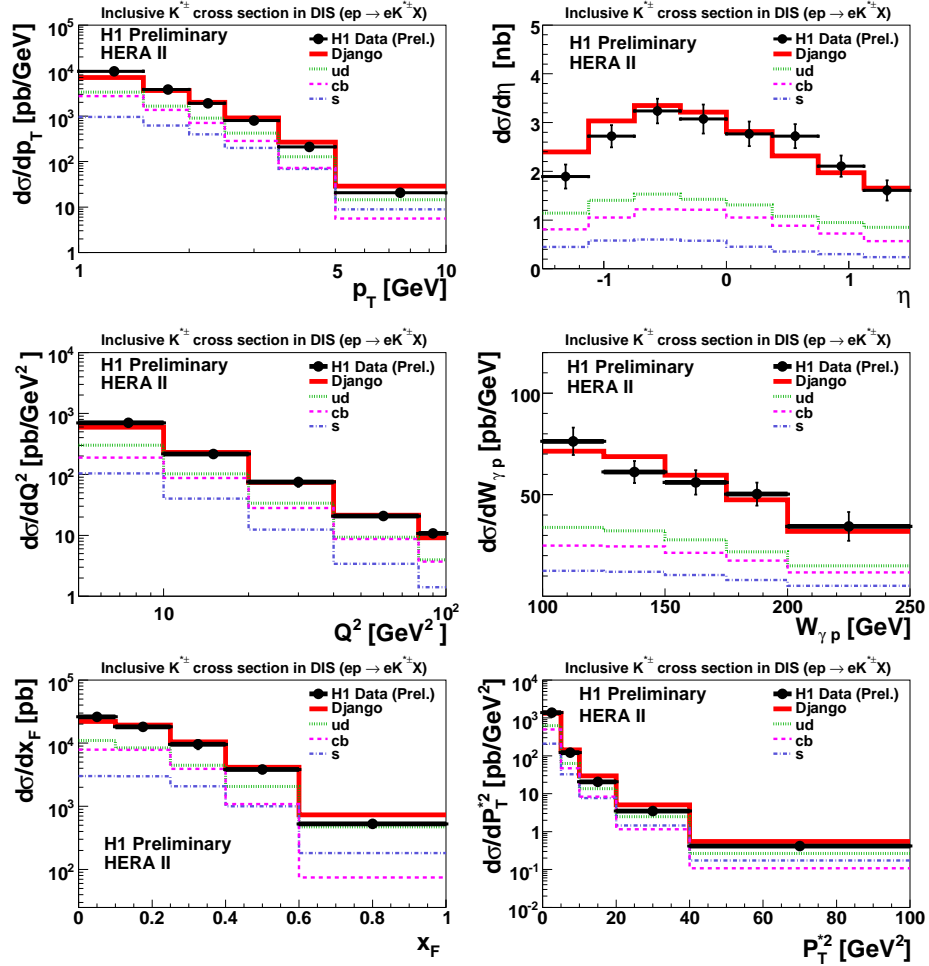
Figure 2.6: The $K^*$ production cross section as functions of transverse momentum $p_T$, pseudorapidity $\eta$ and photon virtuality $Q^2$ laboratory variables and center of mass energy $W_{\gamma p}$, x-Feynmann $x_F$ and transverse momentum squared $P_T^{*2}$ in the hadronic center of mass system frame. The Django model describes the data in general features but fails to describe the shape of the cross section as function of $\eta$. The contribution of quark flavours are presented in order to study the production mechanism of strange particles.

(PDF) and interfased to Lund string fragmentation model with strangeness suppresion factors set to ALEPH collaboration tunning. Both, Django and Rapgap models, describe the data very well in overall features but fail to describe in detail the shape of $\eta$ production. The plots of the measurements are presented in Figure 2.6 where the contribution of the quark flavours to the production studied with Django are displayed.

The contribution of different flavours to the cross section can provide clues to the strange particle production mechanisms. It is observed that $K^*$ coming from $ud$ quarks are mainly from fragmentation; those coming from $cb$ quarks belong mostly to heavy hadron decays (heavy quarks created by BGF) and give the second highest contribution; while the $K^*$ from $s$ quark (mainly due to the hard subprocess) correspond to only the 20% of the total cross section prominently at high values of $x_F$ and $p_T^*$. It was observed that the $x_F$ variable provides good sentitivity to the flavour composition studies.

### 2.5.3   $K_S^0$ and $\Lambda$ studies at low $Q^2$

The H1 collaboration has recently published [66] the measurement of the $K_s^0$, $\Lambda$ and $\overline{\Lambda}$ cross sections together with the ratios of baryon to meson and meson to charged particles using DIS events at the phase space defined by $2 < Q^2 < 100$ GeV$^2$, $0.5 < p_T < 3.5$ GeV, -1.3 $< \eta <$ 1.3 using HERA I data with $\mathcal{L} = 50$ pb$^{-1}$. The decay channels used for the identifications are $K_S^0 \to \pi^- \pi^+$ with BR $\simeq 69.2\%$ and $\Lambda \to p\pi$ with BR $\simeq 63.9\%$.

The measurements are presented in the laboratory frame as a function of $Q^2$, $\eta$ and $p_T$ and in the Breit frame (appendix E) in the current and target hemispheres as a function of the momentum fraction $x_p^{BF}$ and the $K_S^0$ transverse momentum $p_T^{BF}$. The results were compared to Django (CDM) and Rapgap (MEPS) models with $\lambda_s = 0.2$, 0.286 and 0.3 for CTEQ6L, H12000LO and GRV94 parton density functions.

The 213,000 $K_S^0$ candidates taken from the fit to the invariant mass distribution,
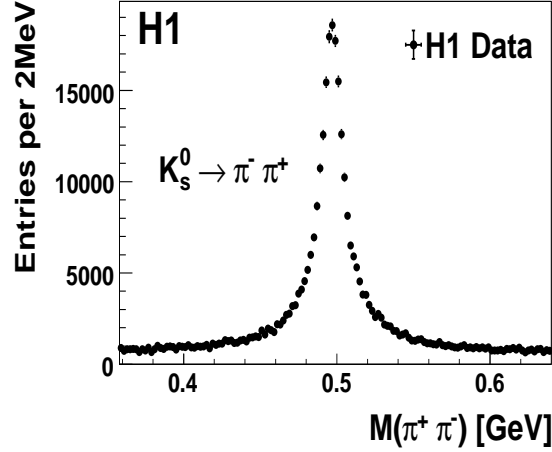
Figure 2.7: The $K_S^0$ invariant mass distribution from data with statistical uncertainty denoted with the error bars for each point.

showed in Figure 2.7, are used for the measurement of the inclusive $K_S^0$ cross section in the visible range, giving:

$$\sigma_{vis} = 21.28 \pm 0.09(\text{stat.})^{+1.19}_{-1.23}(\text{syst.}) \text{ nb.}$$

In analogy, the inclusive cross section of both the 22000 $\Lambda$ and 20000 $\overline{\Lambda}$ identified is measured as $\sigma_{vis} = 7.88 \pm 0.10(\text{stat.})^{0.45}_{0.47}(\text{syst.})$ nb.

Figures 2.8 and 2.9 show the differential cross section of the $K_S^0$ mesons as a function of laboratory and Breit frame variables, respectively. The MC over data ratio are plotted in the bottom part of each distribution. It shows the comparisons to CDM and MEPS. It seems that CDM with $\lambda_s = 0.3$ makes a good description of the differential cross section as a function of $Q^2$, $x$, $\eta$ and $p_T$, but finds difficulties to describe the shape of $\eta$ and low $p_T$. Whereas the Breit frame calculations agree with CDM model taking a strangeness factor $\lambda_s = 0.3$.

Similar plots for $\Lambda$ were obtained and can be seen in references [66] and [67], CDM with $\lambda_s = 0.3$ behaves more like data in this case but one should not forget that sensitivity to $\lambda_{qq}$ and $\lambda_{sq}$ is expected. The $\Lambda$ asymmetries, $A_\Lambda = (\sigma_\Lambda - \sigma_{\overline{\Lambda}})/(\sigma_\Lambda + \sigma_{\overline{\Lambda}})$,
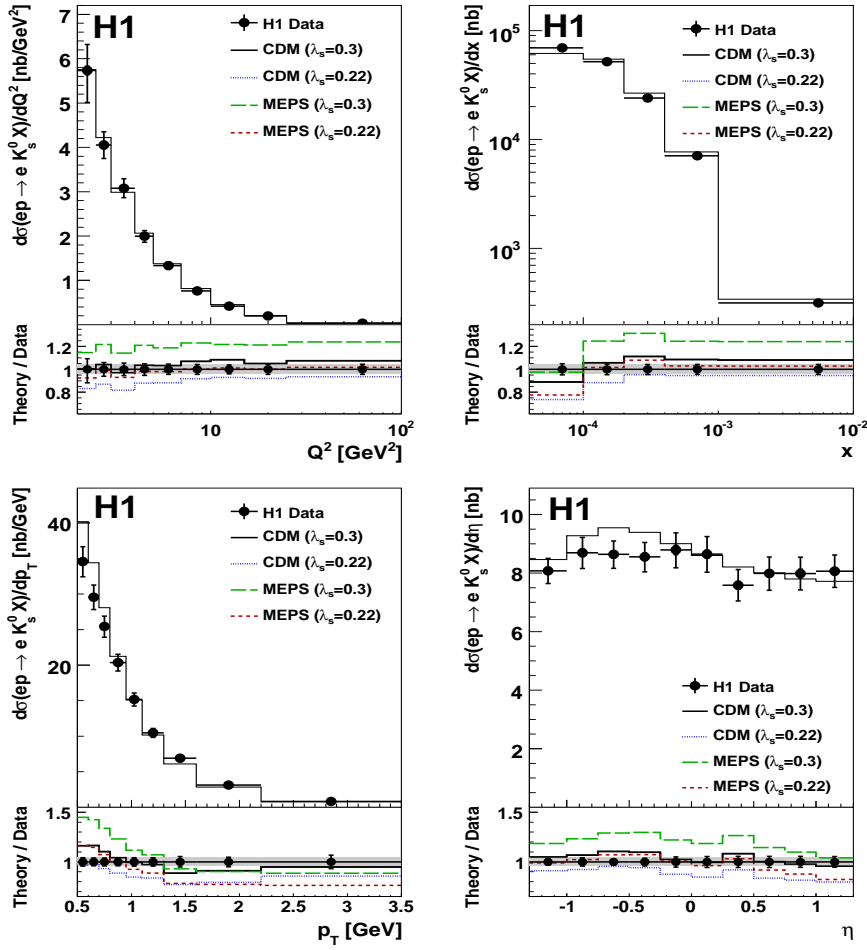
Figure 2.8: The differential production cross sections for $K_S^0$ in the laboratory frame as a function of the four-momentum of the virtual photon $Q^2$, Bjorken scaling variable $x$, $K_S^0$ transverse momentum $p_T$ and $K_S^0$ pseudorapidity $\eta$. The theory/data ratios on the bottom show the comparison to the model predictions. Inner (outer) error bars for statistical (total) uncertainties.
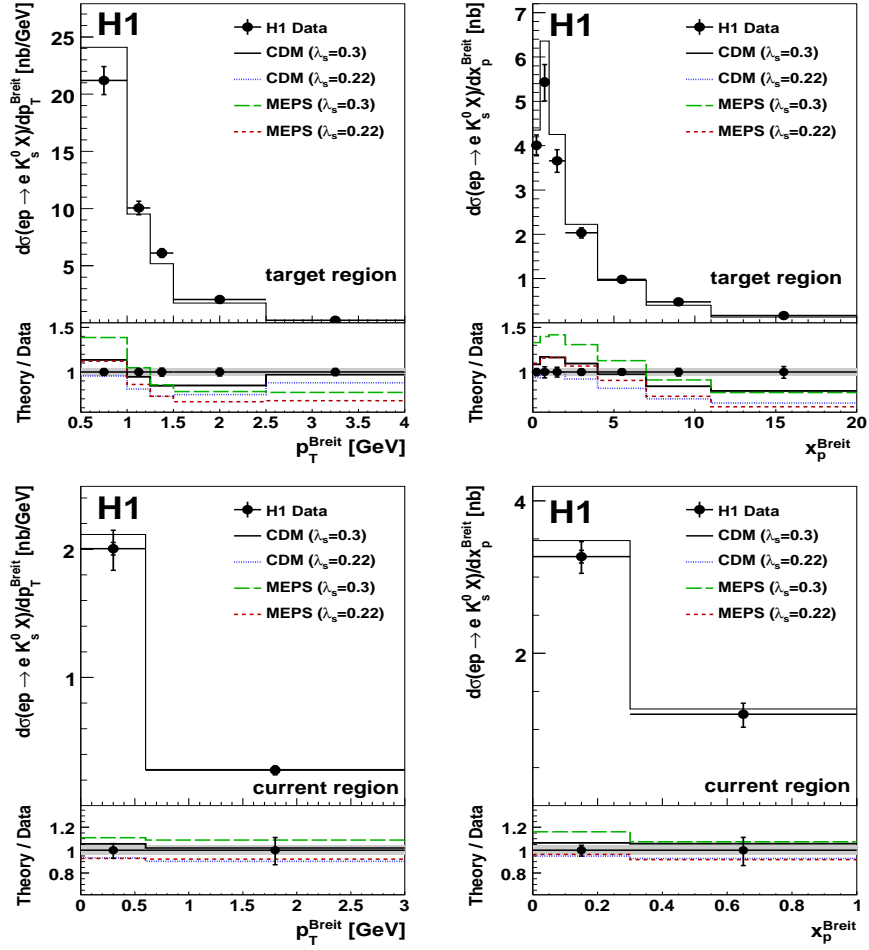
Figure 2.9: The differential $K_S^0$ production cross sections in the Breit frame as a function of $p_T^{BC}$ and $x_p^{BC}$ in the target and current hemisphere. The theory/data ratios on the bottom show the comparison to the different model predictions. Inner (outer) error bars for statistical (total) uncertainties

measured in the laboratory and the Breit frames are consistent with zero showing no evidence of baryon number transferred from the proton beam to the $\Lambda$ final state.

The meson to charged particles ratio with an averaged measurement of:

$$\frac{\sigma_{vis}(ep \rightarrow eK_S^0 X)}{\sigma_{vis}(ep \rightarrow eh^\pm X)} = 0.0645 \pm 0.0002(\text{stat.})^{+0.0019}_{-0.0020}(\text{syst.})$$

was calculated differentially as shown in Figure 2.10 for the laboratory frame as function of $Q^2$, $x$, $\eta$ and $p_T$. The parameter $\lambda_s$ is expected to be less model dependent here. The ratio strongly rises with increasing $p_T$ but remains approximately constant as a function of all the other variables. The models describe reasonably well the ratio but none is able to describe the shape, especially of $\eta$ and low $p_T$.

The measured baryon to meson ratio average is

$$\frac{ep \rightarrow e\Lambda X}{ep \rightarrow eK_S^0 X} = 0.372 \pm 0.005(\text{stat.})^{+0.011}_{-0.012}(\text{syst.}). \tag{2.6}$$

The CDM model agrees with data but not completely for the differential measurement in the laboratory frame, no model dependence was found in the Breit frame since no sensitivity to $\lambda_s$ is expected but $\lambda_{qq}$ and $\lambda_{sq}$ can contribute.

The comparison between three different proton PDFs: CTEQ6L, GRV-94 (LO) and H1 2000 LO, with $\lambda_s = 0.286$ does not show any dependence.
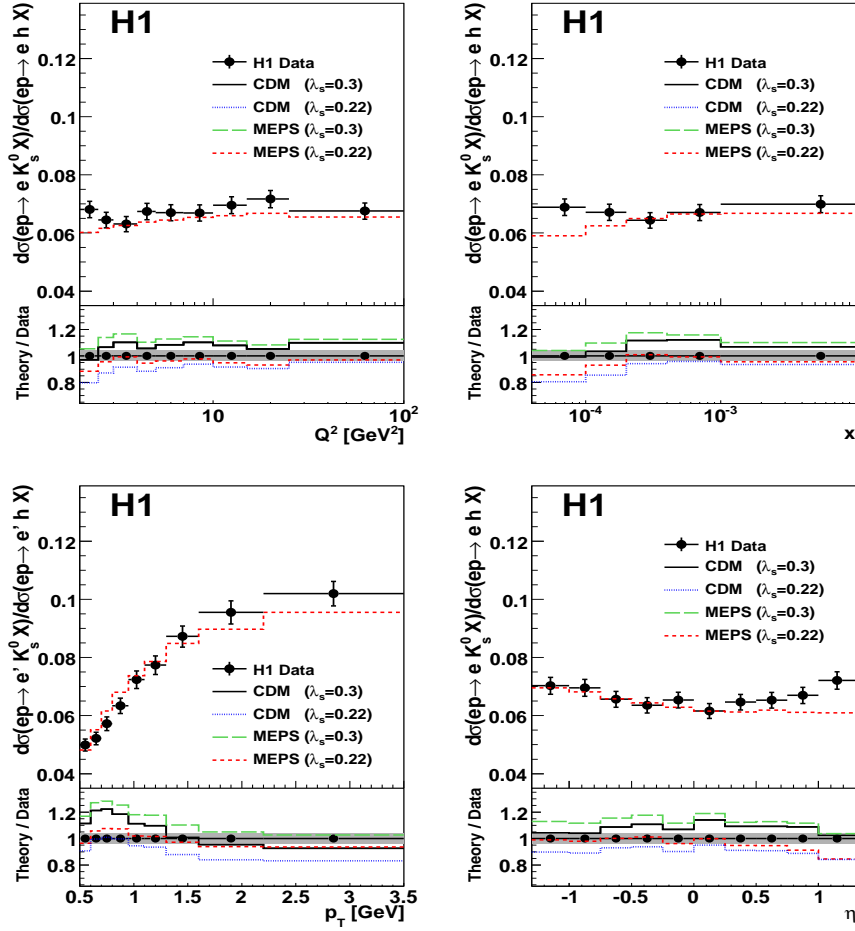
Figure 2.10: The differential $K_S^0$ mesons to charged particles cross sections ratio as a function of the four-momentum of the virtual photon $Q^2$, the Bjorken scaling variable $x$, the transverse momentum $p_T$ and the pseudorapidity $\eta$ in the laboratory frame. The theory/data ratios on the bottom show the comparison to the model predictions. Inner (outer) error bars for statistical (total) uncertainties

# Chapter 3

# HERA and the H1 Detector

The *electron-proton* collider HERA, located at DESY in Hamburg, Germany, offers the opportunity to study the structure of the proton. HERA consists of four different experiments spaced evenly along its circumference. One of those experiments, the H1 detector, provided the data analysed in this work. H1 is composed of several kind of detectors, fixed in a whole unit, designed to measure the particles properties.

A brief introduction to the HERA machine and the H1 detector components relevant for the studies presented on this thesis can be found here.

## 3.1   The HERA collider

The electron-hadron accelerator ring, HERA[1], was built at the German electron synchrotron laboratory, DESY[2], in Hamburg, Germany. It consists of two independent rings working as accelerators and storing proton and electrons with a center of mass energy of 319 GeV.

In Figure 3.1 a schematic picture of HERA collider and the pre-accelerator PE-

---

[1]**H**adronen **E**lektronen **R**ing **A**nlage
[2]**D**eustches **E**lektronen **SY**nchrotron

TRA[3] can be found. This pre-accelerator is located at the south-west and it is amplified in Figure 3.1 b). The performance of the accelerator begins with injection of protons[4] with an energy of 50 MeV from the linear accelerator, $H^-$-linac, to the DESY III ring, where they are accumulated and accelerated until having 70 bunches with 7.5 GeV. Then, one by one are sent to the PETRA ring to be accelerated up to 40 GeV, to finally be transferred to the HERA ring. HERA operates with 180 circulating bunches of protons, every one of them consisting of approximately $10^{10}$-$10^{11}$ protons, separated in time by 96 ns and accelerated to an energy of 920 GeV.
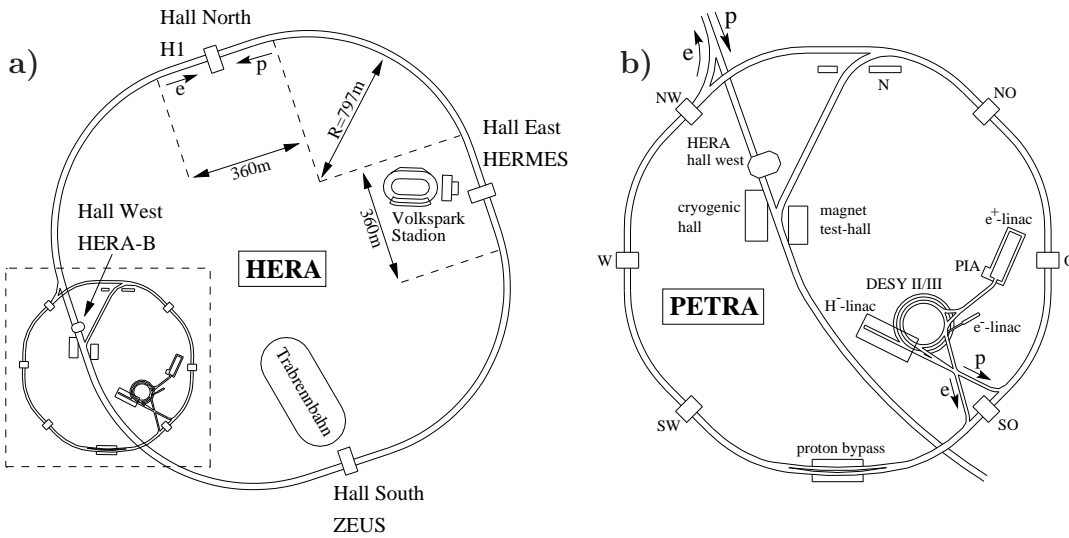


Figure 3.1: a) The HERA accelerator and b) the PETRA pre-accelerator circumferences. The four experiments around HERA: HERA-B, H1, HERMES and ZEUS are indicated in a) together with the traveling direction of the electron $e$ and proton $p$ beams.

The electrons (or positrons) acceleration begins at the $e^-$ ($e^+$)-linac accelerator, the electrons are injected from there to the DESY II ring, where they are accelerated from 450 MeV to 7 GeV. After the storage of 70 bunches is completed, they start to be sent to PETRA for their acceleration up to 14 GeV. At the end, 180 bunches

---

[3]**P**ositron **E**lektron **T**andem **R**ing **A**nlage
[4]The protons are taken from hydrogen ions

of electrons are injected to HERA until they get an energy of 27.5 GeV, separated by the same time interval as proton bunches. Sometimes, some bunches, called *pilot bunches*, are left empty to be used for the background estimation, of protons colliding with the beam pipe or residual gas.

The proton bunches lifetime easily exceeds 24 h, but the lifetime of the electron bunches is limited to about 6 h (the lifetime for positrons is approximately a factor of 2 higher). Both electrons and positrons are more difficult to keep circulating due to the synchrotron radiation.

The HERA accelerator ring has a circumference of 6.3 km where superconducting dipole and focusing quadrupole magnets are distributed to guide the particles trajectories and to keep the bunches positionally stables. Between the quadrupoles, $\sim$12 m of free space is available for a detector. The beams pass inside a 190 mm inner diameter beam pipe with a wall of 150 $\mu$m Aluminium on the inside backed by 2 mm carbon fiber. The beam pipe is cooled with nitrogen gas and kept in vacuum conditions. It crosses the detector in its center at a height of 5.9 m above the floor level at an inclination of 5.88 mrad.

Around HERA, four experiments are located: HERMES, HERA-B, ZEUS and H1. Their locations are graphically shown in Figure 3.1 a). The electrons and protons, traveling to the right and left hand sides respectively, are made to collide head on (as in H1 and ZEUS detectors) or against a target (as in HERMES and HERA-B detectors) every 96 ns or 10.4 MHz. HERMES, HEra MEasurement of Spin, is dedicated to spin studies of the proton, HERA-B is interested in CP violations in $B^0 - \bar{B}^0$ systems and, ZEUS and H1 study the proton structure.

An important characteristic of any accelerator operation is the produced luminosity which gives directly the number of events per second for a cross section of 1 cm$^2$ (units of cm$^{-2}$s$^{-1}$). The instantaneous luminosity $\mathcal{L}$, can be calculated with the revolution frequency $f$ of the bunches, the number of protons $N_p$ and electrons

$N_e$ per bunch and the beam radii $\sigma_x$ and $\sigma_y$ of the bunches at the crossing point:

$$\mathcal{L} = \frac{f * N_e * N_p}{2\pi * \sqrt{2}\sigma_x * \sqrt{2}\sigma_y}, \tag{3.1}$$

due to the uncertainty in the beam collimation the luminosity is measured as explained in the subsection 3.2.3.

The luminosity is also related to the effective cross section $\sigma$ as: $dN/dt = \mathcal{L}\sigma$. The accumulated luminosity at a period T of time is denoted as:

$$L = \int_T \mathcal{L}dt \tag{3.2}$$
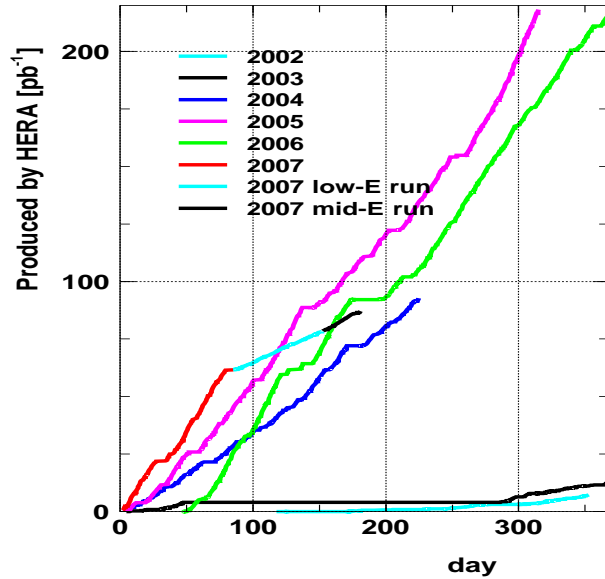


Figure 3.2: Accumulated luminosity by HERA II collider in $pb^{-1}$ vs number of days for six years of operation. In 2007 two periods of several months were dedicated to the operation of the machine at low and middle energies.

The HERA operation time is divided in two periods called HERA I and HERA II. HERA I corresponds to data taken from 1992 to 2000 while HERA II goes from 2002 to 2007. The separation responds to the improvements made to the accelerator in

2001. Several super-conducting quadrupole magnets where installed, improving the focusing of the beams and consequently increasing the luminosity by a factor of 4 to 5. In Figure 3.2 is possible to see the produced luminosity by HERA in pb$^{-1}$ per year. The HERA accelerator ended its performance in summer 2007.

## 3.2 The H1 detector

The H1 experiment [68] is located in the northern side of the HERA ring, at 20 m underground. The detector measures 12 x 10 x 15 m$^3$ and its weight is 2,800 tons. The coordinate system of H1 is right-handed with the origin settled up on the interaction vertex (also called nominal point), the $x$ axis points to the center of HERA, $y$ pointing up and the $z$ axis defined by the incoming proton beam direction (from right to left hand side in Figure 3.3). In polar coordinates, the azimuthal angle $\phi$ rests in the $xy$ plane being $\phi = 0$ over the $x$ axis while the polar angle $\theta$ is zero on the positive $z$ axis. The pseudorapidity is defined as $\eta = -ln\left[tan(\theta/2)\right]$.

Figure 3.3 presents a longitudinal cut of the H1 detector with the protons and electrons coming into the detector from the right and left hand side, respectively. The H1 detector is composed by several kind of sub-detectors in order to measure the energy, momentum and charge of the particles produced during and after the $ep$ collisions. The difference of energy between electrons and protons makes that most of the particles are scattered in the outcoming proton direction or the so called forward region. This is the reason why the H1 detector is considerably more massive and highly segmented in that direction.

The detector is arranged as follows: immediately outward from the interaction vertex is the tracking system, consisting of the Central Silicon Tracker (CST), a central (CJC, COZ, CIZ, COP and CIP) and a Forward Tracking System (FTS) used for the trajectory particle reconstruction. Two calorimeters surrounding the trackers are the liquid argon calorimeter (LAr Cal) in the central and forward region, and the scintillator spaghetti calorimeter (SpaCal) in the backward region, both
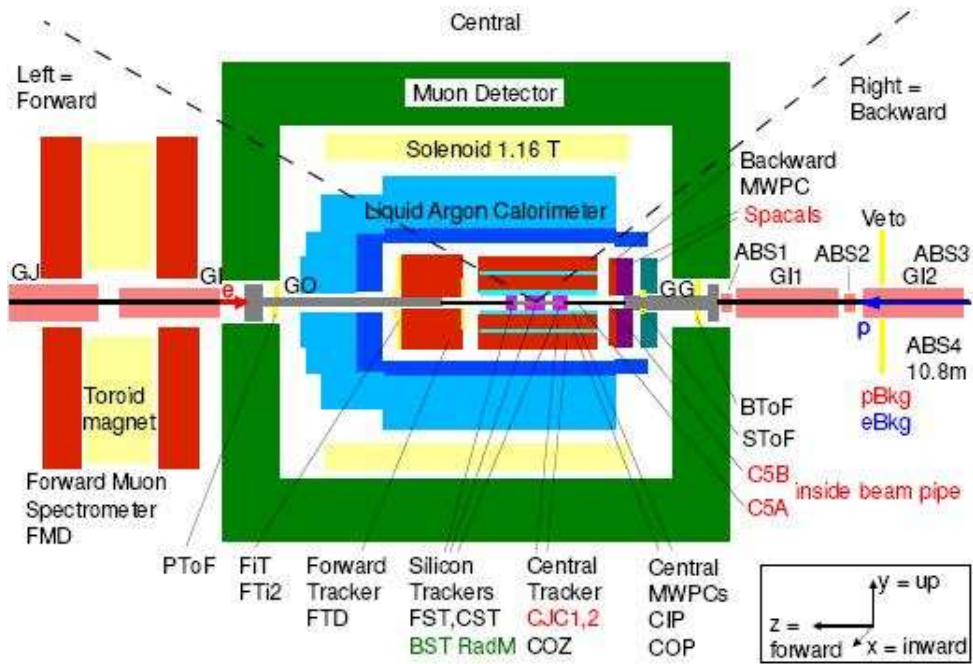
Figure 3.3: Cut along the $z$ beam axis of the H1 detector. The components of the tracker, calorimeter and muon systems are indicated. The separation in central, forward at the left hand side and backward to the right hand side can be also schematically seen.

calorimeters have electromagnetic and hadronic sections ideal to measure the energy of the particles. Housing all these systems is a superconducting solenoidal cylindrical magnet with a diameter of 6 m and a length of 5.75 m which provides a homogeneous magnetic field of 1.16 T parallel to the $z$ axis. This magnetic field makes that charged particles produced in the collision move in an helical trajectory. The projection of this trajectory in the $xy$ plane yields a circle with radius $r = 1/p_t$ where $p_t$ is the transverse momentum of the particle. The iron return yoke of the magnet is laminated and filled with limited streamer tubes.

The small fraction of hadronic energy leaking out the calorimeter and the muon tracks are measured by the central muon identification system (CMS) placed after the solenoid coil. Stiff muon tracks in the forward direction are analysed in a supplementary toroidal magnet sandwiched between drift chambers. See Figure 3.3.

An electron tagger located at $z = $ -33 m from the interaction point in coincidence with a corresponding photon detector at $z = $ -103 m upstream (not shown in Figure 3.3) detect the tag electrons and photons produced with very small scattering angle and monitor the luminosity by the Bethe-Heitler process.

The H1 detector, as well as the HERA accelerator, was updated substantially during the time changing from HERA I to HERA II to cope with the new challenges at HERA II. The innermost detector regions saw major modifications to accommodate the superconducting quadrupoles of HERA II. The new silicon detector system (Forward Silicon Tracker) completely surrounds the interaction region to significantly improve vertexing and tracking in conjunction with the upgraded inner tracking system (new Forward Tracker). Combined with upgrades in the trigger (new Time Of Flight System, new multiwire proportional chamber CIP2k replacing the CIP and CIZ to overcome the increased non-ep background, an upgraded neural net event trigger for the second level, a new processing farm for the third level and a new Fast Track Trigger at the very first level) and data acquisition system (DAQ) to make best use of the luminosity increase in all physics areas. As well as, the installation of a new superconducting magnet G0 and GG (see Figure 3.3) to obtain a better

longitudinal polarisation of the electron beam at the interaction point.
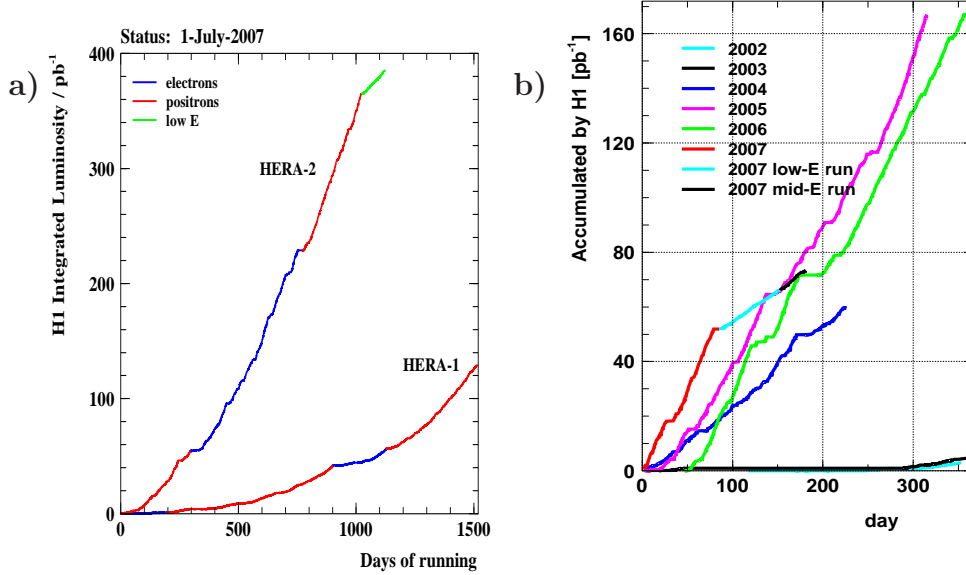


Figure 3.4: Accumulated luminosity in pb$^{-1}$ of the H1 detector a) during the HERA I (1992-2000) and HERA II (2002-2007) data taking, indication of the periods with the machine operating with electrons and positrons are plotted in blue and red, b) the HERA II accumulated luminosity, as function of the number of days, separated by years.

The H1 accumulated luminosity is plotted in the Figure 3.4 a), where can be seen the comparison between the collected luminosity during HERA I and HERA II periods, with HERA operating electrons and positrons alternatively. A clear increase in the accelerator performance can be observed. The plot in Figure 3.4 b) shows the HERA II period luminosity separated year by year since 2002 to 2007.

This study is done with the data taken from 2004 to 2007 where the integrated luminosity has a value of $\sim 340$ pb$^{-1}$.

The H1 phase space is pretty wide in $x$-Bjorken and virtuality $Q^2$ as can be seen in Figure 3.5, where the comparison to different experiments is presented. The range of $Q^2$ considered for this analysis lies in the regime of the LHC experiments, ATLAS

Table 3.1: The HERA *ep* collider characteristics.

| | HERA I | | HERA II | |
|---|---|---|---|---|
| | $e^-$ | $p$ | $e^-$ | $p$ |
| Energy | 27.6GeV | 920 GeV | 27.6 GeV | 920 GeV |
| Total current | 52 mA | 109 mA | 45 mA | 110 mA |
| Number of available bunches | 180 | 180 | 180 | 180 |
| Number of bunches in collision | 174 | 174 | 174 | 174 |
| Number of particles per buch | $3.5 \times 10^{10}$ | $7.3 \times 10^{10}$ | $4.2 \times 10^{10}$ | $10 \times 10^{10}$ |
| Transverse cross section per buch $\sigma_x$ x $\sigma_y$ ($\mu$m x $\mu$m) | 192 x 50 | 189 x 50 | 112 x 30 | 112 x 30 |
| Length of the bunch | 10 mm | 191 mm | 10 mm | 191 mm |
| Luminosity | $6.5 \times 10^{-3}$ (nb$^{-1}$s$^{-1}$) | | $17.2 \times 10^{-3}$ (nb$^{-1}$s$^{-1}$) | |
| | $6.5 \times 10^{30}$ (cm$^{-2}$s$^{-1}$) | | $17.2 \times 10^{30}$ (cm$^{-2}$s$^{-1}$) | |

and CMS.

In the next sections a brief description of the most important subdetectors for this analysis can be found. For more information about the H1 detector, see the Table 3.1 or consult the reference [69].

## 3.2.1 Tracker system

The tracker system consists of drift and multiwire proportional chambers detectors, see appendix B, for triggering and the identification of particles by the measurement of their charges, momentum and the reconstruction of their trajectories, with resolutions of $\sigma_p/p^2 \approx 3 \times 10^{-3}$ GeV$^{-1}$ and $\sigma_\theta \approx 1$ mrad. The tracking chambers are built to interfer as little as possible with the passing track.

This system is the main detector at H1, designed for the reconstruction of jets with high particle densities. Each component of the tracking system was built and
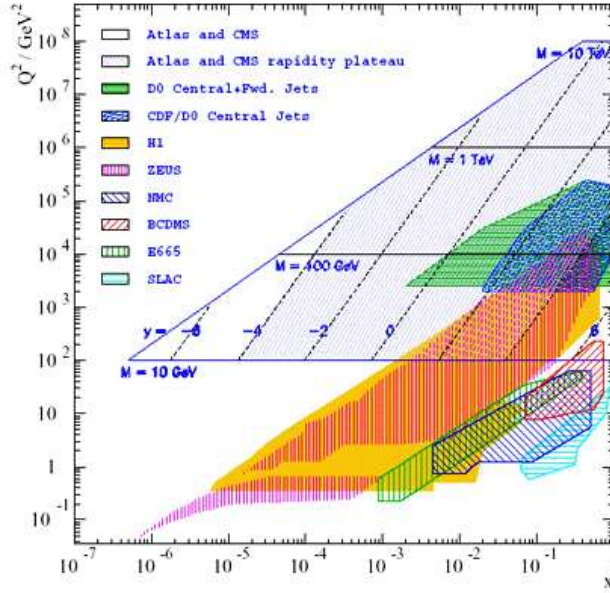
Figure 3.5: Phase space of different experiments presented in x-Bjorken vs. $Q^2$. The H1 detector has pretty wide range, so that the $Q^2$ considered for this analysis lies in part of the regime from ATLAS and CMS experiments.

tested separately, then assembled and locked to one mechanical unit to provide precise alignment relative to outside support, but with electrostatic shielding and independent gas volume. A schematic picture of the tracking detectors can be found in Figures 3.6 and 3.7.

The tracker system is divided in the central (CTD), the forward (FTD) tracker detectors and the backward proportional chamber (BPC).

The CTD is covered by the central (CST), the forward (FST) and the backward silicon tracker (BST), the central jet chamber (CJC), the central inner (CIZ) and central outer $z$-chamber (COZ), and the central inner (CIP) and central outer (COP) multiwire proportional chambers.

The CJC is based on two large concentric drift chambers, CJC1 and CJC2, designed for transverse track momentum determination by the signals recorded, in addition, the specific energy loss $dE/dx$ can be used to improve particle identifica-
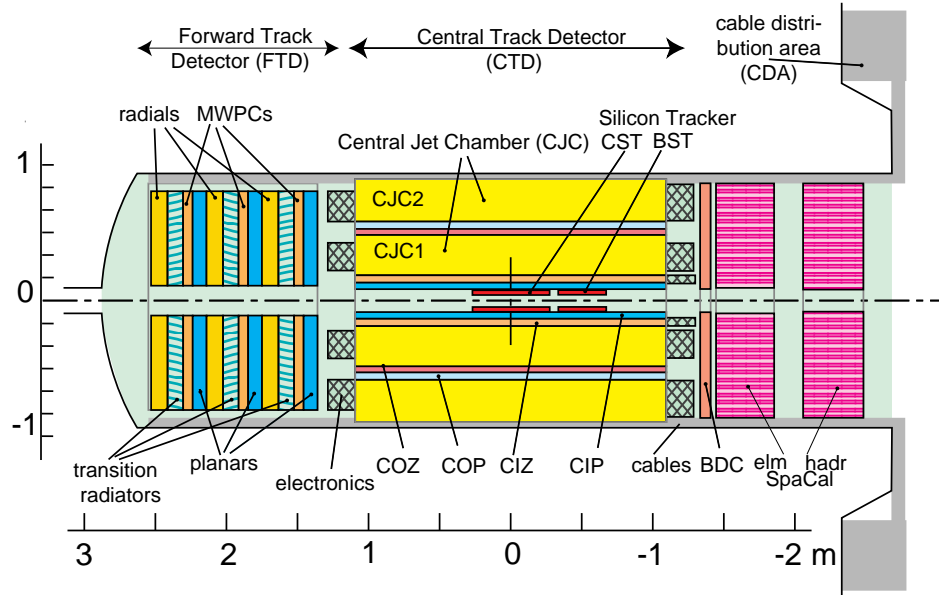
Figure 3.6: Longitudinal view of the forward and central tracker systems. The CST, CJC, COZ, CIZ, COP and CIP detector locations are shown.

tion. The measurement is complemented by the two thin $z$ drift chambers, CIZ and COZ, which give better accuracy by measuring the $z$ coordinate of the tracks.

The FTD, electrically isolated from the CTD, has three supermodules covering a polar angle range of $5° < \theta < 25°$. Each supermodule consists of planar drift chambers orientated in different wire geometries, a multiwire proportional chamber (FWPC), a passive transition radiator and a radial drift chamber, all them with wires strung perpendicular to the beam direction, Figure 3.6. This tracker allows accuracy in $\theta$, $r\phi$ measurements and fast triggering.

The CIP, COP and the FWPC, are used to trigger on tracks coming from a nominal interaction vertex, providing the first level (L1) trigger decision which is also used to distinguish between successive beam crossings.

The following subsections will refer in detail the detector components of the central tracker system.
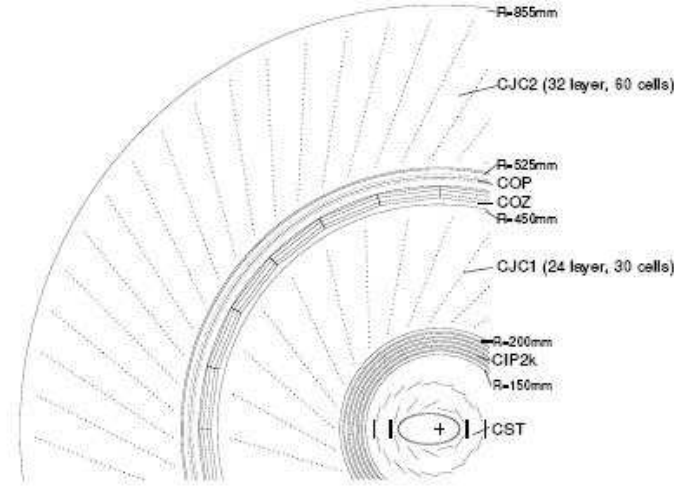
Figure 3.7: Transversal view of the central tracker system (CTD). The main detectors, CST, CJC1, CJC2, CIP2k, COZ and CIP are indicated together with their radial distances.

### 3.2.1.1 Central silicon tracker

The central silicon tracker [70], CST, is the nearest detector surrounding the beam pipe. It was installed in 1997 but updated during the time changing from HERA I to HERA II. The BST and FST were installed later to complement the device performance. Its main use is to improve the CJC reconstruction of tracks relating them to the interaction vertex.

The silicon trackers consist of two radial cylindrical layers of silicon strip detectors, the inner layer with 12 ladders and the outer layer with 20 sensor ladders (each containing 6 sensors). The CST covers an acceptance of $30° < \Theta < 150°$. Its intrinsic resolution is $\sigma_z = 22$ $\mu$m and $\sigma_{r\phi} = 12$ $\mu$m.

### 3.2.1.2 Central jet chambers

The inner CJC1 and outer CJC2 jet chambers [71] measure the trajectories of charged particles[5], both having a longitude of 2.5 m parallel to the $z$ axis. The CJC1,

---

[5]See appendix B for an explanation of the drift chambers performance.

with an inner (outer) radius of 20.3 cm (45.1 cm), has 720 sense wires distributed in 30 azimuthal cells. On the other hand, the CJC2 has 32 sense wires in each of its 60 cells and its inner (outer) radius is 53 cm (84.4 cm). All cells are tilted by about 30° in radial direction, in order that also the tracks with high momentum (low curvature) can be reconstructed, see Figure 3.7. In fact, the separation of tracks coming from different bunch crossings is possible to an accuracy of $\sigma \sim 0.5$ ns.

Each cell is composed by three planes of wires, the cathode wires planes marking the limits of the cell and the anode sense wires plane lying in between. All wires parallel to the $z$ beam line axis. The diameters of the wires limits the surface field to $\leq 2$ KV/mm.

The jet chambers are closed and filled in the first phase with a gas mixture of $Ar/CO_2/CH_4$ by 89.5/9.5/1.0 %, and $Ar/C_2H_6+H_2O$ by (50/50) + 0.5 % during the second phase. In this condition, when a charged particle passes through the jet chambers, the electrons will drift to a velocity of 50 mm/$\mu$s$^{-1}$ towards the anode wires to induce the current signal which allows the measurement of the hit position in the $xy$ plane with a resolution of $\sigma_{r\phi} = 170$ $\mu$m. Then, comparing the collected charge at both ends on the wire, the $z$ position can be determined with a precision of $\sigma_z =$ 2.2 cm. For a better explanation of the way of charge $Q$ and time $t$ measurements, read appendix C.

### 3.2.1.3 Central $z$ chambers

The $z$ central inner CIZ and outer COZ drift chambers measure the $z$-coordinate and complement the CJC for the track reconstruction. They are also used for the trigger of straight tracks pointing to the interaction region.

The CIZ chamber is located between the CST and CJC1, just after the CIP while COZ is found between the CJC chambers. See figures 3.6 and 3.7. They cover polar angles of $16° < \theta < 169°$ and $25° < \theta < 156°$, respectively.

The CIZ chamber is a regular polygon with a length of 2.467 m and thickness of 26.5 mm, it is composed by 15 independent ring cells with 4 sense and 3 potential

wires each of them. The gas mixture inside is $Ar/C_2H_6 + H_2O$ at a proportion of $(70/30) + 0.2$ allowing a drift velocity of 52 mm/$\mu$s and measurement resolutions of $\sigma_{r\phi} = 28$ mm and $\sigma_z = 26$ $\mu$m.

The COZ polygonal chamber is 2.59 m long and 25 mm width, has 24 cells (or rings), each cell containing 4 sense and 6 potential wires. It has a gas mixture of $Ar/C_2H_6 + C_3H_7OH$ by $(48/52) + 1$ %, so the drift velocity is 48.5 mm/$\mu$s with accuracy of $\sigma_{r\phi} = 58$ mm and $\sigma_z = 2.0$ $\mu$m.

The wires are all tilted by 45° with respect to the normal to the chamber axis. The first backward nine cells of CIZ are backward tilted but the other six in the forward direction are tilted forward.

### 3.2.1.4   Central proportional chambers

There are two multiwire proportional chambers[6] (MWPC's) in the H1 detector: the central inner (CIP) and the central outer (COP). During HERA II period, the CIP chamber, together with CIZ, were replaced by a high granularity central inner proportional chamber (CIP2k) [72] to increase the non-$ep$ background rejection and to deliver a precise information about the event timing ($t_0$).

The CIP2k chamber has an inner (outer) radius of 15 cm (20 cm) and an active length of 2.2 m. It is located between the CST and the CJC1. It consists of five cylindrical detector layers segmented into 16 azimuthal sectors with cathode pad readout about 2 cm along the $z$ axis. Due to the very fast response to ionizing particles (depending on the chamber gas and the field strength) this chamber is used to provide a precise information about the event timing $t_0$ (the typical intrinsic time resolution is 10 ns) to suppress background events.

The COP detector is located between the CJC1 and CJC2 (Figure 3.6). It is used in parallel to the CIP2k trigger to suppress tracks with a low momentum transfer ($p_t$ cut) and to the z-vertex trigger to reconstruct the exact vertex in a $z$ region of $\pm$ 43.9 cm around the nominal interaction point ($\sigma_z \approx 5.5$ cm).

---

[6]See appendix B for an explanation of the multiwire proportional chambers performance.

## 3.2.2   Calorimeters

The calorimeters of the H1 detector were designed to identify and provide a precise measurement of charged and neutral particles, specially the electron parameters of the DIS events in a wide range of solid angle, as well as jets with high particle densities. This kind of detector have the purpose of measuring the energy of the particles by their total or partial absorption.

According to the material of construction they can provide signal such as ionization, as the liquid argon calorimeter in H1, or scintillated light, as the SpaCal detector.

### 3.2.2.1   Liquid argon calorimeter

The liquid argon calorimeter [73] (LAr) surrounds the system of tracker detectors but it is still inside the superconducting coil. It has 1.5 m of thickness active diameter and measures 7 m of longitude, covering a polar angle range of $4° \leq \theta \leq 154°$ and $4\pi$ coverage in $\phi$. The calorimeter is complemented in the forward region (between the beam pipe and the liquid argon cryostat) by the PLUG, the Spacal and the tail-catcher system (TC) in the backward direction, to cover the region were hadronic particles can be leaking out of the detector.

The LAr is segmented in eight wheels each of them divided in $\phi$ into eight identical units in the $xy$ plane. The first two wheels starting from forward region, are two half rings assembled. The Figure 3.8 presents longitudinal and transversal views of the LAr calorimeter.

The LAr has a fine granularity for e/$\pi$ separation (electromagnetic and hadronic showers) and energy flow measurements as well as homogeneity of response. Each wheel is divided in an electromagnetic (EM) and a hadronic section (HAD), see Figure 3.8. The octants are segmented in 45000 cells, where 30000 belong to the EM and the rest to the HAD part.

A EM cell consists of two lead absorber plates of 2.4 mm interleaved with LAr active material interspaces of 2.35 mm. Over each face of the absorber, next to the LAr,
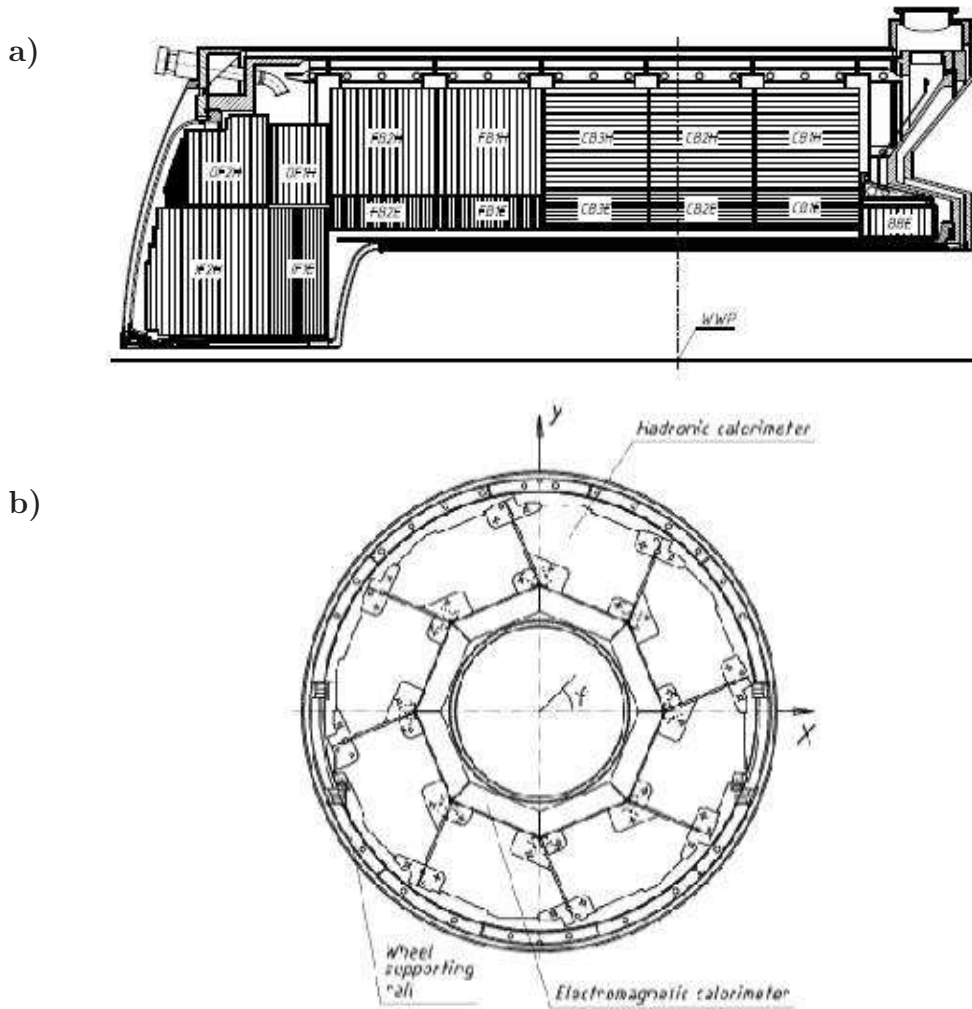
Figure 3.8: a) Longitudinal views of the LAr Calorimeter with the eight wheels divided in electromagnetic and hadronic sections. b) Transversal cut of the calorimeter showing one wheel where the separation between electromagnetic and hadronic sections are also indicated, the inclination of the 8 units is visible.

there are circuit planes impressed in G10 (a composite made of glass fiber and epoxy resin) which have the copper lecture modules (the pads). The electrons produced in the liquid argon are collected at these plates. Since there is no charge multiplication, the collected charge is quite small, and the detector requires a preamplifier and associated electronics for each channel. The chamber must operate at liquid argon temperatures (80K) and thus requires a cryogenic system (circulation of helium gas).

The hadronic cells has a similar EM structure, an absorber material made of 16 mm (19 mm) stainless steel with sheets connected to high voltage and a double gap of 2.4 mm liquid argon. The double gap is separated by the G10 plate which contains the lecture pads.

The liquid argon was chosen because its easy calibration, good stability and homogeneity in the response. Although the detector is relatively slow, it is stable, is not adversely affected by the presence of a magnetic field, and is easily segmented. The detector has uniform sensitivity, and it is possible to make a highly accurate charge calibration.

The radiation length of the electromagnetic part is about 20 $X_0$ in the central region and 30 $X_0$ in the forward while it is about 5 interaction lengths $\lambda$ in the central and 8 $\lambda$ in the forward area for the hadronic part.

The energy resolution for EM and HAD showers are:

$$\frac{\sigma_E^{EM}}{E} = \frac{11\%}{\sqrt{E[GeV]}} \oplus 1\%$$

$$\frac{\sigma_E^{HAD}}{E} = \frac{50\%}{\sqrt{E[GeV]}} \oplus 2\%$$

### 3.2.2.2   Spaghetti calorimeter (SPACAL)

The spaghetti calorimeter (SpaCal) consists of scintillating fibers embedded in a lead absorber, parallel to the $z$-axis. As the LAr, the SpaCal also has electromagnetic (EM) and hadronic (HAD) sections. The angular range covered is $155° < \theta < 177°$. The SpaCal has 1192 channels which are read out with a time resolution of 1 ns.

The molecules, excited by the particles passing through, emit scintillation light which travels by the fibers to the photomultiplier tubes to be converted in electrical signals. The SpaCal is used to measure the scattered electron at low $Q^2$ and to contribute to the reconstruction of hadronic final states.

The EM (HAD) corresponds to 27.8 $X_0$ (2 $\lambda$). The EM and HAD energy resolution are:

$$\frac{\sigma_E^{EM}}{E} = \frac{7\%}{\sqrt{E[GeV]}} \oplus 1\%$$
$$\frac{\sigma_E^{HAD}}{E} = \frac{56\%}{\sqrt{E[GeV]}} \oplus 7\%$$

### 3.2.3   Luminosity system

The H1 luminosity system [74] main task is the relative measurement of the luminosity as seen by the main detector. The measurement is based in the Bethe-Heitler [75] process, $ep \rightarrow ep\gamma$, determined by the electron tagger (ET), photon detector (PD) and Cherenkov counter (VC) detectors located close to the beamline but far away from the interaction point (ET at $z =$-33.4 m and PD at $z =$-102.9 m) to cover the small angles of the electrons and photons traveling in the primary electron beam direction. The VC detector and a Pb filter $2X_0$ protect the PD from the high synchrotron radiation flux.
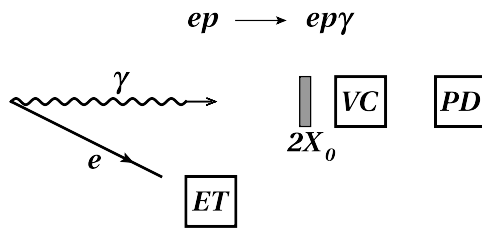


Figure 3.9: Detection of the Bethe-Heitler event ($ep \rightarrow ep\gamma$) by the electron tagger (ET), photon detector (PD) and Cherenkov counter (VC).

The ET (PD) detects the scattered electrons (the photons) at approx. 0 - 5 (0 - 0.45) mrad as shown in Figure 3.9. The event rate $R'$, corrected of background

(mainly from electrons bremsstrahlung), is used for the luminosity determination:

$$L = \frac{R'}{\sigma_{vis}}, \tag{3.3}$$

where $\sigma_{vis}$ is the visible part of the Bethe-Heitler cross section (with acceptance and trigger efficiency included).

### 3.2.4 Trigger system

The H1 trigger system has the function of separating out the $ep$ events containing interesting physics from the background sources in the total 10.4 MHz input rate, while keeping a minimum dead-time.

This system is divided into four levels, called L1 - L4, to facilitate the making of decision as more H1 detector components combines their information. The events fulfilling all level requirements are written to tape for permanent storage. The final rate for storage is limited to 10 Hz. See Figure 3.10.

The first trigger level L1 provides a decision for each bunch crossing. The full system run deadtime free at 10.4 MHz and is phase locked to the RF signal of HERA. The decision delay is 2.3 $\mu$s and must reduce the event rate to 1 kHz.

The L1 must provide a sophisticated identification of the characteristics of an event. It widely uses the track origin information, that uniquely distinguishes $ep$ interactions from the beam gas background, and for the $ep$ events, where the vertex information may not be the best requirement, the hadronic final state topology. So, at first level only the MWPC and LAr calorimeter data are correlated in such a way.

The L1 output are called trigger elements (TE) which are sent to the central trigger control (CTC) to be combined with other subtriggers.

The intermediate levels L2 and L3 are called synchronous, because they operate during primary dead time of the readout. They are based on the same information prepared by the L1 trigger.

The level 2 decision is made evaluating a large number of subsystems signal correlation in detail. Its time decision is only 20 $\mu$s but is able to reduce the event
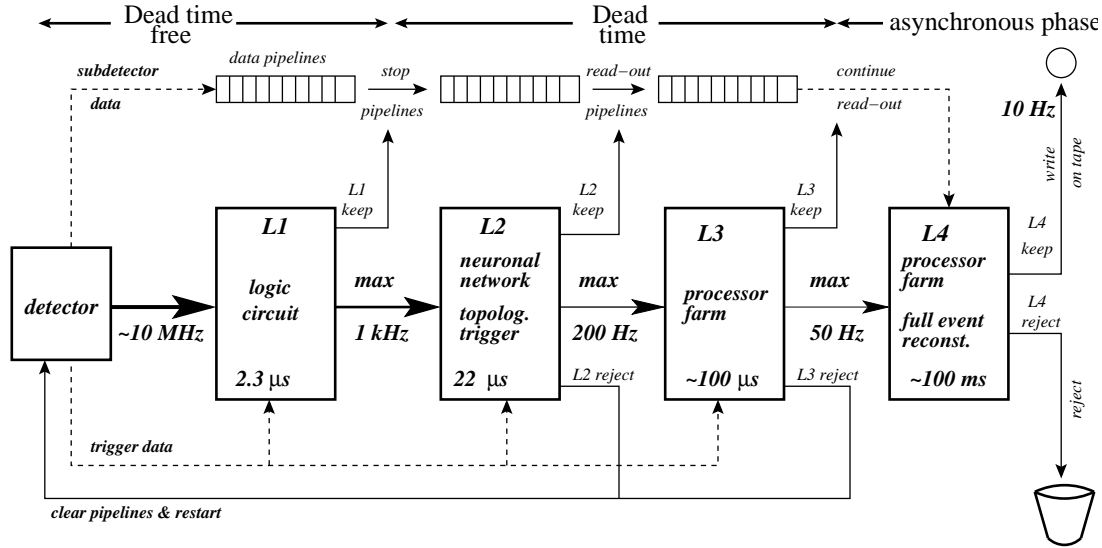
Figure 3.10: The H1 trigger system consisting in four levels (L1 - L4). The events fulfilling all level requirements are written to tape for permanent storage.

rate to 200 Hz. L2 consists of two independent systems, the neural net trigger (NNT) and the topological trigger (TT) trained with $ep$ and background events and a geometry of the detector in the $\theta$ and $\phi$ space samples.

In parallel, a flexible third level has 100 $\mu$s to take a decision using software algorithms running on a microprocessor. It can potentially refine the trigger giving a 50 Hz rate event at the end. In case of a rejection, the readout operations are aborted and the experiment is alive again after a few $\mu$s.

The L4 filter farm is an asynchronous software integrated into the central data acquisition system. It is divided into several logical modules to make a quick decision of the events (100 ms). If the event passes the selection criteria, it is written to POTs (production output tape), in a rate of approx. 5 Hz, together with the detectors information and an online calculation of the trajectory, energy signature and momentum of all particles of the event, which is used for an event classification.

A small fraction of about $\sim$ 1% of the rejected events is kept for monitoring purposes.

# Chapter 4

# Selection of DIS events and $K_S^0$ candidates

The selection of the DIS event sample requires several steps, which focus in cleaning the sample by reducing the contamination of the events of interest. The first selection is independent of the analyser, hence this stage is called online selection, and consists in the action of the trigger as described in section 3.2.4. Next, the offline selection is carried out by many steps as the analyser decides depending in the aim of study or the cleanliness wished for.

In the first section of this chapter a clear description of the online selection can be found. The offline part is also described in detailed in the following sections, starting with the selection of events containing the information of the needed detectors, the commonly called run sample selection. Then, general cuts and the DIS event selection are presented, finishing with the $K_S^0$ candidates reconstruction. As it was already pointed out, the $K_S^0$ travel some distance before decaying to $\pi^+\pi^-$, in the corresponding section it is explained how the $V^0$ (the vertex of decaying) is reconstructed and the $K_S^0$ identified from their daughters signature.

Several control plots of the used variables are going to be presented with the comparison to the Django and Rapgap models.

## 4.1   Trigger

The online selection consists of the subtrigger elements only. The subtrigger chosen for this work corresponds to the level L1, the so called S67, which is defined as:

$$S67 \equiv LAr \quad \&\& \quad T0 \quad \&\& \quad VET$$

where LAr means the condition of the LAr calorimeter, T0 the timing condition, VET the veto condition and the symbol && meaning the logical condition 'AND'.
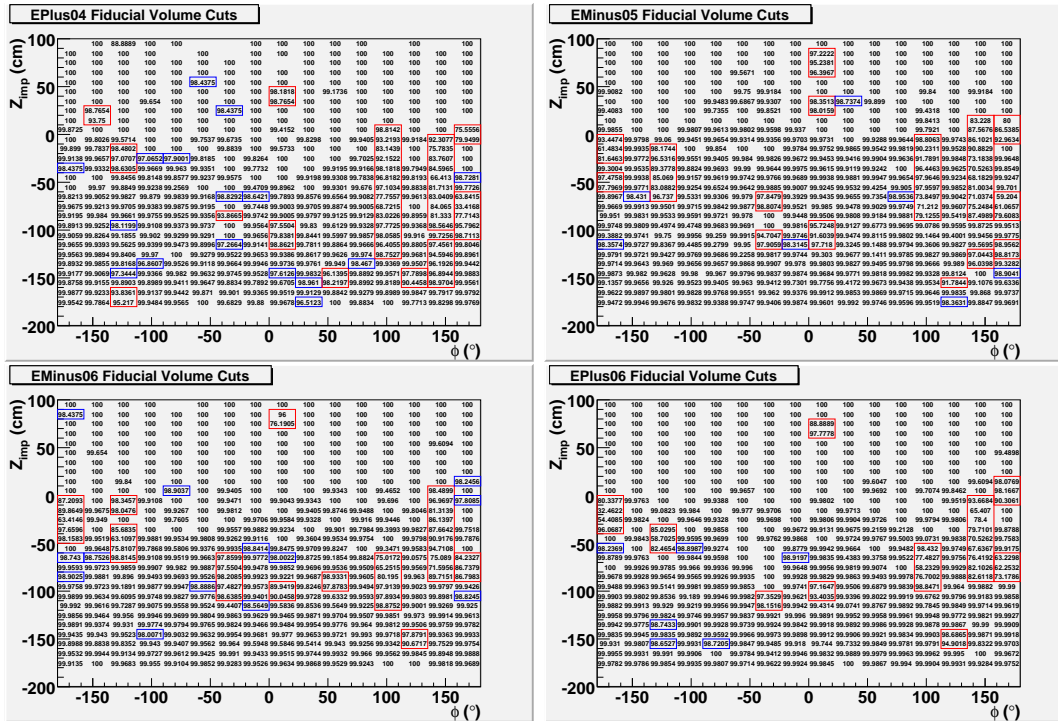


Figure 4.1: Trigger efficiency plots as functions of azimutal angle $\phi$ and $z$ impact position of the electron in the LAr calorimeter for $2004e^+p$, $0405e^-p$, $2006e^-p$ and $0607e^+p$ periods. The enclosed areas correspond to the fidutial volume cuts negleted from the entire data (in red) and for some periods (in blue).

The LAr efficiency ($\varepsilon_{LAr}$) is measured with the events firing the S67 after removing the subtrigger and fidutial volume cuts[1]. This can be determined thanks to the

---

[1]Cells switched off because high noise, damage or malfunctioning hardware.

independence between the electron fired and the hadronic final states fired, so one can be used to monitor the other one. The LAr efficiency becomes close to 100 % as can be seen in the Figure 4.1 for the four periods (plots made by Maxime Gouzevitch), where the efficiency value of each cell is depicted as function of $\phi_e$ angle and $z_{impact}$ position of the electron. The enclosed areas correspond to the fidutial volume cuts (rejected cells) negleted from the entire data (in red) and for some periods (in blue).

The T0 efficiency $\varepsilon_{T0}$ is determined in a similar way as the $\varepsilon_{LAr}$ using the independent LAr calorimeter and the CIP2k detector as monitors. As it uses the LAr, the fidutial cuts are also applied here. A 100 % efficiency is obtained.

The veto efficiency $\varepsilon_{veto}$ is calculated by the contributions of the time of flight (ToF), CIP2k and MUON detectors. It is found a $\varepsilon_{veto} = 98.83 \pm 0.42$ for $e^-$ and $\varepsilon_{veto} = 99.13 \pm 0.24$ for $e^+$.

When the AND condition is made, the efficiency $\varepsilon_{S67}$ is found to be $\sim 99$ %.

For an extended explanation of the trigger efficiency determination see the sections 2.6, 2.7 and 6.2 of reference [76].

## 4.2 Data quality constrains

The first steps of the offline selection consists in the choice of the recorded events containing all the data information needed for the study of this thesis. The run sample selection also provides the luminosity value which is subsequently used in the cross section determination.

The cuts belonging to the general event selection constrains are explain now and listed in the first column of Table 4.2.

### 4.2.1 Run sample selection

The data recorded at the H1 tapes are separated in *runs*, which are basically events occurring in a time interval and containing very similar operating detector and accelerator conditions. They are classified as *good*, *medium* or *poor* depending

on the turn on subdetectors, the operating status and the quality of the lepton and proton beams.

The run selection is a filter to obtain a sub-set of events where the detector components relevant to this analysis are switched on and working properly. The components required for $K_S^0$ studies are CJC1, CJC2, CIP, LAR, SPACAL, TOF, LUMI and VETO, with the additional condition of the trigger S67 and a primary vertex range of $\pm$ 35.0 cm.

Table 4.1 lists the data periods considered here, the type of lepton, the run ranges and the luminosity corresponding to the periods. It is important to remark that not all runs of each year were used, some of them were rejected because of detector malfunction, powerglitch, high voltage problem, noise or low yield, etcetera; however the luminosity values presented are corrected for the rejected events. A total luminosity of 339.6 pb$^{-1}$ is obtained for the HERA II data.

Table 4.1: Run selection sample and corresponding luminosity value.

| Year | Collision Part. | First Run | Last Run | $\mathcal{L}$ [$pb^{-1}$] |
|---|---|---|---|---|
| 2004 | $e^+p$ | 367284 | 392213 | 49.02 |
| 2004 | $e^-p$ | 398286 | 398679 | 0.160 |
| 2005 | $e^-p$ | 399629 | 436893 | 99.90 |
| 2006 | $e^-p$ | 444307 | 466997 | 56.87 |
| 2006 | $e^+p$ | 468531 | 492541 | 87.70 |
| 2007 | $e^+p$ | 492559 | 500611 | 45.92 |
| Total | | | | 339.6 |

## 4.2.2   Vertex cuts

The $ep$ collision should occur at the idealized primary interaction vertex $(x_{vtx}, y_{vtx}, z_{vtx}) = (0, 0, 0)$, however there are technical difficulties to achieve this properly, specially at the $z$ axis, then a range of several centimeters around this nominal vertex should be

considered. A typical range of $|z_{vtx}| < 35$ cm is acceptable specially to reject contamination of either the interactions of the particles from the beam with the residual gas in the beampipe or the interactions between the electrons and the proton *satellites*[2]. The distributions are shown in Figure 5.1 a) and Figure 5.4 a) for the DIS and the $K_S^0$ samples, respectively.

In addition, it is required that the vertex be central. This means that the vertex is found by the central tracker chambers which provides high precision and reconstruction of the parameters compared with those reconstructed by the forward trackers.

### 4.2.3 DIS kinematic range

The kinematic variables referred here were already introduced in the subsection 1.1.1. The values of the photon virtuality $Q^2$, inelasticity $y_e$ and $x$-Bjorken were determined by the $e$ method and $e\Sigma$ method, as explained in appendix A, finding at the end the same results within the systematic errors. The $e$ method has been chosen for the reconstruction of event kinematics in this work.

This analysis is focused at high $Q^2$, meaning $Q^2$ greater than 145 GeV$^2$. This cut ensures that the scattered electron is measured in the LAr calorimeter. An upper cut, $Q^2 < 20000$ GeV$^2$, is also applied as precaution due to the limited phase space at HERA. The $Q^2$ distributions are shown in logarithm scale in Figure 5.1 b) for the DIS sample and Figure 5.4 b) for the $K_S^0$ sample.

The $y_e$ cut in the range $0.2 < y_e < 0.6$ is done to avoid the fake electrons and for to be in a safety range of resolution of the $e$ method, see Figures 5.1 c) and 5.4 c) for the corresponding DIS and $K_S^0$ sample distributions. There is not explicit cut applied to $x$ but due to its relation with the other kinematic variables it is affected, see the distribution for DIS events in Figure 5.1 d).

---

[2]Small bunches delayed with respect to the main bunch.

## 4.3 Selection of DIS events

The next step consists in the DIS event selection, based on the identification of the scattered electron $e'$. The criteria list in this case was chosen because high efficiency of detection, resolution, geometrical acceptance of the detectors, physical rules of conservation or because rejection of others kind of processes that are considered as background in this analysis. The applied cuts have already been widely studied and tested for other analysers and they are settle as the best for DIS events selection. All these cuts are listed in the second column of the Table 4.2.

### 4.3.1 Scattered electron energy

According to the four-momentum $Q^2$ of photon participating in the interactions at HERA, $e'$ can be detected by the LAr or the SpaCal calorimeter. For this thesis, the chosen phase space dictates that the electron must be identified by the LAr Calorimeter.

The electron energy restriction is done to avoid the fake electrons (typically hadronic clusters from photoproduction events) or the non well identified electrons, but also to take advantage of the LAr efficiency which is close to 100% at $E'_e > 11$ GeV (the distribution is presented in Figure 5.2 a)). The clear recognizion of the electron is possible because the position, shape and size of the cluster left by its energy deposition in the LAr is very well known.

### 4.3.2 Scattered electron polar angle and $z_{impact}$ coordinate

The limits on the polar angle $\theta_e$ and the impact coordinate in the $z$ axis of the electron $z_{impact}$ are based on geometrical acceptance of the H1 LAr Cal detector.

The polar angle is defined as the angle between the incident proton beam direction and the line given by the primary interaction vertex and the center of the energy cluster in the LAr. The chosen range is $10° < \theta_e < 150°$ (see its distribution in Figure 5.2 b)).

The $z$ coordinate of the electron impact is chosen to be $z_{impact} > -180$ cm (Figure 5.2 c)) to ensure that the electron falls on the acceptance of the LAr calorimeter.

### 4.3.3 Four-momentum conservation

By conservation of energy and momentum, the value of the total $E - p_Z$ measured in H1 should be twice the energy of the incoming electron, that means $2*27.5$ GeV$\simeq55$ GeV, but several effects can affect this, for instance if the electron was not detected in the LAr calorimeter, if there were initial or final state radiation so the energy of the electrons is reduced or if photoproduction events occurred. Mainly due to these possibilities the constrain $35 < E - p_Z < 70$ GeV is made, as shown in Figure 5.1 e).

## 4.4 Reconstruction of $K_S^0$ candidates

Once the DIS sample is available, one goes ahead with the particle identification of interest, in this case the $K_S^0$ meson. As the $K_S^0$ is a neutral particle, it only can be detected through its daughter particles. As was listed in Table 2.2, this meson have several decay channels but the one chosen for this analysis is the more frequent and the one with only charged particles, $K_S^0 \rightarrow \pi^+\pi^-$; see Figure 4.6.

A general explanation of how to deal with the reconstruction of the $K_S^0$ candidates is the following:

1) Look for central tracks with opposite charge which satisfy the selection criteria mentioned in section 4.4.1.

2) As the $K_S^0$ has a relatively large lifetime it travels some distance before decaying. The decay occurs at a vertex, displaced from the primary vertex, known as secondary vertex $V^0$. The selected tracks in 1) are assumed to be the daughters of a neutral particle and are associated to the $V^0$.

3) The last step consists in a series of cuts applied to the identified neutral particle to decide if it can be considered as a candidate to $K_S^0$ .

The summary of all the cuts applied to the tracks and the $K_S^0$ candidate can be found in the two last columns of the Table 4.2.

### 4.4.1   Track cuts

In H1, the tracks can be reconstructed by only central trackers, only forward trackers or by the combination of both, but the best quality of reconstruction comes from the central trackers. That is the reason why these are chosen here.

Reconstructed tracks with a starting radius less than 30 cm are chosen (see Figure 5.3 a)). This condition implies tracks whose beginning is located inside the CJC1 detector avoiding in this way the consideration of pieces of trajectories produced by the interaction with the material between the CJC1 and CJC2.

A combination of the track segments of the CJC1 and CJC2 chambers provides a better reconstructed track, then a cut to the length of the transverse projection of the tracks is applied with the restriction of radial length $> 10$ cm to get a track of good reconstruction quality, Figure 5.3 b).

It is known from previous studies that the reconstruction of the tracks get worse at very low transverse momentum values because of the multiple interactions with the material of the detector and the curling of the trajectory, therefore a cut of $p_t > 0.12$ GeV is applied to each track to have a good identification and to avoid background of wrong tracks. The distribution is presented in Figure 5.3 c) for the $\pi^-$ of the $K_S^0$.

The cut $dca(\pi^+) * dca(\pi^-) < 0$, where $dca$ means the distance of closest approach to the origin of the interaction as explained in appendix D, is done to ensure that a pair of selected opposite charged tracks share the same $V^0$; but also to test the charge of the considered particles, because due to the magnetic field the tracks with opposite charges should bend in different directions giving a negative value of their $dca$ product.

The so called significance $|dca'|/\sigma_{dca'}$, the ratio of the absolute value of the $dca'$ (the distance of closest approach of the track in the $r\phi$ plane to the primary vertex) and its error $\sigma_{dca'}$ is chosen to be greater than 3; this constrain helps to reject tracks coming from the primary vertex. Studies made by D. Pitzl and A. Falkiewicks showed that more statistic and better signal to background ratio is obtained with the application of this cut complemented with the $dca(\pi^+) * dca(\pi^-) < 0$ constrain. The distribution of significance for the $\pi^-$ from the $K_S^0$ can be seen in Figure 5.3 d).

Table 4.2: Summary of the selection criteria.

| Event selection | Electron cuts | Tracks cuts | $K_S^0$ cuts |
|---|---|---|---|
| central vertex | Trigger 67 | Central tracks $> 1$ | Number of $K_S^0$ $>0$ |
| $|z_{vtx}|$ $<35$ cm | $E_e > 11$GeV | Different charges | Daughters $= 2$ |
| $145< Q^2 < 20000$GeV$^2$ | $10° < \theta_e <150°$ | Start radius $< 30$cm | Decay length $>2$cm |
| $0.2< Y_e <0.6$ | $z_{impact}$ $>$-180cm | Radial length $> 10$cm | $|\eta|$ $<1.5$ |
| | $35< E - p_z < 70$GeV | $p_t > 0.12$GeV | $p_t$ $>0.3$GeV |
| | Fiducial cuts | $dca(\pi^+) * dca(\pi^-)$ $<0$ | $M(p\pi^-)$ $>1.125$GeV |
| | | $|dca'|/\sigma_{dca'}$ $>3$ | $M(e^-e^+)$ $>0.05$GeV |
| | | | Fit $\chi^2$ $<5.4$ |
| | | | $|\cos(\theta^\star)| < 0.95$ |

## 4.4.2 Cuts to the $K_S^0$ candidates

Until here, the selection criteria provides the two candidates to $\pi$s tracks and the $V^0$ position. If the number of found $V^0$'s is different of zero. Then, one can follow with the next conditions.

The phase space of this analysis is characterized by the $Q^2$ and $y_e$ kinematic ranges but also by the transfer momentum $p_t(K_S^0)$ and the pseudorapidity $|\eta(K_S^0)|$ limits of the $K_S^0$ :

$$0.3 \text{ GeV} < p_t(K_S^0) \qquad |\eta(K_S^0)| < 1.5$$

The $p_t(K_S^0)$ cut is chosen to have good acceptance and good efficiency on the reconstruction of the $V^0$ from the pions tracks, while the $\eta(K_S^0)$ cut is used to ensure that the $K_S^0$ is contained within the geometrical acceptance of the central detectors. Positive (negative) values of $\eta$ corresponds to the forward (backward) region of the H1 detector, so it can be traduced to $\theta$ cuts, see Figure 5.4 d) and e).

The distance in the $r\phi$ plane between the primary vertex and the secondary vertex $V^0$, known as the radial decay length, is chosen to be $DL > 2$ cm (Figure 5.4 f)), mainly due to the efficiency of $V^0$ reconstruction and the boost of the $K_S^0$ lifetime to the laboratory frame.

Another cut applied to the vertex finding is the $\chi^2$ quantity which expresses the quality of the fit of the two daughter particles to the secondary vertex. A value of $\chi^2 < 5.4$ is considered as good enough since the distribution decays exponentially and start to be almost flat from approx. $\chi^2 = 3$, as shown in Figure 5.5 a). A value of 5.4 allows to have a little bit more statistic.

The angle between the positive track in the rest frame of the $K_S^0$ and the direction of the $K_S^0$ in the laboratory frame is the so called $\theta^*$ angle. A requirement of $|cos\,\theta^*| < 0.95$ is applied to the selection in order to avoid background from photon conversion $(\gamma \to e^+e^-)$ and ensure that the $K_S^0$ candidate comes from the primary vertex. Figure 5.5 b) shows the distribution of this variable.

The way to improve the rejection of neutral particles faking the $K_S^0$ reconstruction, for instance the photon conversion, $\Lambda_0$ and $\overline{\Lambda_0}$ particles, between others, is calculating the invariant mass and making some cuts to it.

The invariant mass $M$ can be calculated under the hypothesis of the $\pi$ mass for both negative and positive tracks[3] by the formula:

$$M(\pi^+, \pi^-) = \sqrt{(E_{\pi^+} + E_{\pi^-})^2 - (\bar{p}_{\pi^+} + \bar{p}_{\pi^-})^2} \qquad (4.1)$$

where $\bar{p}_{\pi^i}$ is the momentum vector, $E_{\pi^i} = \sqrt{\bar{p}_{\pi^i}^2 + m_\pi^2}$ the energy, $m_\pi$ the pion mass [11] of the pion $i\ = +$ or $i\ = -$.

---

[3]From the track reconstruction is possible to extract the momentum vector but not the mass of the particle. The four-momentum can only be obtained by assuming a mass value.
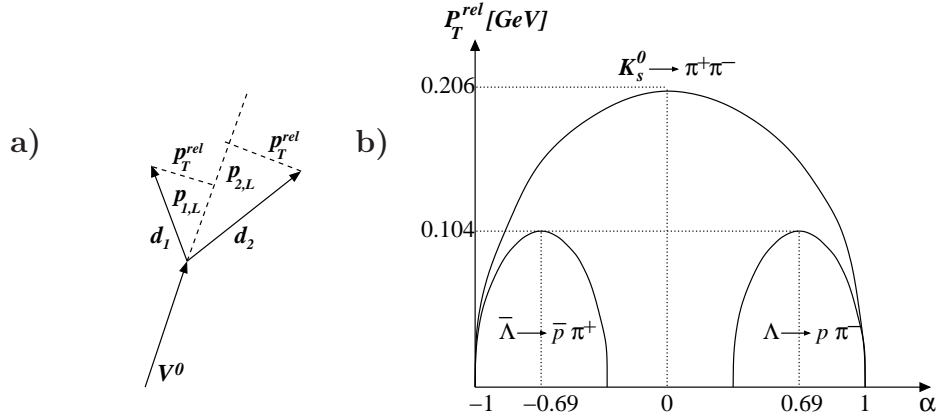
Figure 4.2: a) Definition of longitudinal $p_L$ and the relative transverse $p_T^{rel}$ momentum variables. b) The armenteros plot where half ellipses with its center lying at $\alpha$ axis belong to $V^0$ particles. The value of the centers gives the difference between the masses of the daughters.

The $\Lambda_0$ and $\overline{\Lambda}_0$ contributions are eliminated by requiring $M(p\pi) > 1.125$ GeV, assuming the $\pi^-$ and $p$ masses for the invariant mass calculation when the search is for $\Lambda_0$, or the $\pi^+$ and $\bar{p}$ masses for $\overline{\Lambda}_0$ [11]. The track with the highest momentum is considered to be the $p$ or $\bar{p}$ according to the charge of the track.

In the same way, the photon conversion contribution is avoided by $M(e^+e^-) > 0.05$ GeV. The masses considered here are those of the electron $e^-$ and positron $e^+$ [11].

The values of the last two cuts were obtained using the Armenteros-Podolsk-Thompson plots [77], which plot the $\alpha$ vs. $p_T^{rel}$ variables to describe the kinematic of a body decaying to two daughters $d_1$ and $d_2$. $\alpha$ is defined as:

$$\alpha = \frac{p_L^{d_1} - p_L^{d_2}}{p_L^{d_1} + p_L^{d_2}}$$

where $p_L^{d_i}$ is the longitudinal momentum measured in the laboratory frame of the daughters with respect to the flight direction of the mother particle; $p_T^{rel}$ is the value of the relative transverse momentum of the daughters, see Figure 4.2 a). The condition $p_T^{rel}(d_1) = p_T^{rel}(d_2)$ is imposed by momentum conservation.
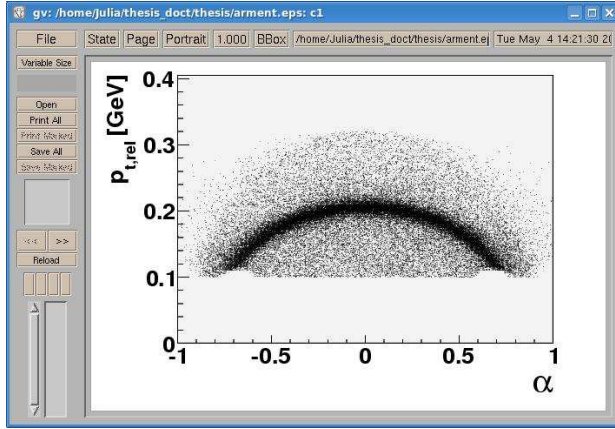
Figure 4.3: Armenteros plots from all HERA II data.
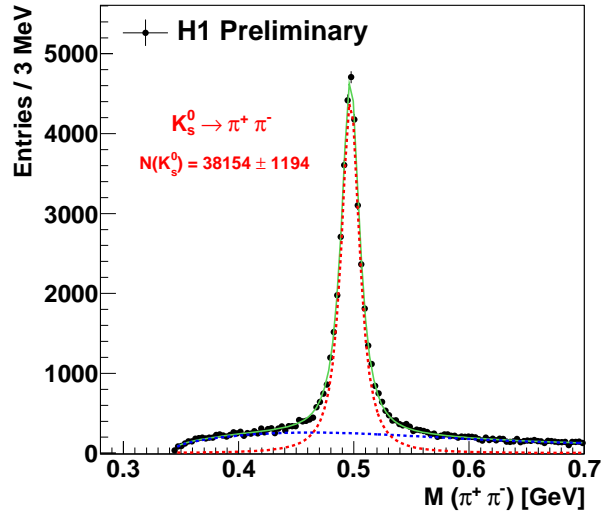


Figure 4.4: Invariant mass distribution of the $K_S^0$ candidates reconstructed from the decay channel $\pi^+\pi^-$. The corresponding fits to describe signal and background are shown in red and blue lines respectively, while the total fit is plotted with the green line.

A typical Armenteros plot is shown in Figure 4.2 b) where half ellipses with its center lying on $\alpha$ axis belong to $V^0$ particles. The value of the centers gives the difference between the masses of the daughters. The band structure is due to momentum conservation of the different $V^0$ decays, while the band widths are determined by the widths of the $V^0$s combined with the detector resolution. The bands of $\Lambda_0$ and $\overline{\Lambda_0}$ are lower than the $K_S^0$ band. The reason is that the sum of the pion and proton masses is only 38 MeV smaller than the $\Lambda_0$ mass, while the sum of the two pions is $\sim$219 MeV below the $K_S^0$ mass. Due to the finite resolution the measured distributions are smeared out. However, the separation of $K_S^0$ and $\Lambda_0$ still can be seen. In Figure 4.3, the Armenteros plot from HERA II data is presented, the rejection of $\Lambda_0$ particles has already be done.
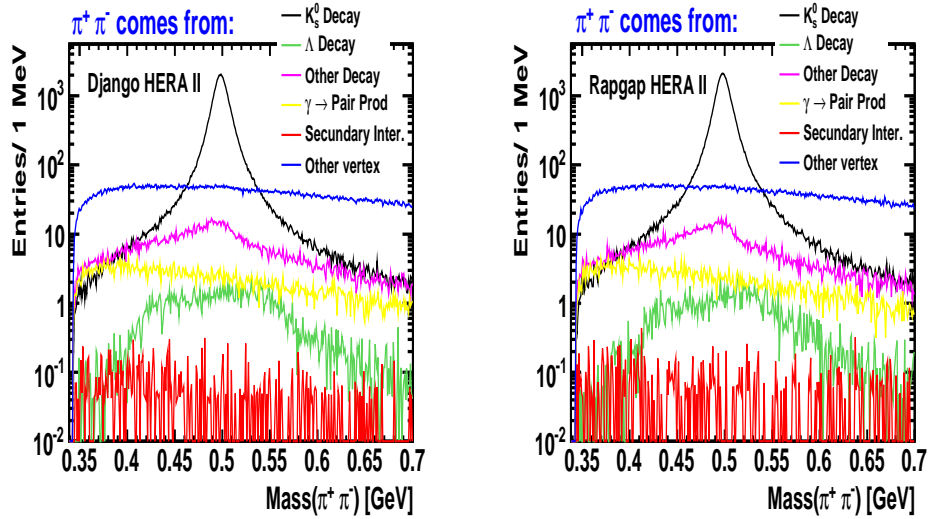


Figure 4.5: Invariant mass distribution of the $K_S^0$ for Django and Rapgap models. The study of the remaining contamination shows some contribution of $\Lambda$ decays, other particles decaying to two charged daughters, photon conversion, interactions with the dead material of the detector and events coming from other vertex.

After applying all mentioned cuts, the mass distribution of the $K_S^0$ candidates is plotted and shown in Figure 4.4. A clear peak is obtained concluding that most of the background has been rejected. However, using Monte Carlo models, a study of

the remaining contamination can be done showing that still some few events of $\Lambda$ decays, other particles decaying to two charged daughters, photon conversion ($\gamma \to$ pair production), secondary interactions (interactions with the dead material of the detector) and events coming from other vertex are part of the sample, in Figure 4.5 Django and Rapgap models results are presented, similar predictions are obtained.
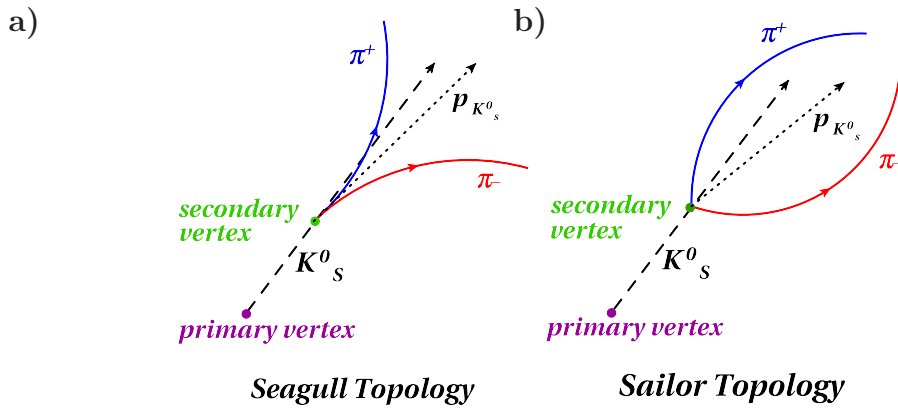


Figure 4.6: Seagull and sailor decay topologies identified by the sign of the cross product of the three-momentum of the pions, $(\vec{p}_{\pi^+} \times \vec{p}_{\pi^-})_z > 0$ for seagull and $(\vec{p}_{\pi^+} \times \vec{p}_{\pi^-})_z < 0$ for sailor.

The invariant mass distribution shown in Figure 4.4 contains in fact two different track combinations of curvatures or decay topologies, the outward-curved or *seagull* and the inward-curve or *sailor* topologies both depicted in Figure 4.6. The separation of these can be done by the cross product of the three-momentum of the pions, the seagull decay topology is defined as $(\vec{p}_{\pi^+} \times \vec{p}_{\pi^-})_z > 0$, whereas the sailor decay topology corresponds to $(\vec{p}_{\pi^+} \times \vec{p}_{\pi^-})_z < 0$. The $K_S^0$ mass distributions for each topology are presented in Figure 4.7.

## 4.5   Event yield

The event yield $Y$ is defined as the ratio of the number of events in the sample ($N$) and the integrated luminosity as measured in section 3.2.3, corresponding to the
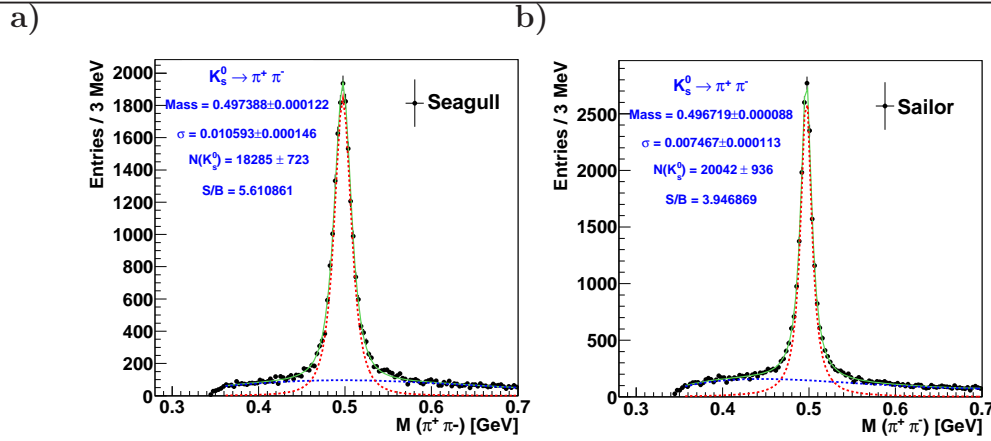
Figure 4.7: Invariant mass distribution of the seagull and sailor topologies showing 9% higher contribution from sailor compared with seagull.

selected run period, then $Y = N/\mathcal{L}$.

An abnormal low or high yield may indicate a period where the detector efficiency or measured integrated luminosity is not well understood. In Figure 4.8 the yield plots as a function of the run number, also separated by year periods, are presented for the DIS sample and $K_S^0$ sample, respectively. It is in general stable. The small changes have been observed in other analysis and have been attributed to biases in the integrated luminosity measurement (acceptance of the photon tagger).

## 4.6 Signal extraction

To know the number of $K_S^0$ candidates is necessary to make a fit to the invariant mass distribution. Figure 4.4 shows the total fit $f_{tot}(m_{\pi^+,\pi^-})$ as a green line, which is in fact a sum of two functions, one to describe the signal $f_{sig}(m_{\pi^+,\pi^-})$ showed with a red line in the Figure and one describing the background $f_{bgrd}(m_{\pi^+,\pi^-})$ in blue line:

$$f_{tot}(m_{\pi^+,\pi^-}) = f_{sig}(m_{\pi^+,\pi^-}) + f_{bgrd}(m_{\pi^+,\pi^-}).$$

The function chosen for the signal is the $t$-student distribution:

$$f_{sig}(x_{m(\pi^+,\pi^-)}) = \frac{N \; \Gamma((\nu+1)/2)}{\sqrt{\nu\pi} \; \Gamma(\nu/2)} (1 + \frac{t^2}{\nu})^{-(\nu+1)/2},$$

a)



b)
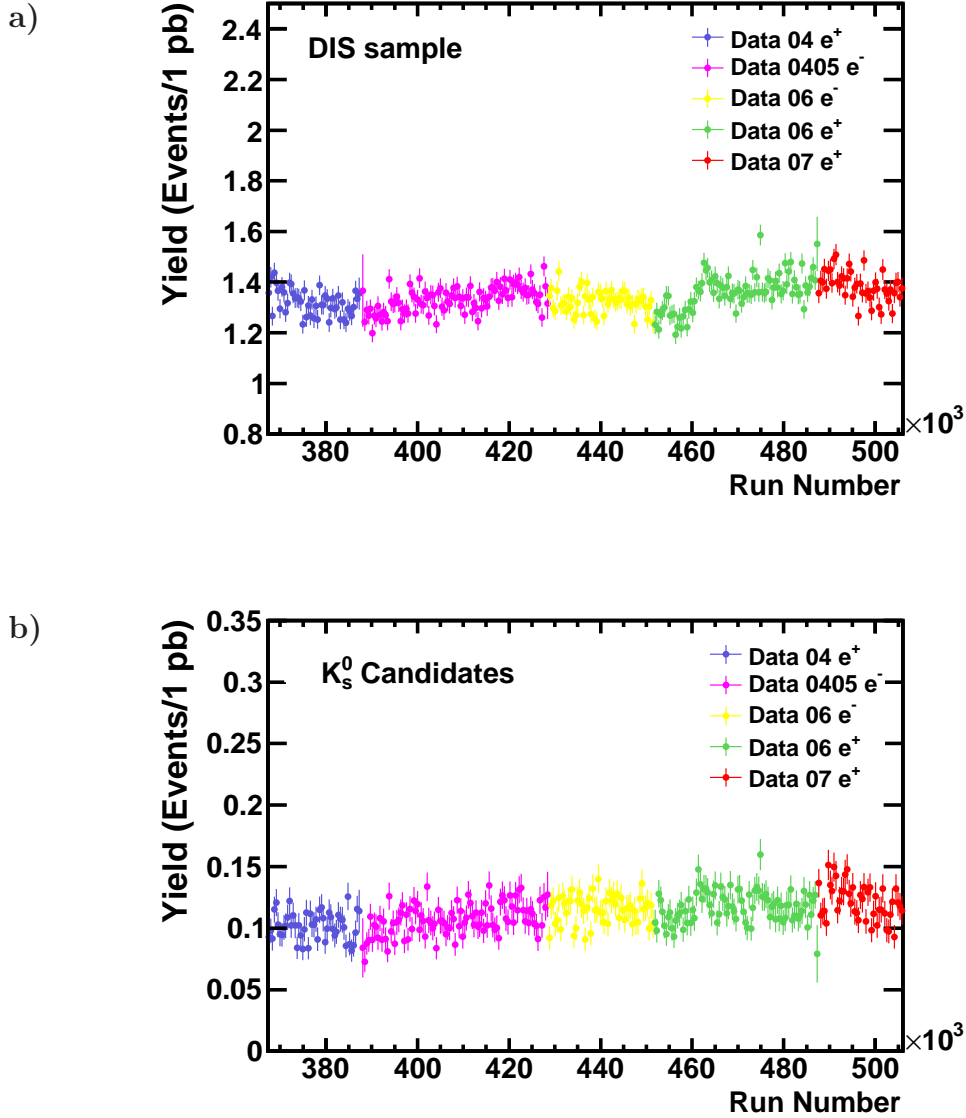


Figure 4.8: Yield plots as a function of run number for a) the DIS sample and b) the $K_S^0$ sample. The $2004e^+p$ period in blue, $0405e^-p$ in magenta, $2006e^-p$ in yellow, $2006e^+p$ in green and $2007e^+p$ period in red.

$$t = \frac{x_{m(\pi^+,\pi^-)} - \mu_{K_s^0}}{\sigma},$$

where the normalization $N$, the mean value of the mass $\mu_{K_s^0}$, the standard deviation $\sigma$ and the number of degrees of freedom $\nu$ are free parameters. The variable $x_{m(\pi^+,\pi^-)}$ runs over the complete $x$ axis range of the invariant mass distribution.

The $t$-student, as many other functions, is very useful to estimate population values from the data samples, specially when the media and standard deviation are not known. Some advantages are its continuity and symmetry with respect to the average but one should pay special attention to the parameters and the $\chi^2$ values to be sure that the fit is valid. In this case for instance, one should look at $\nu > 1$, $\mu_{K_s^0}$ close to the value provided by PDG [11], small $\sigma$ and $\chi^2$ normalized to the degrees of freedom (NDF) as close to 1 as can be possible.

This function was also chosen because of its bell shape a little bit lower and wider than the normal standard distribution; as well due to its approximation to the Breit-Wigner function when $\nu = 1$; also because if $\nu$ has a high value (approx. $\nu > 200$) the distribution is more like a normal standard distribution; and because it behaves as Gaussian when $\nu \to \infty$.

The best function for the background was found to be:

$$f_{bgrd}(x_{m(\pi^+,\pi^-)}) = p_0(x_m - 0.344)^{p_1} * Exp(p_2 x_m + p_3 x_m^2 + p_4 x_m^3)$$

where $p_i$ are the free parameters. This choice gives a good description of the background shape which goes to zero at the value 0.344 GeV, due to a cut in the relative transverse momentum of the pion ($p_T^{rel}$) of 100 MeV which traslates to a minimum mass of $2\sqrt{m^2 + (0.10)^2} = 0.344$.

The number of $K_S^0$ candidates are taken from the integral of the signal function. The fit to the invariant $K_S^0$ mass for all HERA II data, Figure 4.4, gives $38154 \pm 1194$ $K_S^0$ candidates with a estimated mass in the peak of 496.97 MeV and low $\sigma$ ($8.85 \times 10^{-3}$). The ratio signal over background S/B in the range [0.45 GeV, 0.55 GeV] is 4.5.

## 4.7    Selection of charged particles

The charged particles ($h^\pm$) sample is needed for the determination of the $K_s^0/h^\pm$ cross section ratio. They are selected in the same phase space as the $K_S^0$, $145 < Q^2 < 20000$ GeV$^2$ and $0.2 < y < 0.6$, together with additional conditions to ensure the good quality of the tracks.

The tracks are detected by the CTD specially by the CJC chambers. The characteristics to fulfill are:

- The track of the scattered electron is not considered in the sample.

- The cosine of the angles between the momemtum of the scattered electron and the track of the charged particle must be less than 0.99 to reject tracks close to the scattered electron.

- All tracks must be associated to the primary vertex such that the distance of closest approach of the track in the $r\phi$ plane to the primary vertex is chosen to be $|dca'| < 2.0$ cm.

- The minimum radial length of the reconstructed track must be greater than 10 cm.

- The tracks must have the first hit in the CJC1, then the start radius is chosen to be less than 30 cm.

- The tranverse momentum required to be larger than $p_T > 0.3$  GeV for good efficiency of the track reconstruction and compatibility with the phase space of the $K_S^0$ sample.

- The psedorapidity range being between $-1.5 < \eta < 1.5$ as the $K_S^0$ sample which means that the tracks are in the central region of the detector.

After the selection a sample consisting of 2,615,100 charged particles is obtained, mainly populated by charged pions.

# Chapter 5

# The measurement of the cross section

As mentioned previously, the goal of this thesis is the measurement of the $K_S^0$ particle production. In this chapter is explained how the total production cross section is determined and the way to calculate differential cross section as a function of one or more variables; also a series of important issues of data correction that one should not forget to take into account during the calculations.

The measurement from data is never an exact value. It is always accompanied of additional quantities which represents the statistical and the systematic uncertainties; this last one consisting on several sources which are explained in the last part of this chapter.

## 5.1 Determination of the cross section

The interaction between two particles is generally described in terms of the cross section. This quantity essentially gives a measure of the probability for a reaction to occur and may be calculated if the form of the basic interaction between the particles is known.

Two methods are commonly used to directly measure total cross sections. The

first method is the transmission experiment where one measures the intensity of particles before and after the target and infers the total cross section from the relation $I = I_0 exp(-N\sigma_T)$, where $I(I_0)$ is the transmitted (incident) intensity and $N$ is the number of target nuclei per cm$^2$. This method is frequently employed at fixed target accelerators. In the second method one attempts to record every interaction that takes place, this requires a detector with $\sim 4\pi$ acceptance. This method is often used for colliding beam experiments, like at HERA. The total cross section is given by $\sigma_T = N/\mathcal{L}$ where $N$ is the measured total interaction rate and $\mathcal{L}$ is the measured incident luminosity.

The total $K_S^0$ cross section in the visible phase space defined by:

$$145 < Q^2 < 20000 \text{ GeV}^2, \qquad 0.2 < y_e < 0.6,$$
$$-1.5 < \eta(K_s^0) < 1.5, \qquad 0.3 \text{ GeV} < p_T(K_s^0), \qquad (5.1)$$

is measured using the relation:

$$\sigma_{vis}(ep \to e'K_s^0 X) = \frac{N_{K_s^0}^{data}}{\varepsilon \cdot BR(K_s^0 \to \pi^+\pi^-) \cdot \mathcal{L}} \qquad (5.2)$$

where $N_{K_s^0}^{data}$ is the number of $K_S^0$ mesons gotten from the fit to the invariant mass distribution of data, as described in the section 4.6; $\varepsilon$ the efficiency of detection with the QED corrections included; $BR$ the branching ratio of the $K_S^0$ decaying to two pions and $\mathcal{L}$ the accumulated luminosity.

The differential cross section in terms of a variable $\wp$ is calculated by:

$$\frac{d\sigma_{vis}(ep \to e'K_s^0 X)}{d\wp} = \frac{N_{K_s^0}^{data}}{\Delta\wp \cdot \varepsilon \cdot BR(K_s^0 \to \pi^+\pi^-) \cdot \mathcal{L}} \qquad (5.3)$$

where $\Delta\wp$ will take values of the different intervals of $\wp$, the so called bins. $N_{K_s^0}^{data}$ and $\varepsilon$ should be now calculated for each bin. The values for $N_{K_s^0}^{data}$ were obtained after fitting the mass distribution for each bin, as shown from Figure F.1 to F.16 in appendix G for the bins of laboratory and Breit frame[1] variables refered in the

---

[1] Description of the Breit frame in the appendix E.

Table 5.1. The same will be applied when double differential cross section as a function of $\wp$ and $\eth$ are required, the values needed for the measurement of the cross sections should correspond to those bins of $\Delta\wp$ and $\Delta\eth$.

## 5.1.1 Binning scheme

For the calculation of the differential cross section of the $K_S^0$ belonging to the final sample, one must split in different intervals the variable range. The size of the intervals, known as *bins*, are chosen depending on the statistical data sample as fine as one could, but ensuring that they are wide enough to get a good fit to the invariant mass distribution of each bin, so it can occur that some bins are larger that others. The bin width is also checked to be at least twice its resolution. A good binning choice can help to limit the statistical error on the differential cross section.

Here, the data sample was binned as a function of the kinematic variables $Q^2$, $x$ and the $K_S^0$ variables $\eta$ and $p_t$ in laboratory frame and also as a function of $x_p^{CBF}$, $x_p^{TBF}$, $p_T^{CBF}$ and $p_T^{TBF}$ in the Breit frame using the bin boundaries listed in Table 5.1 and bounded by the corresponding phase space cuts.

Table 5.1: The bin boundaries list.

| $Q^2[GeV^2]$ | x | $\eta$ | $P_T$ [GeV] | $X_p^{CBF}$ | $X_p^{TBF}$ | $P_t^{BF}[GeV]$ |
|---|---|---|---|---|---|---|
| 145,167 | 0.0,0.004 | -1.5,-0.5 | 0.3,0.8 | 0.0,0.07 | 0.0,0.07 | 0.0,0.35 |
| 167,200 | 0.004,0.008 | -0.5, 0.0 | 0.8,1.1 | 0.07,0.13 | 0.07,0.13 | 0.35,0.6 |
| 200,280 | 0.008,0.017 | 0.0, 0.45 | 1.1,1.55 | 0.13,0.2 | 0.13,0.2 | 0.6,1.0 |
| 280,500 | 0.017,0.2 | 0.45, 0.95 | 1.55,2.23 | 0.2,0.33 | 0.2,0.33 | 1.0,1.8 |
| 500,1000 | | 0.95, 1.5 | 2.23,3.5 | 0.33,1.0 | 0.33,1.0 | 1.8,14 |
| 1000,5000 | | | 3.5,14 | | 1.0,2.0 | |

However, the binning used for the differential cross section is acceptable only if it also satisfies other detector requirements (the efficiency $\varepsilon$, stability $\mathcal{S}$, purity $\mathcal{P}$ and acceptance $\mathcal{A}$) as described in the following section.

## 5.2    The correction of data

For the cross section extraction, the data is submitted to corrections because of loses of the $K_S^0$ from the sample or the inclusion of fake $K_S^0$ in the sample, both possibilities can occur due to the incapability of the detectors to capture all the particles produced (geometrical and electronic acceptance), the limitations in the track reconstruction due to the selection criteria, fluctuations in the physical variables determination due to finite resolution, the possible rejection of particles of our interest during the signal extraction, etc.

The corrections are done using Monte Carlo simulations. There are three different kinds of MCs mentioned in section 1.4, the generated MCs and the reconstructed MC. The generated are *the radiative MC* and *the non-radiative MC*, based in the simulations of the HERA collision. The first one takes into account QED radiative effects. The reconstructed MC has the consideration not only of the HERA collider but also the H1 detector conditions of operation. The reconstructed particles pass by the same selection criteria and cross section extraction as data.

### 5.2.1    Control plots

A comparison between the data and the reconstructed Monte Carlo is done for the complete event sample. The kinematic, DIS, tracks, $K_S^0$ and other detector variables are compared in order to know the quantitative agreement between the data and simulation. Those plots, called control plots, were done and checked for each year period, as well for all HERA II data sample as shown in Figures 5.1, 5.3 and 5.4 where the data are compared to the Django and Rapgap models with normalization to the number of events. It can be concluded that the simulations of the two models describe reasonably well the distribution of several variables from data (the background as well). Then, the detector response to expected physics is well understood and represented by efficiency reweights and detector simulation.
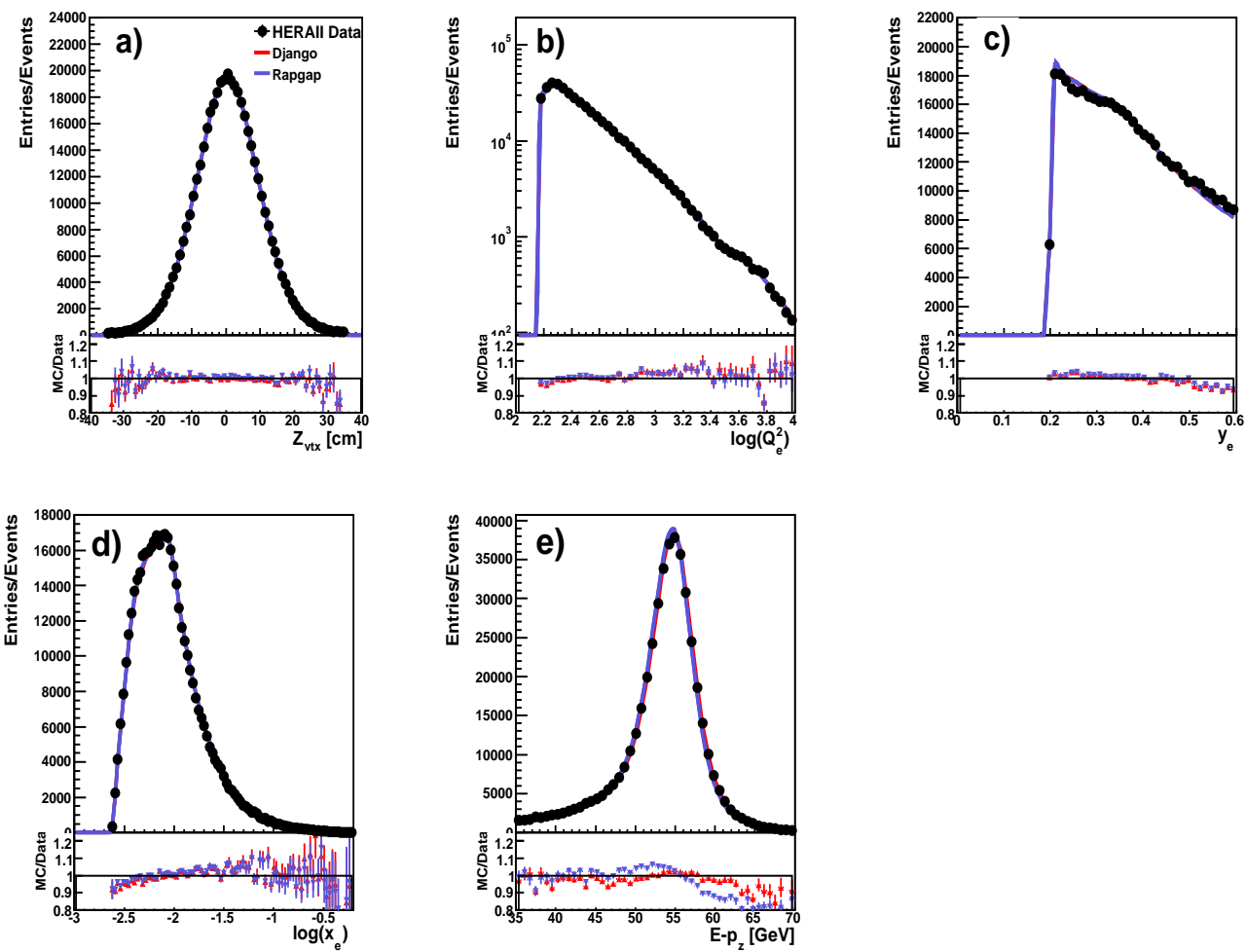
Figure 5.1: Control plots of a) the $z$ vertex distribution of the interaction, b) the logarithm of the photon virtuality $\log(Q^2)$, c) the inelasticity of the scattered electron $y_e$, d) the logarithm of the x-Bjorken $\log(x_e)$, and e) the four-momentum conservation $E - p_z$. The data are plotted as black dots while Django and Rapgap Monte Carlo are in red and blue respectively.
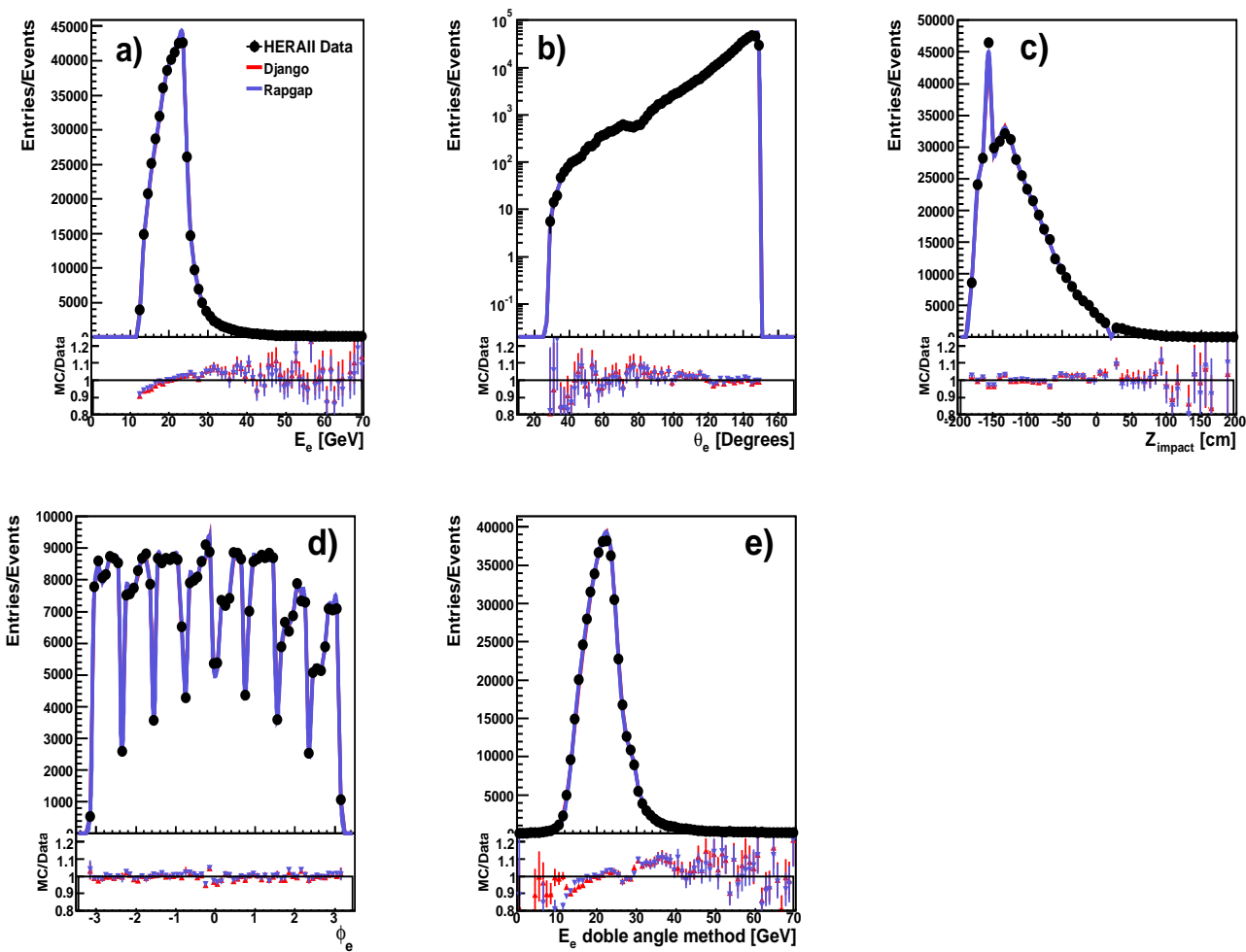
Figure 5.2: Control plots of a) the energy $E_e$, b) the polar angle $\theta_e$, c) the $z$-impact coordinate, d) the azimuthal angle $\phi_e$ and e) the energy calculated with the double angle method of the scattered electron. The data are plotted as black dots while Django and Rapgap Monte Carlo are in red and blue respectively.
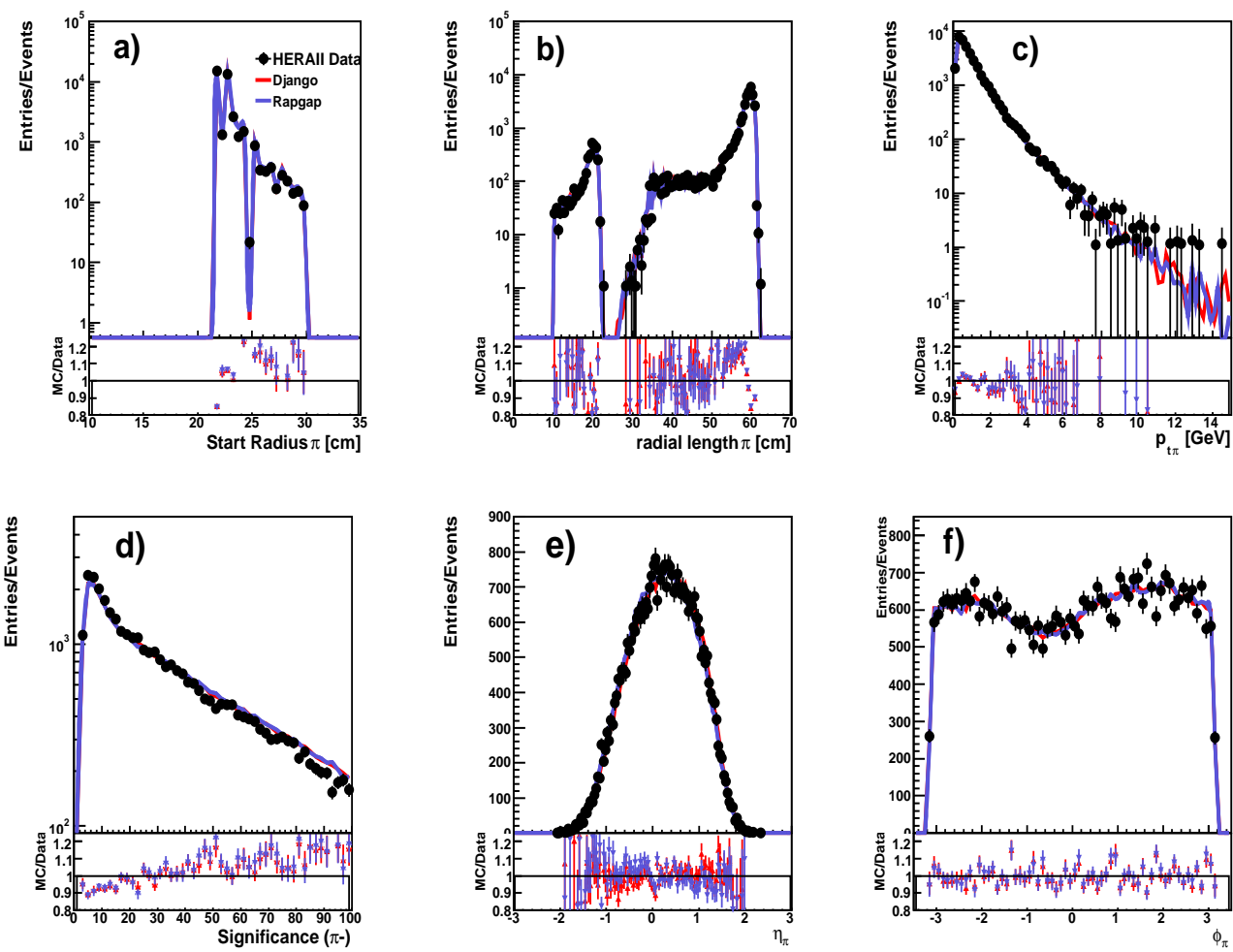
Figure 5.3: Control plots corresponding to the negative pion daugther $\pi^-$ of the $K_S^0$ candidate, a) the start radius and b) the radial length of the track, c) the transverse momentum of the pion $p_{T\pi}$, d) the significance of the track, e) the pseudorapidity distribution $\eta_\pi$ and f) the azimuthal angle $\phi_\pi$. Similar distributions and model agreement are found for the positive pion $\pi^+$. The data are plotted as black dots while Django and Rapgap Monte Carlo are in red and blue respectively.
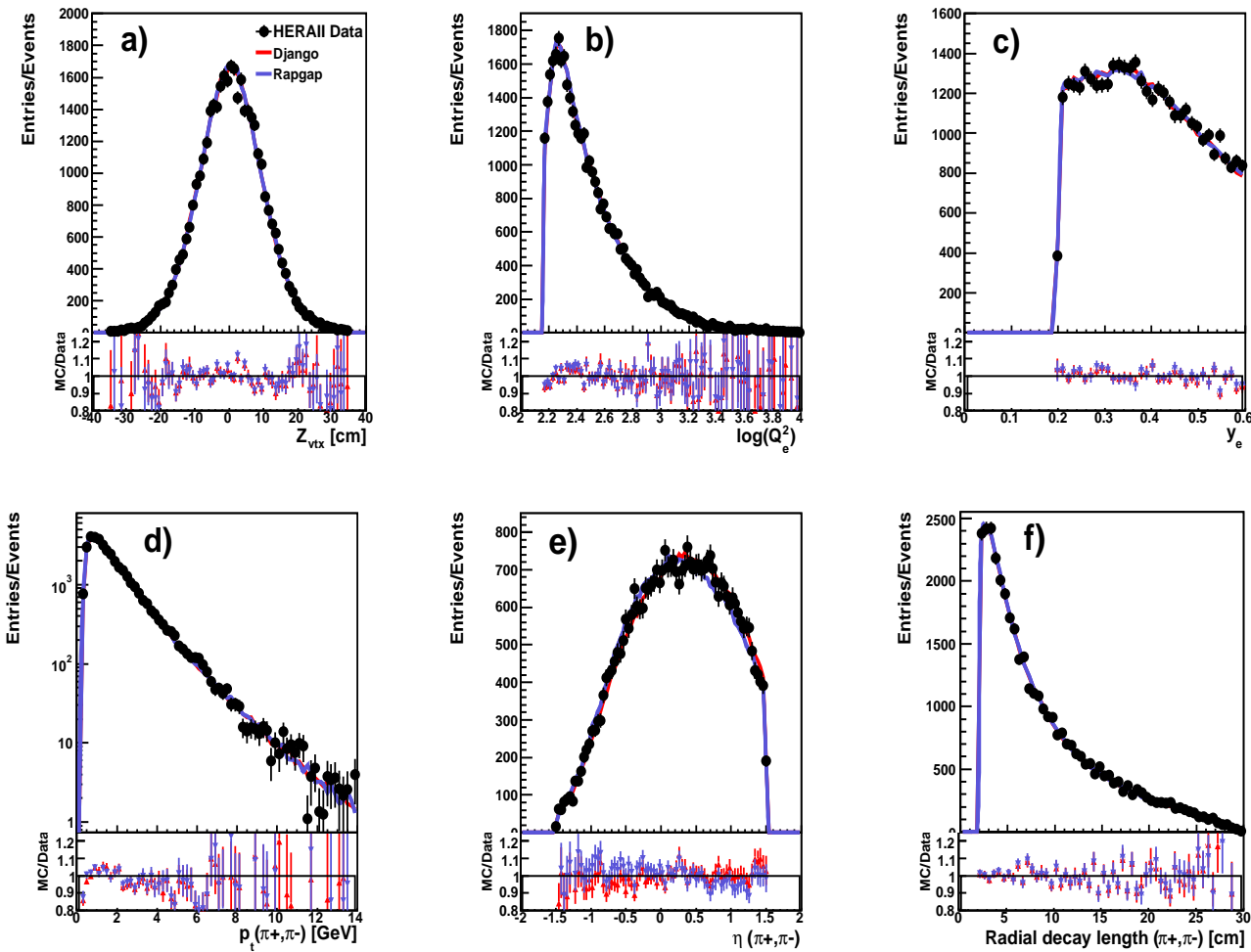
Figure 5.4: Control plots corresponding to the $K_S^0$ sample, a) the $z$ vertex position of the $K_S^0$ origin, b) the logarithm of the photon virtuality $\log(Q^2)$, c) the inelasticity of the scattered electron $y_e$, d) the transverse momentum $p_T$, e) the pseudorapidity distribution and f) the radial decay length of the $K_S^0$ candidates. The data are plotted as black dots while Django and Rapgap Monte Carlo are in red and blue respectively.
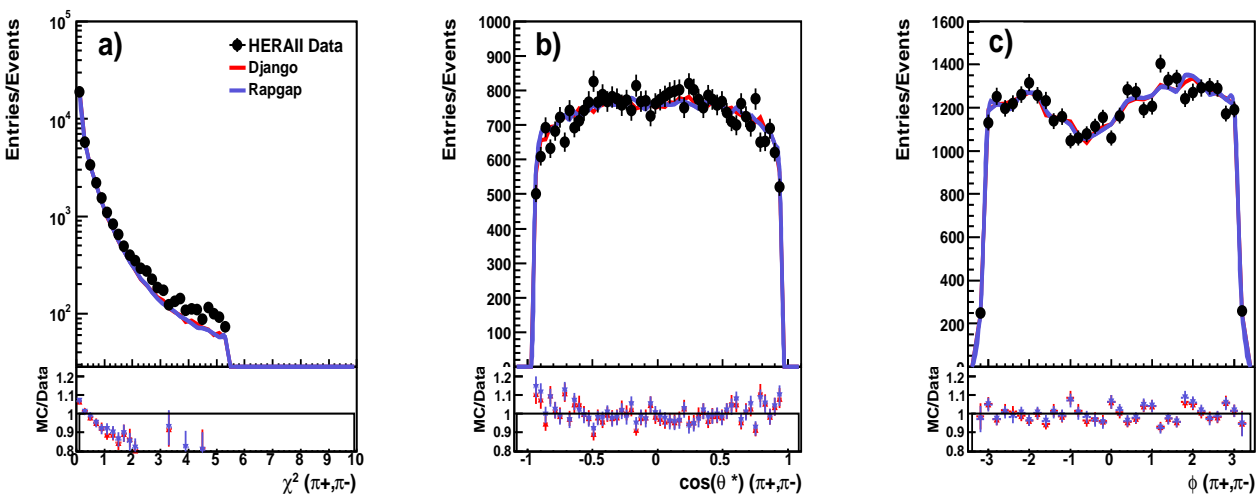
Figure 5.5: Control plots corresponding to the $K_S^0$ sample, a) the $\chi^2$ distribution, b) the $\cos(\theta*)$ and c) the azimuthal angle of the $K_S^0$ candidates. The data are plotted as black dots while Django and Rapgap Monte Carlo are in red and blue respectively.
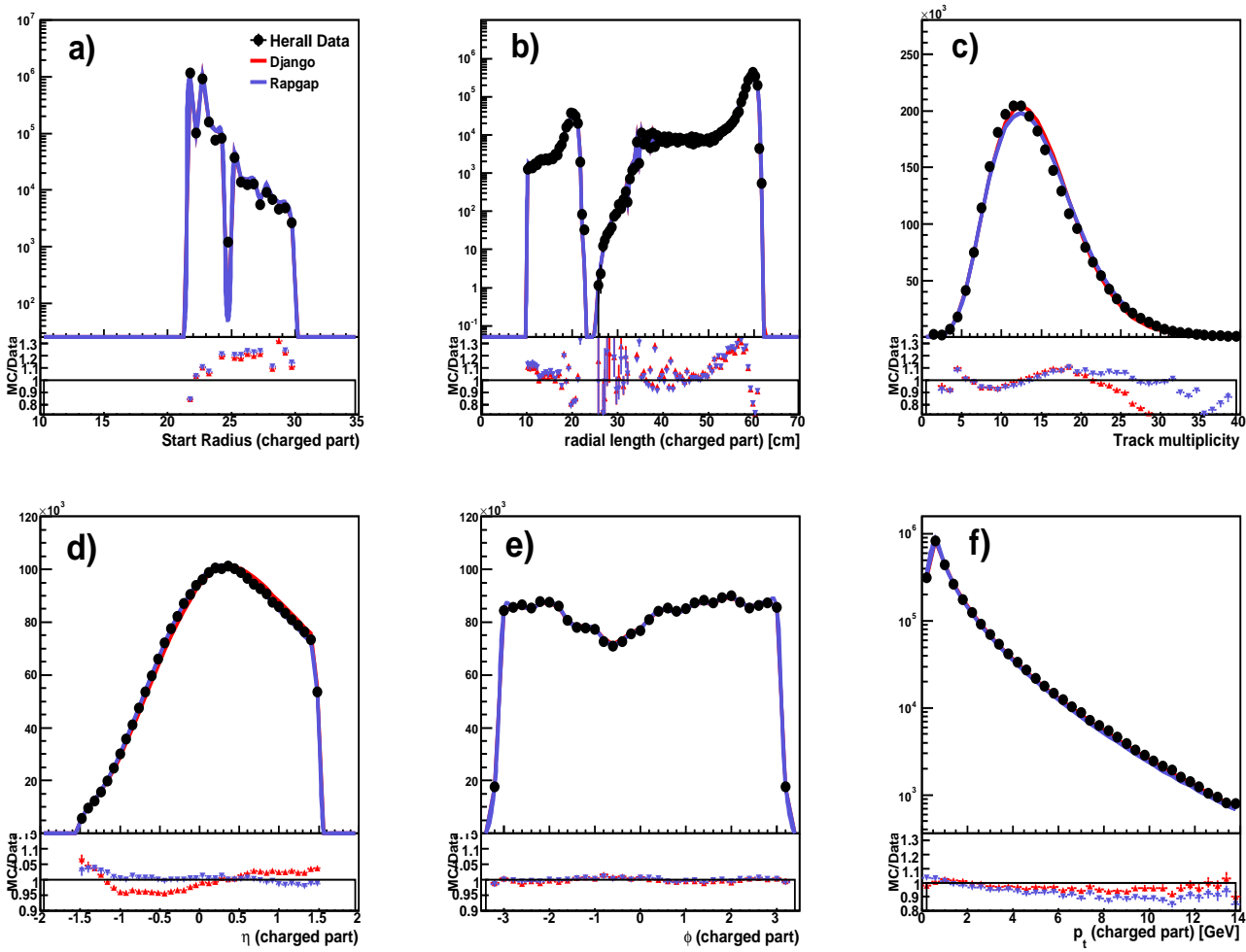
Figure 5.6: Control plots corresponging to the selected charged particles, a) the start radius and b) the radial length of the tracks, c) the track multiplicity, d) the pseudo-rapity distribution $\eta$, e) the azimuthal angle $\phi$ and f) the transverse momentum of the tracks $p_{T\pi}$. The data are plotted as black dots while Django and Rapgap Monte Carlo are in red and blue respectively.

## 5.2.2 Reweighting procedure

As mentioned in the previous subsection and also to have reliability of the generated Monte Carlo data to be used further on, it is important that the Monte Carlo models describes well the data distributions. Sometimes the first comparison shows that the MC does not agree with data, in that case (if the differences are not too large) a satisfactory description can be achieved by applying a reweighting procedure to the MC.

One takes a measured distribution in data and the corresponding in Monte Carlo to determine the event weight. In this thesis a reweighting of the observable $(E - p_z)_{HFS}$ of the hadronic final states was done. The first step is to get the ratio of the MC over the data distribution, secondly the event weight is calculated fitting the ratio to a function $\mathcal{F}((E - p_z)_{HFS})$ of an appropriate shape. The fit function used here is the polynomio:

$$\mathcal{F}(\S) = p_0 + p_1 x + p_2 x^2.$$

The procedure is done for each year period independently, so the weights are not the same. Besides an improvement of the data description by MC in the reweighted distributions, which is of course expected, other distributions are also positively affected. A spoiling of the description of other distributions has not been observed.

There are cases where the MC reweighting of one observable is not enough, then the procedure can be done using another observables and, under the assumption that these quantities are uncorrelated, the total event weight is given by the product of single weights $W_{tot}(obs_1, obs_2, obs_3) = W(obs_1)W(obs_2)W(obs_3)$. This assumption seems to be approximately correct, since usually already after the first iteration a quite reasonable data description is achieved.

Altogether with $(E - p_z)_{HFS}$ reweighted other default H1 weights are applied in this analysis: $z_{vtx}$, trigger and PDF. Whereas the first two are related to the detector simulation, the remaining is directly sensitive to the physics implemented in the MC model.

### 5.2.3   Purity and Stability

Other detector effects can be studied using both reconstructed and generated MC simulations, as the migrations effects (the purity $\mathcal{P}$, stability $\mathcal{S}$ and resolution $\sigma_{res}$) described in this subsection, which corrects the reconstruction or generation of events in wrong bins. The migrations effects are quantifed by the purity $\mathcal{P}$ and stability $\mathcal{S}$; which can be defined as the ratio of $K_S^0$ *generated and reconstructed* in a given bin over the $K_S^0$ reconstructed for $\mathcal{P}$ (generated for $\mathcal{S}$) in the same bin, respectively:

$$\mathcal{P} = \frac{N_i^{stay}}{N_i^{rec}}, \qquad \mathcal{S} = \frac{N_i^{stay}}{N_i^{gen} - N_i^{lost}},$$

where the following combinations were taken into account:

- $N_i^{stay}$: the number of events reconstructed (passing the selection) and generated *in* the same given bin $i$, Figure 5.7 a).

- $N_i^{smear-out}$: the number of events generated *in* the given bin $i$ but reconstructed *in* the bin $j$. Figure 5.7 b).

- $N_i^{smear-in}$: the number of events reconstructed *in* the bin $i$ but generated *from* the bin $j$. Figure 5.7 c).

- $N_i^{lost}$: the number of events generated *in* the given bin $i$ but do not reconstructed because did not pass the selection. Figure 5.7 d).

- $N_i^{rec} = N_i^{stay} + N_i^{smear-in}$, the number of events reconstructed *in* the bin $i$.

- $N_i^{gen} = N_i^{stay} + N_i^{smear-out} + N_i^{lost}$, the number of events generated *in* the bin $i$.

As their name indicates, they say how much pure and stable the $K_S^0$ sample is. The unity is never completely reached, nevertheless is expected that the large fraction of events belongs to the bin where they are measured in. For this thesis the purity and stability values calculated for $Q^2$, $x$, $\eta(K_s^0)$ and $p_T(K_s^0)$ are presented in
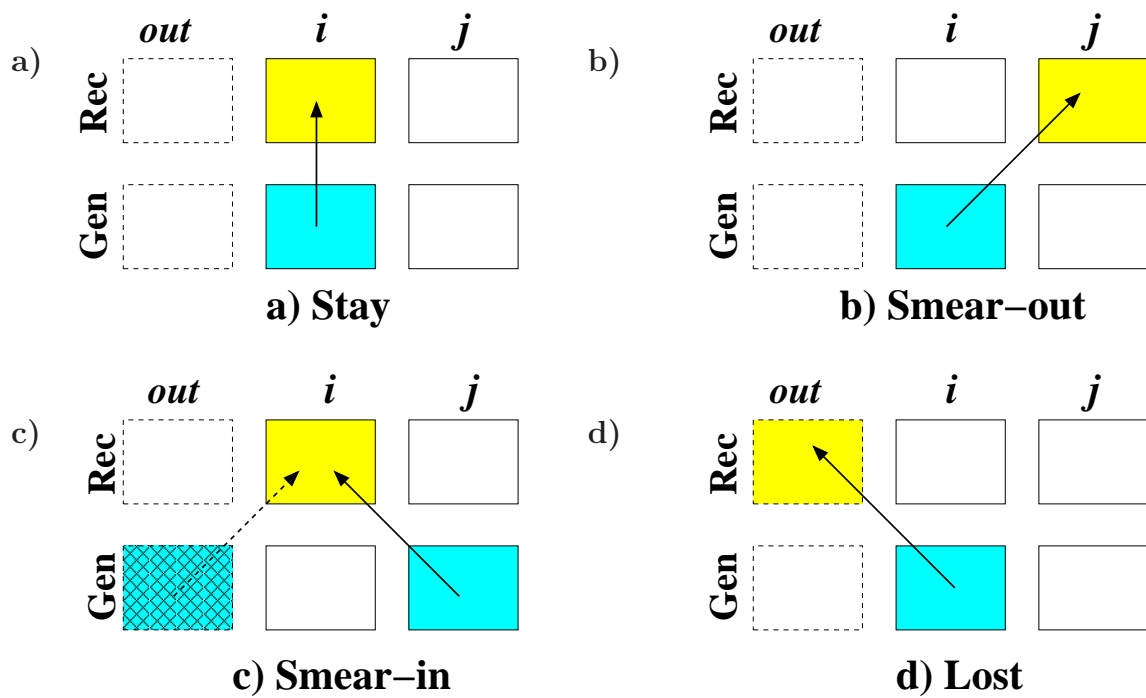
Figure 5.7: Schematic view of migrations possibilities: stay, smear-out, smear-in and lost.

Figure 5.8 in the laboratory frame, while the corresponding plots for $x_p^{BF}$ and $p_T^{BF}$ in the current and the target hemispheres of the Breit frame are shown in Figure 5.9. The Figures correspond to Django MC; Rapgap gives similar values as shown in Table 5.2 for bins of $x$.

Table 5.2: Purity and Stability values in bins of $x$ estimated from Django and Rapgap models.

|            | Purity |        | Stability |        |
|------------|--------|--------|-----------|--------|
|            | Django | Rapgap | Django    | Rapgap |
| $x$ - Bin 1 | 86.95  | 86.62  | 82.37     | 82.56  |
| $x$ - Bin 2 | 88.32  | 88.13  | 87.67     | 87.74  |
| $x$ - Bin 3 | 86.21  | 86.47  | 87.94     | 87.80  |
| $x$ - Bin 4 | 91.49  | 91.92  | 94.08     | 94.20  |

The purity and stability are greater than 80% as functions of $Q^2$, $x$ and $\eta(K_s^0)$. A rise is observed as $Q^2$ goes higher, the same can be said for $x$, while $\eta(K_s^0)$ is almost flat from the second bin. The purity as function of $p_t(K_s^0)$ improves a little bit from $\sim 74\%$ to around 82%, then decreases again but not less than 70%; the stability, on the contrary, starts around 80% then decreases to 76%, at high $p_T$ bins the values increases until $\sim 83\%$. In the Breit frame, the purity and stability as function of $x_p^{BF}$ are around 80% for both regions, although flatter for the current hemisphere; however as function of $p_T^{BF}$ the values oscilate between 60% to 80%.

### 5.2.4   Efficiencies

The efficiency of reconstruction $\varepsilon$ appearing in the equation 5.2 and 5.3 is in fact a combination of two efficiencies $\varepsilon = \varepsilon_{det}^{non-rad} \cdot \varepsilon_{trigger}$, the non-radiative detector efficiency $\varepsilon_{det}^{non-rad}$ and the trigger efficiency $\varepsilon_{trigger}$. However the efficiency of the S67 trigger used in this analysis at high $Q^2$ as explained in section 4.1 is $\sim 100\%$, so it is taken as 100% and an error of 1% is included in the systematic uncertainties, then
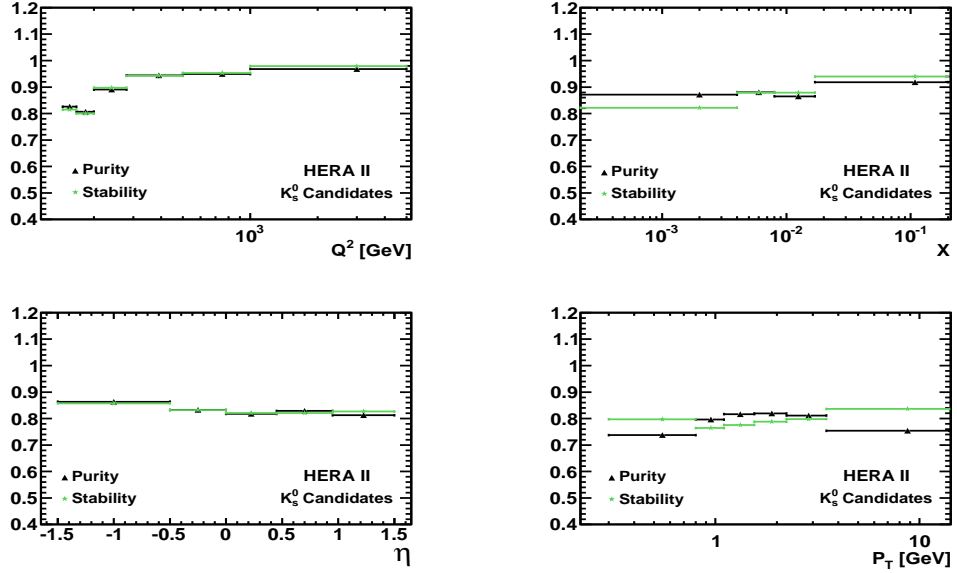
Figure 5.8: The $K_S^0$ purity (in black) and stability (in green) as a function of $Q^2$, x, $\eta$ and $p_T$ in the laboratory frame.
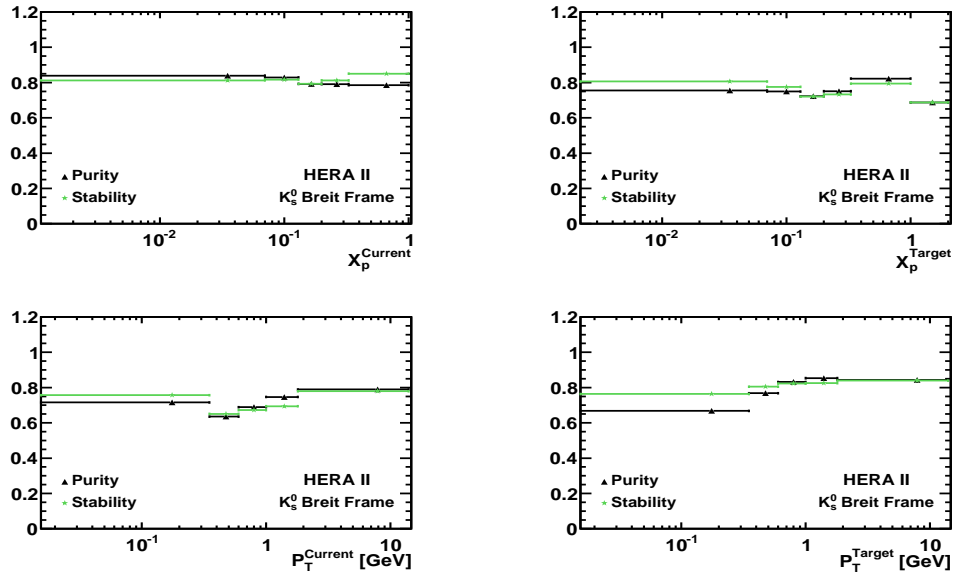


Figure 5.9: The $K_S^0$ purity (in black) and stability (in green) as a function of $x_p$ and $p_T$ in the current and the target hemispheres of the Breit frame.

the efficiency becomes $\varepsilon = \varepsilon_{det}^{non-rad}$. The $\varepsilon_{det}^{non-rad}$ is defined as the ratio between the number of $K_S^0$ taken from the signal extraction of the reconstructed Monte Carlo sample and the number of $K_S^0$ from the generated MC, both in the same phase space and satisfying the complete selection criteria listed in Table 4.2:

$$\varepsilon_{det}^{non-rad} = \varepsilon_{det}^{rad} * (1 + \delta_{QED}) = \frac{N^{rec}(K_s^0)}{N_{rad}^{gen}(K_s^0)} * (1 + \delta_{QED}), \qquad (5.4)$$

here $N_{rad}^{gen}(K_s^0)$ indicates that this number was taken from the MCs including QED initial and final state radiation, then could be that wrongly reconstructed (falling in a different bin) $K_S^0$ exists due to the change in the four-momentum of the scattered electron. The way to correct for these QED events is introducing in QED correction factor $(1 + \delta_{QED})$ defined as:

$$1 + \delta_{QED} = \frac{N_{gen}^{rad}}{N_{gen}^{non-rad}} \cdot \frac{\mathcal{L}^{non-rad}}{\mathcal{L}^{rad}}, \qquad (5.5)$$

where, $\mathcal{L}^{non-rad}$ and $\mathcal{L}^{rad}$ denotes the luminosity of the generated radiative and non-radiative samples.

The QED corrections for bins of $Q^2$, $x$, $\eta(K_S^0)$ and $p_T(K_S^0)$ in the laboratory frame are shown in Figure 5.10 for $K_S^0$ and 5.11 for charged particles using Django and Rapgap models, the QED correction average is found around 5.5% with a flat behaviour in terms of $Q^2$, $x$ and $p_T(K_S^0)$ while $\eta(K_S^0)$ presents a QED correction increasing in the forward direction.

The plots of QED corrections for $K_S^0$ in the Breit frame variables are shown in Figure 5.12, the $x_p^{CBF}$ and $p_T^{CBF}$ in the current region presents lower QED corrections compared to the same variables in the target region. At high values of both variables $(x_p$ and $p_T)$ at target region a difference in the models corrections is observed.

The plots of the efficiency of reconstruction $\varepsilon_{det}^{non-rad}$ are shown in Figures 5.13, 5.14 and 5.15 for the same variables as QED corrections, the average efficiency used for the total inclusive cross section determination is $\sim 30.55$ % but it varies from bin to bin. As functions of $x$ and $\eta$ it behaves very stable but for $Q^2$ and $p_T(K_S^0)$ goes from $\sim 20\%$ in the first bins to around $40\%$ (a little bit higher for $p_T$) in their
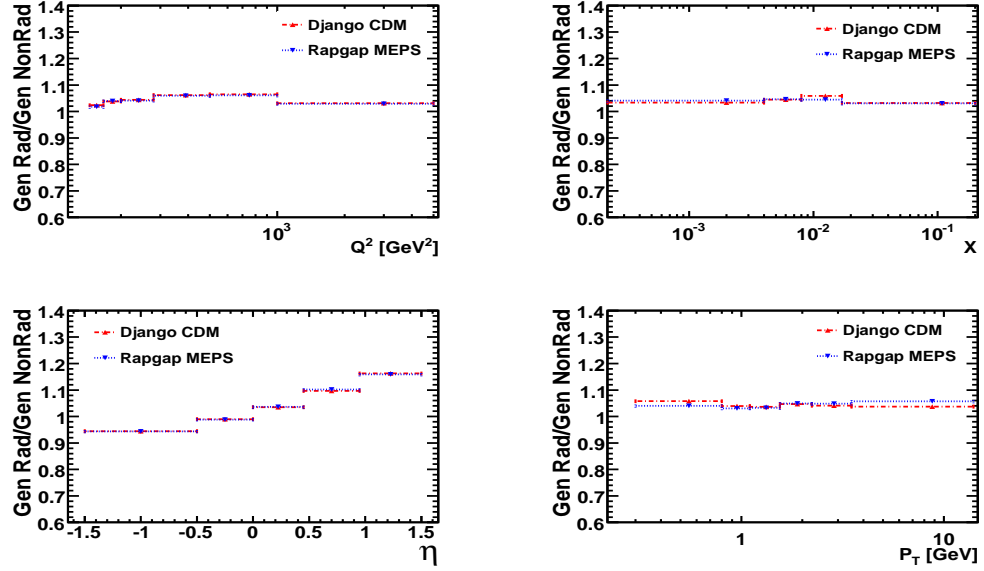
Figure 5.10: QED corrections of $K_S^0$ as a function of $Q^2$, x, $\eta$ and $p_T$ in the laboratory frame. The Django MC presented in red and the Rapgap MC in blue.
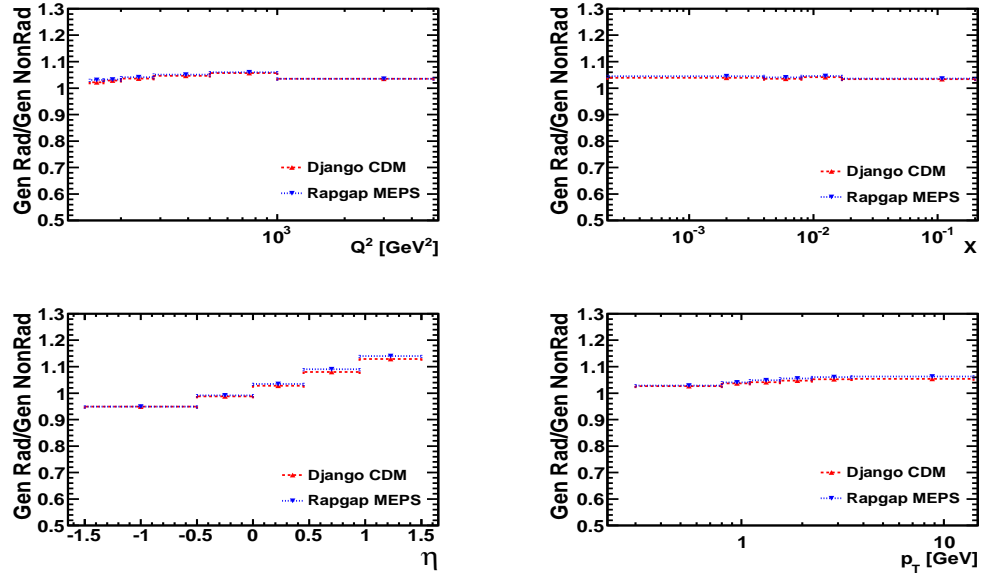


Figure 5.11: QED corrections of charged particles as a function of $Q^2$, x, $\eta$ and $p_T$ in the laboratory frame. The Django MC presented in red and the Rapgap MC in blue.
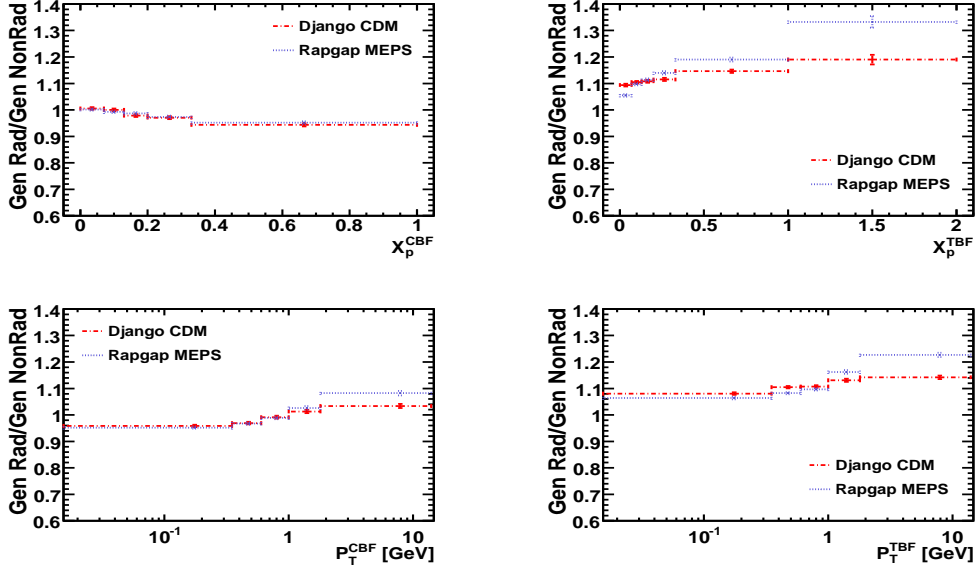
Figure 5.12: QED corrections of $K_S^0$ as a function of $x_p$ and $p_T$ in the current and the target hemispheres of the Breit frame. The Django MC presented in red and the Rapgap MC in blue.
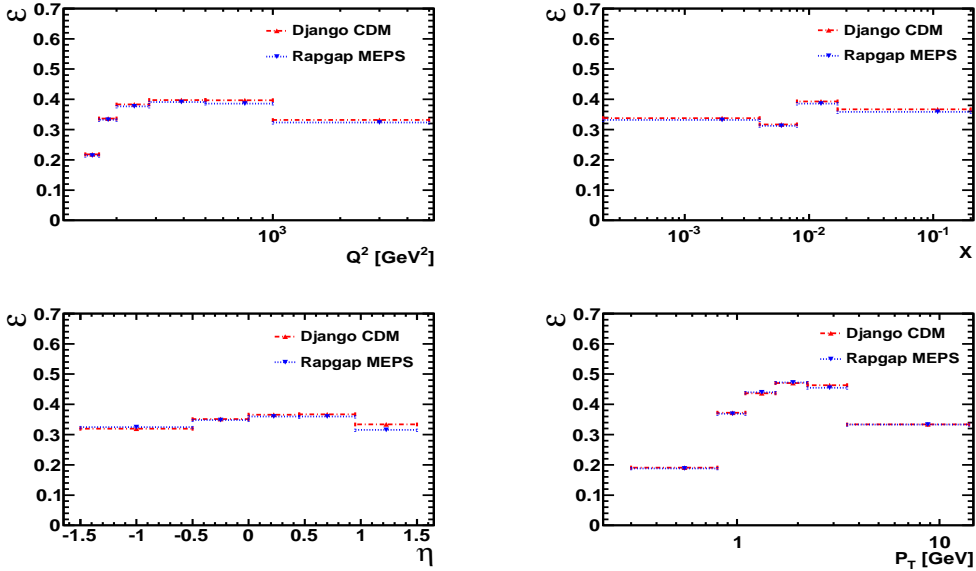


Figure 5.13: Efficiencies of $K_S^0$ as a function of $Q^2$, x, $\eta$ and $p_T$ in the laboratory frame. The Django MC presented in red and the Rapgap MC in blue.

middle range, going down again to around 32% at the highest bins. This shows an up and down behavior which is also observed in the Breit frame variables where the difference in the models at high values in the target regions still remains.
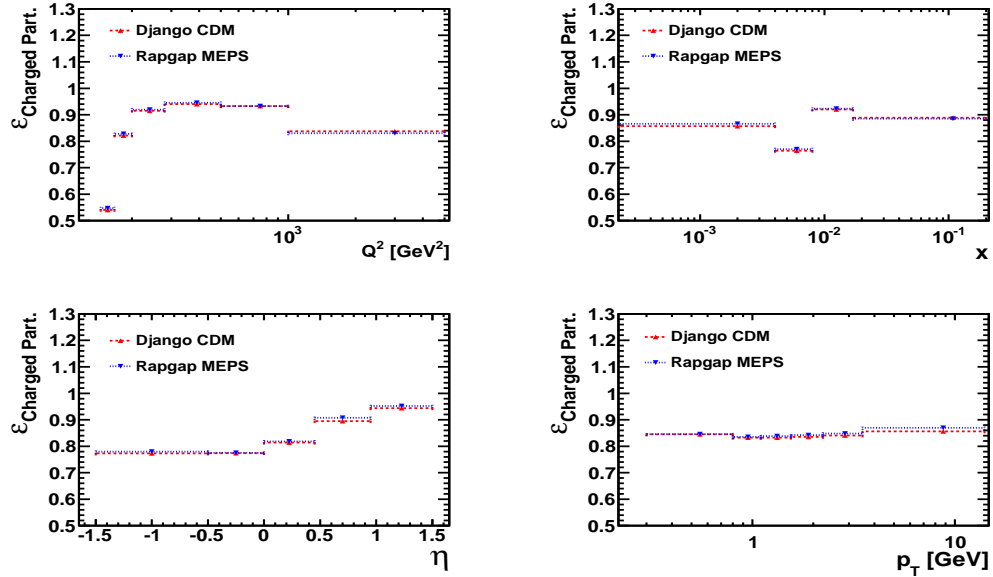


Figure 5.14: Efficiencies of charged particles as functions of $Q^2$, x, $\eta$ and $p_T$ in the laboratory frame. The Django MC presented in red and the Rapgap MC in blue.

### 5.2.5 Resolution

The resolution of a variable $X$ is defined as the width of the distribution:

$$\sigma_{res} = X_{rec} - X_{gen}$$

where $X_{rec}$ and $X_{gen}$ denotes the reconstructed and the generated value of the variable $X$, respectively. The resolutions are shown in Figures 5.16 and 5.17.

## 5.3 The systematic uncertainties

The accuracy of the cross section measurement is altered by several sources of uncertainty which change the determined value by a $\Delta\sigma$. The study of these changes
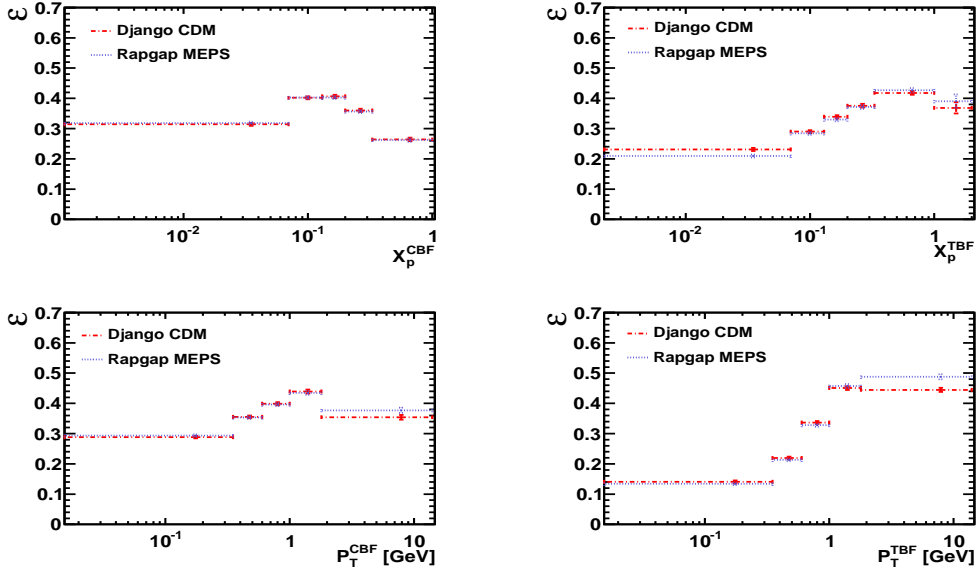
Figure 5.15: Efficiencies of $K_S^0$ as functions of $x_p$ and $p_T$ in the current and the target hemispheres of the Breit frame. The Django MC presented in red and the Rapgap MC in blue.
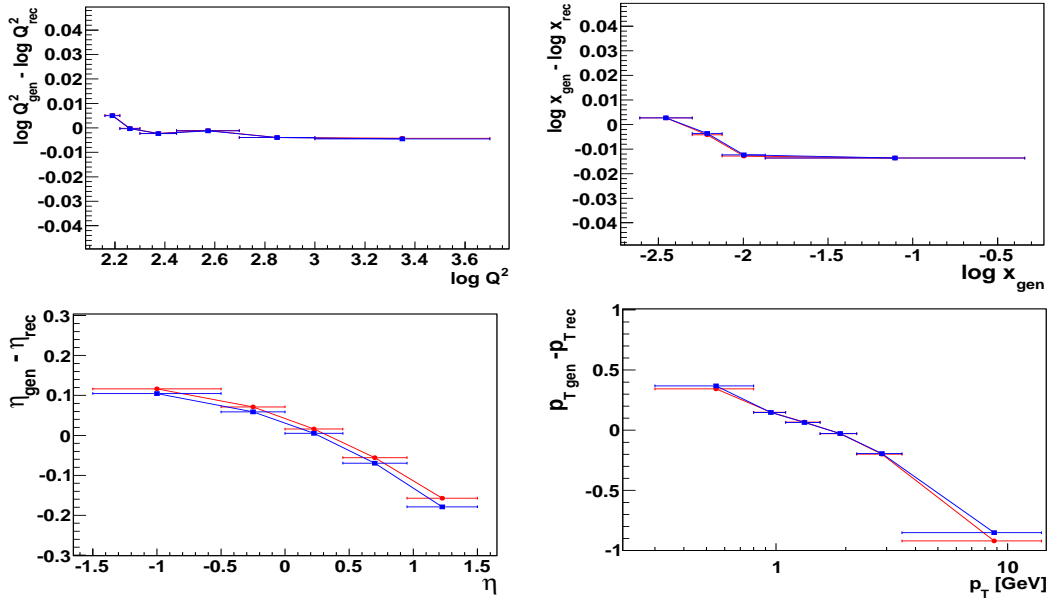


Figure 5.16: Resolutions as functions of $Q^2$, x, $\eta$ and $p_T$ variables in the laboratory frame. The Django MC presented in red and the Rapgap MC in blue.
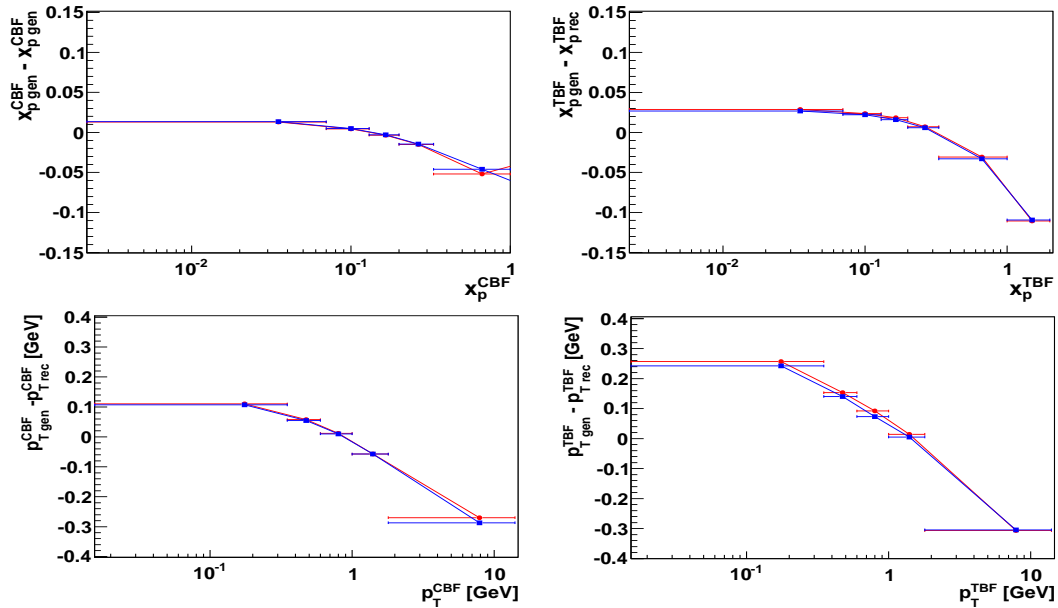
Figure 5.17: Resolutions as functions of $x_p^{CBF}$, $x_p^{TBF}$, $p_T^{CBF}$ and $p_T^{TBF}$ variables in the Breit frame. The Django MC presented in red and the Rapgap MC in blue.

is done varying each possible uncertain quantity under investigation by some reasonable deviation in both sides, upward and downward, then all the analysis procedure is repeated and the corresponding cross section is calculated again under the same selection criteria in order to know the sensitivity of the applied cuts. Depending on the kind of source the uncertainty is calculated using data and MC models or MCs only.

The sources can be classified as *reconstruction* uncertainties if the source comes from or depends on the reconstruction of the electron and hadronic final states particles (as the energy and the polar angle of the electron), the luminosity measurement, the $V_0$ finding efficiency and the topology reconstruction; and *correction* uncertainties if they are applied to simulation models (model dependence), efficiencies (trigger and track efficiency) or signal extraction.

The total uncertainty consists of the addition in quadrature of the systematic

and the statistic uncertainties:

$$\Delta \sigma_{tot} = \sqrt{\sigma_{stat}^2 + \sum_i \sigma_{i,sys}^2}.$$

where $i$ runs over all sources of systematics uncertainties. When one is dealing with differential cross section the uncertainties should be calculated for each bin.

The estimation of the systematic uncertainties expectations are detailed separately in the following subsections.

### 5.3.1   Energy and polar angle of the electron

The energy and the polar angle of the scattered electron is used for the estimation of the kinematic variables $Q^2$, $x$ and $y$ but also for the boost to the Breit frame, so a variation in the energy range can directly affect the $K_S^0$ rate production.

The systematic effect due to the energy scale can be studied varying by $\pm$ 1% the reconstructed energy on the LAr calorimeter. The resulting uncertainty for the inclusive cross section is found to be +1.5 % and -2.9 %, a higher uncertainty when the energy is down.

For the differential cross section the variation is calculated bin by bin, the uncertainty plots as functions of variables in the laboratory and the Breit frames are shown in Figures 5.18 and 5.19. It is observed that the uncertainties when the energy of the electron is varied up are between 0.2 and 2 % for most of the bins in the laboratory frame but for the fist bin of $Q^2$ the uncertainty is higher, up to around 8 %; when the energy of the electron is varied down the uncertainties are between 1 and 4 % except for the last two bins in x where the uncertainty goes to 8 %. In the Breit frame the higher uncertainty appears in the current hemisphere with a higher value of 7 % when the energy of the electron is varied down.

The resulting uncertainty, due to effects in the polar angle reconstruction of the LAr Cal, is estimated to be +2.9% and -3.1% by changing the $\theta_{e'}$ angle by $\pm$ 3 mrad. Figures 5.20 and 5.21 present the uncertainties bin per bin in the laboratory and

the Breit frame variables, except for the bins in $Q^2$ all the other plots show more symmetry when the $\theta_{e'}$ angle varies up and down.
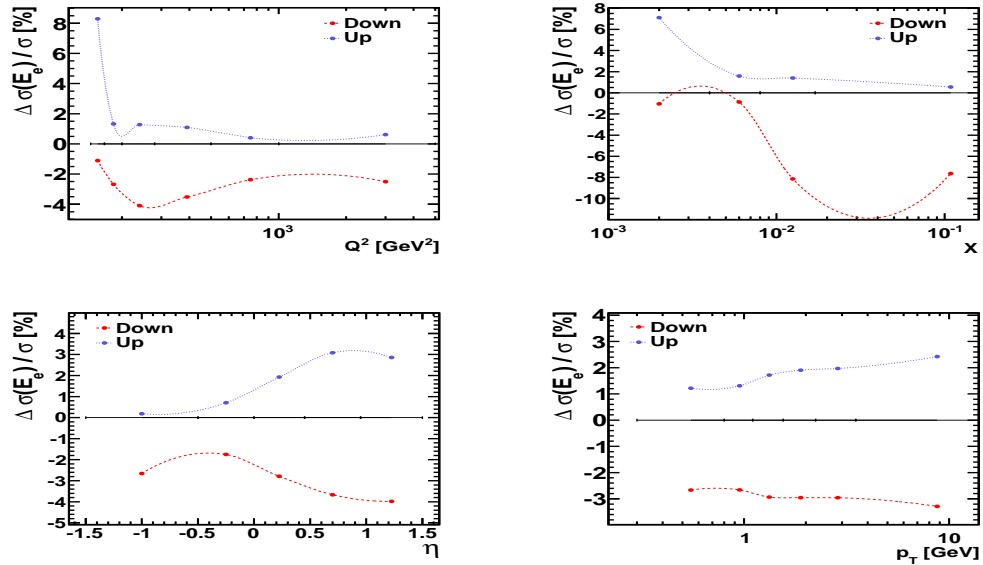


Figure 5.18: The systematic uncertainties due to the variation on the energy of the scaterred electron $E_{e'}$ as functions of the laboratory frame variables.

## 5.3.2 Luminosity

The uncertainty in the luminosity measurement (subsection 3.2.3) is not the same for all year periods, for 2004 $e^+p$ it is 2.92 %, for 0405 $e^-p$ the value is 2.44 % and 2.69 % for the year 2006 $e^-p$ while it is 2.28 % for 0607 $e^+p$ period. At the end, the contribution to the total systematic uncertainty for the HERA II data is taken to be 2.6 %.

## 5.3.3 Topology

The topology error comes from the difference in the seagull and sailor topologies reconstruction efficiency. The uncertainty is estimated, first taking the ratio of the $K^0_S$ number extracted from the fit to the invariant mass distribution of the data and
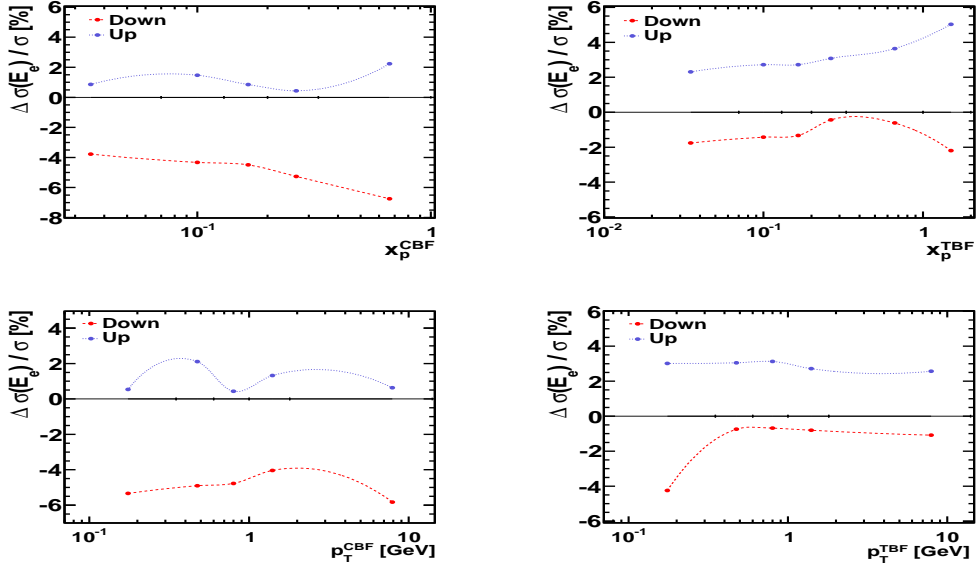
Figure 5.19: The systematic uncertainties due to the variation on the energy of the scattered electron $E_{e'}$ as functions of the Breit frame variables.
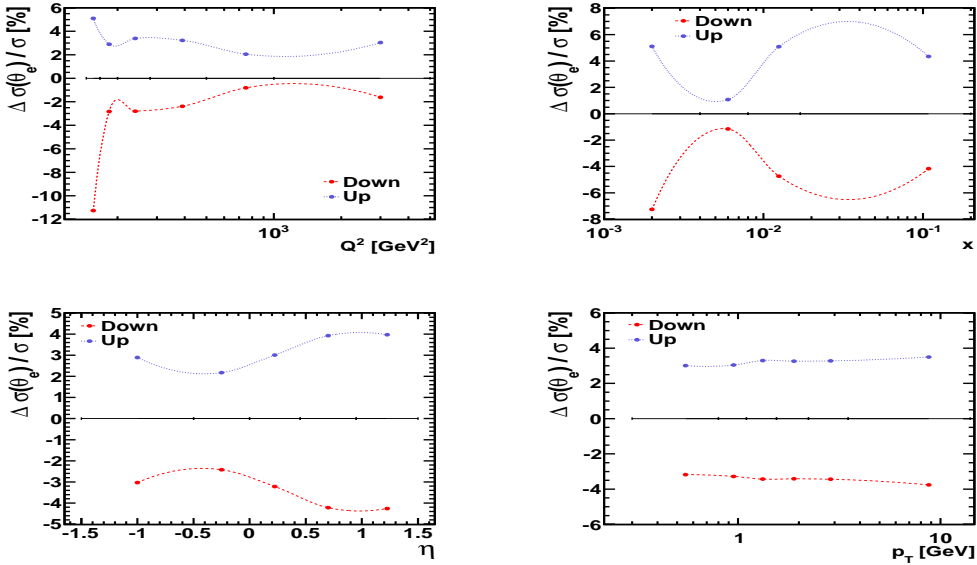


Figure 5.20: The systematic uncertainties due to the variation on the polar angle of the scattered electron $\theta_{e'}$ as functions of the laboratory frame variables.
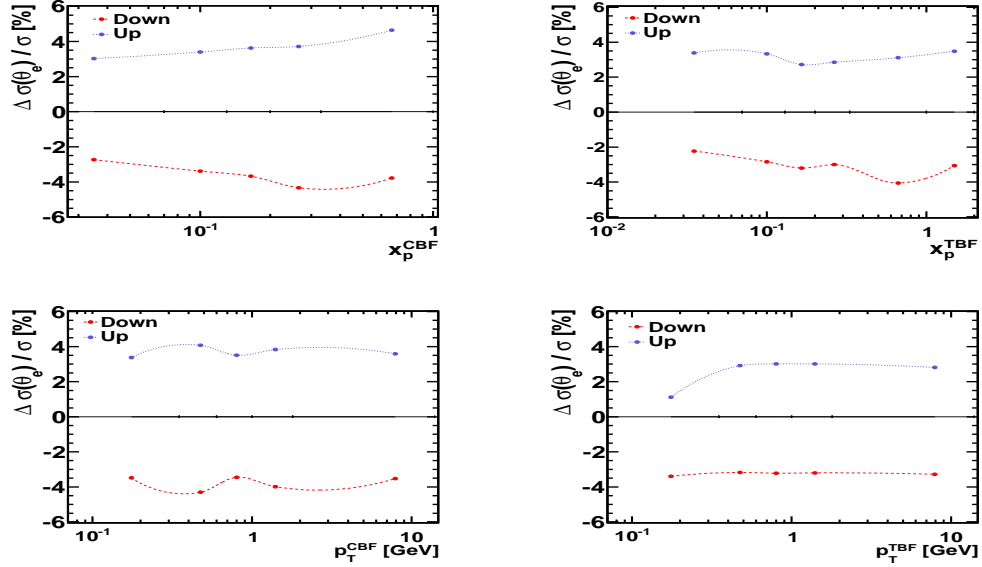
Figure 5.21: The systematic uncertainties due to the variation on the polar angle of the scattered electron $\theta_{e'}$ as functions of the Breit frame variables.

the model $R^i = N^i_{data}/N^i_{model}$ where $i$ represents the topology types, seagull or sailor. Then, the double ratio $R_{double} = R^{sailor}/R^{seagull}$ leads to a uncertainty contribution. A value of $\pm 3.0\%$ is calculated for the visible inclusive cross section of the $K^0_S$. This 3 % is applied to all bins in the laboratory and the Breit frames.

## 5.3.4 Model dependence

The full analysis is corrected using Django MC which uses CDM as parton cascade. To test the effect of the parton evolution scheme on the $K^0_S$ production, the analysis is also done using Rapgap with a different parton evolution (MEPS); A contribution of $\pm$ 0.05 % to the total uncertainty is gotten by half of the ratio between the difference in the efficiencies obtained from both models and the efficiency using Django:

$$0.5 * \frac{\varepsilon^{CDM} - \varepsilon^{MEPS}}{\varepsilon^{CDM}}.$$

The variations per bins in the laboratory and the Breit frame variables are seen

in Figures 5.22 and 5.23, the uncertainties oscillate between 0.1% to 1.2% in the laboratory but it goes to higher values in the Breit frame, specially in the target hemisphere where the values are between 0.1% and 3.4%.
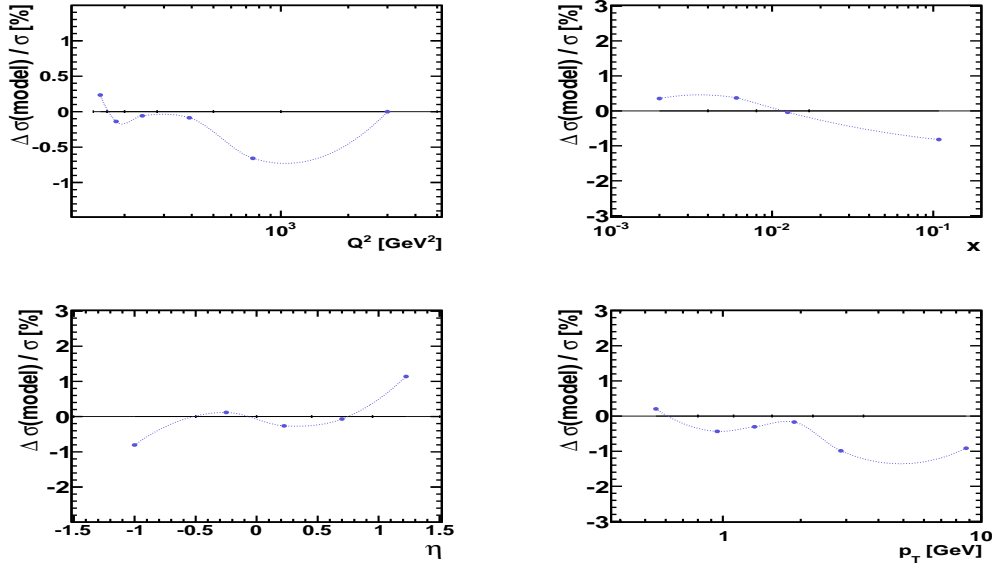


Figure 5.22: The systematic uncertainties due to the variation on the model dependence as functions of the laboratory frame variables.

### 5.3.5　Track efficiency

The track efficiency uncertainty is considered due to the imperfection in the reconstruction of the tracks that can mainly affect the $K_S^0$ tag. In H1 detector, there is no other component besides the central trackers to be used for checking the track reconstruction efficiency, then a 2 % uncertainty is choosen for each track which is determined by the tracks curling up at the CJC.

As two tracks compose the $K_S^0$, an uncertainty of $\pm$ 4 % (the sum of 2 % per track) is considered for the total uncertainty calculation becoming the dominant systematic error of the analysis. The same 4% value is applied to all bins in the laboratory and the Breit frames.
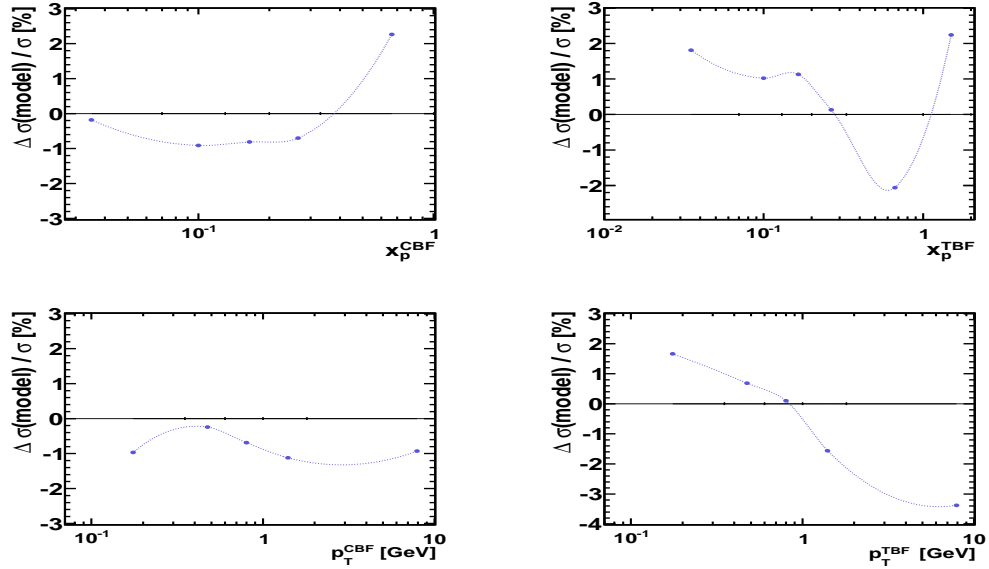
Figure 5.23: The systematic uncertainties due to the variation on the model dependence as functions of the Breit frame variables.

### 5.3.6 Trigger efficiency

The uncertainty on the trigger efficiency is chosen to be ± 1 % as mentioned in the first paragraph of the section 5.2.4, since the efficiency of the S67 trigger used in this analysis is approximately 100 %. The same percentage is applied to all bins for the uncertainty trigger contribution.

### 5.3.7 Signal extraction

The systematic effect of the signal extraction over the number of $K_S^0$ candidates is estimated using different procedures for the signal description. In the analysis, the fit to a polynomial-exponential function for the background and a $t$-student distribution for the signal were used, but the alternative way chosen to get the uncertainty here is the side band subtraction method (SBS). The SBS gets the number of $K_S^0$ candidates by counting the number of events contained in the range [0.4 GeV, 0.6 GeV] around the $K_S^0$ mass peak from the original histogram of invariant mass distribution (without

any fit), then the number of background events is taken from the integral to the background function previously used, in the same range [0.4 GeV, 0.6 GeV]. Then, $N_{K_S^0}^{SBS} = N_{K_S^0}^{signal}$(counting the histogram)$- N_{K_S^0}^{bgrd}$(integral to background function) is the number of $K_S^0$ candidates from the SBS method.

The resulting uncertainty is finally gotten from the ratio:

$$\frac{N_{K_S^0}^{fit} - N_{K_S^0}^{SBS}}{N_{K_S^0}^{fit}},$$

where $N_{K_S^0}^{fit}$ is the number of $K_S^0$ from the signal extraction as discussed in section 4.6. For the total HERA II systematic determination the contribution is $\pm$ 2.0 %.
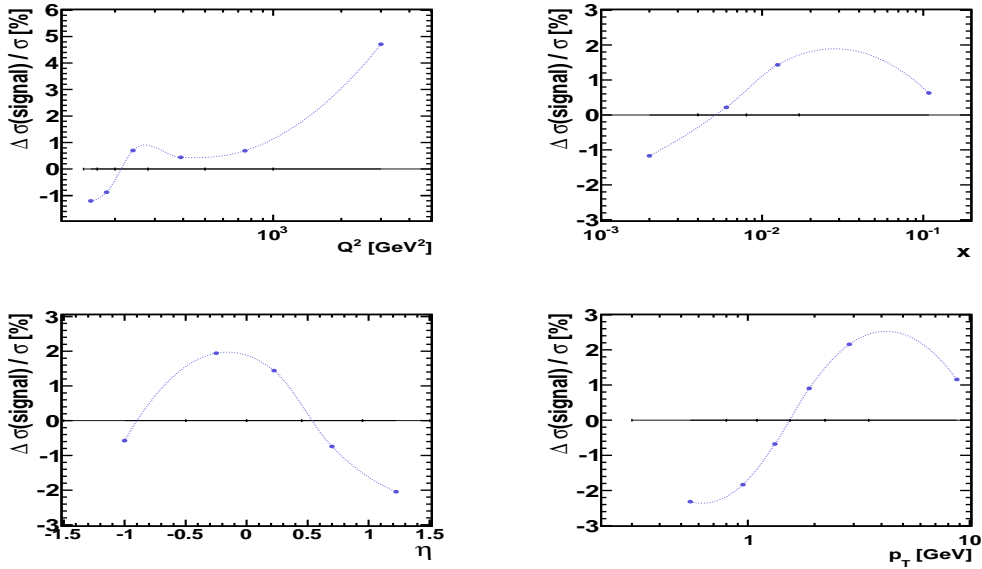


Figure 5.24: The systematic uncertainties due to the variation on the signal extraction as functions of the laboratory frame variables.

The plots of the uncertainty variation due to signal extraction bin by bin are in Figures 5.24 and 5.25. The oscillation of the values shows the difficulties to obtain a fit of better quality to the mass invariant distribution, per example the last bin in $Q^2$ (Figure F.1) and $x_p^{TBF}$ (Figure F.6) and the first bin of $p_T^{TBF}$ (Figure F.8).
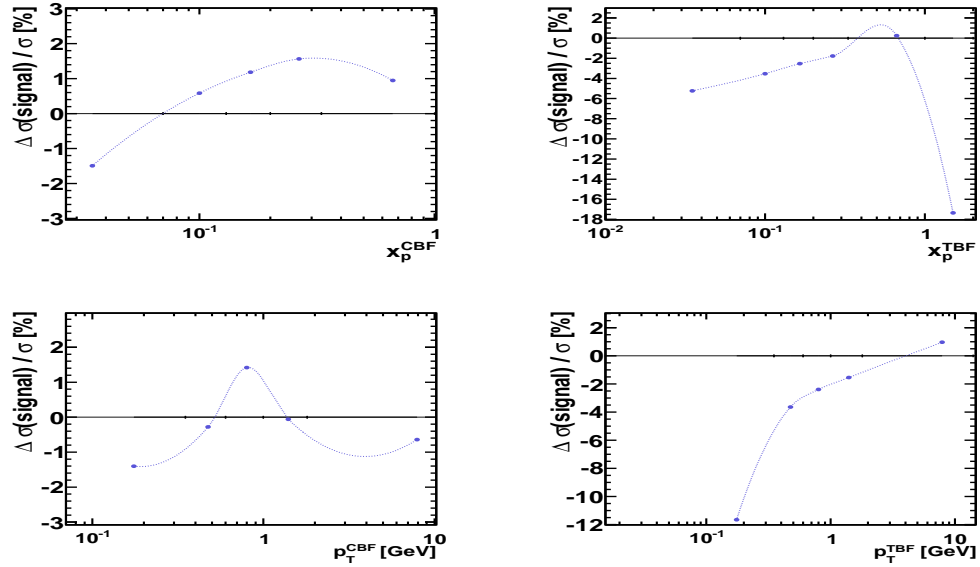
Figure 5.25: The systematic uncertainties due to the variation on the signal extraction as functions of the Breit frame variables.

### 5.3.8   Branching ratio

This uncertainty is taken into account because the branching ratio of the $K_S^0$ decaying to $\pi^+\pi^-$ is not exactly known, the PDG reports a BR = $(0.6920 \pm 0.0005)\%$ [11], then $\pm 0.1\%$ is considered for the contribution to the total uncertainty determination. As this contribution is very small, it could be neglected. The same uncertainty values is applied to all bins in the laboratory and the Breit frames.

All sources contributing to the total systematic uncertainty for the measured inclusive $K_S^0$ cross section from the HERA II data are listed in Table 5.3; the variation used for the estimation and the $\Delta\sigma$ obtained are also presented. It is possible to distinguish that the dominat contributions come from the topology reconstruction, the $\Theta_{e'}$ variation and the track efficiency reconstruction. At the end, a systematic uncertainty of +6.9 % and -7.4 % is estimated.

Table 5.3: Summary of systematic uncertainties.

| Source | Variation | $\Delta\sigma(K_s^0)$ |
|---|---|---|
| $E'_{e'}$ | 1 % | $+1.5\%/-2.9\%$ |
| $\Theta_{e'}$ | $\pm$ 3 mrad | $+2.9\%/-3.1\%$ |
| signal extraction | $\frac{N^{fit}-N^{SBS}}{N^{fit}}$ | $\pm$ 2.0% |
| model dependence | $0.5*\frac{\varepsilon^{CDM}-\varepsilon^{MEPS}}{\varepsilon^{CDM}}$ | $\pm$ 0.05 % |
| topology rec | | $\pm$ 3.0 % |
| luminosity | | $\pm$ 2.6 % |
| track rec | 2 % per track | $\pm$ 4.0 % |
| branching ratio | | $\pm$ 0.1 % |
| trigger efficiency | | $\pm$ 1.0 % |
| total uncertainty | | $+6.9\%/-7.4\%$ |

The statistical uncertainty is obtained by:

$$\sigma_{stat.} = \sqrt{\left(\frac{\sigma_{N_{K_s^0}}}{N_{K_s^0}}\right)^2_{data} + \left(\frac{\sigma_{N_{K_s^0}}}{N_{K_s^0}}\right)^2_{rec-MC}} \qquad (5.6)$$

where $N_{K_s^0}$ is the number of $K_S^0$ extracted from the fit and $\sigma_{N_{K_s^0}}$ is the statistical uncertainty from the fit procedure.

As $N_{K_s^0} = 38154$ and $\sigma_{N_{K_s^0}} = 1194$ for data, and $N_{K_s^0} = 39984$ and $\sigma_{N_{K_s^0}} = 233$ for reconstructed-MC, a total statistical uncertainty of $\sim$ 3 % is calculated.

# Chapter 6

# Results and conclusions

The measurements of the inclusive $K_S^0$ meson cross section as total, differential and double–differential are presented in this chapter. The cross section ratio of the $K_S^0$ over the charged particles, and the density measurements are also calculated and explained here.

The comparison to Django (CDM) and Rapgap (MEPS) model predictions are shown in all plots in order to establish if the data favour any model or strangeness supresion factor $\lambda_s$ value. The Django model is used for the QCD studies varying the PDF and $\lambda_s$ parameters, while Rapgap is chosen for the study of the quark flavour contribution to the $K_S^0$ cross section.

## 6.1 Total $K_s^0$ cross section

The inclusive $K_S^0$ production cross section $\sigma_{vis}$ measured in the visible range defined by the phase space in equation 5.1 is found to be:

$$\sigma_{vis} = 531 \pm 17 \text{ (stat)}^{+37}_{-39} \text{ (sys) pb,} \tag{6.1}$$

where the efficiency $\varepsilon \sim 30.55\%$ with the included QED correction $\delta_{QED} \sim 5.5\%$ as determined in the subsection 5.2.4, the BR $= 0.692$ from the Table 2.2 for the $K_S^0$ $\rightarrow \pi^+\pi^-$ decay channel, the luminosity value of 339.6 pb$^{-1}$ as listed in the Table 4.1

and the $N_{K_S^0} = 38154$ as extracted from the fit in Figure 4.4 are used for the cross section determination with the equation 5.2. The statistical (3 %) and systematic uncertainties (+6.9 % and -7.4 %) obtained in the subsection 5.3, are calculated from the application of the corresponding percentage to the cross section.

The predictions of Django and Rapgap Monte Carlo programs with different strangeness values $\lambda_s$ but same CTEQ6L PDF were estimated giving the cross sections values presented in the Table 6.1. The statistical errors are very small since the luminosity of the non-radiative MCs used for the predictions (sections 1.4.1 and 1.4.2) is around 74 times larger than the luminosity of data (339.6 $pb^{-1}$).

Table 6.1: The Monte Carlo cross section predictions for different strangeness suppresion factors ($\lambda_s$).

|                 | $\lambda_s = 0.22$ | $\lambda_s = 0.286$ | $\lambda_s = 0.3$ |
| --- | --- | --- | --- |
| Django (CDM)    | $\sigma = 443$ pb | $\sigma = 516$ pb | $\sigma = 518$ pb |
| Rapgap (MEPS)   | $\sigma = 444$ pb | $\sigma = 536$ pb | $\sigma = 519$ pb |

The Monte Carlo predictions are in good agreement with the measurement within the uncertainties, specially with $\lambda_s = 0.286$ and $\lambda_s = 0.3$, while the predictions with $\lambda_s = 0.22$ for both models underestimate the measurement.

The inclusive cross section was calculated year by year to look for stability of the measurement. In Figure 6.1, the visible cross section $\sigma_{vis}$ measured for all HERA II data (equation 6.1) is represented with a black dashed line, the statistical uncertainty forms the shadow rectangle around the $\sigma_{vis}$ value. The measured cross section per period are depicted as blue points with their respective statistical uncertainty, while the cross sections obtained with the Django Monte Carlo are plotted with red points. It is found that the measurements per period are consistent with the cross section estimated with the full data sample.

The measured ratio of the inclusive cross section of the $K_S^0$ meson over the charged
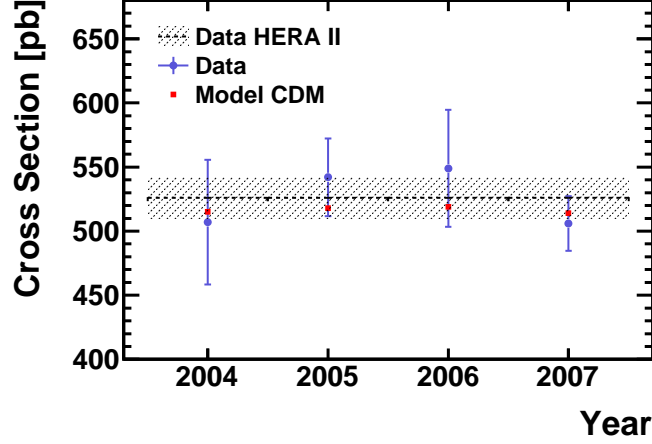
Figure 6.1: Inclusive cross section for the four year periods of HERA II data. The measurement (in blue) presented with statistical uncertainty is compared to the prediction of the Django model (in red). The measured cross section for the full HERA II data is shown in the black line with the shadow being its statistical uncertainty.

particle production:

$$\frac{\sigma_{vis}(ep \rightarrow eK_S^0X)}{\sigma_{vis}(ep \rightarrow eh^{\pm}X)} = 0.05867 \pm 0.0019 \text{ (stat)} \pm 0.0024 \text{ (sys)}, \tag{6.2}$$

is in agreement (within the uncertainties) with the prediction of the CDM model: 0.05922. It is also consistent with the results obtained from the analysis at low $Q^2$, presented in subsection 2.5.

The density ratio gives a measurement of:

$$\frac{\sigma_{vis}(ep \rightarrow eK_S^0X)}{\sigma_{vis}(ep \rightarrow eX)} = 0.3842 \pm 0.0115 \text{ (stat)} \pm 0.0159 \text{ (sys)}, \tag{6.3}$$

and the prediction of Django gives 0.3988, showing good consistency.

## 6.2 Differential $K_s^0$ cross section

The differential cross section in the laboratory frame as functions of the four-momentum of the virtual photon $Q^2$, the Bjorken scaling variable $x$, the pseudo-rapidity $\eta$ of the $K_S^0$, and the transverse momentum $p_T$ of the $K_S^0$ are shown in

Figure 6.2, where the cross section graphs are placed in the upper part of each plot, while the ratio between the models and data for the two strangeness factor ($\lambda_s = 0.22$ and $\lambda_s = 0.286$) for Django and Rapgap are presented in the bottom of each plot in order to have a better visualization of the comparisons.

The measurement decreases quickly when $Q^2$ and $p_T$ take higher values. While the behaviour as functions of $x$ and $\eta$ is a small increasing that then falls down. The data are better described by the models with $\lambda_s = 0.286$ in normalization and shape, independenly of the MC model, since both Django and Rapgap give similar descriptions. The models with $\lambda_s = 0.22$ subestimate the measurements in most of the bins. The results are bin-averaged and no bin-center corrections are applied.

The corresponding differential $K_S^0$ cross section in the Breit frame as function of the scaled momentum fraction $x_p^{BF}$ and the $K_S^0$ transverse momentum $p_T^{BF}$ in the current (CBF) and the target (TBF) hemispheres are shown in Figure 6.3. The production decreases at high values of the variables. The comparison to Django and Rapgap Monte Carlo programs shows good description of data by the models with $\lambda_s = 0.286$ in the current region were the preferred production mechanism is the hard interaction process, while in the target region the models allow to observe some sensitivity to the $\lambda_s$ factor, as expected due to the domination of the hadronization process in this hemisphere of the BF. The differential cross sections together with statistical, systematic uncertainties and the CDM model prediction values can be found in the Tables 6.2 and 6.3.

## 6.3   Ratios of the differential cross sections

Due to the cancellation of some uncertainty sources the total uncertainty is reduced for the cross section ratios, for instance the $K_S^0$ cross section over the charged particle production and the $K_S^0$ over the DIS cross section ratios. Therefore the ratios are used for looking at global description of all observed cross sections or test different aspects of the meson production within the fragmentation models. They
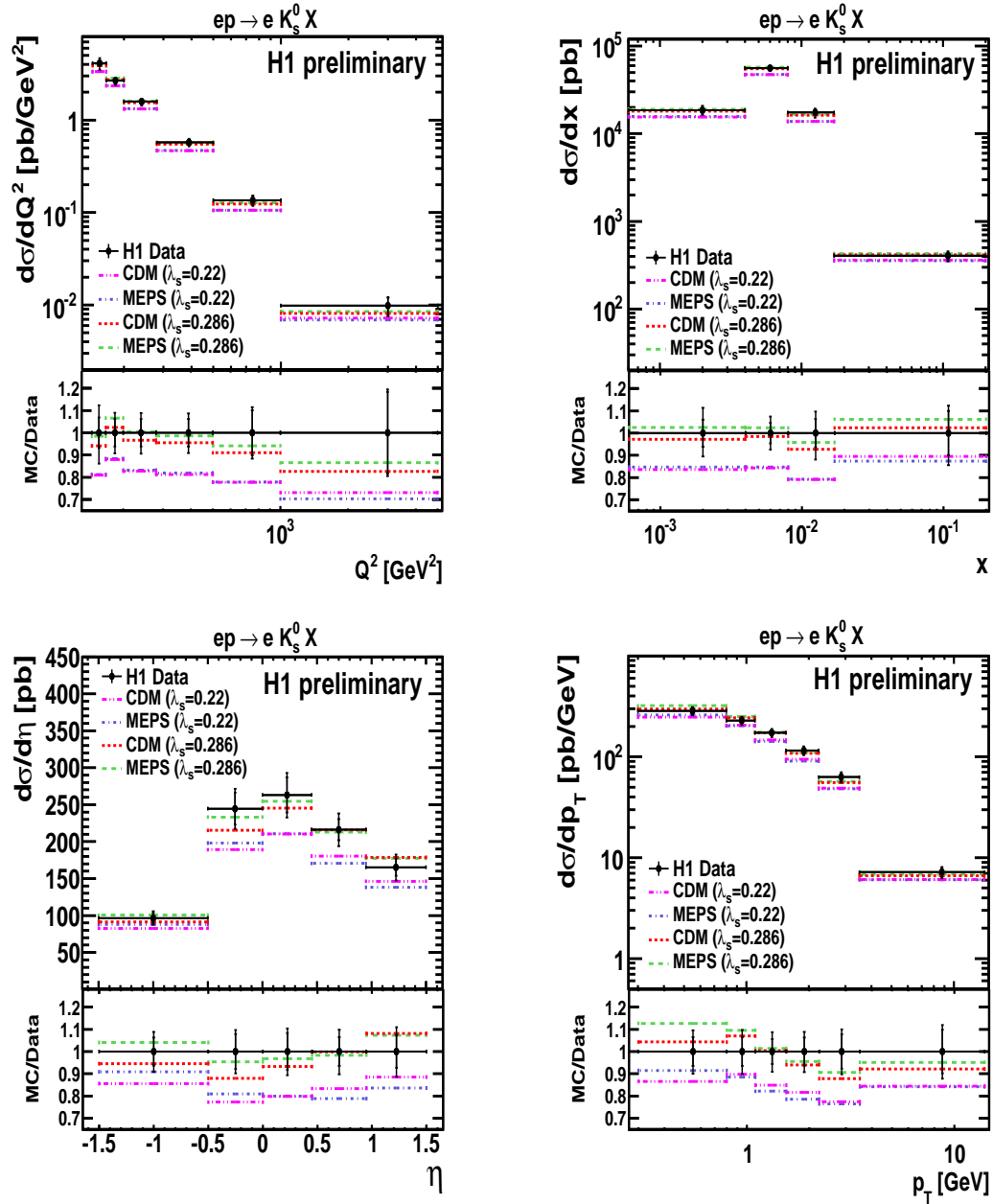
Figure 6.2: Cross sections of the $K_S^0$ meson in the laboratory frame as functions of the four-momentum of the virtual photon $Q^2$, the Bjorken scaling variable $x$, the pseudorapidity $\eta$ of the $K_S^0$, and the transverse momentum $p_T$ of the $K_S^0$. The comparisons are clearer in the MC model over data ratio plotted in the bottom of each plot. The outer (inner) error bar indicates the total (statistical) uncertainty.

| $ep \rightarrow e\,K_s^0\,X$ | | | | | |
|---|---|---|---|---|---|
| $Q^2$ [GeV$^2$] | $\mathrm{d}\sigma/\mathrm{d}Q^2$ | stat. | syst. (+) [pb/GeV$^2$] | syst. ($-$) | MC Pred |
| 145 $-$ 167 | 4.12 | 0.30 | 0.45 | 0.54 | 3.88 |
| 167 $-$ 200 | 2.67 | 0.16 | 0.17 | 0.18 | 2.73 |
| 200 $-$ 280 | 1.59 | 0.10 | 0.11 | 0.12 | 1.54 |
| 280 $-$ 500 | 0.58 | 0.04 | 0.04 | 0.04 | 0.55 |
| 500 $-$ 1000 | 0.14 | 0.02 | 0.008 | 0.008 | 0.12 |
| 1000 $-$ 5000 | 0.010 | 0.002 | 0.0007 | 0.0007 | 0.008 |
| $x$ | $\mathrm{d}\sigma/\mathrm{d}x$ | stat. | syst. (+) [pb] | syst. ($-$) | MC Pred |
| 0.0 $-$ 0.004 | 18595 | 1180 | 1860 | 1674 | 18087.4 |
| 0.004 $-$ 0.008 | 56023 | 2631 | 3361 | 3361 | 55195.1 |
| 0.008 $-$ 0.017 | 17479 | 1205 | 1398 | 1923 | 16217.8 |
| 0.017 $-$ 0.20 | 405 | 39 | 28 | 41 | 414.853 |
| $\eta$ | $\mathrm{d}\sigma/\mathrm{d}\eta$ | stat. | syst. (+) [pb] | syst. ($-$) | MC Pred |
| -1.5 $-$ -0.5 | 96.6 | 6.41 | 6.18 | 6.7 | 91.5 |
| -0.5 $-$ 0.0 | 244.6 | 21.8 | 15.7 | 16.4 | 215.3 |
| 0.0 $-$ 0.45 | 263.2 | 23.7 | 17.9 | 18.9 | 245.3 |
| 0.45 $-$ 0.95 | 216.3 | 14.3 | 16.4 | 17.3 | 215.9 |
| 0.95 $-$ 1.5 | 165.3 | 11.5 | 12.9 | 13.9 | 178.8 |
| $p_T$ [GeV] | $\mathrm{d}\sigma/\mathrm{d}p_T$ | stat. | syst. (+) [pb/GeV] | syst. ($-$) | MC Pred |
| 0.3 $-$ 0.8 | 285.0 | 17.8 | 19.7 | 21.1 | 297.3 |
| 0.8 $-$ 1.1 | 228.8 | 14.2 | 15.6 | 16.7 | 244.7 |
| 1.1 $-$ 1.55 | 172.9 | 9.6 | 11.8 | 12.6 | 173.8 |
| 1.55 $-$ 2.23 | 115.6 | 7.8 | 7.9 | 8.4 | 108.7 |
| 2.23 $-$ 3.5 | 63.0 | 5.5 | 4.5 | 4.8 | 55.3 |
| 3.5 $-$ 14.0 | 7.18 | 0.8 | 0.5 | 0.55 | 6.6 |

Table 6.2: The differential $K_s^0$ cross section values as functions of $Q^2$, $x$, $\eta$ and $p_T$ in the visible kinematic region defined by $145 < Q^2 < 20000$ GeV$^2$, $0.2 < y < 0.6$, -1.5 $\eta(K_S^0)$ 1.5 and $p_T > 0.3$ GeV. The bin ranges, the bin averaged cross section values, the statistical and the positive and negative systematic uncertainties, as well as the predictions from Django are listed.
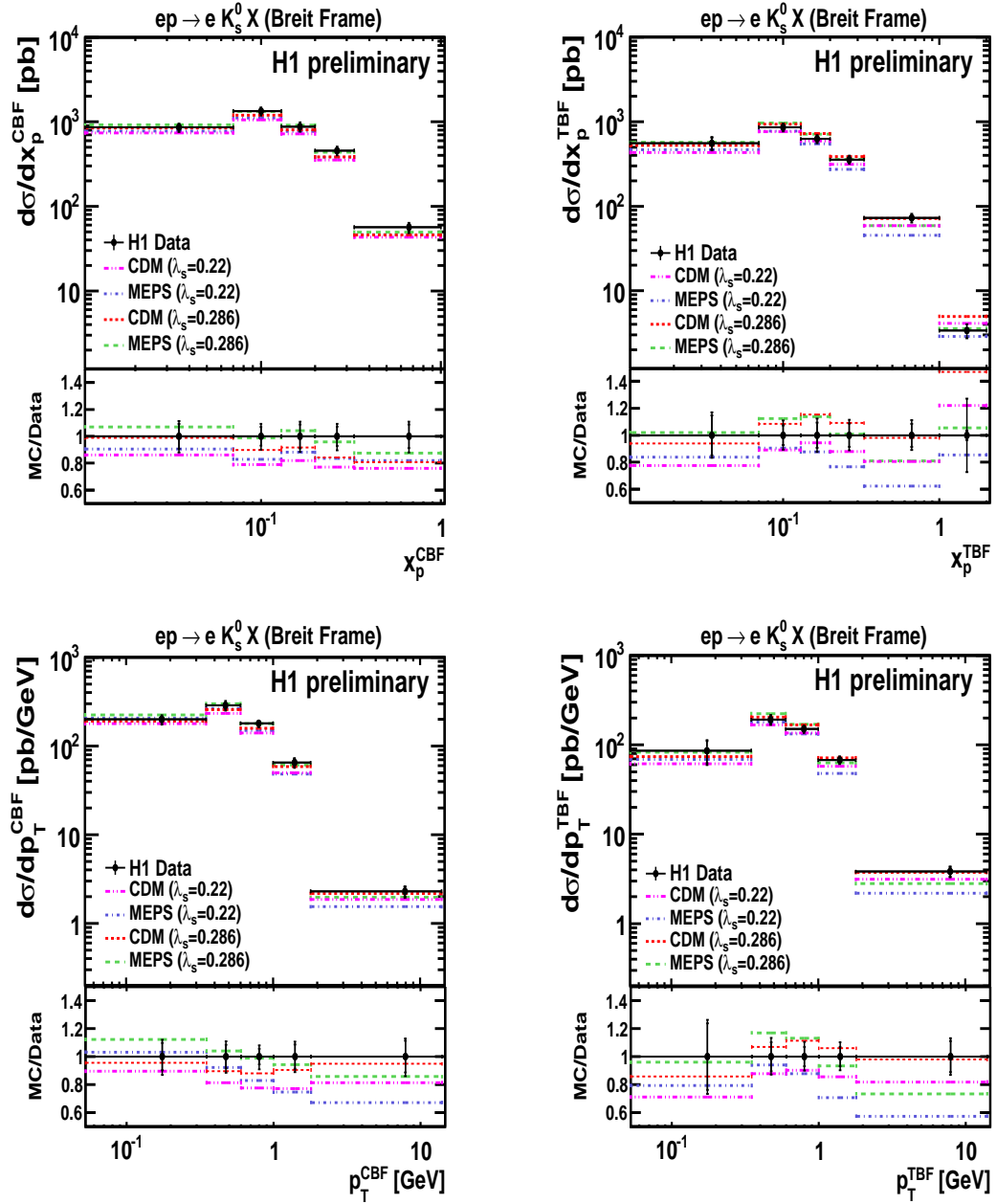
Figure 6.3: Cross section of the $K_S^0$ meson in the Breit frame as function of the scaled momentum fraction and the transverse momentum in the current region ($x_p^{CBF}$ and $p_T^{CBF}$ in the left hand side of the figure) and the target region ($x_p^{TBF}$ and $p_T^{TBF}$ in the right hand side). The outer (inner) error bar indicates the total (statistical) uncertainty. More details in caption of Figure 6.2

| $ep \rightarrow e\,K_s^0\,X$ | | | | | |
|---|---|---|---|---|---|
| $x_p^{Breit}$ current | $d\sigma/dx_p^{Breit}$ | stat. | syst. $(+)$ | syst. $(-)$ | MC Pred |
|  | | | [pb] | | |
| $0.0\ -\ 0.07$ | 859.1 | 78.8 | 56.6 | 64.3 | 848.4 |
| $0.07\ -\ 0.13$ | 1339.5 | 102.6 | 90.9 | 107.0 | 1202.1 |
| $0.13\ -\ 0.2$ | 879.2 | 84.5 | 61.5 | 71.9 | 805.4 |
| $0.2\ -\ 0.33$ | 458.1 | 38.3 | 32.0 | 42.2 | 385.1 |
| $0.33\ -\ 1.0$ | 56.7 | 5.9 | 4.5 | 5.7 | 45.7 |
| $x_p^{Breit}$ target | $d\sigma/dx_p^{Breit}$ | stat. | syst. $(+)$ | syst. $(-)$ | MC Pred |
|  | | | [pb] | | |
| $0.0\ -\ 0.07$ | 557.7 | 88.4 | 50.1 | 46.8 | 522.5 |
| $0.07\ -\ 0.13$ | 859.1 | 59.0 | 67.8 | 63.5 | 929.7 |
| $0.13\ -\ 0.2$ | 625.7 | 52.6 | 46.2 | 44.9 | 721.6 |
| $0.2\ -\ 0.33$ | 356.3 | 29.7 | 25.6 | 23.5 | 388.2 |
| $0.33\ -\ 1.0$ | 72.9 | 6.7 | 5.6 | 5.3 | 71.3 |
| $1.0\ -\ 2.0$ | 3.4 | 0 | 0.6 | 0.6 | 4.9 |
| $p_T^{Breit}$ current | $d\sigma/dp_T^{Breit}$ | stat. | syst. $(+)$ | syst. $(-)$ | MC Pred |
| [GeV] | | | [pb/GeV] | | |
| $0.0\ -\ 0.35$ | 200.2 | 19.2 | 13.6 | 17.4 | 190.9 |
| $0.35\ -\ 0.6$ | 288.7 | 26.4 | 21.0 | 24.8 | 258.2 |
| $0.6\ -\ 1.0$ | 180.8 | 11.3 | 12.3 | 14.9 | 159.0 |
| $1.0\ -\ 1.8$ | 65.2 | 6.5 | 4.6 | 5.2 | 58.9 |
| $1.8\ -\ 14.0$ | 2.3 | 0.3 | 0.15 | 0.2 | 2.18 |
| $p_T^{Breit}$ target | $d\sigma/dp_T^{Breit}$ | stat. | syst. $(+)$ | syst. $(-)$ | MC Pred |
| [GeV] | | | [pb/GeV] | | |
| $0.0\ -\ 0.35$ | 86.45 | 23.9 | 11.2 | 12.1 | 74.1 |
| $0.35\ -\ 0.6$ | 191.4 | 18.9 | 15.3 | 14.3 | 204.5 |
| $0.6\ -\ 1.0$ | 150.7 | 9.6 | 11.3 | 10.5 | 167.4 |
| $1.0\ -\ 1.8$ | 67.6 | 4.7 | 4.9 | 4.7 | 71.5 |
| $1.8\ -\ 14.0$ | 3.8 | 0.5 | 0.3 | 0.3 | 3.7 |

Table 6.3: The differential $K_S^0$ cross-section values as functions of $p_T^{Breit}$ and $x_p^{Breit}$ in the current and target hemispheres of the Breit frame. More details in caption of Table 6.2.

also provide a rather direct constrain of $\lambda_s$, or/and $\lambda_{qq}$ and $\lambda_{sq}$.

### 6.3.1 Differential $K_S^0/h^\pm$ cross section

The $K_S^0/h^\pm$ cross section, defined as the ratio of the $K_S^0$ production over the charged particle cross section measured in the same phase space as the $K_S^0$, were determined in the laboratory frame as shown in Figure 6.4. The measured production shows an almost flat ratio as function of $Q^2$; as function of $\eta$ there is a small falling, and as function of $p_T$ rises at higher values due to the $K_S^0$, which takes most of the momentum than the usually lower massive charged particles.

The shape and normalization of the ratios are reasonably well described by the CDM and MEPS models with $\lambda_s = 0.286$ for the four plots. The values of the ratio cross sections, the statistical and systematic uncertainties and the CDM model predictions for each bin can be found in Table 6.4.

### 6.3.2 Differential $K_s^0/$DIS cross section

The density plots, defined as the ratio between the cross section of the $K_S^0$ and the DIS event production in the same kinematic region as the $K_S^0$, are measured differentially as functions of $Q^2$ and $x$ as shown in Figure 6.5. The $K_S^0$ multiplicity average lies at $\sim 0.4$ independently of the variables, indicating that the $K_S^0$ production fraction with respect to the DIS events is almost equal at any region. The Django and Rapgap models with $\lambda_s = 0.286$ describe quite well the measurements in $Q^2$ but they predict a small falling as function of $x$ which is not observed from data. The cross section values of the ratio with their corresponding statistical and systematic uncertainties as well as the CDM model predictions bin by bin can be found in Table 6.5.
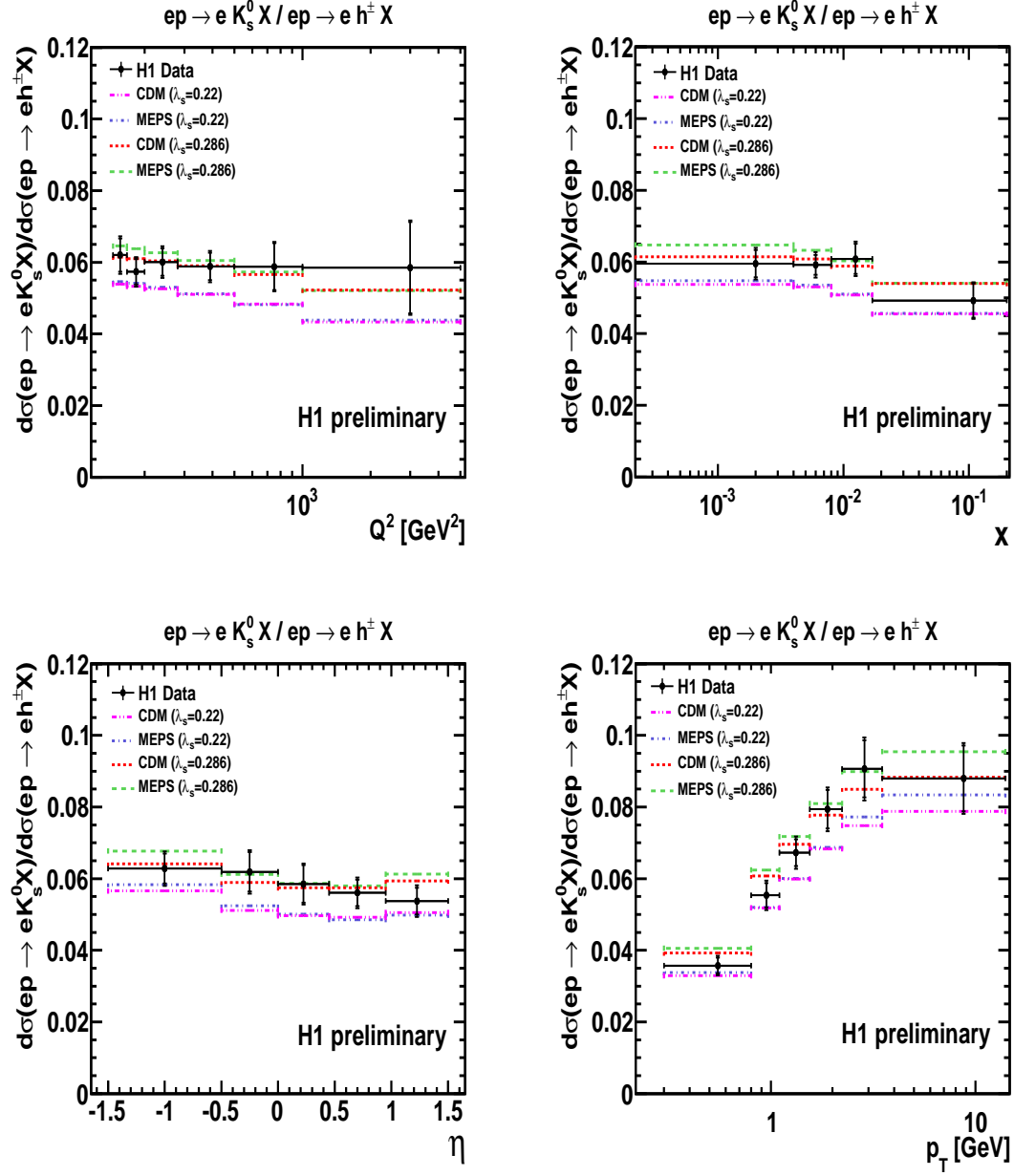
Figure 6.4: Ratio between the cross sections of the $K_S^0$ and the charge particles in the laboratory frame as functions of $Q^2$, $x$, $\eta$ and $p_T$. The outer (inner) error bar indicates the total (statistical) uncertainty. The CDM and MEPS models with $\lambda_s = 0.22$ and $\lambda_s = 0.286$ are presented for comparison.

| $\mathbf{R(K_s^0/h^{\pm})}$ | | | | |
|---|---|---|---|---|
| $Q^2$ [GeV$^2$] | $R(K_s^0/h^{\pm})$ | stat. | syst. | MC Pred |
| 145 − 167 | 0.0620 | 0.00464 | 0.00240 | 0.0614 |
| 167 − 200 | 0.0574 | 0.00353 | 0.00214 | 0.0610 |
| 200 − 280 | 0.0601 | 0.00382 | 0.00221 | 0.0604 |
| 280 − 500 | 0.0588 | 0.00382 | 0.00214 | 0.0590 |
| 500 − 1000 | 0.0588 | 0.00657 | 0.00219 | 0.0566 |
| 1000 − 5000 | 0.0585 | 0.01273 | 0.00345 | 0.0522 |
| $x$ | $R(K_s^0/h^{\pm})$ | stat. | syst. | MC Pred |
| 0.0 − 0.004 | 0.0596 | 0.00378 | 0.00229 | 0.0615 |
| 0.004 − 0.008 | 0.0592 | 0.00278 | 0.00216 | 0.0608 |
| 0.008 − 0.017 | 0.0609 | 0.00420 | 0.00236 | 0.0588 |
| 0.017 − 0.20 | 0.0492 | 0.00477 | 0.00185 | 0.0540 |
| $\eta$ | $R(K_s^0/h^{\pm})$ | stat. | syst. | MC Pred |
| -1.5 − -0.5 | 0.0628 | 0.00417 | 0.00237 | 0.0642 |
| -0.5 − 0.0 | 0.0619 | 0.00552 | 0.00254 | 0.0590 |
| 0.0 − 0.45 | 0.0585 | 0.00527 | 0.00228 | 0.0574 |
| 0.45 − 0.95 | 0.0560 | 0.00371 | 0.00210 | 0.0574 |
| 0.95 − 1.5 | 0.0537 | 0.00375 | 0.00232 | 0.0593 |
| $p_T$ [GeV] | $R(K_s^0/h^{\pm})$ | stat. | syst. | MC Pred |
| 0.3 − 0.8 | 0.0357 | 0.00223 | 0.00154 | 0.0392 |
| 0.8 − 1.1 | 0.0553 | 0.00343 | 0.00227 | 0.0607 |
| 1.1 − 1.55 | 0.0673 | 0.00375 | 0.00249 | 0.0696 |
| 1.55 − 2.23 | 0.0794 | 0.00536 | 0.00294 | 0.0777 |
| 2.23 − 3.5 | 0.0906 | 0.00796 | 0.00372 | 0.0849 |
| 3.5 − 14.0 | 0.0880 | 0.00922 | 0.00352 | 0.0884 |

Table 6.4: The values of the ratio of the differential production cross sections for mesons and charged hadrons as functions of $Q^2$, $x$, $p_T$ and $\eta$. More details in caption of Table 6.2.
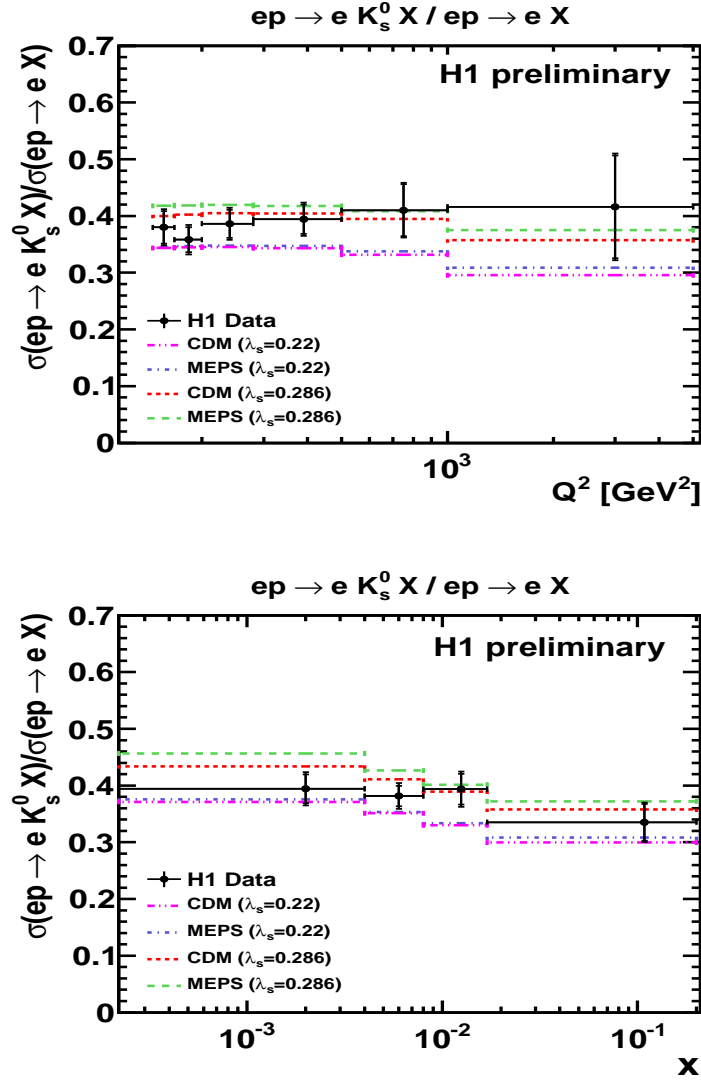
Figure 6.5: Density plots in the laboratory frame as functions of $Q^2$ and $x$. The outer (inner) error bar indicates the total (statistical) uncertainty. The CDM and MEPS models with $\lambda_s = 0.22$ and $\lambda_s = 0.286$ are presented for comparison.

| $R(K_s^0/X)$ | | | | |
|---|---|---|---|---|
| $Q^2$ [GeV$^2$] | $R(K_s^0/X)$ | stat. | syst. | MC Pred |
| 145 – 167 | 0.3801 | 0.02852 | 0.01459 | 0.4001 |
| 167 – 200 | 0.3581 | 0.02210 | 0.01332 | 0.4022 |
| 200 – 280 | 0.3862 | 0.02460 | 0.01421 | 0.4048 |
| 280 – 500 | 0.3943 | 0.02568 | 0.01435 | 0.4045 |
| 500 – 1000 | 0.4102 | 0.04588 | 0.01530 | 0.3947 |
| 1000 – 5000 | 0.4161 | 0.09060 | 0.02455 | 0.3573 |
| $x$ | $R(K_s^0/X)$ | stat. | syst. | MC Pred |
| 0.0 – 0.004 | 0.3943 | 0.02513 | 0.01510 | 0.4340 |
| 0.004 – 0.008 | 0.3816 | 0.01797 | 0.01393 | 0.4108 |
| 0.008 – 0.017 | 0.3936 | 0.02718 | 0.01527 | 0.3894 |
| 0.017 – 0.20 | 0.3352 | 0.03250 | 0.01257 | 0.3577 |

Table 6.5: Values of the differential production cross section ratio of the $K_S^0$ mesons and the deep inelastic scattering events as function of $Q^2$ and $x$ in the laboratory frame. More details in caption of Table 6.2.

## 6.4 Double differential cross section

The double differential cross section of $K_S^0$ as functions of $Q^2$ and $x_p^{CBF}$ normalized to the $\sigma_{vis}$ of the corresponding $Q^2$ range is presented in Figure 6.6 for three different ranges of $Q^2$ and five bins of $x_p^{CBF}$.

In the Figure is possible to see that the $K_S^0$ production grows up as the $Q^2$ range is larger and the increase is more significant at low $x_p^{CBF}$ values, which is the same behavior observed for the fragmentation functions in $e^+e^-$ annihilation and DIS as shown in reference [11].

The Django (CDM) model with $\lambda_s = 0.286$ chosen for the comparison describes quite well the measurements.

## 6.5 Comparison to QCD models

Thanks to the many parameters found in the models, it is possible to do some additional studies, mainly changing the most relevant parameter values for the $K_S^0$
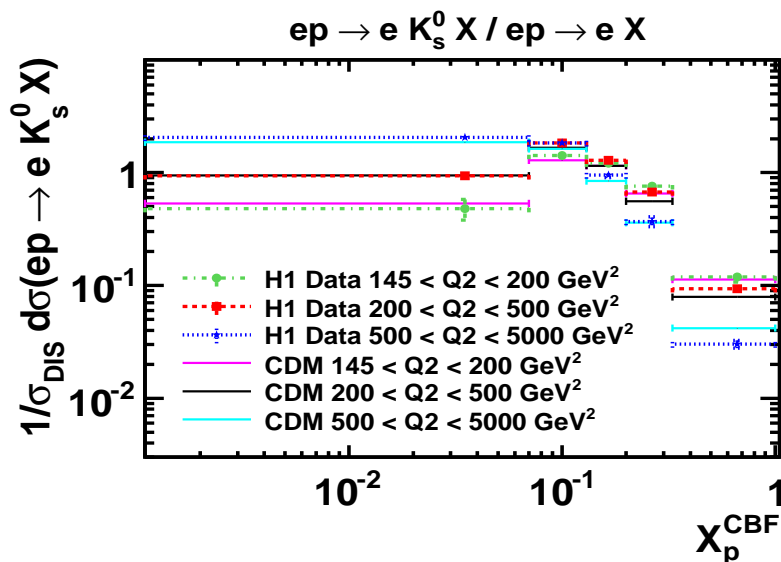
Figure 6.6: Double differential cross section in bins of $x_p^{CBF}$ in three different ranges of $Q^2$. The comparison to Django model shows good agreement.

production and comparing the results of the predictions to data. Previously, two different values of strangeness suppresion factor for Django and Rapgap were presented, now the parton density function PDF is changed in the Django model with $\lambda_s = 0.286$.

The study of disentangling the flavour contribution of the $K_S^0$ production is carried out using the Rapgap model with $\lambda_s = 0.286$.

## 6.5.1  Parton distribution functions

In order to test for possible dependencies of the $K_S^0$ strange meson production on the proton parton density functions (PDFs), the measured $K_S^0$ cross sections are compared to the CDM model with $\lambda_s = 0.286$ using three different PDF parametrizations, CTEQ6L, H12000L0 and GRVL0, as shown in Figure 6.7. The model descriptions are similar in shape for the three PDFs but in normalization only the CTEQ6L and H12000LO PDFs agree with data, while GRVLO98 underestimates considerably the measurements due to the absence of $c$ and $b$ flavour. Then, one could uses GRVLO98

PDF as an estimation of the contribution of $c$ and $b$ quarks to the total $K_S^0$ production to understand or quantify the mechanisms of production from these quarks. Similar results are obtained in the Breit frame.

### 6.5.2 Flavour contribution

The flavour contributions to the $K_S^0$ cross section are investigated using the Rapgap (MEPS) prediction with $\lambda_s = 0.286$. The choice was made because a separation between the QPM, QCDc and BGF production mechanism are possible with this model but not with Django (CDM).

Figures 6.8 and 6.9 show the contribution of the different flavours in the laboratory and the Breit frames, respectively. The light $ud$ quarks contribution from fragmentation mechanism dominates for all variables, then the main contribution process is due to hadronization. The heavy quark contribution of charm $c$ is highest that the one of bottom flavour $b$ which goes to zero or close to zero in some bins; both ($c$ and $b$) make the second dominat contribution coming mainly from the heavy decay process. The $s$ contribution remains to be the lowest in all variables but it becomes more relevant at high values of $Q^2$, $x$ and $p_T$ (see the logarithm scale) while in $\eta$ is almost constant, here the production processes are the boson gluon fusion and the QPM hard interaction.

As functions of the Breit frame variables, the $s$ contribution becomes more important at high $x_p$ and $p_T$ values, specially in the current region where the contribution as function of $x_p^{CBF}$ even equals the heavy quark contribution.

The contributions can be approximately quantified as 52% of the $K_S^0$ coming from $ud$, 36% from $cb$ quarks and only a 12% from $s$ quarks.

## 6.6 Conclusions

The $K_S^0$ meson production in the phase space defined by $145 < Q^2 < 20000$ GeV, $0.2 < y < 0.6$, $-1.5 < \eta(K_S^0) < 1.5$ and $0.3$ GeV $< p_T(K_S^0)$ presented in this thesis cor-
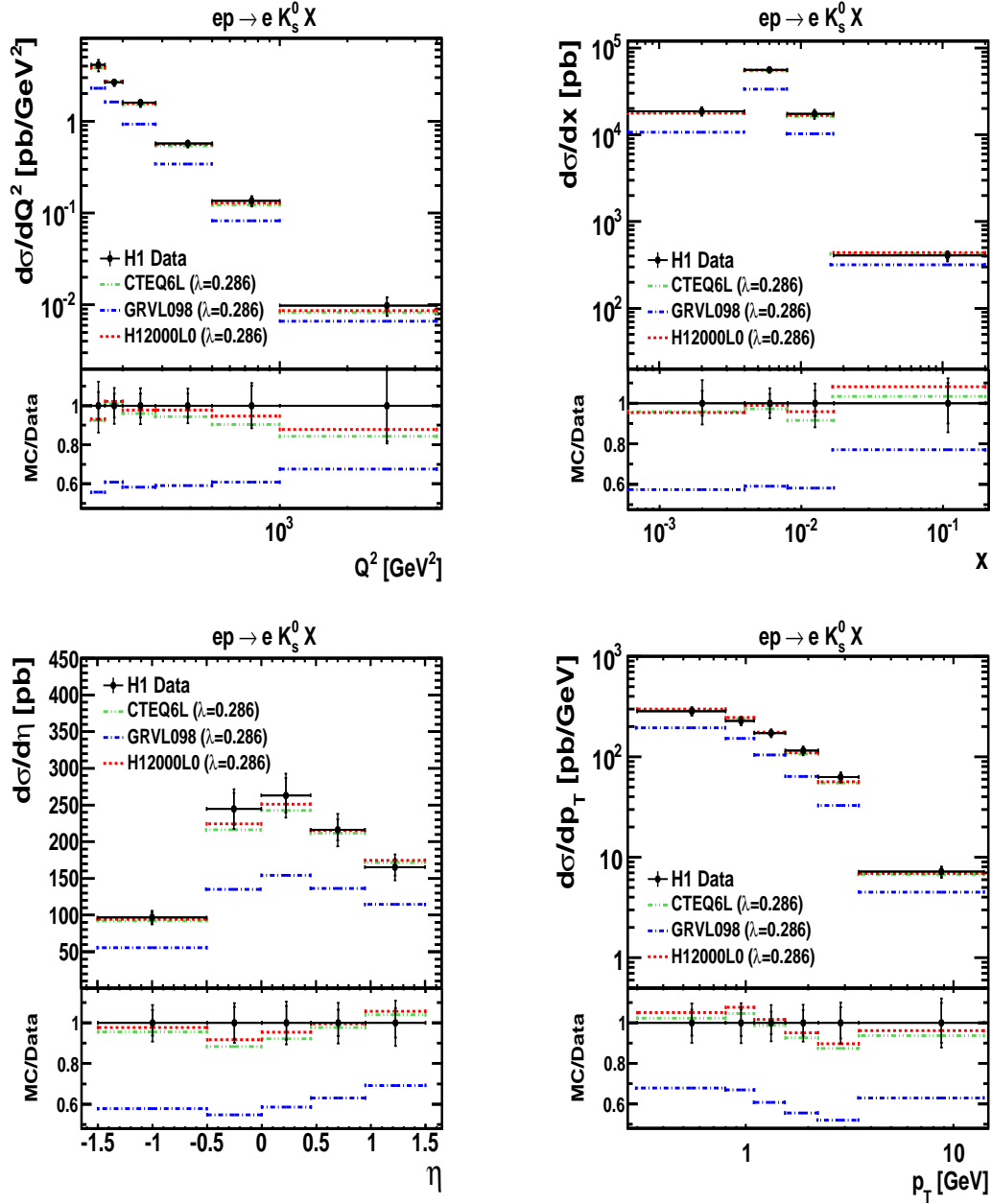
Figure 6.7:   Comparison of cross section to three different PDFs:   CTEQ6L, GRVLO98 and H12000LO in the laboratory frame as functions of $Q^2$, $x$, $\eta$ and $p_T$. No dependence is found between CTEQ6L and H12000LO, the underestimation of GRVLO98 is due to the absence of the charm and beauty quark contribution.
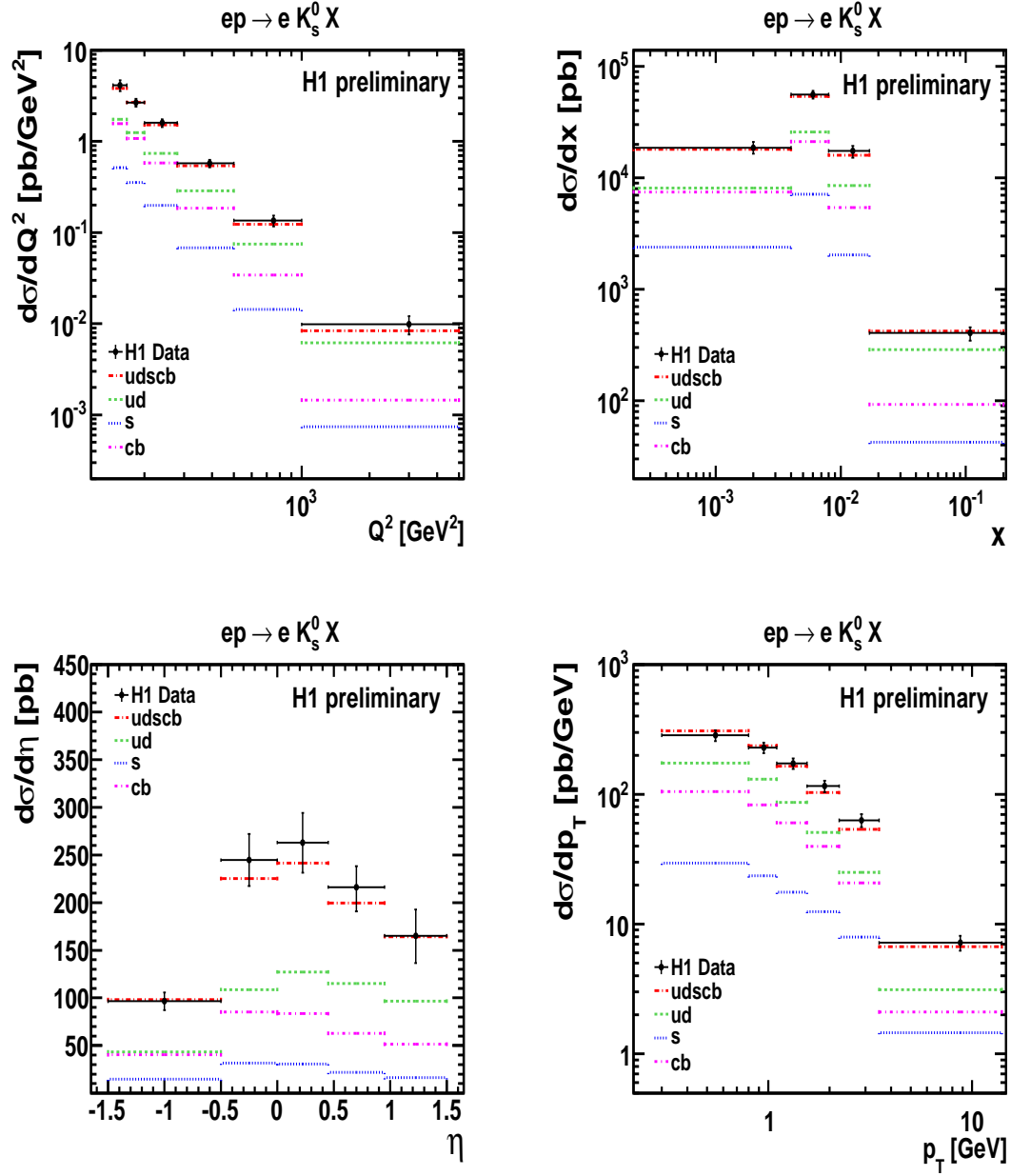
Figure 6.8: Flavour contribution of the light *ud* quarks, the strange *s* quark and the heavy *cb* quarks to the $K_S^0$ cross section studied with the Rapgap model in the laboratory frame as functions of $Q^2$, $x$, $\eta$ and $p_T$. The outer (inner) error bar indicates the total (statistical) uncertainty.
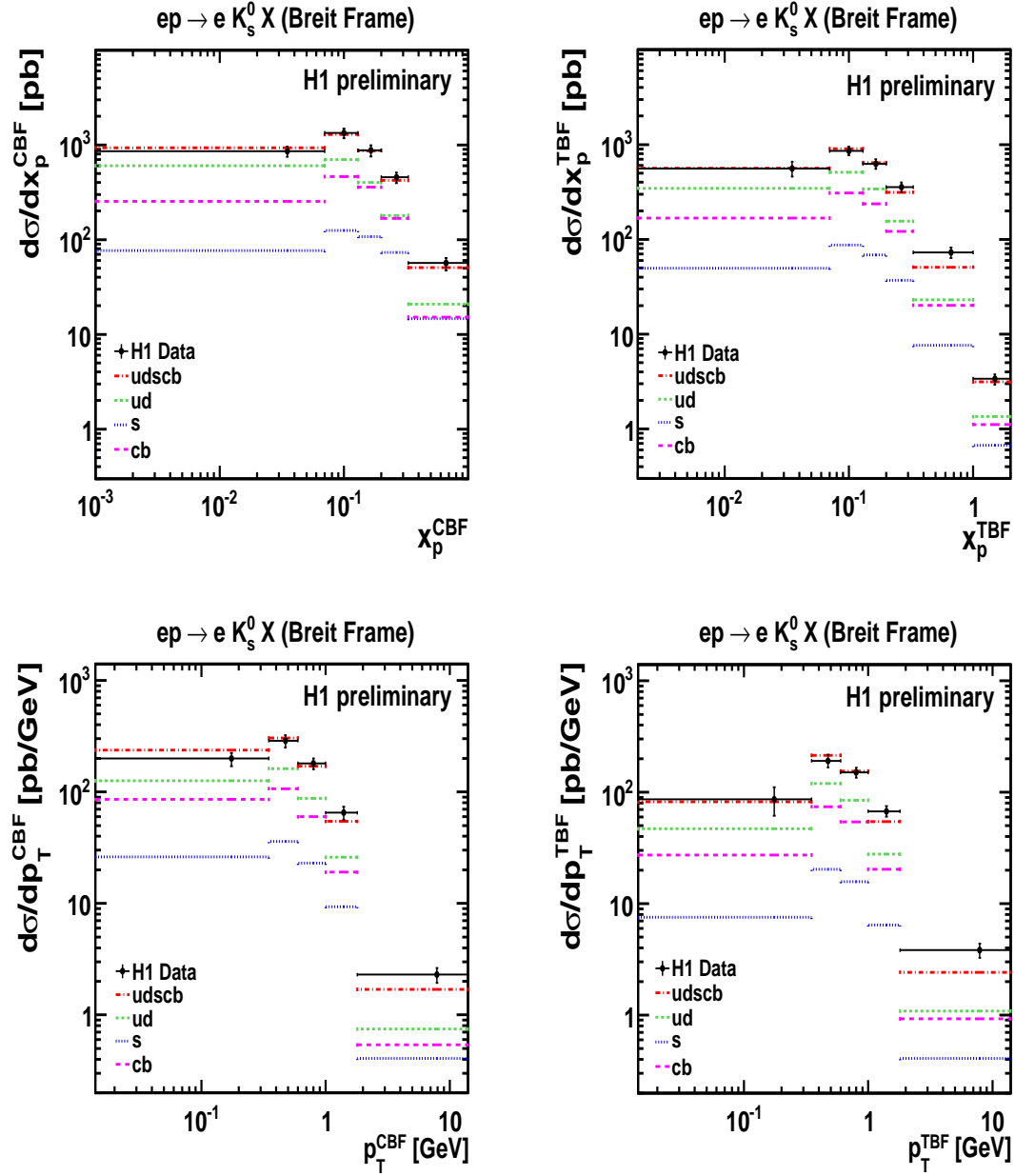
Figure 6.9: Flavour contribution of the light $ud$ quarks, the strange $s$ quark and the heavy $cb$ quarks to the $K_S^0$ cross section studied with Rapgap model in the Breit frame as functions of $x_p^{CBF}$, $x_p^{TBF}$, $p_T^{CBF}$ and $p_T^{TBF}$. The outer (inner) error bar indicates the total (statistical) uncertainty.

responds to the first measurement of the H1 collaboration in the high $Q^2$ range [79]. The production is studied total and differentially in the laboratory and the Breit frames.

The Django and Rapgap DIS events simulation programs are used with matrix elements plus colour dipole model and parton showers, respectively. The CTEQ6L parton distribution function and strangeness suppresion factor $\lambda_s$ with ALEPH tunning are taken for corrections. The comparison of Monte Carlo to data shows good agreement in general features for all variables.
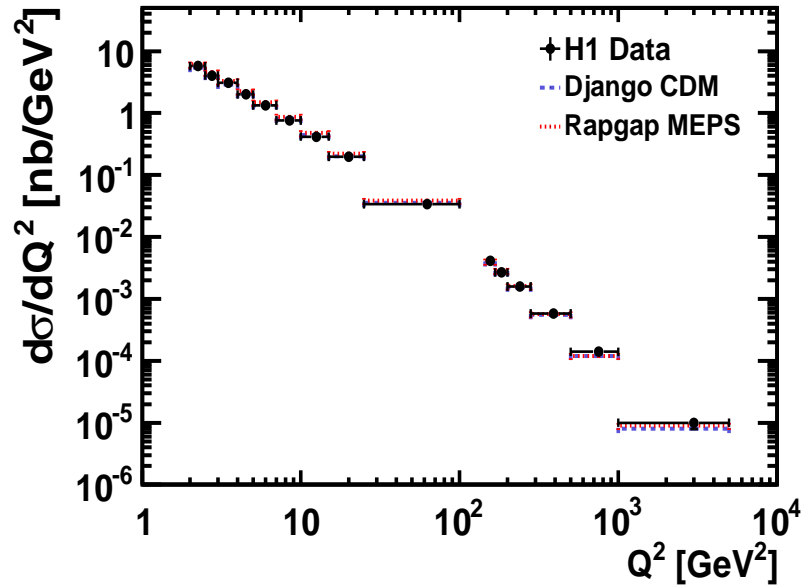


Figure 6.10: Cross section production of $K_S^0$ at low $Q^2$ [66] and high $Q^2$ ranges compared to the Django and Rapgap simulation programs with $\lambda_s = 0.3$ for low $Q^2$ results and $\lambda_s = 0.286$ for high $Q^2$.

The shape of the differential $K_S^0$ production in the laboratory and the Breit frames are similar to those obtained at low $Q^2$ analysis, as discussed in the subsection 2.5.3, although the data in that case were better described with $\lambda_s = 0.3$.

Figure 6.10 presents the results obtained at low $Q^2$ analysis [66] and the ones

measured at high $Q^2$ range as done in this thesis (in the same phase space defined at the low $Q^2$ analysis) and the two Monte Carlo predictions taken into account. It is possible to see agreement between the measurements and theory. The decreasing behavior of the $K_S^0$ production continues from low to high $Q^2$ values due to the $1/Q^4$ factor in the cross section formula.

The ratio of the $K_S^0$ over the charged particle productions and the so called density, the ratio of the $K_S^0$ over the DIS event cross sections, are measured differentially in the laboratory frame. They show almost flat behavior indicating the same rate of production in all regions of the H1 phase space considered here. As function of $p_t$, there is an increase, which is expected due to the higher mass of the $K_S^0$ compared to the charged particles which are mainly pions.

The Django model with $\lambda_s = 0.286$ and CTEQ6L, H12000LO and GRVLO98 parton density functions are used for the study of the PDF dependence, but no evidence of dependence is found between CTEQ6L and H12000LO PDFs. In other hand, the GRVLO98 PDF underestimates the results due to the absence of the charm and beauty quark contributions.

The cross section separated by flavour contributions is studied with the Rapgap model with $\lambda_s = 0.286$ and CTEQ6L PDF. It is found that the $K_S^0$ production is dominated by the hadronization process ($ud$ quarks contribution) but the $s$ quark contribution becomes more important at high momentum values, which is consistent with the conclusion of the $K^*$ analysis, as mentioned in the section 2.5.2.

Further studies will be focus in the production ratio of strange baryons to strange mesons ($\Lambda/K_S^0$) for a better understanding of the di-quarks pair production in the Lund string model. The ratio of the production of vector to pseudoscalar mesons ($K^*/K_s^0$) could provides some information about the relative probabilities for the corresponding spin states which to be produced on the hadronization process. Studies of asymmetric quark sea in the proton can be carried out analysing the difference in the production of charged kaons (as $K^{*+}$ and $K^{*-}$). As well, as the studies of $K_S^0 K_S^0$ states and resonances which have $K_S^0$ particles in their decays channels can be done

to improve the current knowledge of strangeness physics.

# Appendix A

# Reconstruction methods

The methods of reconstruction at HERA physics are governed by the two body elastic collision. The final states can be completely reconstructed using two variables when the energies of the initial particles are known, the energy of the incident electron ($E_e$) and proton ($E_p$) in the case of H1.

The variables of a DIS event can be determined by two of the following independent variables: the energy of the scattered electron ($E'$), its polar angle ($\theta_{e'}$) or some quantities reconstructed out of the hadronic final state particles, as the four-momentum conservation $\Sigma_h = \sum_h (E_h - p_{z,h})$ of each particle ($h$, the total transverse momentum ($p_{T,h}$) or the angle of the scattered quark ($\gamma$) within QPM:

$$\Sigma_h = \sum_h (E_h - p_{z,h}), \qquad p_{T,h} = \sqrt{(\sum_h p_{x,h})^2 + (\sum_h p_{y,h})^2}, \qquad tan\frac{\gamma}{2} = \frac{\Sigma_h}{p_{T,h}}.$$

There are three basic methods of reconstruction, the electron $e$, the hadron $h$ and the double angle (DA) methods. However mixtures of them have been created in order to optimize the calculation of the kinematic variables [80]. A brief description of the most known methods can be found in the next sections.

## A.1   The electron method

As its name indicates, this method uses only the information of the electron, $E_e$, $E'_e$ and $\theta_e$ measured by the electromagnetic section of the calorimeters, to calculate

the kinematic variables, the four-momentum transfer $Q^2$, the inelasticity $y$ and the Bjorken-$x$:

$$Q^2 = 4E_e E'^e cos^2\frac{\theta_e}{2}, \quad y_e = 1 - \frac{E_e}{2E'_e}(1 - cos^2\frac{\theta_e}{2}), \quad x_e = \frac{Q_e^2}{sy_e}.$$

At high $y$, where the electron is very well detected by the CTD and the SpaCal, this method provides a high precision, but at low $y$ it is not due to the $1/y$ dependence of the resolution $(\delta y/y)$. In the case of initial state radiation (ISR) the energy of the electron is reduced from $E_e$, thus $Q^2$ and $y$ are overestimated, while $x$ suffers a degradation.

## A.2   The hadron method

This method, also called Jacquet-Blondel method, makes use of $\Sigma_h$ and $p_{T,h}$ for the reconstruction. For this reason, it is mainly used for charged current DIS events, because the scattered neutrino is undetected and the kinematic variables determination lies on the hadronic final states measured by the calorimeters:

$$Q_h^2 = \frac{p_{T,h}^2}{1 - y_h}, \quad y_h = \frac{\Sigma_h}{2E_e}, \quad x_h = \frac{Q_h^2}{sy_h}.$$

The angle $\gamma$ of the hadronic final states is determined as:

$$cos\gamma = \frac{Q_h^2(1 - y_h) - 4E_e^2 y_h^2}{Q_h^2(1 - y_h) + 4E_e^2 y_h^2}.$$

## A.3   The double angle method

The DA method reconstruct the kinematic variables using only the $\theta_e$ and $\gamma$ angles. If the energy measured is considered as continuous over the full solid angle, the event kinematics are independent of any calorimetric energy scale uncertainties:

$$Q_{DA}^2 = \frac{4E_e^2 sen\gamma(1 + cos\theta_e)}{sen\gamma + sen\theta_e - sen(\theta_e + \gamma)}, \tag{A.1}$$

$$y_{DA} = \frac{sen\theta_e(1 - cos\gamma)}{sen\gamma + sen\theta_e - sen(\theta_e + \gamma)},$$

$$x_{DA} = \frac{Q_{DA}^2}{sy_{DA}}.$$

## A.4   The sigma method

The sigma method, $\Sigma$, compensates for the cases where missing energy exits due to ISR. The photon is usually undetected because travels in the same electron beam direction and escapes out of the beam pipe. What it does is to balance the missed energy by a factor calculated by conservation of longitudinal momentum of the hadronic and the detected electron energies. Then, $y$ and $Q_\Sigma^2$ are independent of ISR-QED and the resolution is optimal. The kinematics is formulated like:

$$Q_\Sigma^2 = \frac{P_{T,e}^2}{1 - y_\Sigma}, \quad y_\Sigma = \frac{\Sigma_h}{\Sigma}, \quad x_\Sigma = \frac{Q_\Sigma^2}{sy_\Sigma}$$

Another good point is that the experimental errors on $\Sigma_h$ measurements cancel between numerator and denominator at high $y$, where $\Sigma_h$ becomes dominant.

## A.5   The electron-sigma method

The e$\Sigma$ method [81] improves the imprecise reconstruction of $Q_\Sigma^2$ and $x_e$ using $Q_e^2$ and $x_\Sigma$, respectively. In that way, the precision at high $y$ is also improved. Then:

$$Q_{e\Sigma}^2 = Q_e^2, \quad y_{e\Sigma} = \frac{Q_\Sigma^2}{sx_\Sigma}, \quad x_{e\Sigma} = x_\Sigma.$$

For high $Q^2$ the better methods to chose are the $e$, the DA, and the $e\Sigma$. The DA method has good purity in the full range of $x$ and $Q^2$ but is in general less precise that the other two, which behave similar at high $Q^2$ and at high and low $x$. Reference [81] remarks the weakness of the $e$ method at low $y$; however the lower limit of $y$ in this analysis is not so low and the inclusive cross section calculated with $e$ and $e\Sigma$ gives the same value, within the systematic errors. The total systematic error for the $e\Sigma$ method has a contribution from the determination of the hadronic energy and is of the same size as the systematic error from the $e$ method. This method has been chosen for the reconstruction of event kinematics in this work.

# Appendix B

# Multiwire proportional and drift chambers

The **multiwire proportional chambers** (MWPC) were developed by Charpak and his collaborators at CERN in 1968. It is a particle detector consisting essentially of a container of gas subjected to an electric field whose operating principle is based in the collection of electrons and ions left by an incident particle when passing through the chamber.

A particle passing by a gaseous medium losses energy by elastic scattering, by excitation and by ionization of the gas atoms. The energy loss of the incident particle in elastic scattering is generally so small that it does not play a significant role in the operation of the detector. The excitation process raises the gas atoms or molecules to an excited energy level which deexcite by photon emission, but the most important process for the operation is the ionization. This occurs when the energy imparted to the atoms in the medium exceeds its ionization potential and they liberate one or more electrons leaving positive ions.

The primary ionization is defined to be the number of ionizing collisions per unit length suffered by the incident particle. Some of the liberated electrons may still have sufficient energy to cause more ionization what is called secondary ionization. The MWPC's use an electric field in the active region so the charged ionization products have a net motion in the direction of the field.
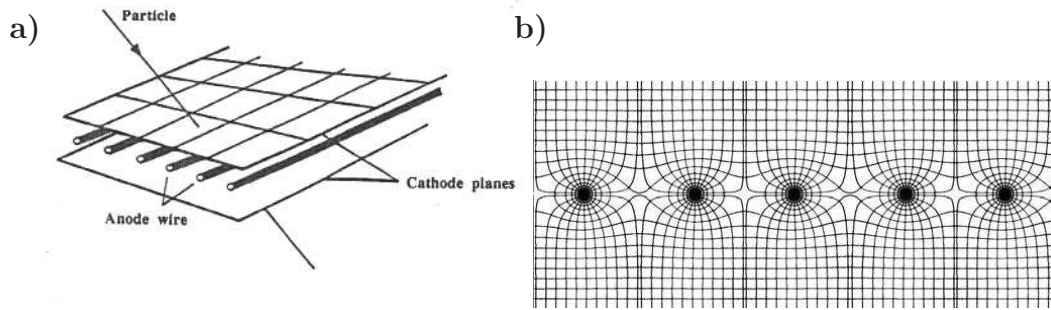
Figure B.1: a) Typical desing construction and b) electric field configuration of a multiwire proportional chamber.

A typical geometry of a MWPC can be seen in Figure B.1a), where a plane of anodes wires is lying between two cathodes planes. A positive voltage is connected to the sensing wires while the cathode wires are set to a negative voltage in order to create an electric field configuration as shown in Figure B.1b). An important point to take care during the construction is that the wire spacing be very uniform throughout all the detector because a small displacement of a wire or any irregularity in their diameters can lead to a large change in the charge provided by the displaced wire and on adjacent wires.

Due to the voltage applied to the wires, electrostatic forces are present. These forces can cause a net attraction of the cathode toward the anode plane producing a curvature in the center varying the gap separation and therefore the gain. Another effect is the displacement of the wires from the nominal positions if the electrostatic force on the wires is greater than the tension of the wire.

The filling gas should satisfy the desirable properties, mainly low working voltage, high gain, good proportionality, high rate capability, long lifetime, high specific ionization, fast recovery and avoid recombination that can damage or contaminate the chamber electrodes. Usually mixtures of gases are needed to optimize the desirable features as possible.

When a charged particle passes through the chambers, a primary ionization is

produced, the electrons liberated will travel with a known velocity towards the anode wires inducing secondary collisions or avalanche, which occurs within a few wire diameters of the anode because of the $1/r$ electric field dependence. Therefore, the amount of multiplication is a strong function of the wire diameter. On the other hand, the wire diameter must not be too small or else it would be incapable of maintaining the tension necessary to resist the electrostatic forces acting on it.

This avalanche is collected at the chamber electrodes and induces a convenient current signal along the wires to the external circuit. The output pulse is proportional to the number of primary ion pairs hence the name of the chamber.

Analysing the detected signal it is possible to reconstruct the trajectory of the particle using the distribution of sense wires hits and the charge distribution.

Although MWPC have no energy resolution, they are almost 100% efficient for the detection of single, minimum ionizing particles (MIP), allow a large improvement in spatial resolution and they also have a good response to many simultaneous tracks due to the fact that each anode wire is essentially an independent detector.

The **drift chambers** appear shortly after the MWPC's. The aspect exploited by these new chambers is the spatial information obtained by measuring the drift time of the electrons coming from an ionizing event. For this purpose, a constant drift velocity is necessary to have a linear relationship between time and distance.

The design is basically the same structure used for a MWPC but in order to get electric field uniformity, field wires are intercalated between anodes. So, the anode plane is such that adjacent sense wires are separated by two potential wires. The field wires are held at a slightly higher potential than the cathode. This configuration shapes and adjusts the drift field but also does that the chamber volume forms a Faraday cage screening against external electromagnetic noise.

They are generally easier to operate compared to MWPC's but much more attention must be given to the field uniformity and is of utmost importance the correct choice of the fill gas since a precise knowledge of the drift velocity is necessary.

The advantages of the design (besides the already mentioned for the MWPC's)

are its shorter deadtime and better resolving time, so a drift chamber can be also used as trigger detector.

Now the trajectory of the particle can be reconstructed using besides the distribution of sense wire hits and the charge distribution, the drift times to the sense wires. The spatial and time resolutions depend on the anode wire spacing[1], and the uncertainty in the arrival time of a pulse at the logic electronics after the passage of an ionizing particle.

In several experiments, the location of the MWPCs or drift chambers is in or near the field of a magnet. In such cases, the path of the drifting electrons and the drift velocity will be altered by the Lorentz force. So, it is necessary a precise knowledge of the magnetic field in order to correlate the drift time with position. It may also be possible to adjust the electric field direction so as to compensate the effects of the magnetic field.

---

[1]It is typically one-half the wire spacing value.

# Appendix C

# $Q$ and $t$ measurement

All the wires of the CJC, CIZ, and CIP2k (and COP when it was in operation) are individually read at both ends separately (or combined), the information is used for the $z$ determination with the help of the signal parameters, the signal time $t$ and the pulse integral $Q$.

The analog signal pulse passes through an amplifier connected to the signal wires, then the amplified signal is carried to the H1 electronic trailer by a coaxial cable 28 m long. There, the signal is digitized by F1001-FADCs[1] synchronized to HERA frequency (104MHz), which means that every 10 ns a digitizations occurs. The FADC system signals are continuously digitized and stored in the memories. Sixteen FADC-channels are housed on one F1001-card and up to 16 F1001 cads are housed in a F1000 crate. In each F1000 front end crate there is a scanner card acting as a sample controller for the FADCs. Its function is the copy of data from the FADCs, during this action, the data is compared with programmable thresholds and any significant transition is recorded in a hit table. The signal pulses gotten in this way are analysed for the charge and arriving time determination, analysis $(Q, t)$, during the L4 level of the trigger.

The electrons created by primary ionization in places with approx. the same drift time arrive all to the signal wire more and less at the same time (the isochrones).

---

[1]Fast Analog to Digital Converter.
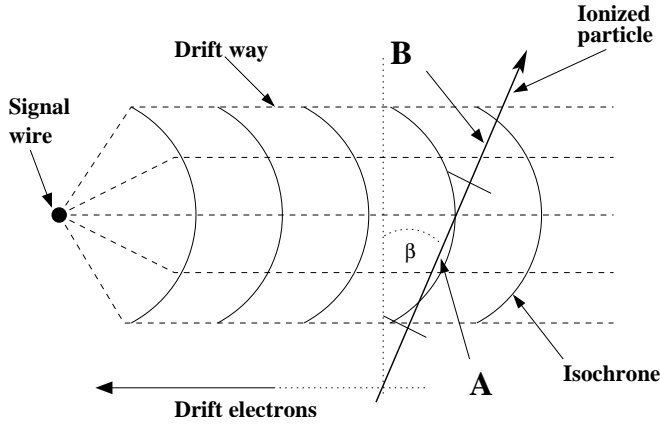
Figure C.1: Isochrones model.

Figure C.1 illustrates it, marked with 'A'. The electrons liberated in 'B' arrive to the wire at a different time.

If a charged particles goes through perpendicularly to the drift direction, the contribution of an isochrone tangent due to the electrons produced by the primary ionization is maximum. While the $\beta$ angle (angle between the perpendicular direction to the drift direction and a trajectory) is larger, less can be depart from a tangential approximation to an isochrone.

Figure C.2 shows a typical signal pulse after the digitization. The essential information for the drift determination comes from those electrons produced in 'A' which contribute to the sharp rise of the pulse, while the ones produced in 'B' arrive later and belong to the smeared out edge of the pulse. A larger contribution of electrons from 'B' mean a flatter pulse.

The $(Q, t)$ analysis consists of several steps. First the FADC data are first linearised, then the pedestal for the signal pulses in the hit memory (threshold) is determined by the average of the 6 bins before the rise of the signal. The next step is to put in order both pulses from $-z$ and $+z$ originated by the same primary electrons. If there are two pulses in the same wire close to each other such that they overlap a standard pulse shape is adjusted to each signal pulses and a substraction of the pulses is made in both wire ends, improving in this way the resolution of two
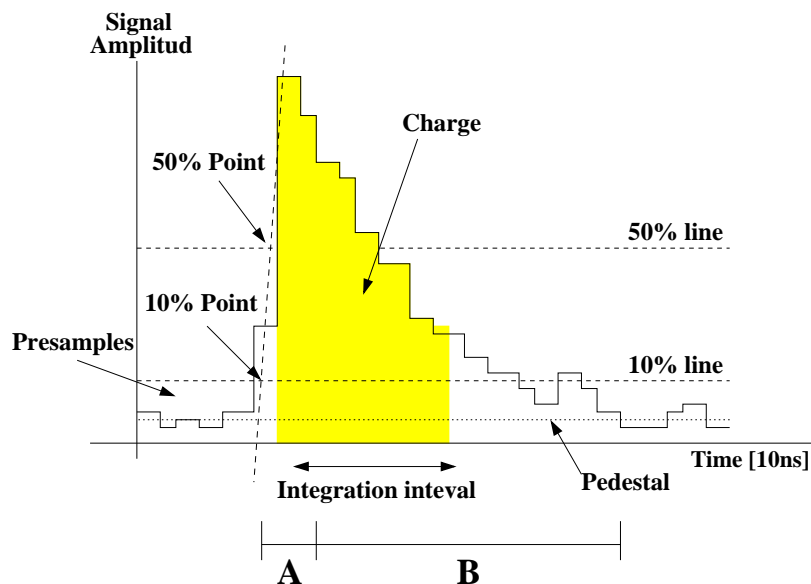
Figure C.2: Example of a pulse signal.

hits.

The method for the arriving time determination is called leading edge algorithm. For both ends, the 50% point of the signal $t_{50\%}$ is determined independenly by a linear interpolation, which corresponds to the half of the maximum value of the signal $s_{max}$. In the same way, it is determined the maximum slope between two digitalizations in the rise signal region. The line defined is used for the $t_{10\%}$ determination in which a pulse signal of 10% of the maximum amplitud (determined by $t_{50\%}$ and $s_{max}$) is reached. The time $t_{10\%}$ is interpreted as the arriving time of the signal.

The determination of the charges $Q_{z+}$ and $Q_{z-}$ is gotten by the integration of the signal pulse. The optimal integral interval must be chosen not too short or an error in the charge determination will be made, but not too large since the small statistic induces variations in the pulse fall. The chosen mode consists in an interval of 80 FACD digitizations (80 ns) departing from the $t_{50\%}$.

At the end of the readout, the arriving time $t_A$ and the charge $Q$ of both wire ends for each hit is determined. The values are stored in a data bank to be used for the reconstruction of the tracks.

# Appendix D

# Track reconstruction

A charged particle passing through the central tracking detector will describe a helix trajectory due to the effect of the magnetic field acting over it[1]. For tracks reconstruction, a projection in the $r\phi$ (or $xy$) plane is done to get some parameters, which are then combined with the $z$ dimension to have the three-dimensional reconstructed trajectory of the particle.

In the $r\phi$ plane, the track projection is described as function of the curvature $\kappa = 1/R$, defined as positive (negative) if the direction of $\phi$ is clockwise (anticlockwise); the closest distance to the origin of the $r\phi$ plane, closest distance of approach or $dca$, with positive sign if the vector going from the origin to the $dca$ point together with the trajectory direction form a right-handed system; and the angle between the $x$ axis and the transverse momentum vector in the $dca$ point, the so called azimuthal angle $\phi_0$. The transverse momentum vector in the $dca$ point is seen in the $sz$ plane as a straight line starting at a $z_0$ position and forming an angle $\theta$ with respect to the $z$ axis, see Figure D.1.

The helix parameters $dca$ and $z_0$ are defined with respect to nominal position, the origin $(0, 0, 0)$, but a more appropriate definition would be at the real vertex of the event (the primary), however this is different for each event.

The $\kappa$, $dca$ and $\phi$ parameters are obtained by fitting the data hits to a circle using

---

[1]The Lorentz force $\vec{F} = q(\vec{E} + \vec{v}x\vec{B})$.
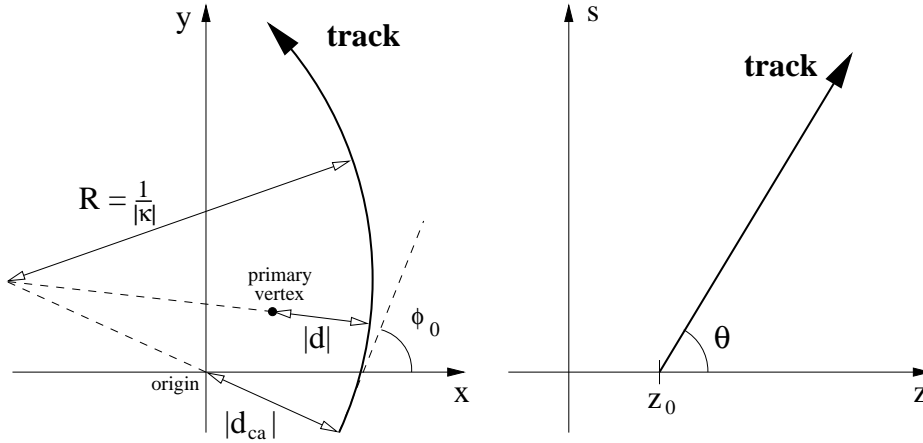
Figure D.1: Picture of the track reconstruction with the parameter definition to characterize them.

the non-iterative algorithm of Karimäki [82], the equation is in polar coordinates:

$$\frac{1}{2}\kappa \ (r^2 + dca^2) + (1 + \kappa \ dca) \ r \ sen(\phi - \varphi) - dca = 0,$$

while $\theta$ and $z_0$ are determined by a linear least-squares fit:

$$z_i = z_0 + S_i^{r\phi}(dz/dS),$$

where $S_i^{r\phi}$ is the track length for the point $z_i$ in the $r\phi$ projection, when $S^{r\phi} = 0$ at $dca$, and the slope $dz/dS$ is converted to $\theta$ by $\theta = arc \ tan(1/(dz/dS))$.

The reconstruction of tracks is done by a software with a fast version at fourth trigger level L4, which is efficient for tracks originating from the primary vertex with momentum greater than 100 MeV/c, and by a standard track finding version more complete and efficient for all kind of tracks but 10 times slower than the first one.

The *fast reconstruction*, used for background rejection and fast classification of events, consists of the determination of the bunch crossing time $T_0$ of the events and the calculation of the drift time of each hit, the search for tracks elements defined by three hits (triplets) and, from the triplets, assignation of individual trajectories to get the track parameters.

The $T_0$ of the event can be gotten from a drift time histogram, as mentioned in appendix C. The drift time of each hit $t_{A,i}$, stored in a data bank, can be transduced

in position information by $s_i = v_{drift}(t_{A,i} - T_0)$ where $s_i$ represents the distance between the trajectory and the signal wire $i$, this is the drift distance of the electrons from the primary ionization, and $v_{drift}$ being the drift velocity considered as constant. It is also important to consider the beginning time of each wire $t_{0,i}$, the drift direction known by the electric field and the Lorentz angle $\alpha_{Lor}$. The values obtained provide the new calibration constants which are stored in the H1 database.

The search of track elements start by taking three wires with a distance of two wires $(n-2, n, n+2)$ and trying all pairs of hits. Defining $i, k$ as the hit index, the drift distances $\bar{d}^n$ are calculated by $(d_i^{n-2} + d_k^{n+2})/2$ and $|d_i^{n-2} - d_k^{n+2}|/2$, if there are small differences when it is compared to the measured value $d_j^n$ (small $|d_j^n - \bar{d}^n|$) then, the index of the hits at the triplet wires are stored as a possible track element together with their $\kappa$ and $\phi$ values calculated assuming $dca \equiv 0$. After trying all different three wire combinations, there is a cluster of hit triplets with their own $\kappa$ and $\phi$ values; from their coordinates a iterative process is made to fit a circle but now allowing $dca \neq 0$ to get a specific track candidate. Those with large $|dca|$ and $\kappa$ are rejected.

The *standard phase* of track reconstruction also searches for track elements by triplets but now on adjacent wires, so at the end chains of hits are extracted, which are eventually split into two shorter chains if they are long. The accepted chains are stored as track elements with parameters from the fit. When the track element is short, it is merged with the previous ones within the same cells, then with the neighbouring, within one ring and lastly from both CJC1 and CJC2.

The algorithm of merging start comparing pairs of track elements with similar helix parameters. If the distance between them suggests that they could belong to the same track, a $\chi^2$ fit is performed (in the $r\phi$ plane). In case that one element of a pair has been used in the construction of a new element, the fit to the modified element(s) is repeated and rejected eventually. In this way, wrong combinations of short track elements are avoided with high probability.

Finally the drift length is calculated for all possible wires and for all track elements

ordered by their length and compared to the measurement to reject incompatible hits and the fits are repeated but now using the acceptable hits, so the track finding efficiency is improved.

The energy loss $dE/dx$ for a given track is determined from the mean of single-hit values $1/\sqrt{k_i} = 1/\sqrt{(dE/dx)_i}$, excluding hits which are close to another track.

# Appendix E

# Breit frame of reference

The DIS kinematic is mainly described by $Q^2$, $x$, $y$ and $W^2$ in the laboratory frame (subsection 1.1.1), but there is another frame also commonly used to study the dynamics of the hadronic final state in DIS, the Breit Frame [83] (BF). This frame is special because makes things easier for comparison to results of $e^+e^-$ colliders, allowing the test of the universality concept of fragmentation in different processes.

The $ep$ BF is reached when the laboratory frame is Lorentz boosted to the hadronic center of mass frame, followed by a longitudinal boost along a common $z$ direction such that the incident virtual photon is *space-like* (has zero energy, zero transverse momentum and a $z$ component of momentum $-Q$). The $z$ direction is chosen to be, as in laboratory frame, positive in the direction of the incoming proton.

The Figure E.1 presents a illustration of the boost. The advantage of the BF is the maximal separation of the incoming and outgoing partons in the QPM, the two regions assigned according to the sign of the momentum in the $z$ axis of the BF, $p_z$. The *current hemisphere* if $p_z < 0$ and the *target hemisphere* if $p_z > 0$.

The current region is dominated by the fragments of the struck quark alone which makes it analogous to the single hemisphere of $e^+e^- \rightarrow q\bar{q}$ annihilation. The proton remnants go entirely into the target hemisphere. The incoming quark have four-momentum $(Q/2,0,0,Q/2)$, after the scattering the four-momentum is $(Q/2,0,0,-Q/2)$, so the maximum momentum a particle can have in current region
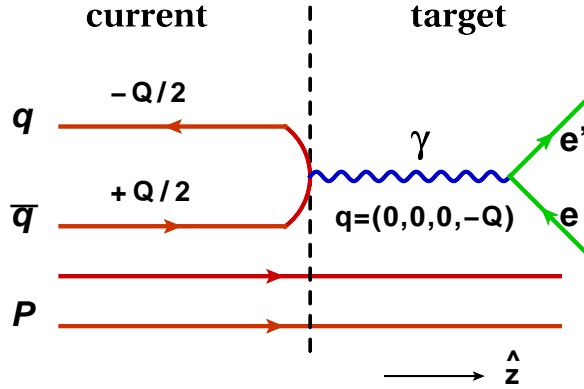
Figure E.1:  Breit frame scheme with the separation in current and target hemi-spheres.

is $Q/2$ while the target region with much higher momentum can reach a maximum of $Q(1-x)/2x$. The two regions are then asymmetric, particularly at low x, where the target region occupies most of the available phase space. The central detector in H1 provides excellent acceptance for the current region studies.

In $e^+e^-$ annihilation, the two quarks are produced with equal and opposite momenta ($\pm\sqrt{s_{ee}/2}$) and the scaled hadron momentum is $x_p = 2p_{hadron}/E^*$, with $E^*$ being its center of mass energy. The fragmentation of the quarks in $e^+e^-$ interactions can be compared to that in the current region where the scaled momentum spectra of the particles is then expressed in terms of $x_p = 2p_{hadrons}/Q$ (considering only hadrons in the current hemisphere), the $Q$ dependence is similar to that in $e^+e^-$ at energy $\sqrt{s_{ee}} = Q$ and, as can be easily seen, $E^*$ is equivalent to $Q$.

The BF also enables the study of low $p_T$ tracks[1] since low momenta tracks in the laboratory frame can occasionally be boosted to higher momenta in the BF. In these frames the $p_T$ arising from the electroweak recoil of the hadronic system against the scattered lepton is removed, facilitating the observation of QCD effects.

The consideration of higher order processes can, however, affect the QPM in BF, for instance the BGF and initial state QCDc contribute to the $ep$ cross section but

---

[1]In the laboratory frame of reference, low $p_T$ tracks have poor acceptance and are removed below 150 MeV/c to improve the simulation efficiency.

they are not present (and have no analogue) in $e^+e^-$ annihilation. These processes, together with final state QCDc (which does occur in hadronic $e^+e^-$ collisions) can de-populate the BF current region, even leading to a current hemisphere which is empty, for further explanation go to reference [84]. Empty current hemisphere events are included in this analysis for normalisation purposes.

# Appendix F

# Fits to mass distributions
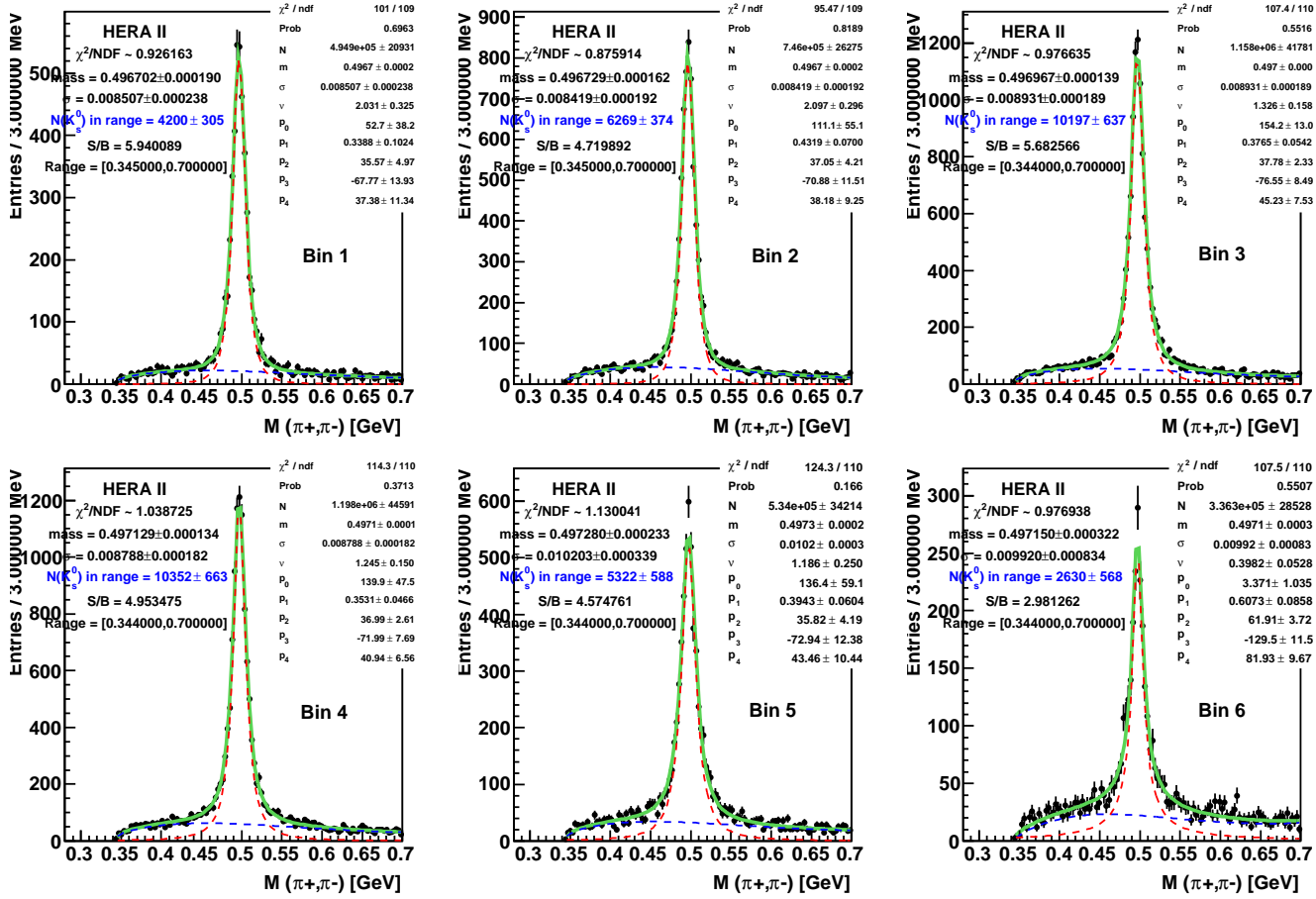
Figure F.1: Fits to the invariant mass distribution from data in bins of $Q^2$.

Figure F.2: Fits to the invariant mass distribution from data in bins of $x$.
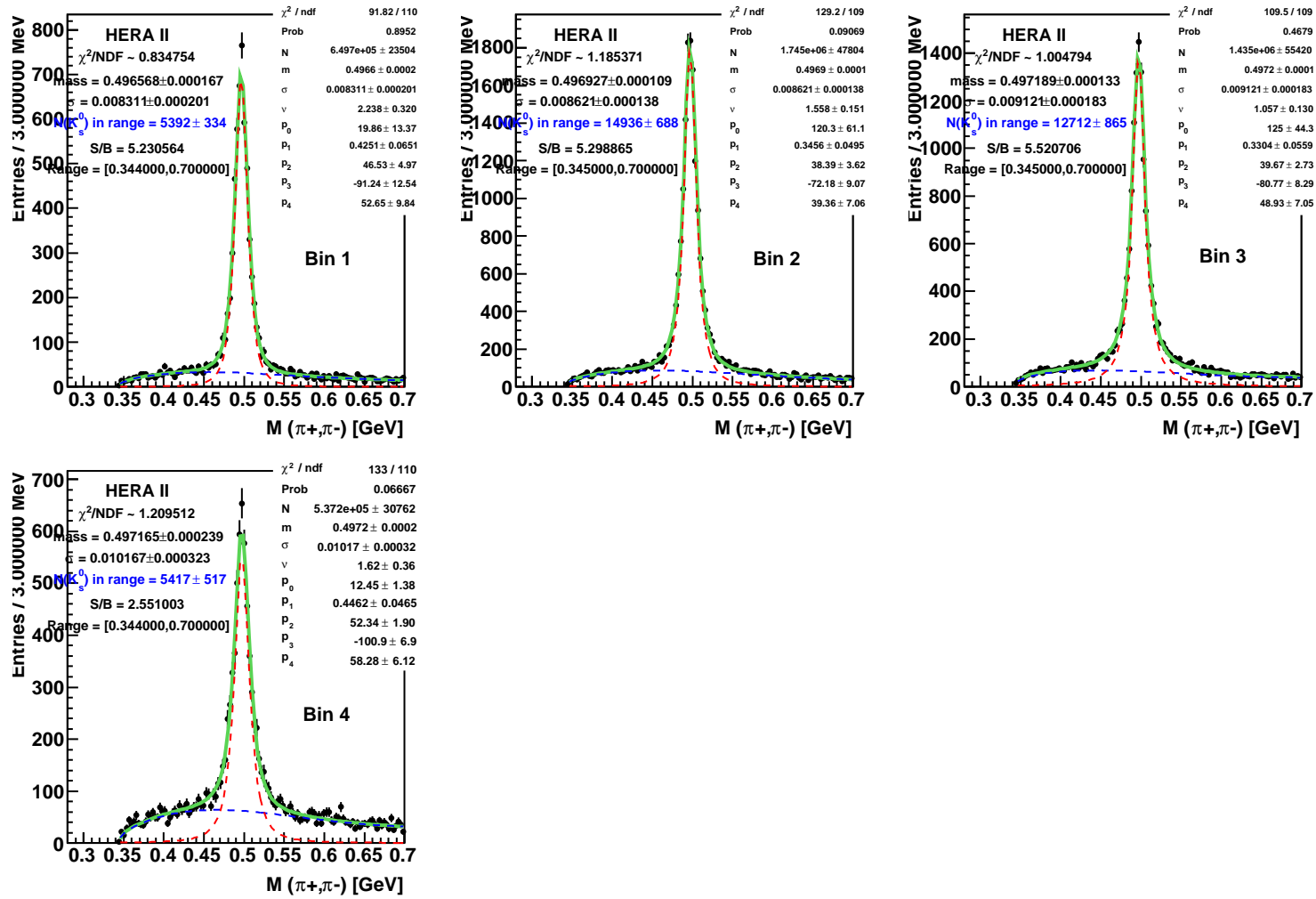
Figure F.3: Fits to the invariant mass distribution from data in bins of $\eta$.
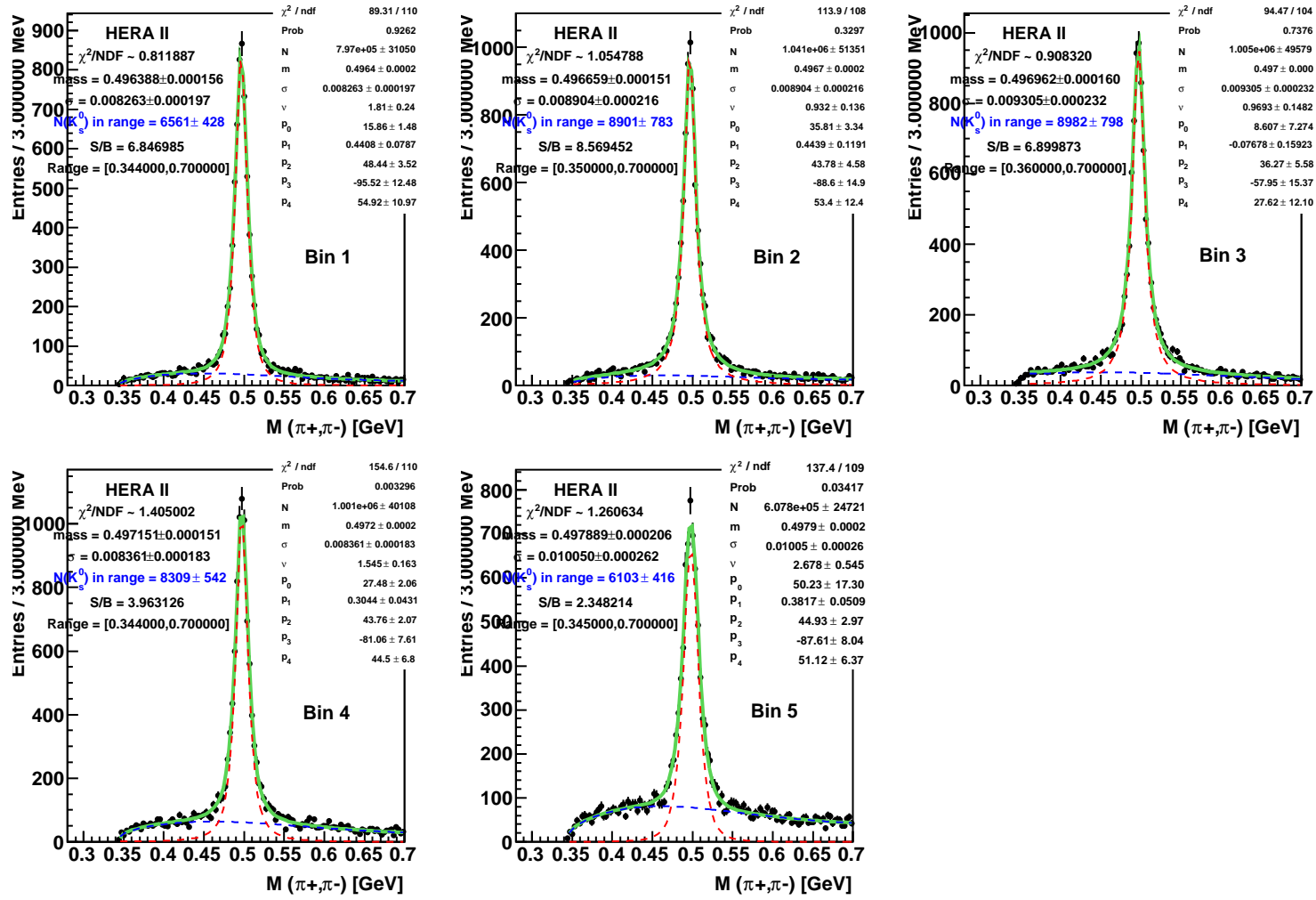
Figure F.4: Fits to the invariant mass distribution from data in bins of $p_T$.
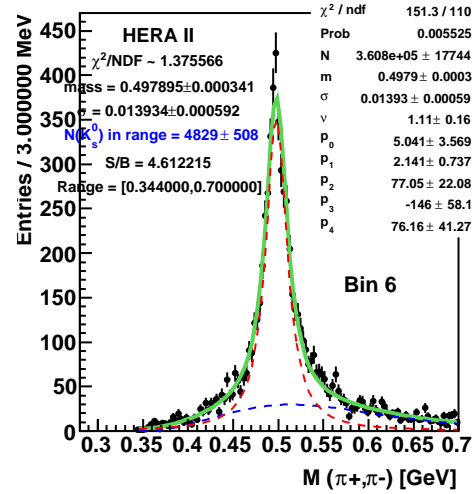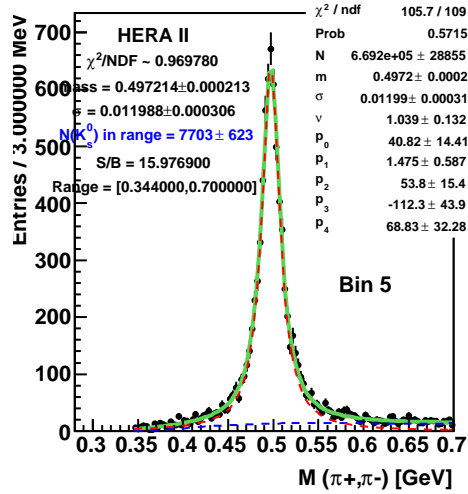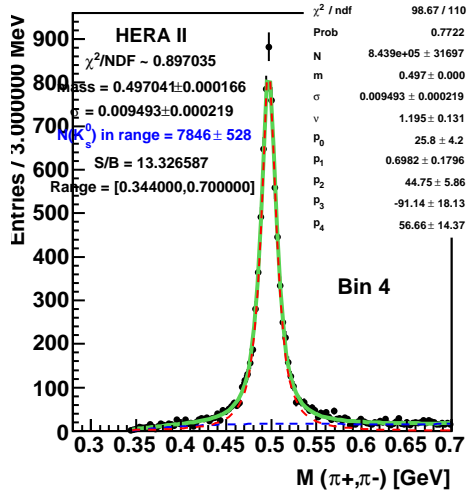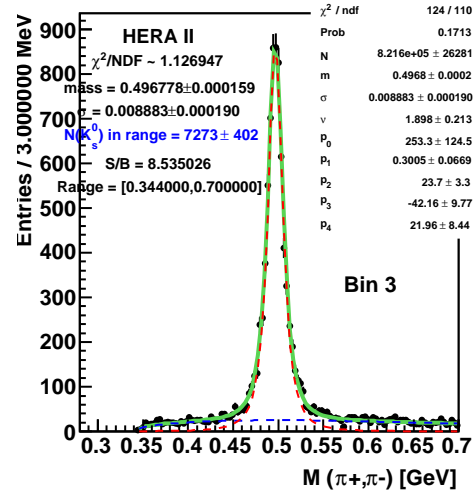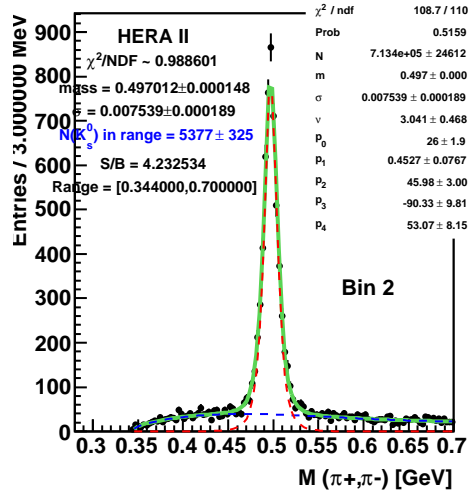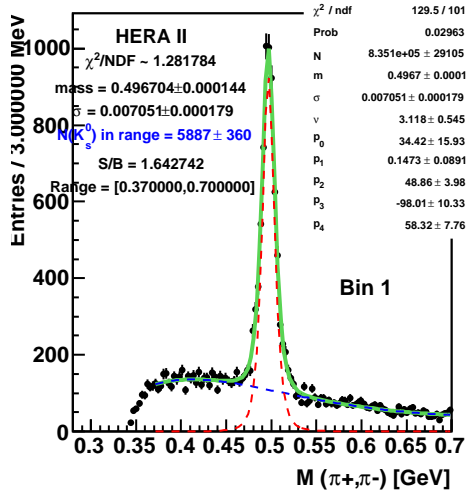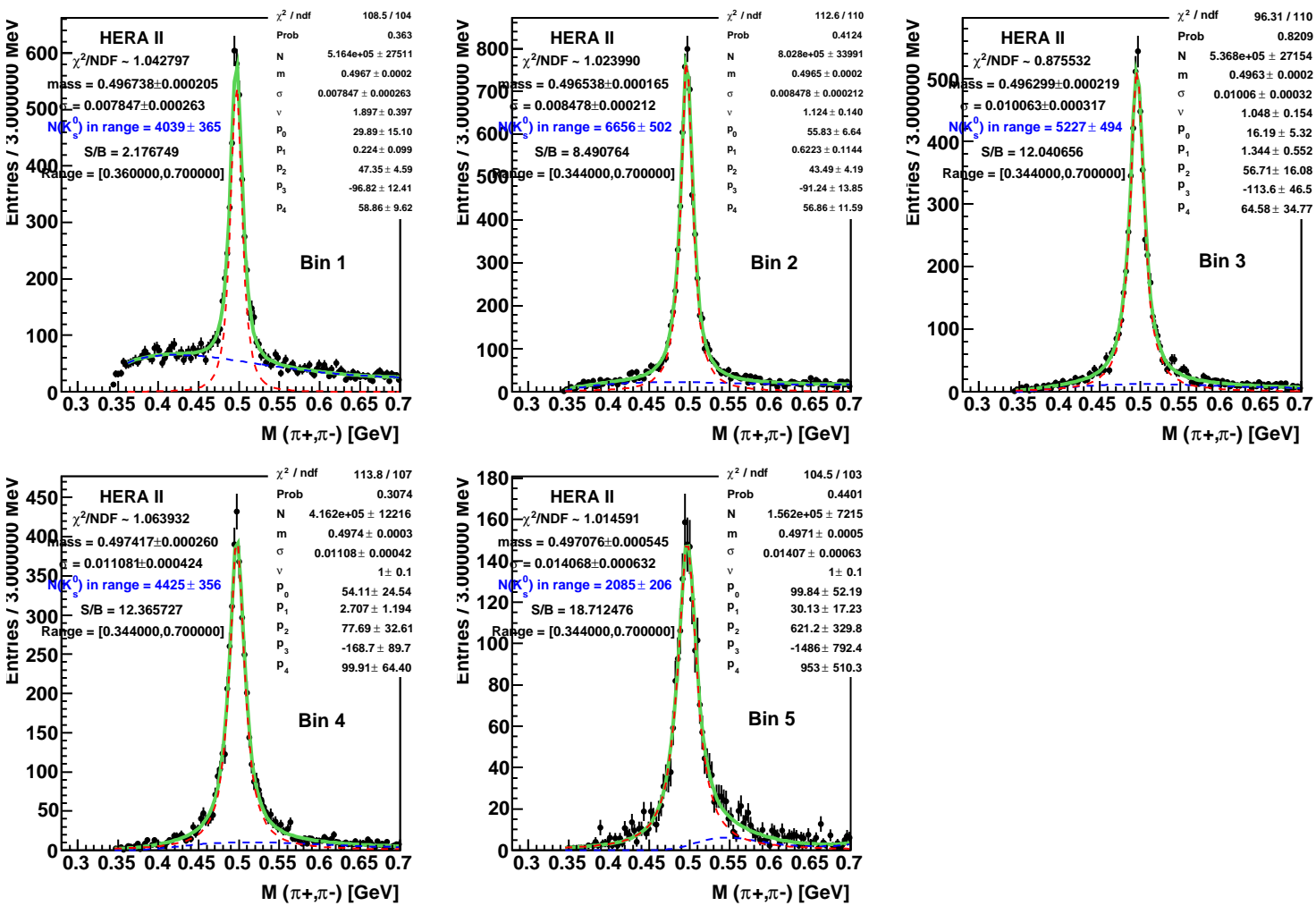
Figure F.5: Fits to the invariant mass distribution from data in bins of $x_p^{CBF}$ for the current hemisphere in the Breit Frame.

Figure F.6: Fits to the invariant mass distribution from data in bins of $x_p^{TBF}$ for the target hemisphere in the Breit Frame.
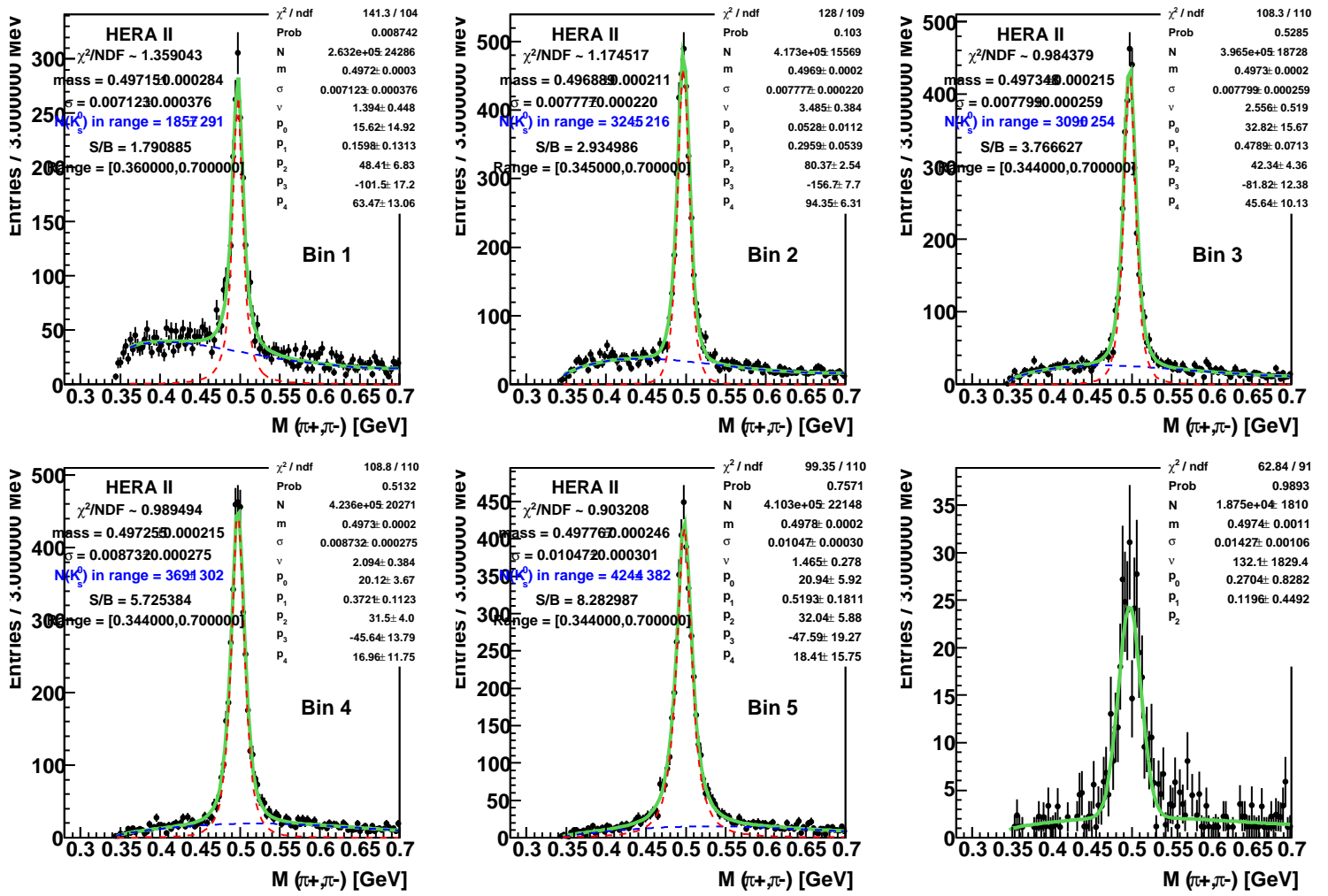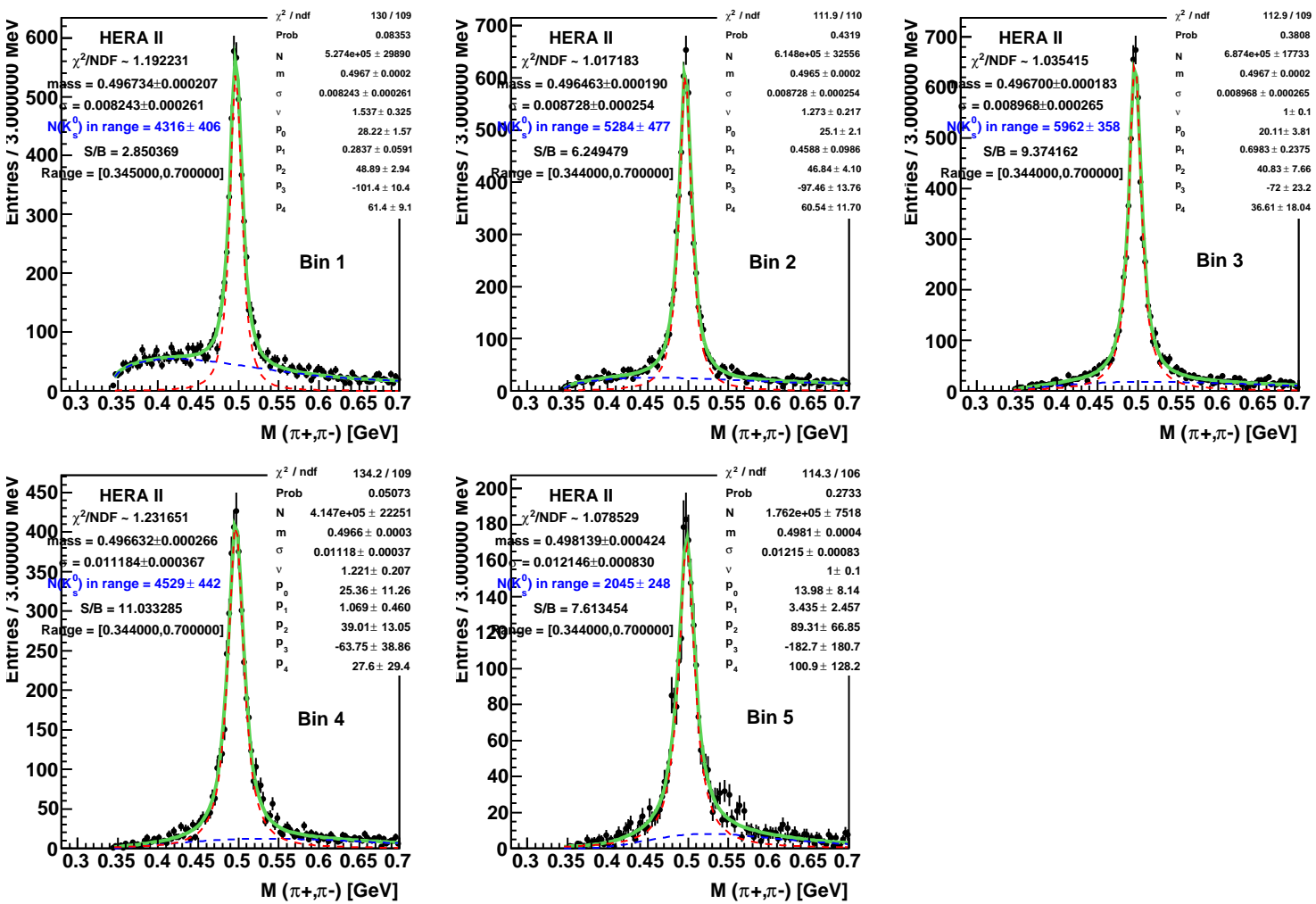
Figure F.7: Fits to the invariant mass distribution from data in bins of $p_T^{CBF}$ for the current hemisphere in the Breit Frame.

Figure F.8: Fit to the invariant mass distribution from data in bins of $p_T^{TBF}$ for the target hemisphere in the Breit Frame.
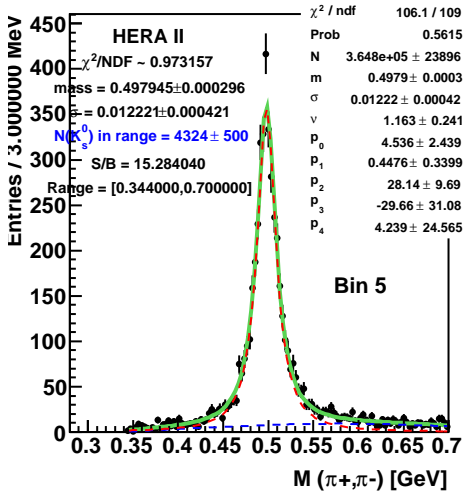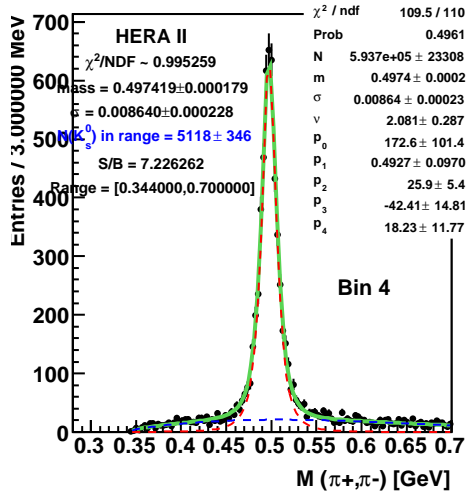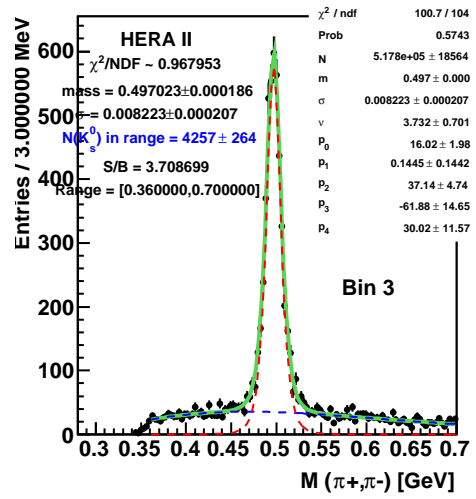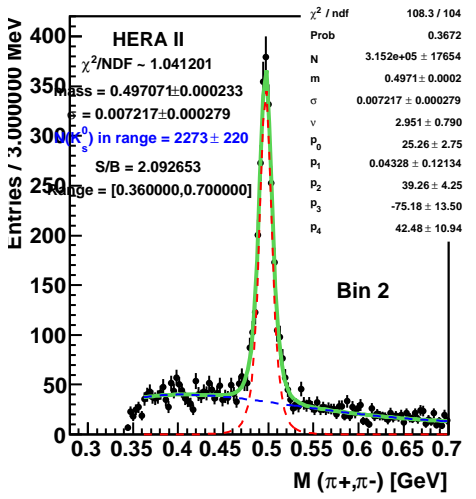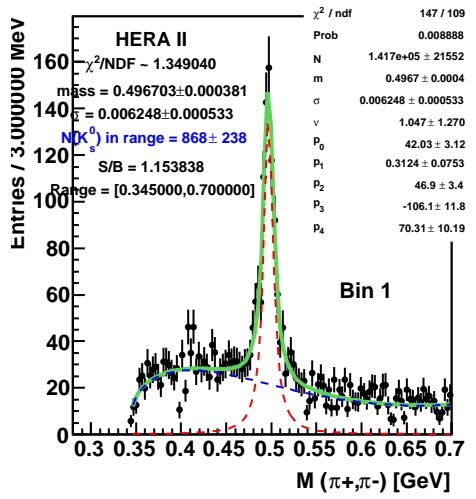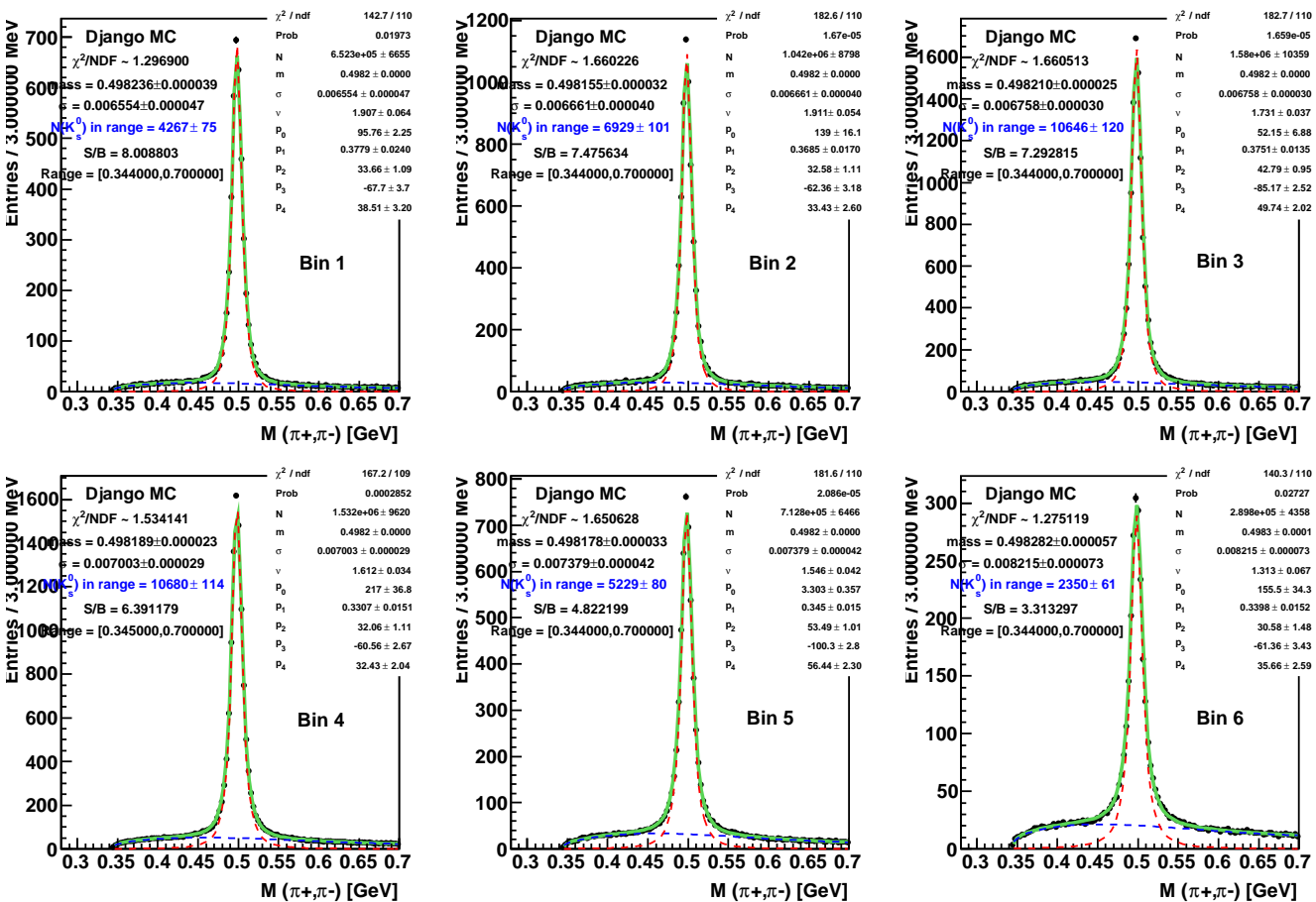
Figure F.9: Fits to the invariant mass distribution from Django Monte Carlo in bins of $Q^2$.

Figure F.10: Fits to the invariant mass distribution from Django Monte Carlo in bins of $x$.
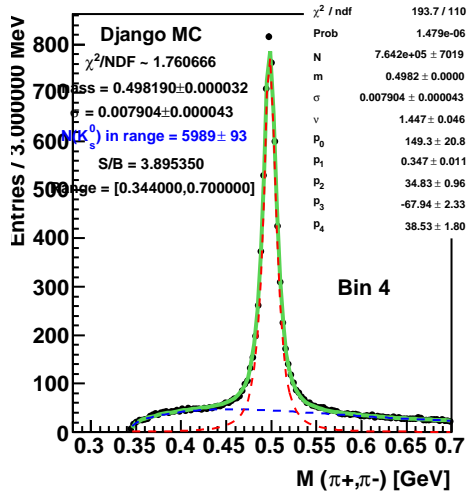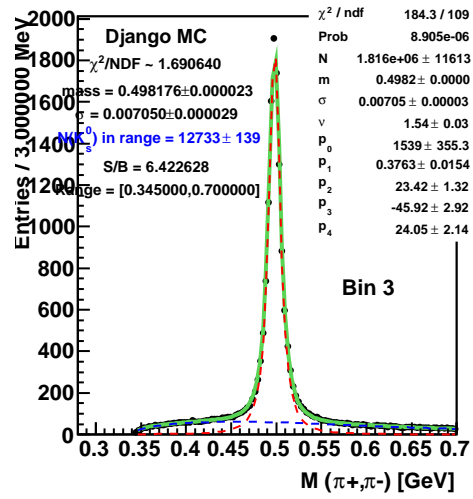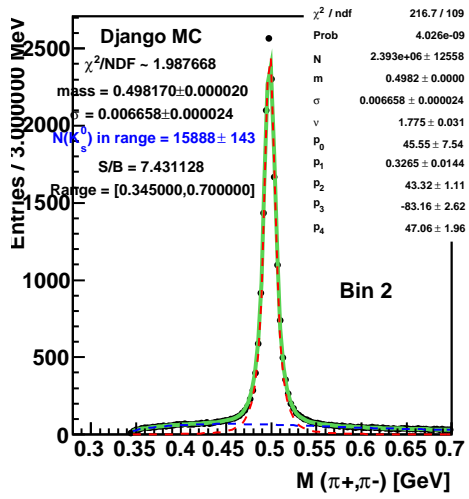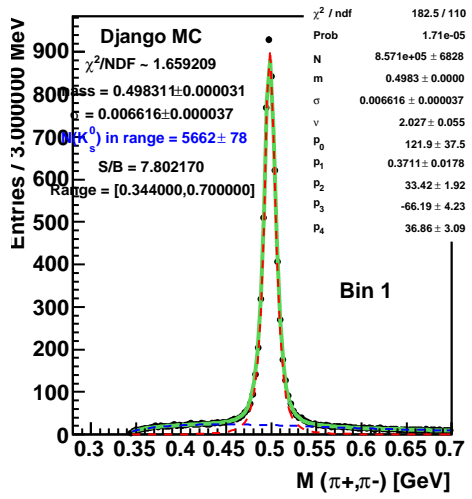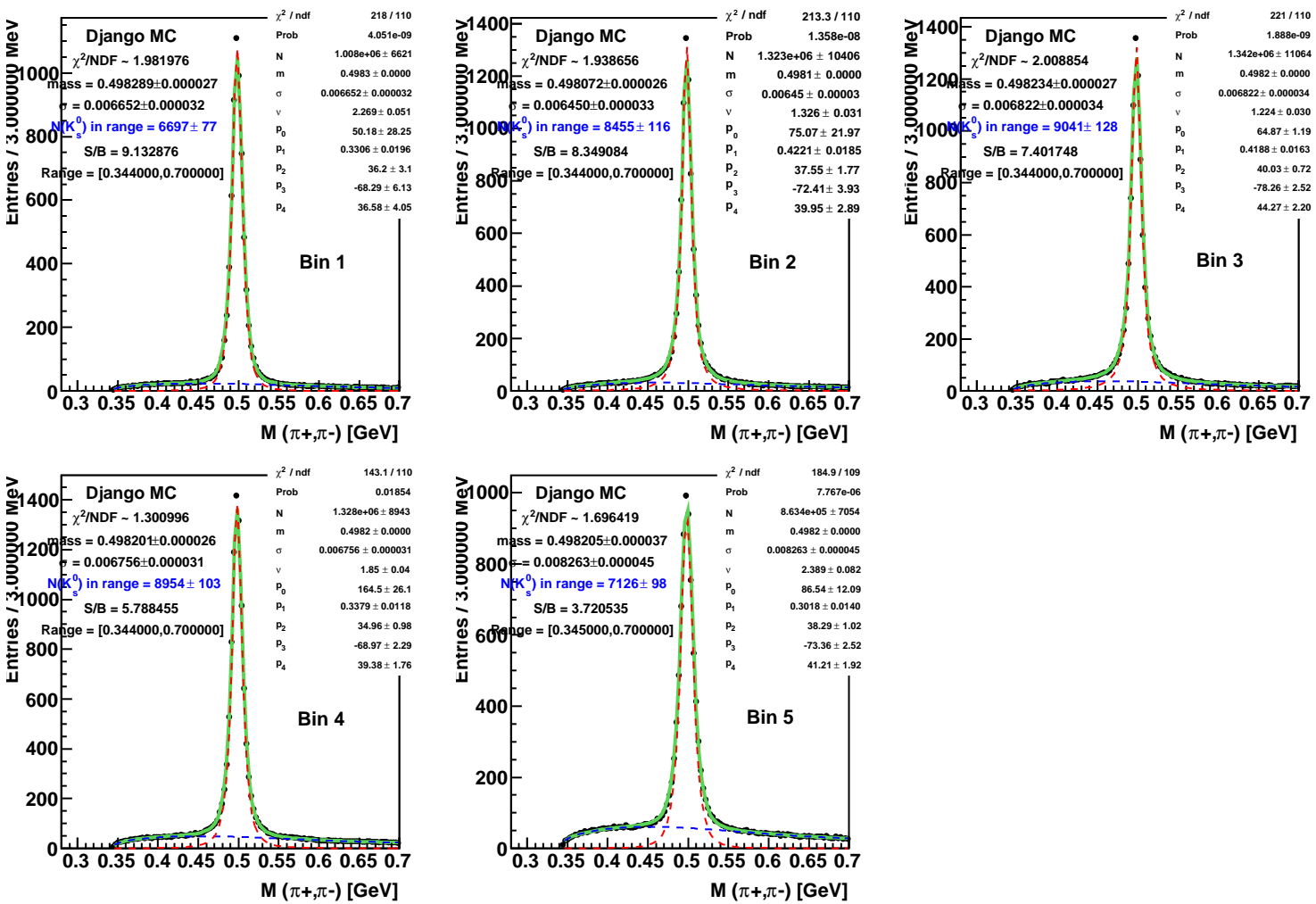
Figure F.11: Fits to the invariant mass distribution from Django Monte Carlo in bins of $\eta$.

Figure F.12: Fits to the invariant mass distribution from Django Monte Carlo in bins of $p_T$.
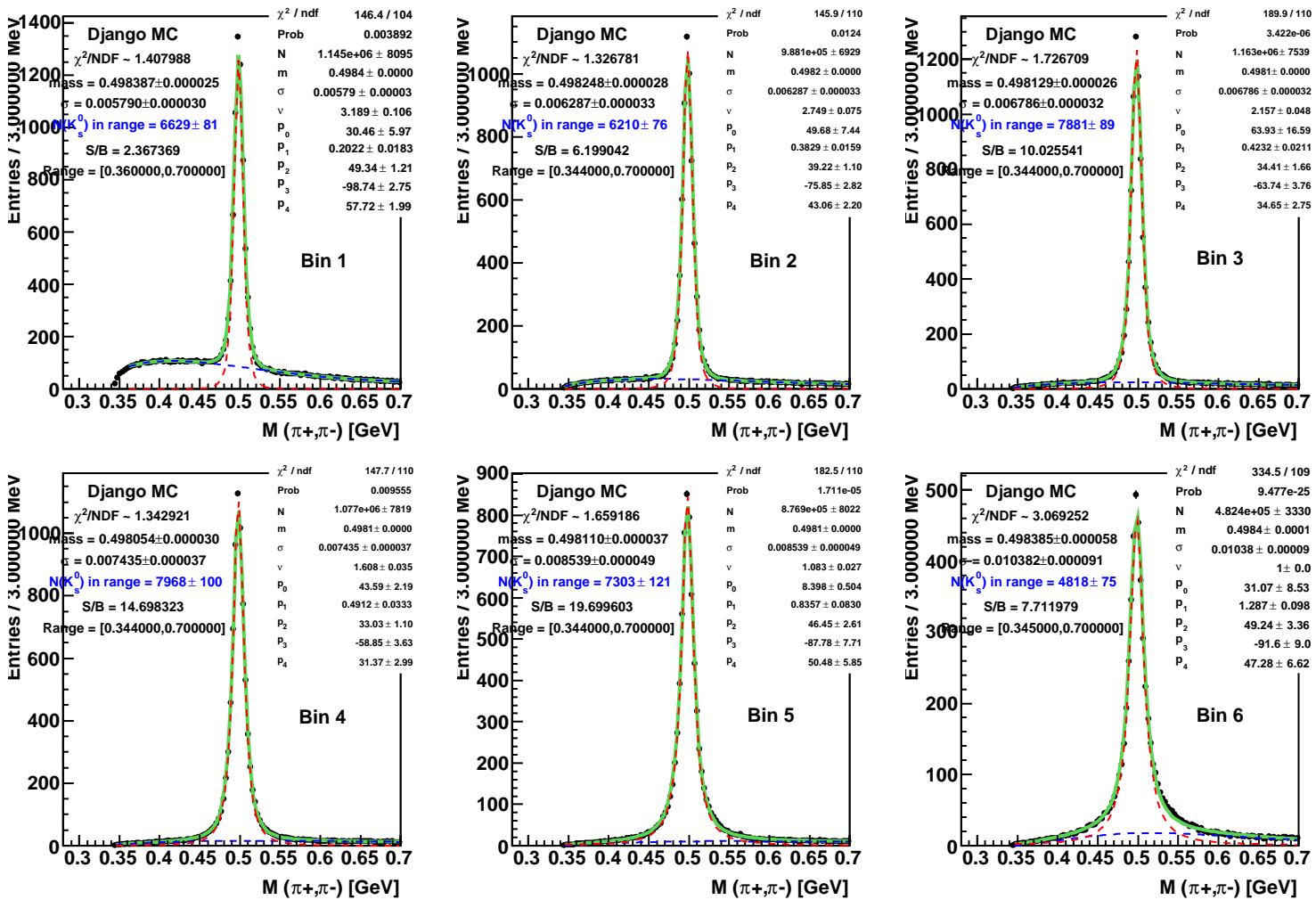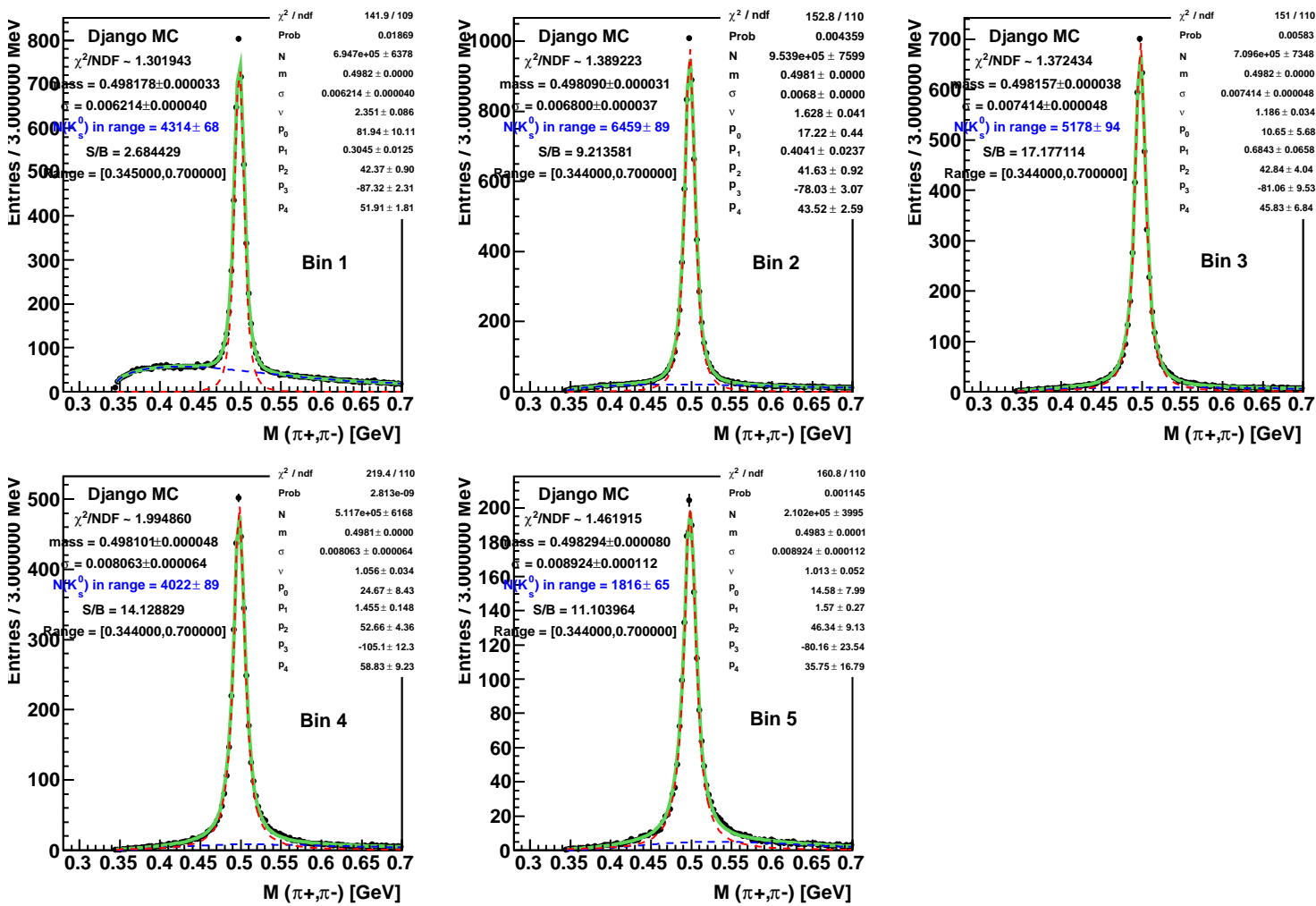
Figure F.13: Fits to the invariant mass distribution from Django Monte Carlo in bins of $x_p^{CBF}$ for the current hemisphere in the Breit Frame.

Figure F.14: Fits to the invariant mass distribution from Django Monte Carlo in bins of $x_p^{TBF}$ for the target hemisphere in the Breit Frame.
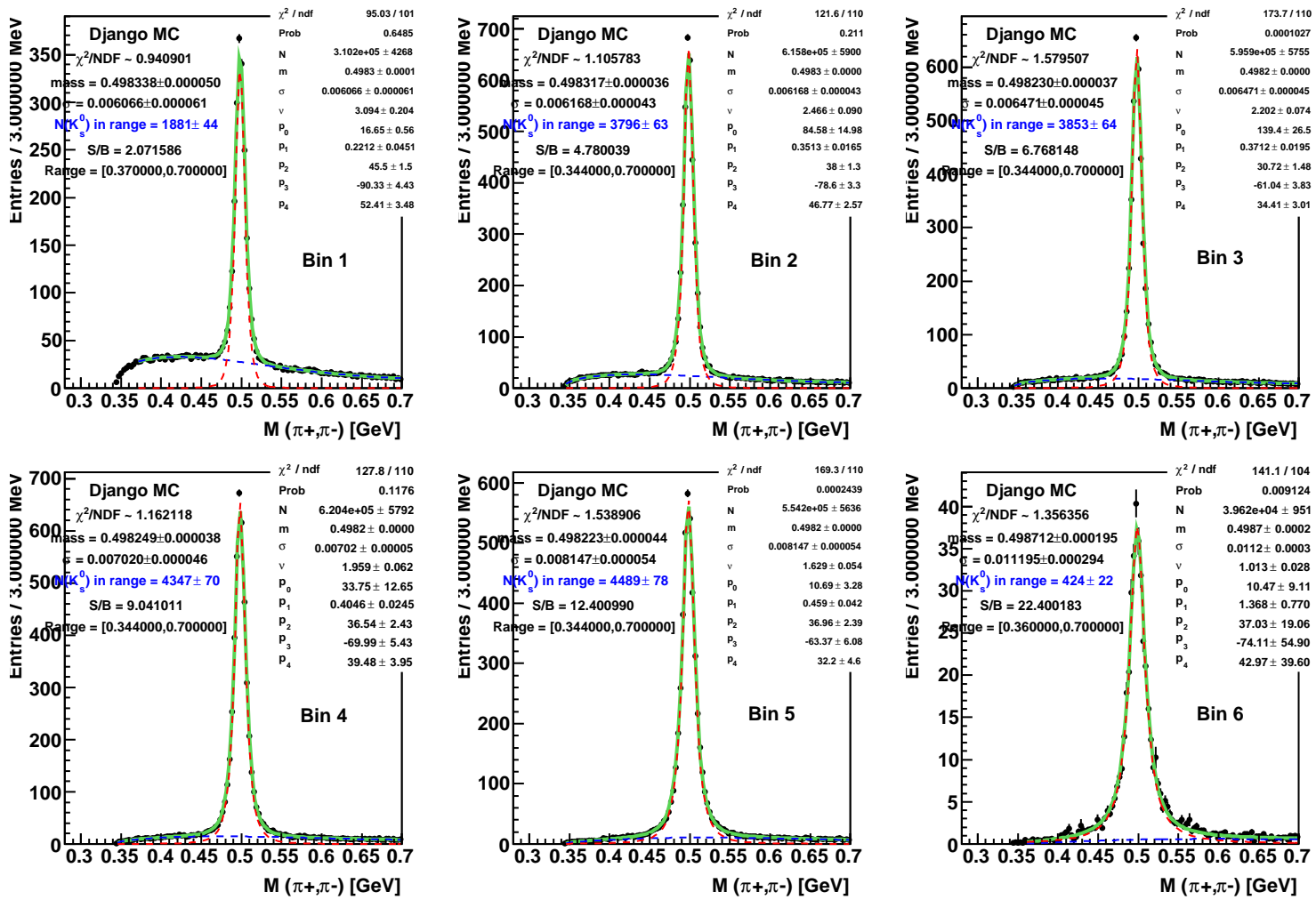
Figure F.15: Fits to the invariant mass distribution from Django Monte Carlo in bins of $p_T^{CBF}$ for the current hemisphere in the Breit Frame.
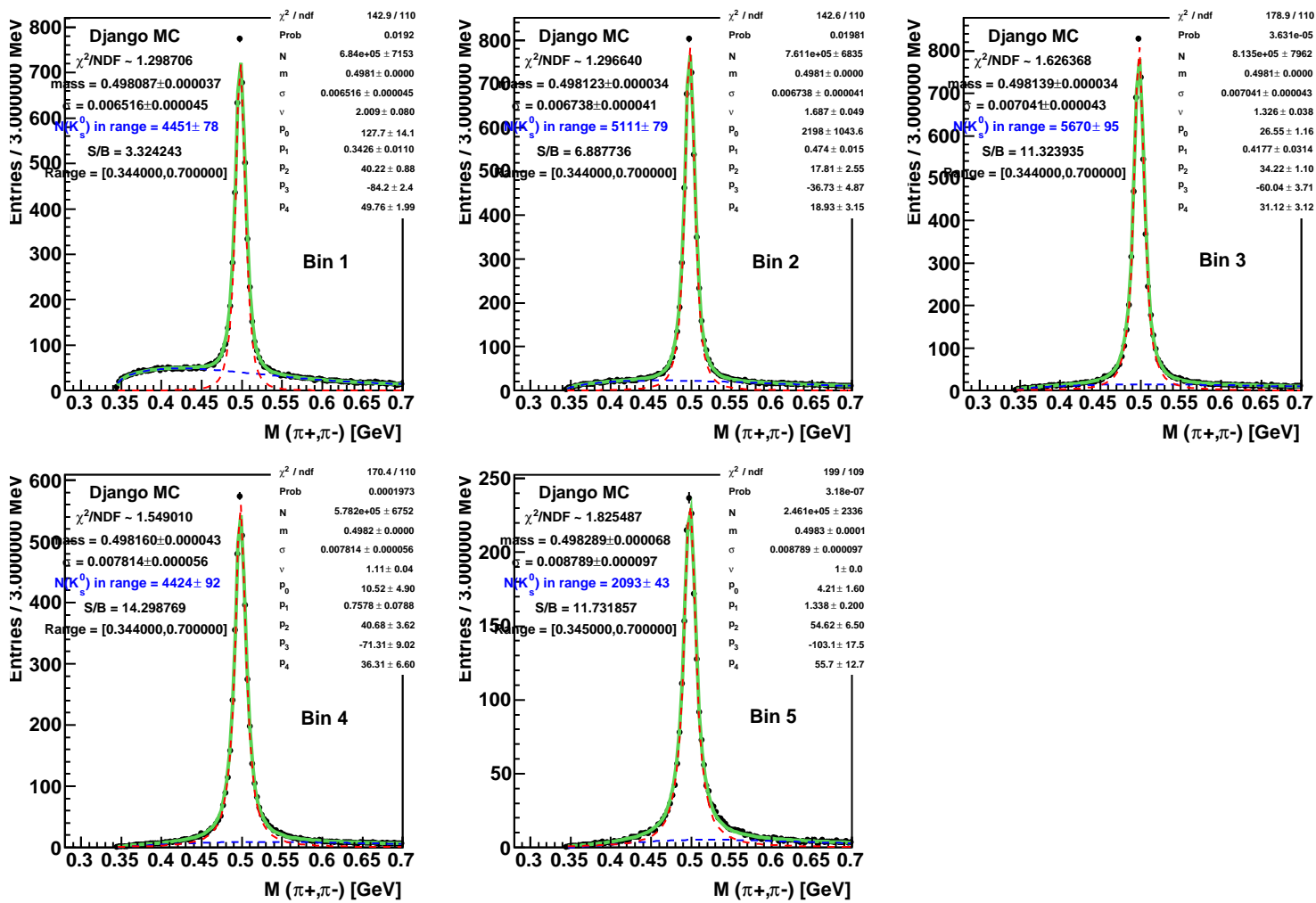
Figure F.16: Fits to the invariant mass distribution from Django Monte Carlo in bins of $p_T^{TBF}$ for the target hemisphere in the Breit Frame.
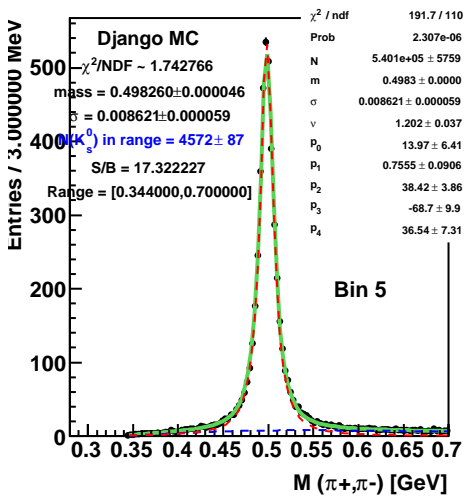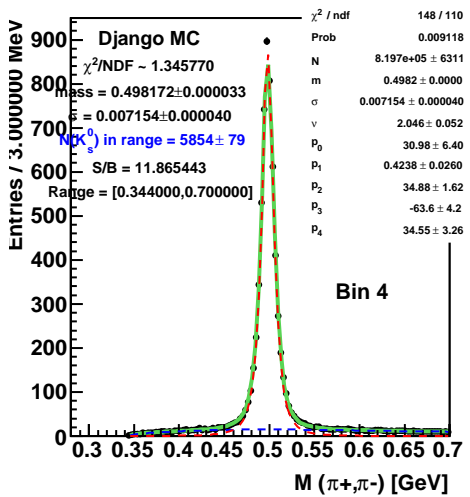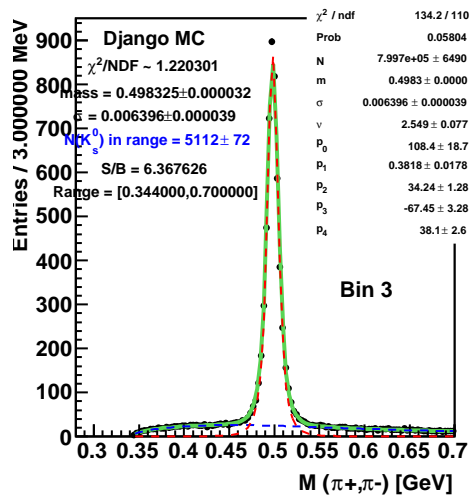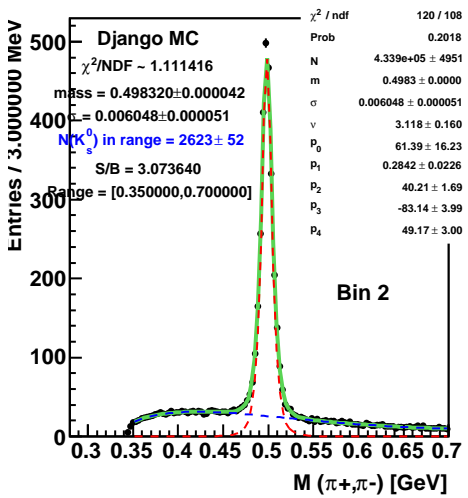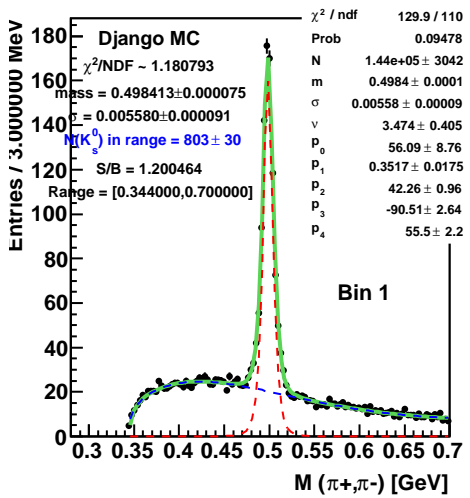
# Appendix G

# Resumen del trabajo de tesis

# Producción de $K_S^0$ a $Q^2$ altas en dispersión $ep$ inelástica profunda en H1

En esta tesis se presentan los resultados correspondientes a la primera medición de la producción de mesones $K_S^0$ a altas $Q^2$ usando los datos colectados con el detector H1 en el laboratorio DESY en Hamburgo, Alemania. Los datos analizados corresponden al período conocido como HERA II, que comprende los años 2004-2007 con una luminosidad acumulada de 340 pb$^{-1}$.

El laboratorio DESY cuenta con un colisionador de partículas llamado HERA que acelera protones hasta una energía de 920 GeV y electrones (o positrones) a energías de hasta 27.5 GeV haciendolas colisionar en cuatro puntos estratégicos alrededor de su circunsferencia, uno de ellos donde se localiza el detector H1 (Figura 3.1).

Este análisis se lleva a cabo despues de seleccionar la muestra de eventos de dispersión inelástica profunda (DIS por sus siglas en inglés) como se muestra en la Figura 1.1. Los eventos DIS de corriente neutra se caracterizan por la interacción dura de un electrón con un protón a través del intercambio de un boson neutro ($\gamma$ o $Z^0$), como resultado se tiene un electrón dispersado y un conjunto de partículas

167

hadronicas resultantes del rompimiento del protón, a este conjunto se le denomina sistema de estados finales hadrónicos.

En el detector H1, los eventos DIS a $Q^2$ altas se identifican por la medición del electrón dispersado usando el calorímetro de Argón líquido (LAr) mientras que los estados finales hadrónicos son reconstruidos con los detectores centrales de trajectoria para determinar su carga y momento, y por el calorímetro LAr para la determinación de su ángulo polar y su energía. Los eventos DIS se describen usando dos de las siguientes variables invariantes de Lorentz, el cuadrimomento transferido al cuadrado del fotón $Q^2$, la inelasticidad $y$ y la variable de Bjorken $x$.

El meson $K_S^0$ puede ser producido por cuatro mecanismos diferentes, ver Figura 2.3:

a) El proceso de producción dura del modelo de quarks partónicos (QPM) que consiste en la interacción directa de un quark extraño procedente del mar de quarks en el protón con el fotón virtual emitido por el electrón.

b) Por fusión de bosón gluón (BGF), en el cual un gluón del quark se divide en un par quark-antiquark extraño y uno de ellos interactúa con el electrón.

c) Por decaimiento de quarks pesados, producidos primeramente por el proceso BGF, a quarks extraños.

d) Por el proceso de hadronización que se da a partir de la fragmentación del campo de color en pares quark-antiquark.

A $Q^2$ altas los cuatro procesos mencionados arriba contribuyen significativamente a la producción de $K_S^0$ .

Los estudios de extrañeza son importantes no sólo por la medición de la producción, sino también porque permiten probar modelos teóricos basados en procesos de hadronización y fragmentación. La comparación directa de las simulaciones Monte Carlo con las mediciones del experimento ayudan a mejorar el entendimiento actual de aspectos de CromoDinámica Cuántica (QCD) así como a optimizar los parámetros de los programas de simulación. En particular, para los programas que

describen el proceso de hadronización por medio del modelo de cuerdas Lund, estas comparaciones de predicción-medición proporcionan una prueba de la universalidad del factor de supresión de extrañeza $\lambda_s$.

En este caso de usan dos programas de simulación de eventos DIS, Rapgap y Django, referidos como MEPS y CDM respectivamente en la Figura 1.3. MEPS se basa en elementos de matriz mas la cascada de partones descritas por medio de las ecuaciones de evolución DGLAP que tienen un orden muy fuerte en el momento transverso $k_T$ de los gluones emitidos. CDM también usa elementos de matrices pero la emisión de gluones es independiente del momento transverso (no hay orden en $k_T$) tal cual lo hace el modelo de color dipolar. Ambos modelos tienen una interfase al modelo Lund para describir la hadronización.

El modelo Lund cuenta con tres parámetros importantes para describir la producción de quarks, el factor de supresión de extrañeza $\lambda_s$ y los factores de supresión di-quark, $\lambda_{qq}$ y $\lambda_{sq}$, que describen la probabilidad relativa de producción de un par quark-antiquark extraño con respecto a los pares quark-antiquark ligeros apartir del campo de color, la probabilidad relativa de creación de un di-par de quarks con respecto a un par de ellos, y la probabilidad de crear di-pares de quarks respecto a pares. Estos parámetros son fijados a los valores proporcionados por la colaboración ALEPH: $\lambda_s = 0.286$, $\lambda_{qq} = 0.108$ y $\lambda_{sq} = 0.690$. Tanto CDM y MEPS son simulados con la función de densidad de partones (PDF) CTEQ6L.

El mesón $K_S^0$ se identifica por medio de su canal de decaimiento mas frecuente: $K_s^0 \to \pi^+\pi^-$. Las partículas hijas, $\pi^\pm$, se reconstruyen a partir de trajectorias de buena calidad medidas en los detectores de trajectoria de H1 que coinciden en un vértice secundario común, el cual esta desplazado cierta distancia del vértice primario de interacción $ep$. El espacio de fase elegido para esta tesis se define por $145 < Q^2 < 20000$ GeV$^2$, $0.2 < y < 0.6$, $-1.5 < \eta(K_S^0) < 1.5$ y $p_T(K_S^0) > 0.3$ GeV, es decir para regiones centrales del detector.

La distribución de masa invariante de los candidatos a $K_S^0$ seleccionados se aprecia en la Figura 4.4 de donde se extraen 38154 $K_S^0$ despues de hacer un ajuste con una

distribución t-student para describir la señal y la función $p_0(x - 0.344)^{p_1} * exp(p_2 x +$
$p_3 x^2 + p_4 x^3)$ para el ruido.

La sección transversal inclusiva medida en la región cinemática accesible es de
$\sigma_{vis} = 531 \pm 17$ (stat)$^{+37}_{-39}$ (sys) pb donde varias fuentes de error sistematico son
consideradas. La producción diferencial de $K_S^0$ en función de las variables $Q^2$, $x$, $\eta$
y $p_T$ del marco de referencia del laboratorio se presentan en la Figura 6.2 donde la
medición corresponde a los puntos negros y la comparación con los modelos CDM
y MEPS con $\lambda_s = 0.22$ y $\lambda_s = 0.286$ respectivamente, se aprecia en la parte baja
de cada gráfica. También es posible ver que las mediciones decrecen rápidamente
cuando $Q^2$ y $p_T$ toman valores cada vez mas altos, mientras que el comportamiento
en función de $x$ y $\eta$ es mas bien de subida y bajada. Los datos son mejor descritos
en forma y normalización por los modelos que tienen el valor de $\lambda_s = 0.286$. Tanto
CDM como MEPS tienen comportamientos similares.

Las secciones trasversales también son medidas diferencialmente en el marco de
referencia Breit (Figure 6.3), tanto en la región de corriente (CBF) como en la región
del blanco (TBF), en función de la fracción de momento $x_p$ y de momento trasverso
$p_T$. La producción de $K_S^0$ decrece a medida que los valores de estas variables son
mayores. Los modelos CDM y MEPS con $\lambda_s = 0.286$ dan buena descripción de los
resultados en la región de corriente donde el mecanismo de producción preferido es
el proceso de interacción dura, mientras que en el hemisferio del blanco los diferentes
modelos permiten observar cierta sensibilidad al parámetro $\lambda_s$ que es lo esperado
debido a que el proceso de hadronización es el que domina en esta región.

Las razón de sección transversal de los mesones $K_S^0$ con respecto a la de partículas
cargadas seleccionadas en el mismo espacio de fase, también se mide en el marco del
laboratorio y se presentan en la Figura 6.4, una de las ventajas es la reducción
de las fuentes de incertidumbre sistemática y por tanto la disminución del error
sistemático total. La razón de producción es casi plana en función de $Q^2$, hay una
pequeña caída en función de $x$ y $\eta$, y sube a medida que $p_T$ incrementa. Este último
comportamiento se debe a que los mesones llevan más momento comparado con

las partículas cargadas más ligeras que en su mayoría son piones. La forma y la normalizacion de las mediciones son descritas por los modelos con $\lambda_s = 0.286$.

Las gráficas de densidad, que se definen como la razón de la producción de $K_S^0$ con respecto a los eventos DIS seleccionados en la misma region cinemática, se miden diferencialmente en función de $Q^2$ y $x$ (Figura 6.5). La razón promedio descansa aproximadamente en 0.4 independientemente de las variables, indicando que la fracción de producción es igual en cualquier región. Los modelos con $\lambda_s = 0.286$ describen los resultados bastante bien en $Q^2$ pero predicen una pequeña caída en $x$ que no corresponde a la medición.

La gráfica 6.6 muestra los resultados de $K_S^0$ en función de $x_p^{CBF}$ en la región de corriente para tres regiones distintas de $Q^2$ normalizadas a la sección trasversal total de eventos DIS en cada región de $Q^2$. Es posible ver el factor de escalamiento de las funciones de fragmentación.

Otros estudios realizados son la comparación de las secciones trasversales diferenciales a modelos CDM con los diferentes PDFs: CTEQ6L, H12000LO y GRVLO, ver Figura 6.7. Los modelos dan descripciones similares en la forma pero solamente CTEQ6L y H12000LO describen las mediciones en normalización, GRVLO subestima los resultados debido a la ausencia de contribución de los quarks pesados encanto $c$ y belleza $b$. Resultados similares se obtienen en el marco de referencia Breit.

La contribución de los sabores de quarks es estudiada usando el programa Rapgap con $\lambda_s = 0.286$ como es posible ver en la Figuras 6.8 y 6.9. Los quarks ligeros $u$ y $d$ del proceso de fragmentación dominan en función de todas las variables, así el mecanismo de producción principal de mesones $K_S^0$ es la hadronización. La contribución de los quarks pesados $c$ y $b$ son la segunda más alta en la mayoría de los bins, estos provienen del proceso de decaimiento principalmente. La contribución del quark $s$ permanece como la más baja pero llega a ser relevante a valores altos de $Q^2$, $x$ y $p_T$ (no olvidar la escala logarítmica), mientras que en función de $\eta$ es casi constante. Los procesos de producción para $s$ son principalmente la interacción dura QPM y la fusión de bosón gluón. En función de variables del marco de referencia Breit, la contribución

del quark $s$ a la producción de $K_S^0$ llega a ser más importantes a valores altos de $x_p$ y $p_T$, especialmente en el hemisferio de corriente donde incluso iguala a la contribución de quarks pesados.

# Bibliography

[1] M. Gell-Mann, *"A Schematic model of Baryons and Mesons"*, Phys. Lett. 8 (1964) 214.

[2] R. P. Feynman, *"Very High-Energy Collisions of Hadrons"*. Phys. Rev. Lett. **23** (1969) 1415.

[3] J. D. Bjorken y Emmanuel A. Paschos. *"Inelastic electron proton and gamma proton scattering, and the structure of the nucleon"*. Phys. Rev., 185 (1969) 1975.

[4] F. Halzen && A. Martin, *"Quarks and Lepton: An introductory course in modern particle physics"*, Wiley && Sons, New York 1990.

[5] C. Adloff, et al. *"Measurement and QCD analysis of neutral and charged current cross sections at HERA"*, Eur. Phys. J. C30 (2003) 1, [`hep-ex/0304003`].

[6] A. C. Benevenutti, et. al., *"Test of QCD and a measurement of $\Lambda$ from scaling violations in the proton structure function $F_2(x, Q^2)$ at high $Q^2$"*, Phys. Lett. **B 223** (1989) 490.

[7] P. Amaudruz, et. al., *"Proton and deuteron $F_2$ structure functions in deep inelastic muon scattering"*, Phys. Lett. **B 295** (1992) 159.

[8] M. Arneodo, et. al., *"Measurement of the proton and the deuteron structure functions"*, $F_2^p$ and $F_2^d$, Phys. Lett. **B 364** (1995) 107.

[9] G. D. Rochester and C. C. Butler, *"Evidence for the existence of new unstable elementary particles"*, Nature 160 (1947) 855.

[10] M. Gell-Mann and A. Pais, *"Behavior of neutral particles under charge conjugation"*, Phys. Rev. 97 (1955) 1387.

[11] Particle Data Book, http://pdg.lbl.gov

[12] U. Bassler and G. Bernardi, *"Structure function measurements and kinematic reconstruction at HERA"*, DESY 97-137, [`hep-ex/9801017`].

[13] Yu. L. Dokshitzer, *"Calculation of the structure functions for deep inelastic scattering and $e^+e^-$ annihilation by perturbation theory in quantum chromodynamics"*, Sov. Phys. **JETP 46** (1977) 641; V. N Gribov and L. N. Lipatov, *"$e^+e^-$ pair annihilation and deep inelastic ep scattering in perturbation theory"*, Sov. J. Nucl. Phys. **15** (1972) 675; G. Altarelli and G. Parisi, *"Assymptotic freedom in parton language"*, Nucl. Phys. **B 126** (1977) 298.

[14] E. A. Kuraev, L. N. Lipatov and V. S. Fadin, *"The pomeranchuk singularity in nonabelian gauge theories"*, Sov. Phys. **JEPT 45** (1977) 199; Y. Y. Balitsky and L. N. Lipatov, *"The pomeranchuk singularity in quantum chromodynamics"*, Sov. J. Nucl. Phys. **28** (1978) 822.

[15] B. Andersson, G. Gustafson, G. Ingelman and T. Sjostrand, *"Parton fragmentation and string dynamics"*, Phys. Rept. **97** (1983) 31.

[16] B. Andersson, G. Gustafson, J. Samuelsson, *"Correlations in the hadronization process"*, Z. Phys. **C 64** (1994) 653.

[17] T. Sjostrand and M. Bengtsson, *"The lund Monte Carlo for jet fragmentation and $e^+e^-$ physics. Jetset Version 6.3: An Update"*, Comput. Phys. Commun. **43** (1987) 367;

[18] R. Barate, et. al., ALEPH collaboration, *"Studies of quantum chromodynamics with the ALEPH detector"*, Phys. Rept. **294** (1998) 1.

[19] R. Brun, et. al., *"GEANT3"*, Technical Report CERN-DD/EE/84-1, CERN, 1987.

[20] H. Spiesberger, *"HERACLES and DJANGOH: Event generation of ep interactions at HERA including radiative processes"*, August 8, 2005.

[21] A. Kwiatkowski, H. Spiesberger and H. J. Möhring, *"Heracles 4.1 - an event generator for ep interactions at hera including radiative processes"*, in Proc. of the Workshop on Physics at HERA, Vol.3, eds. W.Buchüller and G.Ingelman, (1991) 1294.

[22] H. Spiesberger, *"HERACLES and DJANGOH - Event generation of ep interactions at HERA including radiative processes. version 4.6.6"*, (Aug 2005). http://wwwthep.physick.uni-mainz.de/~hspiesb.djangoh/djangoh.html.

[23] G. Ingelman, A. Edin and J. Rathsman, *"LEPTO 6.5 - A Monte Carlo generator for deep inelastic lepton-nucleon scattering"*, Compt. Phys. Commun. **101** (1997) 108 [`hep-ph/9605286`].

[24] L. Lönnblad, *"Ariadne Version 4: A program for Simulation of QCD Cascades Implementing The Colour Dipole Model"*, Comput. Phys. Commun. **71** (1992) 15.

[25] J. Pumplin, D. R. Stump, J. Hunston, H. L. Lai, P. Nadolsky and W. K. Tung, *"New generation of parton distributions with uncertainties from global QCD analysis"*, **JHEP 07** (2002) 012 [`hep-ph/0201195`].

[26] M. Gluck, E. Reya and A. Vogt, *"Dynamical parton distributions of the proton and small X physics"*, Z. Phys. **C 67** (1995) 433.

[27] H. Jung, *"The RAPGAP Monte Carlo for deep inelastic scattering, version 3.2"*, October 5, 2009.

[28] D.H. Perkins, *Introduction to high energy physics*, Addison-Wesley Publishing Company.

[29] B. Müller and J. Refelski, *"Strangeness production in the quark gluon plasma"*, Phys. Rev. Lett. **48** (1982) 1066.

[30] T. Nakano, et. al., *"Evidence for a narrow S=+1 baryon resonance in photoproduction from the neutron"*, Phys. Rev. Lett. **91** (2003) 012002; J. Barth, et. al., *"Observation of an exotic S=+1 baryon in exclusive photoproduction from the deuteron"*, Phys. Rev. Lett. **B572** (2003) 127 [`hep-ex/0307018`]; V. Kubarovsky, et. al., Phys. Rev. Lett. **91** (2003) 252001; V. Kubarovsky, et. al., Phys. Rev. Lett., **92** (2004) 032001; V. Kubarovsky, et. al., *"Observation of an exotic baryon with S=+1 in photoproduction from the proton"*, Phys. Rev. Lett., **92** (2004) 032001.

[31] V. Uvarov, *"Inclusive particle production at LEP"*, 35th Rencontres de Moriond on QCD and High Energy Hadronic Interactions, Les Arcs, France, March 18-25 (2000) [`hep-ex/0011058`]; P. Abreu, et. al., *"Inclusive $\Sigma^-$ and $\Lambda(1520)$ production in hadronic Z decays"*, Phys. Lett. **B 475** (2000) 429 [`hep-ex/0103020`].

[32] J. H. Vossebeld, *"Recent results on particle productin from OPAL"*, 30th International Symposium on Multiparticle Dynamics, Tihany, Hungary, October 1-15 (2000) [`hep-ex/0101009`].

[33] P. Achard, *"$\Lambda$ and $\Sigma^0$ pair production in two-photon collisions at LEP"*, Phys. Lett. **B 536** (2002) 24 [`hep-ex/0204025`].

[34] M. Acciarri, et. al., *"Inclusive $\Sigma^+$ and $\Sigma^0$ production in hadronic Z decays"*, Phys. Lett. **B 479** (2000) 79 [`hep-ex/0002066`].

[35] P. Achard, et. al., *"Study of inclusive strange-baryon production and search for pentaquarks in two-photon collisions at LEP"*, Eur. Phys. J. **C 49** (2007) 395 [`hep-ex/0609054`].

[36] K. Hicks, A. Daniel, *"$K_S^0$ hadronization following DIS at CLAS"*, DIS 2009, Madrid April 26-30 (2009).

[37] A. Förster, et. al., *Phys. Rev.*, **C75** (2007) 024906; H. Oeschler, *"Strangeness production at 1-2 AGeV"*, Conference contribution for Interational school of nuclear physics, Erice, Sicily, September 16-24 (2009) [ArXiv:hep-ph/0902.0865].

[38] O. N. Hartmann, *"Studying strange meson production with FOPI"*, Proceeding of the 10th International Workshop on Meson production, properties and interaction (MESON), Krakow Poland, 2008 [nucl-ex/0810.2437]; M. Merschmeyer, et. al., *"$K_s^0$ and $\Lambda$ production in Ni+Ni collisions near threshold"*, Phys. Rev. **C 76** (2007) 024906 [`nucl-ex/0703036`].

[39] J. Pietraszko, L. Fabbietti, *"Strangeness production at SIS measured with HADES"*, Nucl. Phys. **A 834** (2010) 288c [nucl-ex:0911.0516].

[40] A. Schmah, L. Fabbietti, *"Results on strangeness production from HADES"*, (2009) [nucl-ex/0911.0300]; L. Farbietti, *New strangeness results from HADES*, J. Phys. G Nucl. Part. Phys. **36** (2009) 064005.

[41] S. Radomski, *"CERES measurement of strangeness production at top SPS energy"*, J. Phys. G: Nucl. Part. Phys. **35** (2008) 044003.

[42] A. Mischke, et. al., *"Energy dependence of $\Lambda$ and $\bar{\Lambda}$ production at CERN SPS energies"*, Nucl. Phys. **A 715** (2003) 453 [`nucl-ex/0209002`]; *"Strange particle production in nuclear collisions at CERN-NA49"*, Proceedings of Rencontres de Moriond (2002) [`hep-ex/0205042`].

[43] F. Antinori, et. al., *"Rapidity distributions around mid-rapidity of strange particles in Pb-Pb collisions at 158 A Gev/c"*, J. Phys. **G 31** (2005) 1345 [`nucl-ex/0509009`].

[44] V. Riabov, *"Measurement of the multi-hadron decays of $\Omega$, $K_s$ and $\eta$ mesons in heavy ion collisions at $\sqrt{s_{NN}}$ =200 GeV in the PHENIX experiment at RHIC"*, Proceeding to QM (2006) [`nucl-ex/0702046`].

[45] A. Abulencia, et. al., *"Measurements of inclusive W and Z cross sections in p and $\bar{p}$ collisions at $\sqrt{s}$ = 1.96 TeV"*, J. Phys **G 34** (2007) 2457 [`hep-ex/0508029`]; B.I. Adelev, et.al, *"Identified baryon and meson distributions at large transverse momenta from Au+Au collision at $\sqrt{s_{NN}}$ = 200 GeV"*, Phys. Rev. Lett. **97** (2006) [`nucl-ex/0606003`].

[46] G. G. Barnaföldi, G. Fai, et. al., *"Is strangeness still strange at the LHC?"*, Nucl. Part. Phys. **35** (2008) 044057 [`hep-ph/0710.4373`]

[47] C. Blume, *"Strangeness production at the SPS"*, Proceedings to the ISMD09 conference (2009) [`nucl-ex/0910.5815`].

[48] A. R. Timmins, *"Strangeness production in heavy-ion collisions at STAR"*, Conference proceedings for Quark Matter 2009, Knoxville, Tenesee, March 30 - April 4 (2009), Nucl. Phys. **A 830** (2009) 829c [`hep-ex/0907.4533`].

[49] B. Zou, J.Xie, *"Strangeness production from pp collisions"*, 10th International Conference on Nucleus-Nucleus Collisions, Beijing, China, August 16-21 (2009), Nucl. Phys. **A 834** (2010) 544c [`nucl-th/0910.4421`].

[50] R. Vernet, *"Prospects for strangeness measurement in ALICE"*, Phys. Atom. Nucl. **71** (2008) 1523 [`nucl-ex/0802.0095`].

[51] I. Abt, et. al., *"$K^{*0}$ and rho meson production in proton-nucleus interactions at $\sqrt{s}$ =41.6 GeV"*, Eur. Phys. J. **C50** (2007) 315.

[52] I. Abt, et. al., *"V0 production in p+A collisions at $\sqrt{s}$ =41.6 GeV"*, Eur. Phys. J. **C51** (2008).

[53] S. L. Belostotsky, *"Strange particle production and polarization of lambda hyperons in the HERMES experiment"*, Nucl. Phys. Proc. Suppl., **79** (1999) 526; O. Grebunyuk, *"Transverse polarization of $\Lambda$ and $\bar{\Lambda}$ produced inclusivelyin e N scattering at HERMES"*, Acta Phys. Polon. **B33** (2002) 3797.

[54] D. H. Saxon, *"Inclusive $K_s^0 K_s^0$ resonance production in ep collisions"*, DIS 2009 conference, Madrid April 26-30, (2009); S. Chekanov et al, *"Observation of $K_s^0 K_s^0$ resonances in deep inelastic scattering at HERA"* Phys. Lett. **B578** (2004) 33 [`hep-ex/0308006`].

[55] M. Acciari et. al., *"$K_s^0 K_s^0$ final state in two photon collisions and implications for glueballs"*, Phys. Lett. **B 501** (2001) 173 [`hep-ex/0011037`].

[56] M. Althoff et. al., *"Production of $K\bar{K}$ pairs in photon-photon collisions and the excitation of the tensor meson f'(1515)"*, Phys. Lett. **B 121** (1983) 216.

[57] S. Chekanov, et al., *"Search for pentaquarks decaying to $\Xi\pi$ in deep inelastic scattering at HERA"*, Phys.Lett. **B610** (2005) 212 [`hep-ex/0501069`].

[58] S. Chekanov, et. al., *"Evidence for a narrow baryonic state decaying to $K_s^0 p$ and $K_s^0 \bar{p}$ in deep inelastic scattering at HERA"*, Phys. Lett. **B591** (2004) 7;

[59] S. Chekanov, et. al., *"Measurement of $K_S^0$ , $\Lambda$ and $\bar{\Lambda}$ production at HERA"*, Eur. Phys. J. **C 51** (2007) 1 [`hep-ex/0612023`];

[60] C. Risler, *"Produktion seltsamer neutraler Teilchen in tiefinelastischer streuung bei HERA"*, PhD thesis, Universität Hamburg (2003), DESY-THESIS-2004-038, http://www-h1.desy.de/publications/theses_list.html#YEAR2003 .

[61] M. Del Degan, *"Spectroscopy in ep scattering at HERA"*, PhD thesis, Swiss Federal Institute of Technology Zurich, http://www-h1.desy.de/publications/theses_list.html#YEAR2008 .

[62] A. Falkiewicz, *"Strangeness production in deep inelastic ep collisions in the H1 Experiment"*, PhD thesis, , http://www-h1.desy.de/publications/theses_list.html#YEAR2009 .

[63] A. Aktas, et. al., *"Search for a narrow baryonic resonance decaying to $K_s^0 p$ or $K_s^0 \bar{p}$ in deep inelastic scattering at HERA"*, Phys. Lett. **B 639** (2006) 202 [`hep-ex/0604056`].

[64] A. Aktas, et. al., *"Search for baryonic resonances decaying to $\Xi\pi$ in deep-Inelastic ep Scattering at HERA"* Eur. Phys. J **C 52** (2007),

[65] D. Sunar, *"Measurement of $K^*(892)$ production in deep inelastic ep scattering with the H1 detector at HERA"*, PhD thesis, Universiteit Antwerpen, DESY-THESIS-2009-023, http://www-h1.desy.de/publications/theses_list.html#YEAR2009 .

[66] F. D. Aaron, et. al., H1 Collaboration, *"Strangeness production at low $Q^2$ in deep-inelastic ep scattering at HERA"*, Eur. Phys. J. **C61** (2009) 185 [`arXiv:hep-ex/08104036`]; S. Aid, *"Strangeness production in deep-inelastic positron-proton scattering at HERA"*, Nucl. Phys. **B 480** (1996) 3 [`hep-ex/9607010`].

[67] J. Ruiz Tabasco, *"Strangeness production in deep inelastic ep scattering at HERA"*, EPS 2009 conference, Krakow, Poland, July 16-22 (2009).

[68] The H1 Collaboration, http://www-h1.desy.de.

[69] I. Abt, et. al., H1 Collaboration, *"The H1 detector at HERA"*, Nucl. Instrum. Meth. **A 386** (1997) 310.

[70] D. Pitzl, et. al., *"The H1 silicon vertex detector"*, Nucl. Instrum. Meth. **A 454** (2000) 334 [arXiv:hep-ex/0002044]; B. List, *"The H1 silicon tracker"*, *Nucl. Instrum. Meth.* **A 549** (2005) 33.

[71] J. Burger, et. al., *"The Central Jet Chamber of the H1 Experiment"*, Nucl. Instrum. Meth. **A 279** (1989) 217.

[72] M. C. Urban, *"The new CIP2k z-vertex trigger for the H1 experiment at HERA"*, PhD thesis, Universität Zürich, DESY-THESIS-2004/044.

[73] B. Andrieu, et. al., H1 Calorimeter Group Collaboration, *"The H1 Liquid Argon Calorimeter System"*, Nucl. Instrum. Meth. **A 336:460** (1993).

[74] I. Abt., et. al. *"The H1 Detector at HERA"*, H1-Internal Note, H1-01/98-533. Technical report.

[75] H. Bethe and W. Heitler, *"On the stopping of fast particles and on the creation of positive electrons"* Proc. Roy. Soc. Lond **A 146** (1934) 83.

[76] S. Habib, *"Unpolarized neutral current $e^{\pm}p$ cross section measurements at the H1 experiment, HERA"*, PhD thesis, Universität Hamburg, DESY-THESIS-2009-039, http://www-h1.desy.de/publications/theses_list.html#YEAR2009.

[77] J. Podolanski and R. Armenteros, *"Analysis of V-events"*, Phil. Mag. **45** (1954) 13.

[78] http://indico.ifj.edu.pl/MaKaC/sessionDisplay.py?sessionId=19&slotId=0&confId=11#2009-07-16

[79] J. Ruiz Tabasco, *"$K_S^0$ production in deep inelastic ep scattering at high $Q^2$"*, DIS 2010 conference, Florence, Italy, April 19-23, (2010).

[80] U. Bassler and G. Bernardi, *"On the kinematic reconstruction of deep inelastic scattering at HERA: the sigma method"*, Nucl. Instr. and Meth. **A361** (1995) 197 [`hep-ex/9412004`].

[81] U. Bassler and G. Bernardi, *"Structure function measurements and kinematic reconstruction at HERA"*, Nucl. Instrum. Meth. **A426** (1999) 583 [`hep-ex/9801017`].

[82] V. Karimäki, *"Fast code to fit circular arcs"*, HU-SEFT-1991-10 (1991).

[83] R. P. Feynman, *"Photon-Hadron Interactions"*, *Benjamin, N.Y.* (1972).

[84] K. H. Streng, T.F. Walsh and P.M. Zerwas, *"Quark and gluon jets in the Breit frame of lepton-nucleon scattering"*, Z. Phys **C2**, *Benjamin, N.Y.* (1979) 237, DESY79/10.